Planet Hunting and the Dynamical Structure of Planet-forming Disks

by

Jessica Speedie
Hon.B.Sc., McMaster University, 2020

A Dissertation Submitted in Partial Fulfillment of the
Requirements for the Degree of

DOCTOR OF PHILOSOPHY

in the Department of Physics and Astronomy

© Jessica Speedie, 2025
University of Victoria

All rights reserved. This Dissertation may not be reproduced in whole or in part, by photocopy or other means, without the permission of the author.

We acknowledge and respect the Lək̓ʷəŋən (Songhees and Xʷsepsəm/Esquimalt) Peoples on whose territory the university stands, and the Lək̓ʷəŋən and W̱SÁNEĆ Peoples whose historical relationships with the land continue to this day.

Planet Hunting and the Dynamical Structure of Planet-forming Disks

by

Jessica Speedie
Hon.B.Sc., McMaster University, 2020

Supervisory Committee

Dr. Ruobing Dong, Supervisor
Department of Physics and Astronomy / Kavli Institute for Astronomy and Astrophysics

Dr. Doug Johnstone, Departmental Member
Department of Physics and Astronomy / NRC Herzberg Astronomy and Astrophysics

Dr. JJ Kavelaars, Departmental Member
Department of Physics and Astronomy / NRC Herzberg Astronomy and Astrophysics

Dr. Ryan Loomis, Outside Member
National Radio Astronomy Observatory

Abstract

The assembly of planetary systems unfolds within the reservoir of 'leftover' material surrounding newborn stars. This thesis explores the use of interferometric observations at millimeter wavelengths to provide clues for unseen protoplanets at the earliest stages of formation, and to reveal the physical processes at play.

First we identify how the tell-tale wake driven by an embedded protoplanet manifests in the midplane dust layer of its host circumstellar disk, and quantify the observing requirements to recover the signal in mm continuum emission with ALMA. These constraints establish the feasibility of mm dust wakes as a protoplanet-detection technique.

Next, we apply our framework to a sample of ten circumstellar disks exhibiting kinematic evidence of wakes in ^{12}CO molecular line emission. Such applications are a vital ingredient to distinguishing protoplanetary velocity disturbances from those of non-planetary origin.

We also present the first direct measurement of gravitational instability in a planet-forming disk using ^{13}CO and C^{18}O molecular line emission. Our quantitative constraints on the kinematic structure in a disk with directly-imaged protoplanets demonstrates the physical mechanisms driving planet formation.

Finally, the ^{12}CO emission from AB Aurigae exhibits multiple infalling spiral streamers on 1000-au scales. Kinematic modeling pinpoints the region of impact with the disk to be near to candidate protoplanets, suggesting that planet formation cannot be understood without consideration of the surrounding star formation environment.

Table of Contents

List of Tables

List of Figures

Acknowledgements

This dissertation does not reflect the effort of one person, but the collective effort, mentorship, friendship, and generosity of many communities. I offer my sincerest thanks to:

Ruobing Dong, for your persistent support and guidance as my advisor over the last 5 years. Your confidence in me was the solid ground on which I found my feet, and at the same time, your encouragement was the conveyor belt beneath my feet that spurred me to achieve so much more than I could have imagined. Your constant forward-thinking helped me channel my curiosity productively, and your unlimited thoughtfulness brought so many things to my attention. Thank you for gifting me with well-formed projects that also allowed me to pursue my interests, and for giving me the freedom to turn over every rock whose underside I felt compelled to see. I grew so much from these many explorations.

My collaborators around the world, whose names I associate with such longheld admiration that I'm still jolted with glee every time they appear in my inbox. Working with each of you is a privilege I don't take for granted. The work you do resonates some deep bell of inspiration in me, calling me to rise to your occasion and dream of emulating your ways. The learning contained in this dissertation would not have been possible without your inspired ideas and expertise. It's a complete, pure joy to be part of an incredible global community of such dedicated and curious people. Here's to future projects and life long friendship.

My fellow graduate students in Victoria, for filling my life here with sunshine. Dori Blakely, William Thompson, Camryn Mullin, Xiaoyi Ma, Jiaqing Bi, Logan Francis, Arnaud Michel, Lowell Peltier, Fletcher Waller, Shunyuan Mao, Mars Eduardo, Chris Mann, Adam Johnson, Andre Fogal, Kaitlyn Hessel, Blake Ledger, Sam Fielder, Jaclyn Jensen, Scott Wilksonson, Simon Smith, Breanna Crompvoets, Mallory Thorp, Maan Hani, Mike Chen, Maheyer Shroff, Alex Beaubien, Bryn Lonsbrough, Dan Boyea, Vida Saeedzadeh and Bobby Bickley — you each touched me in unique and long-lasting ways for which I will be forever grateful. Sam, thank you for compiling this dissertation template.

The NRC Herzberg community, for support and inspiration on so many levels. Doug Johnstone, JJ Kavelaars, Nienke van der Marel, Brenda Matthews, Christian Marois, Wes Fraser, James di Francesco, Gerald Schieven and the amazing Helen Kirk — I'm so grateful for all our interactions, from research group meetings to video scripts to summer BBQs to morning coffees. James, your daily emails are a reliable dose of wonder and knowledge. Doug, I count on you for your questions. Nienke, thank you for being the glue that held our group

together during the pandemic. Helen, your and Karun's warmth and kindness knows no bounds, and your support has meant the world to me.

Our UVic P&A department administrative staff, Jennie Bartosik, Susan Gnucci, Cindy Kutyn, Monica Lee-Bonar, for helping me navigate the milestones towards a PhD degree with care and enthusiasm.

The NRAO community, which has come to feel like my home away from home. Ryan Loomis, Adele Plunkett, George Privon, John Tobin, Sebastian Nikischer, Sarah Wood, Cole Wampler, Tristan Ashton, Michael Sanchez, Amanda Kepley, Andy Lipnicky, Patrick Sheehan, Devaky Kunneriath, Dominic Ludovici, Natalie Butterfield, Rick Perley, John Carpenter and Anna Kapinska — you have all been an integral part of my journey as an astronomer. Ryan, I am forever indebted to you for how generous you've been with your time, expertise, ideas, resources, insights, advice, guidance, and encouragement, as a mentor and member of my PhD committee. You are an exponentiating force and an invaluable influence.

Everyone who makes ALMA tick, from the technicians working at 5000 m, to the cleaning and cafeteria staff at 2700 m, to the astronomers-on-duty night and day.

The community sharing open source software, code packages, and scripts. Rich Teague, Jeff Jennings, Ian Czekala, Sean Andrews, the DSHARP, MAPS and exoALMA collaborations, Christophe Pinte, Dan Price, Pablo Benítez-Llambay, Leo Krapp, Frédéric Masset, Tom Robitaille, Eric Koch, Adam Ginsburg, Jaime Pineda, Teresa Valdivia-Mena, Aashish Gupta, Chris White — just to name a few. The work in this dissertation is inseparable from these starting points, which in so many cases is only inches away from the goal line. Rich, your packages in particular are an invaluable tutor, and were instrumental every step of the way.

The developers of the fundamental software infrastructures —`numpy`, `scipy`, `astropy`, `cmasher`, `matplotlib`, and so, so, so many more— that make daily operations possible.

The financial support of the Natural Science and Engineering Research Council (NSERC), the National Radio Astronomy Observatory (NRAO), the North American ALMA Science Center (NAASC), and the Canadian Space Agency (CSA).

My family, whose support is the air beneath my wings for every dream I've ever pursued.

Dedication

For my docking station.

Chapter 1

Introduction

Of all the astronomical objects and environments that can be found in the universe, planets and their moons are the only places we recognize as *worlds*. This terminology betrays a sense of meaning and significance beyond merely aggregations of gas and dust assembled into compact orbs. A world is a place we can *go* — whether in a spaceship, or in the spaceship of the imagination[1].

Since 1960, we have launched some 200 spacecraft to vicariously visit and study the other worlds in our Solar System. These missions revealed an almost unimaginable diversity of worldly conditions, in entrancing detail. Over the decades, with successively higher resolution imaging, spectroscopy, magnetometry, radar, and even in-situ sampling, we have constructed ever-more comprehensive views of realms that are vastly different from the only world our species has ever directly experienced. What we discovered only encouraged our imagination to know no bounds.

When we turned our gaze beyond our Solar System, we confronted —and overcame— the formidable challenge of detecting planets orbiting distant stars: tiny points of light, each an alien Sun potentially hosting worlds of its own. In the years since the first discovery of an exoplanet around a Sun-like star in 1995 (Mayor & Queloz, 1995), we have surveyed the sky with missions such as *Kepler*/*K2* and *TESS* to detect and catalog a remarkable 5,893 exoplanets[2] or-

[1] Yes, of course this is a Carl Sagan reference. *(Cosmos: A Personal Voyage, 1980)*

[2] https://exoplanetarchive.ipac.caltech.edu/docs/counts_detail.html

biting 4,341 alien Suns. In doing so, our imaginations were again rewarded, as we discovered the existence of worlds for which there are no analogs in our Solar System — 'hot Jupiters', 'super-Earths', and 'water worlds'. Our journey led us to the understanding that our Solar System is not the archetype of all planetary systems, but rather stands apart from those discovered so far (Winn & Fabrycky, 2015). Equally striking is the statistical inference that there may be more planets than stars in our galaxy (Lissauer et al., 2023).

Having firmly established that planets are both *diverse* and *ubiquitous*, the pressing question becomes one of origin. To what history do we owe the variety of observed planetary system properties? What physical processes lead so reliably to such diverse end-states? *Where, when, and how does a world come to be?*

To answer these questions, we must look back in time and catch planetary systems in the act of forming. We have found, encircling the *youngest* alien Suns, vast rotating disks of gas and dust —like celestial frisbees— actively undergoing the remarkable transformation into planetary systems. The nascent planets in these environments, lying at the dawn of their lives, also lie at the frontier of our understanding. By scrutinizing these sites, we can assess the diversity of conditions inherited by these forming planets, and begin to understand the physical processes that assemble diffuse gas and dust into compact orbs so reliably.

The focus of this dissertation is twofold. First, to search for the very youngest worlds by recovering the characteristic imprints they leave on their formation environment. Second, to characterize these environments —particularly the internal dynamics— in order to diagnose the physical processes that may govern planet formation. The pursuit of these goals is made possible through the exquisite power of ALMA, the Atacama Large (sub-)Millimeter Array.

Figure 1.1: Eighteen of ALMA's fifty-four 12 m antennas at the Array Operations Site, located at an altitude of 5000 m on the Chajnantor plateau of the Chilean Andes.

Roadmap

This dissertation is organized as follows.

Chapter 1 sets the scene with a description of the planet formation environment (§1.1) and a brief introduction to the observing facility central to this work (§1.2). It then motivates the two main efforts of the dissertation (§1.3 & §1.4).

Chapter 2 establishes how the tell-tale wake of an embedded planet becomes expressed in the midplane dust layer of its host disk, and investigates the observational feasibility of detecting these wakes in mm continuum observations with ALMA.

Chapter 3 applies the previous chapter's findings to observations of a strategically selected sample of 10 disks to hunt for embedded planets and inform kinematic detection methods.

Chapter 4 presents kinematic evidence of a disk exhibiting gravitational instabilities, and develops new analysis techniques to place quantitative constraints on the dynamical structure of the disk.

Chapter 5 demonstrates a new way to disentangle disk dynamical structure from that of the surroundings, and discovers an explanation as to the origins of the observed gravitational instabilities in the same system.

Chapter 6 situates these contributions within the broader context of the field, and concludes by outlining promising directions for future work.

1.1 Protoplanetary disks: The cradles of planet formation

The realization that the orbits of the planets in our Solar System are prograde and nearly coplanar emerged gradually through centuries of early telescopic observations and classical mechanics, with the work of Copernicus (1473-1543), Kepler (1571-1630) and Newton (1643-1727). The "nebula hypothesis" of Laplace (1749-1827) is often credited as the first to suggest this was a consequence of the Solar System's formation (de Laplace, 1796), attributing the nearly coplanar and prograde orbits to angular momentum conservation in a rotating primordial nebula belonging to the newborn Sun.

Today, this insight —that planets can be traced back to their host star's primordial nebula— underpins our modern view of planet formation. We now recognize the formation of planets as the natural byproduct of the formation of their host stars, and conjointly, the material surrounding newborn stars as the birthplaces of planetary systems. Although the presence of this circumstellar material is fleeting (the bulk surviving around a newborn star for only ~ 10 Myr), the processes that unfold within it set foundational properties of the system that will endure for billions of years. Let us start our introduction to the cradles of planet formation, then, by describing the earliest stages of star formation (§1.1.1).

1.1.1 The earliest stages of (low-mass) star formation

Stars are born within over-dense regions of the interstellar medium known as giant molecular clouds, themselves residing primarily in the spiral arms of the galaxy (Shu et al., 1987). These clouds are cold ($\sim 10-20$ K) and composed primarily of molecular hydrogen (H_2), as well as a fractional amount of sub-μm-sized dust grains, approximately 1% by mass (Draine, 2003). With typical densities of $\sim 10^2 - 10^3$ cm^{-3}, their interiors are relatively well shielded from external radiation, enabling the formation of heavier and more complex molecules as well (Herbst & van Dishoeck, 2009). As an example relevant to this dissertation, CO (the second most abundant molecule after H_2) forms via gas-phase ion-neutral reactions with the help of cosmic rays, but subsequently survives with the help of dust absorption and (self-)shielding (van Dishoeck & Black, 1988).

During their lifetime ($\sim 10-30$ Myr; Kawamura et al., 2009), these clouds are subject to a variety of influences —local gravitational forces, galactic shear, magnetohydrodynamic turbulence driven by supernova explosions and stellar winds (e.g. Chevance et al., 2023)— that give rise to a varied internal structure and the formation of clumps (Figure 1.2a). Clumps contain most of the mass of a cloud, and are susceptible to collapse under self-gravity into smaller gravitationally bound cores (a fate which can be approximately assessed by comparing a clump's

mass to the Jeans mass; Jeans, 1902).

The core region of a clump is even colder (~ 10 K) and orders of magnitude more dense (~ $10^5 - 10^6$ cm^{-3}), thousands of au to a tenth of a parcsec in size. With low internal temperatures, low ionization fractions, and high enough densities, a core cannot support itself against its own self-gravity. Overcoming the supporting forces of turbulence, thermal and magnetic pressure, it undergoes gravitational collapse. Dense cores destined for collapse are referred to as pre-stellar cores (Figure 1.2b). During the collapse of a pre-stellar core, the central densities increase and gravitational potential energy is converted to heat, which needs to be radiated away to allow further contraction. This process can continue until the internal pressure becomes high enough to counter-balance the compacting force of gravity, at which point hydrostatic equilibrium is reached and a protostar is born (Larson, 1969).

The proto-stellar core marks the seed of what will evolve, over millions of years, into a new star and planetary system. From here, if the proto-stellar core is in the low-mass regime ($\lesssim 8\ M_\odot$), the ensuing evolution tends to follow a sequence of empirically defined stages, shown in Figure 1.2c-e. (In the high-mass regime, the central protostar becomes a powerful radiator before the gravitational collapse has fully completed, leading to chaotic feedback effects early on, e.g. Zinnecker & Yorke, 2007, but this regime does not concern this dissertation). We'll next briefly review the evolutionary stages of these low-mass young stellar objects, with a particular focus on the emerging rotating disk component.

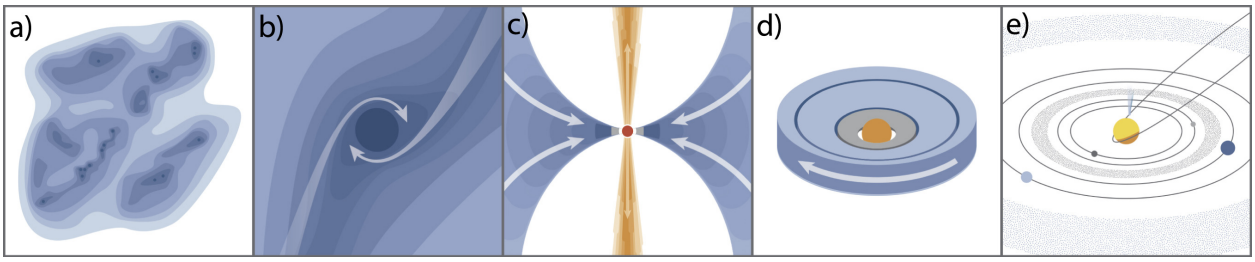

Figure 1.2: Schematic representation of the evolutionary stages of (low-mass) star and planet formation. Credit: Öberg & Bergin (2021).

1.1.2 The emergence of rotating disks

The evolutionary sequence of these nascent systems is inferred from an empirical classification system that has guided the field for over three decades. The foundational Classes I-III stages were originally introduced by Adams et al. (1987) and Lada (1987), with the subsequent addition of Class 0 sources to describe even earlier stages of star formation (Andre et al., 1993) and the

recognition of flat-spectrum (transitional I/II) sources (Greene et al., 1994). The framework relies on measuring the slope of the spectral energy distribution (SED) of the dust emission across near-IR to millimeter wavelengths, which traces the gradual dispersal of material surrounding the young protostar and tracks the system's progression through the archetypal evolutionary stages. Estimates of relative stage durations are derived statistically using occurrence rates of objects in each class within large samples (Evans et al., 2009; Maury et al., 2011).

The previous subsection (§1.1.1) brought us to the embryonic Class 0 stage ("$t = 0$"), when the protostar is fully embedded and completely obscured by the infalling region of the core, referred to as the envelope. Although brief ($\Delta t \sim 0.1$ Myr; Dunham et al., 2014), this phase already sees the emergence of a rotating disk component. As understood with the inside-out model (Shu, 1977) of a slowly rotating cloud core (Ulrich, 1976; Terebey et al., 1984), low angular momentum material from the inner envelope can accrete directly onto the star, while higher angular momentum material from larger distances reaches the equatorial plane at larger centrifugal radii. Conservation of angular momentum organizes this material into the first semblance of a rotationally supported accretion disk (Cassen & Moosman, 1981).

In the Class I phase (Figure 1.2c), a flattened disk appears from the embedded state as a portion of the envelope is accreted or dispersed by protostellar feedback. The envelope continues to play a significant role, transferring mass and angular momentum to the protostar through the mediating accretion disk. This sustains elevated accretion rates and drives the launch of protostellar outflows and jets (Frank et al., 2014). Although this stage too is short-lived ($\Delta t \sim 0.5$ Myr; Dunham et al. 2014), Class I disks can already show impressions of substructure (e.g., Segura-Cox et al., 2020), hinting that planet formation may already commence during this early phase.

The Class II stage (Figure 1.2d) marks the period in the life of the nascent system when the envelope is at last largely absent, having been accreted, dispelled or dispersed. Spanning $\Delta t \sim 10$ Myr (Mamajek, 2009), this phase is the longest-lived stage of gas-rich disk evolution, and represents the window of time when we are offered the clearest and earliest view into the cradles of planet formation at infrared and millimeter wavelengths. During this phase, the remaining accretion disk is fractional in mass relative to the central pre-main-sequence star, but serves as the primary material reservoir for assembling planetary systems. It is in these disks that planetary solids are accumulated, bulk masses are established, orbits are sculpted, and atmospheres are delivered (Williams & Cieza, 2011). This dissertation is dedicated to the study of processes unfolding in this stage.

The solid-body legacy of a Class II system will continue to evolve for the next $\Delta t \sim 10-100$ Myr as a Class III system, often referred to as a debris disk. By this stage, the primordial gas and dust has been incorprated into planets, accreted by the star, or dispersed via stellar

photoevaporative winds (Alexander et al., 2014; Pascucci et al., 2023), leaving behind a gas-poor, collisionally active disk. With the system now optically revealed, its architecture can be traced through high-contrast imaging and scattered light observations, offering insights into the end states of planet formation.

1.1.3 The equilibrium structure of a disk

As discussed above, rotating disks are naturally formed around young stars because the infalling material has too much angular momentum to collapse directly to stellar densities. Disks are born with an inherent *positive* gradient in their specific angular momentum with radius, $l = r\,v_\phi$, and they persist as coherent structures around their parent star for however long it takes that angular momentum to be redistributed or lost. The fact that disks are observed to have lifetimes of several million years ($\gtrsim 10^4$ dynamical times at 100s of au) implies that angular momentum loss is comparatively slow, such that disks become quasi-equilibrium structures.

If a disk's only business during this time was to obediently orbit the star, then its snapshot equilibrium structure is a steady-state solution to the hydrodynamic equations and Poisson equation for the present gravitational potential. Disks are *observed* to be engaged in much more funny business than this, however, with dramatic departures from equilibrium expected as planet formation and other processes unfold within them. Indeed, a central objective of this dissertation is to recognize —or in fact, search for— deviations from the canonical equilibrium disk structure. Nonetheless, it is helpful to first understand what structure we would expect if the disk's only business was to obediently orbit the star, while obeying hydrostatic equilibrium, balancing central forces, and behaving like an ideal gas.

Dynamical structure

The rotational velocity v_ϕ of the gas orbiting the central star is determined by the balance of radially-directed forces. The dominant force is the gravity of the star, but the disk's own internal pressure gradients and self-gravity are at play as well. Considering an axisymmetric disk and working in cylindrical coordinates (r, z), the radial balance of forces requires

$$v_\phi^2(r,z) = r\,\frac{\partial \Phi}{\partial r} + \frac{r}{\rho}\frac{\partial P}{\partial r}\,, \tag{1.1}$$

where $\rho = \rho(r,z)$ is the gas volume density, $P = P(r,z)$ is the gas pressure, and $\Phi = \Phi(r,z)$ is the gravitational potential field, which is comprised of contributions from both the star and the disk itself. This is the governing equation, but let us build up a solution taking one step in

complexity at a time.

If we first ignore all forces but the star's potential ($\Phi = \Phi_\star$), and consider only the disk midplane ($z = 0$), then the rotational velocity would be equivalent to the Keplerian velocity and depend only on the mass of the central star $M_\star$ and the cylindrical distance to it,

$$v_\phi(r) = \sqrt{\frac{G M_\star}{r}} = v_{\rm Kep}(r)\,, \tag{1.2}$$

which is the familiar form of differential rotation in a plane. To extend our consideration to heights above (or below) the disk midplane, we notice that a gas parcel suspended in the disk atmosphere is farther away from the star than a parcel at the midplane directly below it, and experiences a weaker gravitational pull. Furthermore, only the radial component of this gravitational force contributes to the centrifugal balance. This implies differential rotation as a function not only of radius but also of height,

$$v_\phi(r,z) = \sqrt{\frac{G M_\star}{(r^2+z^2)^{3/2}}}\, r\,, \tag{1.3}$$

such that gas in the disk atmosphere orbits the star more slowly than at the midplane, for the same cylindrical radius. A visualization of how this $v_\phi(r,z)$ field differs from vertically-uniform rotation (Eqn. 1.2) is shown in the top left panel of Figure 1.3 (Rosenfeld et al., 2013).

Next, we revisit the governing Equation 1.1 and consider the radial pressure gradient: $\partial P/\partial r$. For an ideal gas, the pressure is proportional to the volume density and gas temperature, $P \propto \rho\, T$. As both tend to decrease with r from the star, a negative pressure gradient tends to pervade most of the disk. Consequently, much of the gas in a disk orbits at slightly sub-Keplerian speeds, as illustrated in the top right panel of Figure 1.3. An analytic expression relating $v_\phi(r,z)$ and $\partial P/\partial r$ can be obtained given parametrizations for the density and temperature (e.g., Lodato et al., 2023; Stadler et al., 2025). As an example (one that considers the midplane only), if the midplane pressure can be written as $P \propto r^{-n}$, then the rotational velocity of the gas at the midplane will be slightly sub-Keplerian by an amount,

$$v_\phi(r) = v_{\rm Kep}\,(1-\eta)^{1/2}\,, \tag{1.4}$$

where $\eta \equiv n(c_{\rm s}^2/v_{\rm Kep}^2)$ (Armitage, 2019). Noting that $c_{\rm s}/v_{\rm Kep} = h \equiv H/r$ (see Equation 1.14 below) and taking $h = 0.05$ with $n = 3$, we have $\eta = 0.15$, such that the rotational velocity of the gas at the midplane is $v_\phi(r) \simeq 0.996\, v_{\rm Kep}$. This ostensibly subtle shortfall from Keplerian has critical implications for the dynamics of the dust component, which will be discussed in the following

subsection.

Lastly, and of particular pertinence to this dissertation, the disk's own mass reservoir can play a role in setting its equilibrium dynamical structure. Its gravitational potential can be represented as an additional term, $\Phi_{\rm disk} = \Phi_{\rm disk}(r,z)$. Ignoring radial pressure support now, but considering the combined gravitational potentials $\Phi = \Phi_\star + \Phi_{\rm disk}$, the rotational velocity profile then becomes

$$v_\phi^2(r,z) = \frac{G M_\star}{(r^2+z^2)^{3/2}} r^2 + \frac{\partial \Phi_{\rm disk}}{\partial r} r \,. \tag{1.5}$$

The spatial behaviour of this second term will depend on the disk volume density distribution through the Poisson equation, $\nabla^2 \Phi_{\rm disk}(r,z) = 4\pi G \rho(r,z)$, and can be computed numerically with some approximation (e.g., Bertin & Lodato, 1999) — but it is safe to say its sign will always be positive because $\partial \Phi_{\rm disk}/\partial r$ is an increasing function of r. This leads to an enhanced radial gravitational acceleration, and super-Keplerian rotational velocities compared to the case considering the star's gravity alone. Such a field is illustrated in the bottom left panel of Figure 1.3.

Considering the combined effects of $\Phi_\star$, $\partial P/\partial r$ and $\Phi_{\rm disk}$, the quasi-equilibrium dynamical structure can be computed numerically with prescriptions for the density and temperature structure (e.g., Rosenfeld et al., 2013; Andrews et al., 2024). The bottom right panel in Figure 1.3 illustrates the combined impact on the rotational velocity compared to vertically-uniform Keplerian rotation. Which effect dominates depends on the vertical and radial location of a considered fluid element, as well as the disk's physical (density and temperature) structure.

Density and temperature structure

The density structure of a disk ρ is determined by the balance of vertically-directed forces. Here again the gravitational and pressure forces are in competition. Vertical hydrostatic equilibrium requires

$$\frac{\partial P}{\partial z} = -\rho \, g_z \,, \tag{1.6}$$

where $\rho = \rho(r,z)$ is the gas volume density, $P = P(r,z)$ is the gas pressure, and g_z is the vertical component of the gravitational acceleration, which is again comprised of contributions from both the star and the disk itself,

$$g_z = \frac{\partial \Phi_\star}{\partial z} + \frac{\partial \Phi_{\rm disk}}{\partial z} \,. \tag{1.7}$$

With an ideal gas, we have the equation of state $P = \rho \, c_{\rm s}^2$, so that hydrostatic equilibrium (Eqn. 1.6) can be re-expressed as

$$-\frac{1}{\rho}\frac{\partial \rho}{\partial z} = \frac{g_z}{c_{\rm s}^2} + \frac{2}{c_{\rm s}}\frac{\partial c_{\rm s}}{\partial z} \,, \tag{1.8}$$

where the isothermal sound speed c_s is a function of the gas temperature, T,

$$c_s(r,z) = \sqrt{\frac{k_B\, T(r,z)}{\mu\, m_p}}, \tag{1.9}$$

with k_B the Boltzmann constant, and μ the mean molecular weight (often taken as $\mu = 2.37$ for ISM composition) in units of the proton mass m_p.

Equation 1.8 represents the governing equation for the equilibrium (ideal gas) density structure, with g_z given by Equation 1.7 and c_s given by Equation 1.9. The three contributing forces are the two gravitational accelerations $\partial\Phi_\star/\partial z$ and $\partial\Phi_{\rm disk}/\partial z$, and pressure support through the vertical temperature gradient $\partial c_s/\partial z$. To self-consistently compute the 2D density struc-

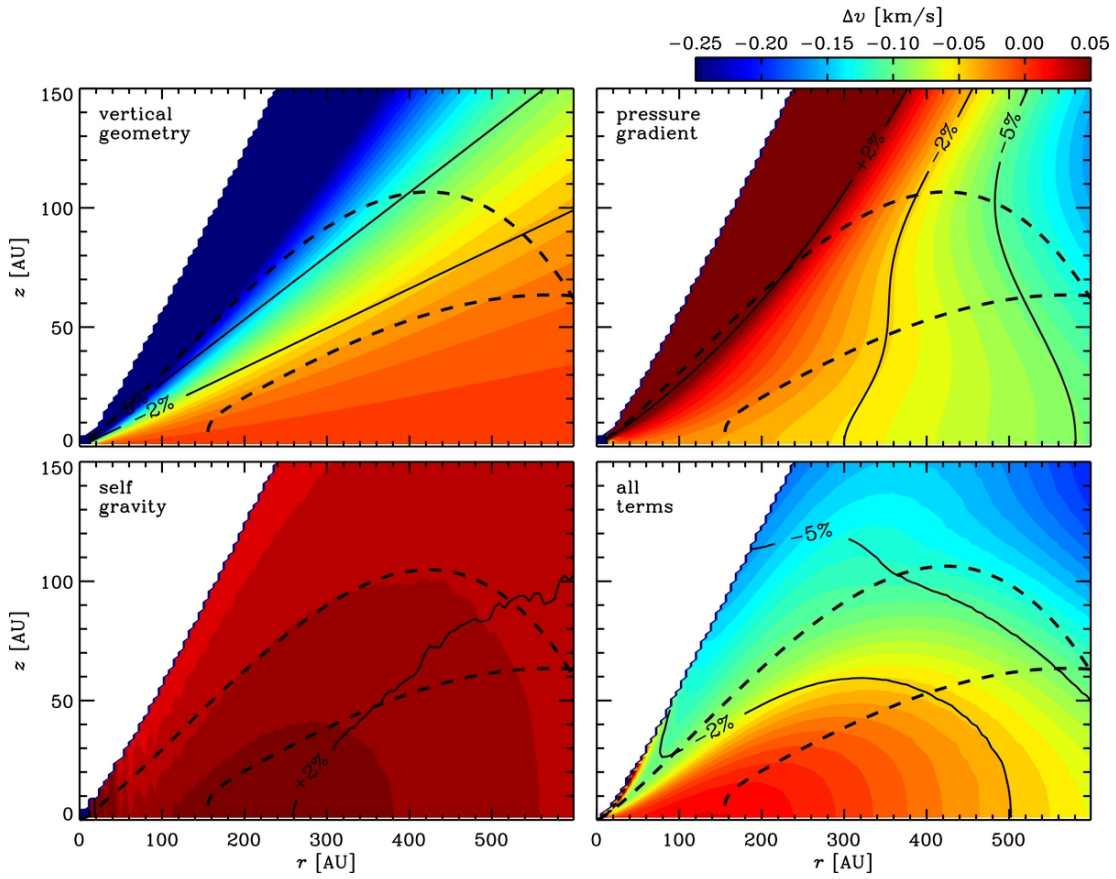

Figure 1.3: Numerical model of the dynamical structure of a disk relative to vertically-uniform Keplerian rotation (Eqn. 1.2), systematically separating the effects of vertical geometry (Eqn. 1.3), pressure support, self-gravity (Eqn. 1.5) and their combination. Contours mark the fractional difference, while the colormap marks the absolute difference. Duly note that the colorbar is not symmetric about zero, and 0.0 lies in the red. Dashed lines enclose a model ^{12}CO molecular layer. Credits: Rosenfeld et al. (2013).

ture maintaining the full (r, z) dependence of these three ingredients requires iterative thermochemical modeling (e.g., Kamp & Dullemond, 2004), which is discussed below. However, if we eliminate the disk's gravitational potential term and the vertical dependence of the temperature, we can arrive at an analytical solution, as follows.

If we first neglect the disk's self-gravity, the gravitational acceleration is solely due to the central star,

$$g_z = \frac{G M_\star z}{(r^2 + z^2)^{3/2}}. \tag{1.10}$$

If we second assume the disk is vertically isothermal, the temperature depends solely on r,

$$\frac{\partial c_s(r)}{\partial z} = 0. \tag{1.11}$$

Our requirement for hydrostatic equilibrium (Equation 1.8) therefore simplifies to

$$-\frac{1}{\rho}\frac{\partial \rho}{\partial z} = \frac{1}{c_s^2}\frac{G M_\star z}{(r^2 + z^2)^{3/2}}. \tag{1.12}$$

The solution to this differential equation is

$$\rho(r, z) = \rho_0(r) \exp\left(\frac{G M_\star}{c_s^2 (r^2 + z^2)^{1/2}}\right), \tag{1.13}$$

where $\rho_0(r)$ represents the radial profile of the midplane density. Imagining a slice through this solution for the density structure at a single r yields a Gaussian profile with the gas density falling off with distance from the dense midplane. Indeed, it is profoundly common to express the solution as

$$\rho(r, z) = \rho_0(r) \exp\left(-\frac{z^2}{2H^2}\right) \tag{1.14}$$

where H is defined as the gas pressure scale height, $H \equiv c_s/\Omega$. This holds in the thin disk limit, $z \ll r$, such that $g_z \simeq \Omega z$ from Equation 1.10, with $\Omega = \sqrt{G M_\star / r^3}$ the angular Keplerian velocity.

Figure 1.4 provides a visualization of the density structure with the above assumptions in action (Teague, 2017). The vertically isothermal temperature is prescribed as a radial power-law,

$$T(r) = T_c \left(\frac{r}{r_c}\right)^{-q}, \tag{1.15}$$

where T_c is the temperature at r_c, and q is a chosen index. If $q < 1$, the disk will be flared. One typical choice is $q = 0.5$, representing that the gas temperature is set by stellar irradiation,

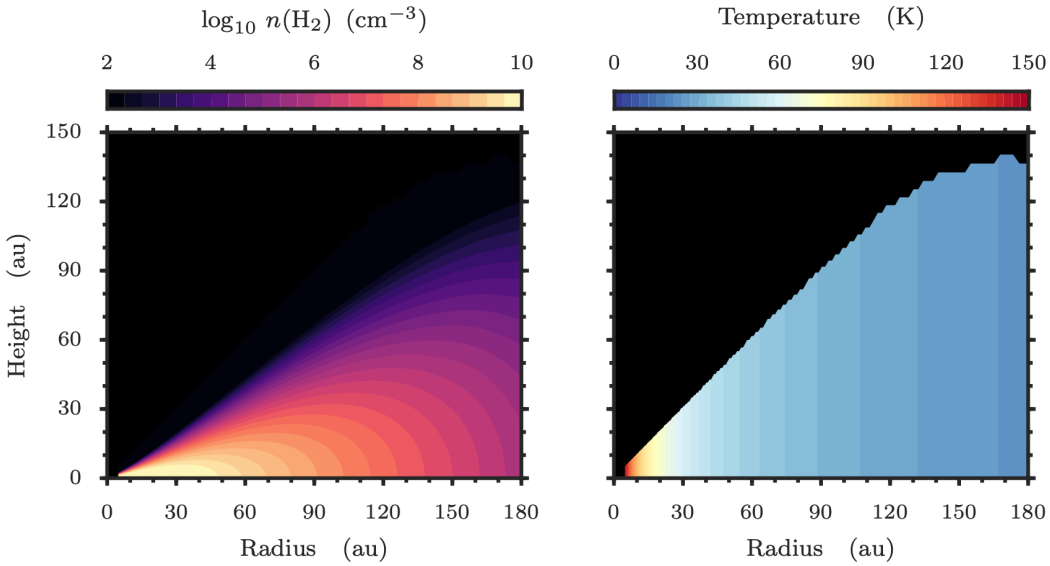

Figure 1.4: Equilibrium density (left) and temperature (right) structure of a vertically isothermal disk in hydrostatic equilibrium. The temperature is given by Equation 1.15 with $T_c = 100$ K at $r_c = 10$ au, and $q = 0.5$. Credits: Teague (2017).

which drops off with radius as $r^{-0.5}$ (Kenyon & Hartmann, 1987). Another is $q = 0.4$, the Chiang & Goldreich (1997) model, which considers the dust's role in re-radiating stellar irradiation.

It is important to note, however, that observed disks in the Class II phase are neither geometrically thin nor vertically isothermal. They are known to have vertical temperature gradients (e.g., D'Alessio et al., 1998), and an extent of geometrical thickness that has been resolvable with molecular line observations for the last decade (de Gregorio-Monsalvo et al., 2013; Rosenfeld et al., 2013; Pinte et al., 2018a; Dullemond et al., 2020; Law et al., 2021; Paneque-Carreño et al., 2025). The vertical density distribution is not necessarily Gaussian, but fundamentally set by hydrostatic equilibrium between gravity and the thermal structure (Eqn. 1.6).

The thermal structure is shaped by a balance of heating and cooling processes. Figure 1.5 illustrates some of the main mechanisms at play (Armitage, 2019). Stellar irradiation impinging on the disk surface is the dominant source of heat, which can be redistributed downward to the disk interior through sequential absorption and thermal re-radiation by dust grains. The efficiency of cooling depends critically on gas-dust collisions, enabling the gas to transfer its kinetic energy to the grains to radiate away, as the bulk of the gas (molecular hydrogen) is inefficient at emitting radiation itself. In lower density regions, such as gaps/cavities or layers above the midplane, gas-dust collisions are infrequent enough for their temperatures to decouple (e.g., Kamp & Dullemond, 2004), and the gas is forced to cool by atomic or molecular line emission (rotational and vibrational transitions!). In all, a disk is qualitatively stratified into three differ-

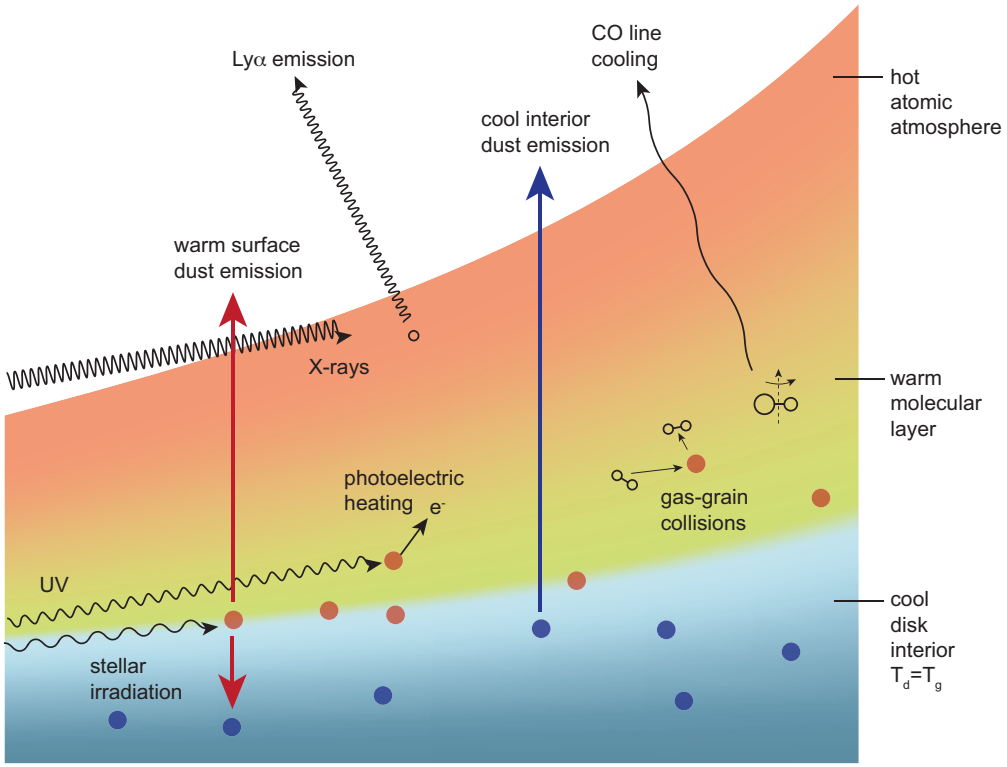

Figure 1.5: Schematic representation of some of the heating and cooling processes setting the thermal structure of an irradiated disk. Credits: Armitage (2019).

entiable layers: a hot low-density atmosphere, a warm intermediate molecular layer, and cold dense midplane (e.g., Miotello et al., 2023). Thermo-chemical modeling is imperative for capturing the balance of the heating and cooling mechanisms in the different regimes in order to compute the density and temperature structure self-consistently (e.g. with codes such as `DALI`; Bruderer et al., 2014).

1.1.4 Dust dynamics

The gas in a disk is structurally supported, both radially and vertically, by pressure. As we saw in the previous subsection, pressure gradients ($\partial P/\partial r$ and $\partial P/\partial z$ in Equations 1.1 and 1.6, respectively) are the disk's means of counteracting the gravitational forces it feels from the star as well as itself. These pressure gradients adjust the gas velocity away from the Keplerian velocity expected from pure gravitational mechanics, to faster or slower orbital speeds depending on the sign and magnitude of the gradient. A negative gradient induces sub-Keplerian rotation speeds (Equation 1.4), while a positive gradient induces super-Keplerian rotation speeds (shown in an upcoming Figure 1.12).

In contrast, dust grains are not subject to pressure support, and in the absence of the gas they would assume pure Keplerian orbits. Embedded within the gas of the disk, they experience a headwind (or tailwind) from the gas and a corresponding aerodynamic drag force that works to align the dust velocity to that of the gas. The magnitude of the aerodynamic force scales with the cross-sectional size of the grain, $F_{\rm drag} \propto \pi\, s_{\rm grain}^2$, while magnitude of the resulting *acceleration* scales inversely with its size, $a_{\rm drag} \propto s_{\rm grain}^{-1}$ (Armitage, 2019). This means the smallest grains are readily accelerated —their velocities are readily adjusted— while larger particles are more immune.

The amount of time it takes for the aerodynamic force to modify a dust grain's velocity significantly is defined as the stopping time, $t_{\rm stop}$, and is proportional to the grain size,

$$t_{\rm stop} \equiv \frac{m\,\Delta v}{|F_{\rm drag}|} = \frac{\Delta v}{|a_{\rm drag}|} \propto \Delta v\, s_{\rm grain}\,, \tag{1.16}$$

where Δv is the relative velocity between the dust and gas (the headwind or tailwind). The stopping time —or its dimensionless form, the Stokes number, $\mathrm{St} \equiv t_{\rm stop}\,\Omega$— quantifies the degree to which a dust grain is aerodynamically coupled to the gas. At one extreme, μm-sized dust grains in the densest regions of the disk are strongly coupled ($\mathrm{St} \ll 1$) and take effectively no time to (de-)accelerate to the gas velocity. At the other extreme, km-sized bodies —9 orders of magnitude larger— are effectively decoupled ($\mathrm{St} \gg 1$) and well maintain their pure Keplerian orbits. In between these two limits, intermediate-sized dust grains try to find a balance between aerodynamic drag acceleration and gravitational acceleration, experiencing a relative velocity with the gas all the while.

Persistent dust-gas relative velocities, which are guaranteed in the presence of any persistent gas pressure gradient, have important consequences for the spatial distribution of dust grains. As aerodynamic drag always works to align the dust velocity to that of the gas, a general rule emerges: *Dust grains migrate in the direction of increasing pressure* (Whipple, 1972). Negative pressure gradients induce sub-Keplerian gas rotation speeds, so that a headwind works to reduce the dust's velocity, decaying its orbit towards increased pressures. Positive gradients induce super-Keplerian gas rotation speeds, so that a tailwind works to hasten the dust's velocity, expanding its orbit toward —again— increased pressures.

The global inward radial drift of dust grains owing to a globally negative pressure gradient presents a problem (Weidenschilling, 1977). The rate of radial drift depends on the Stokes number, peaking at $\mathrm{St} \sim 1$ (Takeuchi & Lin, 2002), corresponding to roughly meter-sized objects. Here the radial drift timescale is just 10^3 orbital periods, suggesting these objects are quickly lost out of the disk. This is the origin of the "meter-sized barrier" plaguing models of planetes-

imal formation (see 1.4.2 for more details; Chiang & Youdin, 2010; Johansen et al., 2014). The existence of local pressure maxima within the disk —generated, for example, by the presence of a planet (see §1.3.1)— represent a solution to this problem, acting as dust traps and halting inward drift (e.g., Pinilla et al., 2012).

Persistent vertical gas pressure gradients have consequences for the vertical distribution of dust grains as well. Dust grains above the midplane wish obey the vertical component of gravitational acceleration from the star (g_z; Equation 1.10) and fall toward the midplane, but have to contend with drag from the gas. The vertical distribution of solids in a disk thus becomes stratified, with well-coupled grains remaining suspended with the help of turbulence, and larger grains sedimenting out of the upper layers onto the midplane (Barrière-Fouchet et al., 2005).

Dust grains constitute the fundamental building blocks of planetary cores. By influencing their spatial distribution —and therefore their concentration, growth, and evolution— aerodynamic forces are a key part of the earliest stages of planet formation (Testi et al., 2014).

This section has only discussed long-standing, persistent pressure gradients. What about *impersistent* pressure gradients? As we will see in §1.3, embedded planets can create pressure features that are transient, co-moving with the planet as they orbits the star. It is not obvious *a priori* how these features become expressed in the dust distribution, particularly by those grains partially aerodynamically coupled to the gas: $\mathrm{St} \lesssim 0.1$. In Chapter 2, we set out to answer this question.

1.2 Observing protoplanetary disks in the (sub)millimeter

At the time of *Protostars and Planets II* (Black & Matthews, 1985), no direct identifications of protostellar disks —then already conceived of as "pre-planetary" disks— had yet been achieved. Nevertheless, the community was convinced that these disks should exist, and circumstantial evidence was mounting. In addition to significant excess emission in the infrared, large-scale structures such as optical jets and bipolar molecular outflows implied non-spherical, axially symmetric distributions of accreting material (e.g., Snell et al., 1980; Mundt, 1985). These phenomena motivated studies of the objects' spectral energy distributions (e.g., Rucinski, 1985) that would ultimately lead to the development of the evolutionary classification system described in §1.1.2 (Adams et al., 1987; Lada, 1987). Direct evidence of disks, however, would have to await the availability of ~arcsecond resolution from millimeter interferometers. Such evidence was in hand by *Protostars and Planets III* (Beckwith & Sargent, 1993).

The breakthrough detection of a rotating disk was reported by Sargent & Beckwith (1987) using mm-wavelength interferometric observations with the Owens Valley Radio Observatory (OVRO) — an array of six 10.4 m radio dishes commissioned during that period in California. The authors observed a flattened distribution of emission from the $J = 1 - 0$ rotational transition of ^{13}CO around the star HL Tauri, and demonstrated that the velocity distribution of this molecule followed the Keplerian rotation curve expected for a gravitational potential dominated by the star (c.f. §1.1.3). In the years to follow, similar discoveries were made in several more systems with the OVRO (in T Tau, R Mon, GM Aur; Weintraub et al., 1989; Sargent & Beckwith, 1991; Koerner et al., 1993) and with the new 3-dish IRAM Plateau de Bure interferometer (in GG Tau; Dutrey et al., 1994), solidifying the idea that gas orbits young stars in bound disks.

Since the turn of the millenium, modern interferometers have ushered in a new era of high angular and spectral resolution imaging in the (sub)millimeter, beginning with the commissioning of the Submillimeter Array (SMA) in 2003 and accelerating with the Atacama Large Millimeter/ submillimeter Array (ALMA) in 2011, the enhanced Karl G. Jansky Very Large Array (JVLA) in 2012, and the expanded Plateau de Bure's Northern Extended Millimeter Array (NOEMA) in 2014. The following subsection (§1.2.1) highlights the unique observational opportunities afforded by the "multi-nocular radio vision" of (sub)millimeter interferometry, and §1.2.2 emphasizes how ALMA, in particular, has propelled the field forward over the last decade with its unparalleled resolution and sensitivity.

1.2.1 Multi-nocular radio vision (interferometry)

(Sub)millimeter wavelength observations are expressly suited for probing the relatively low-energy conditions that pervade the bulk of circumstellar disks ($r \gtrsim 10$ au). Temperatures typically range ~ 10 to 100 K within the warm molecular layer described in §1.1.3. At these temperatures, the low rotational (low J quantum number) transitions of many abundant molecules are readily excited. Small molecules such as CO and its main isotopologues, ^{12}CO, ^{13}CO, and C^{18}O have low excitation energies and their low J transitions lie at (sub)millimeter wavelengths. In contrast, (ro)vibrational transitions at shorter wavelengths ($\lesssim 20$ μm) require much higher temperatures for significant excitation — conditions that only exist within a few au of the central star and therefore trace less of the disk (and are harder to spatially resolve).

In addition to offering access to the bulk of the gas content, (sub)millimeter observations provide a unique window into the dust. As the thermal and scattered continuum emission at a wavelength λ is dominated by grains with size $\lambda/2\pi$ (e.g., Kataoka et al., 2015a; Pavlyuchenkov et al., 2019), millimeter observations predominantly trace sand-sized solids. The absorption and scattering opacity of a grain also depends on its size (Draine, 2016), such that for typical dust composition and size distributions (e.g., Birnstiel et al., 2018a), mm-wave emission remains optically thin over much higher column densities than at shorter wavelengths. Combined with the fact that larger grains tend to vertically settle (§1.1.4), (sub)millimeter observations can penetrate to the dust distribution at the dense —planet-forming— midplane.

In order to reap these benefits of observing in the (sub)millimeter, we need to address a fundamental challenge: the diffraction limit at these long wavelengths. While it is a blessing that the radio regime is essentially diffraction limited[3] even from the ground, the angular resolution of a single (large) 15 m antenna is still only $14''$ at $\lambda = 0.85$ mm.

Interferometry employs an array of multiple physically separated antennas to *synthesize* a larger observing aperture, enabling us to emulate angular resolutions that would otherwise require an individual antenna to be tens of kilometers in diameter. An interferometer's angular resolution is limited not by the size of its individual antennas, but by the greatest separations between pairs of them.

An interferometric array consists of numerous antenna pairs, characterized by their baseline — the projected separation length as seen by the target source, $B_{\rm proj}$. An array with $N_{\rm ant}$ antennas has $N_{\rm bl} = N_{\rm ant}(N_{\rm ant}-1)/2$ baselines. By cross-correlating the cosmic signals between

[3]The angular resolution θ of a filled-aperture single-antenna radio telescope is $\theta = k\lambda/D$, where λ is the observing wavelength, D is the diameter of the antenna and k is a factor of order unity that encompasses details of antenna illumination (Jenkins & White, 2001).

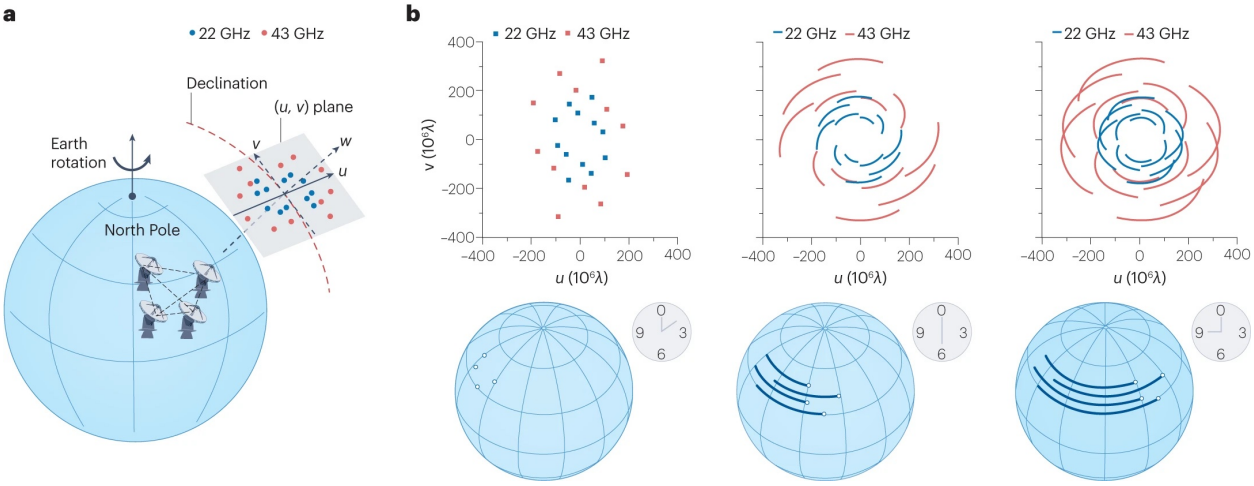

Figure 1.6: Sampling the spatial frequency domain with an interferometric array. (a) The (u, v) plane. An array of 4 antennas on Earth produces 6 baselines. The 6 baselines produce 12 (u, v) points, reflecting how each baseline can be viewed as A to B, or B to A, in the eyes of the source. Two sets of 12 are shown for two observing frequencies, 43 GHz (red) and 22 GHz (blue). (b) Continuous observing traces tracks of the baselines through the (u, v) plane. Credits: Asaki et al. (2023).

each pair of antennas in an array, an interferometer measures the *spatial coherence* of the incoming radio waves. These measurements are mathematically equivalent to discretely sampling the Fourier transform of the sky brightness distribution, with each projected baseline vector sampling a specific Fourier component of spatial frequency $\lambda/B_{\rm proj}$ at a particular orientation (e.g., Asaki et al., 2023) . Increasing $N_{\rm ant}$ (and placing them strategically) diversifies the distribution of baseline orientations, symmetrizing the resulting angular resolution, and increases the combined collecting area, with the sensitivity scaling as $\sqrt{N_{\rm bl}}$.

More specifically, the cross-correlated signal measured between each pair of antennas is called a *visibility*, V, and it is the complex product between the first antenna's output and the complex conjugate of the second antenna's (e.g., Wilson et al., 2013). The visibility domain is the spatial frequency domain, i.e., the conjugate domain of the celestial sphere, and the coordinate system adopted to describe the visibility domain is a plane tangential to the celestial sphere at the target source, as illustrated in Figure 1.6. The u and v coordinates are defined as parallel to the East-West and North-South directions, respectively. The origin of coordinates, $(u, v) = (0, 0)$, is called the *phase center*. The projected baseline $B_{\rm proj}$ defines where, in the (u, v) plane, the visibility is measured.

Recovering the sky brightness distribution —an image— from the measured visibilities relies on the foundational van Cittert-Zernike theorem (van Cittert, 1934; Zernike, 1938), which states that the *visibility function*, $V_\nu(u, v)$, is the Fourier transform of the intensity distribution,

$I_\nu(l,m)$, on the sky,

$$V_\nu(u,v) = \int_m \int_l I_\nu(l,m)\, e^{2\pi i(ul+vm)}\, dl\, dm\, dv. \tag{1.17}$$

It follows that the intensity distribution is the inverse Fourier transform of the visibility function. Here, l and m are sky coordinates, defined as direction cosines in the Right Ascension and Declination directions. As the visibility function contains the same amount of information as its Fourier transform, in principle the sky brightness distribution can be recovered.

As illustrated in Figure 1.7, an interferometric dataset consists of a finite number of visibilities $V(u_i, v_i)$ such that, in practice, the uv-coverage is incomplete: the visibility function is sampled discretely, and non-uniformly. The maximum extent of the uv-coverage determines

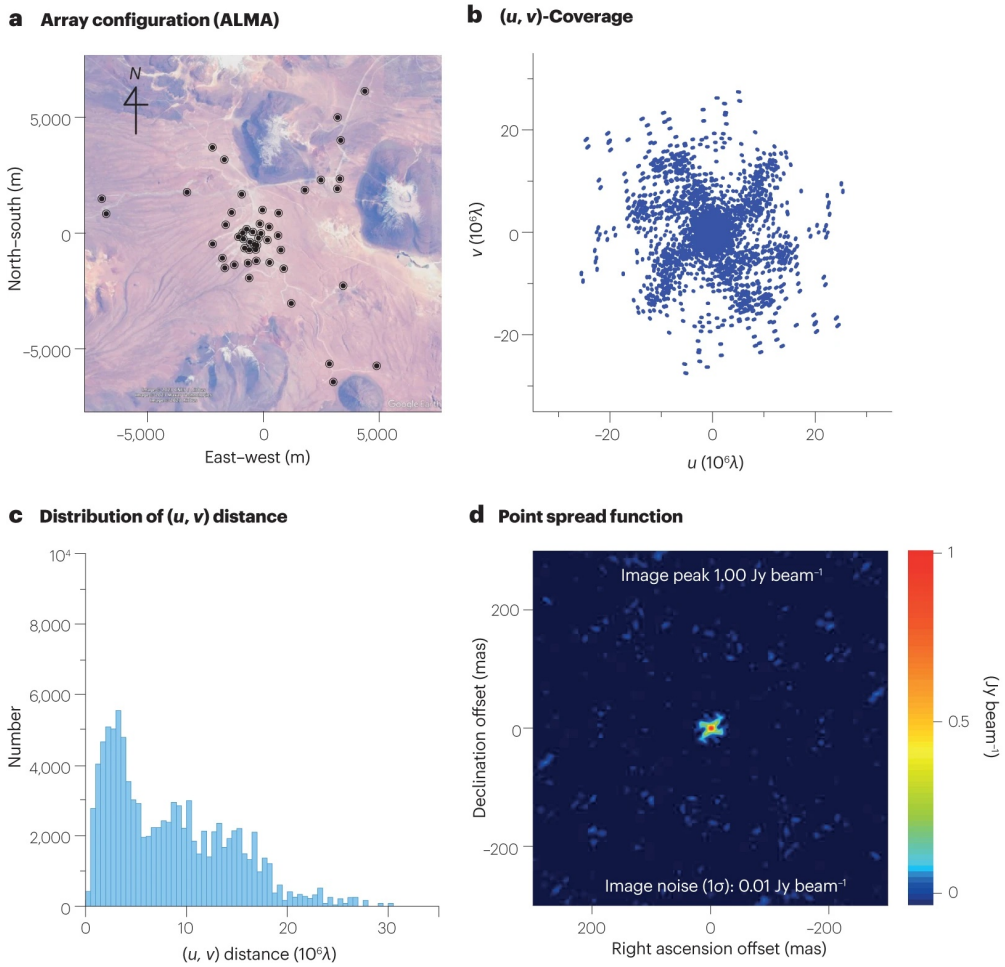

Figure 1.7: (a) Spatial arrangement of 53 ALMA antennas in the Atacama Desert, with a maximum baseline of 14 km. (b) uv-coverage obtained at 669 GHz. (c) Histogram of the uv-coverage expressed as the distance between the points and the phase center. Note that short-spacings are missing. (d) Point spread function, or synthesized beam, generated from the uv-coverage with a Briggs robust weighting parameter of 1.0. Credits: Asaki et al. (2023).

the angular width of the core of the synthesized beam (or point spread function) of an interferometric array, i.e., the smallest spatial scales that can be seen. Symmetrically, the shortest projected baselines of an array impose a limit on the largest spatial scales that can be recovered. The response function, or primary beam, $A(l,m)$ of each individual antenna also plays a role, modulating the integrand in Equation 1.17 by a factor of $A(l,m)$ (e.g., Thompson et al., 2017).

The production of images by aperture synthesis involves many numerical operations, including *weighting* to form an optimal synthesized beam given the achieved uv-coverage (e.g., Briggs, 1995), *gridding* to enable inversion between image and visibility domains by the fast Fourier transform (e.g., Briggs et al., 1999), and *deconvolution* of the synthesized 'dirty' beam to mitigate the inevitable effects of incomplete uv-coverage. The first practical demonstration of aperture image synthesis in radio astronomy was made by (Ryle & Hewish, 1960). Over the last 65 years, the most dramatic improvements in image synthesis have been achieved in parallel with faster digital computers and the development of evermore sophisticated deconvolution algorithms. The CLEAN algorithm (e.g., Högbom, 1974) has emerged as the most widely used deconvolution routine. Indeed, it is adopted for the imaging of ALMA visibility datasets throughout this dissertation.

1.2.2 The ALMA Revolution

Since commencing full operations in the early 2010s, ALMA has stood as the world's largest and most sensitive interferometer operating at (sub)millimeter wavelengths (0.32 – 8.6 mm, or 35 – 950 GHz; Asaki et al., 2023).

The full ALMA array consists of 66 parabolic antennas, strategically situated at an altitude of 5000 m in the dry Atacama desert of northern Chile. The main array is comprised of 50 antennas each 12 m in diameter, whose locations are not fixed in place but instead reconfigurable, and routinely re-positioned across the Chajnantor plateau (see Figure 1.7a) to enable maximum baselines between 150 m and 16 km. In its most extended configuration, the main array can achieve exceptional angular resolutions as fine as 10 mas, equivalent to 1 au at a distance of 100 pc. The uv-coverage of the main array is supplemented by the remaining 16 antennas: twelve 7 m antennas more closely spaced with maximum baselines of 50 m, and four 12 m antennas dedicated to single-dish (total power) observations, together forming the Atacama Compact Array (ACA; Iguchi et al., 2009).

The exquisite angular resolution unlocked by ALMA's long baselines opened new parameter space for (sub)millimeter astronomy. The 2014 Long Baseline Campaign (LBC; ALMA Partner-

ship et al., 2015a) showcased these capabilities for the first time, achieving 25 mas resolution (3.5 au) at 350 GHz. Among the Science Verification (SV) targets was the young star HL Tau — the same disk system where Keplerian rotation was first identified nearly three decades earlier (§1.2; Sargent & Beckwith, 1987). The LBC observations of HL Tau imaged the dust surrounding the star in unprecedented detail, revealing an astonishing pattern of concentric bright rings and dark gaps (ALMA Partnership et al., 2015b). This discovery —that disks contain *substructure*— marked a paradigm shift in our understanding of the planet formation environment.

In parallel, the heterodyne technology of ALMA's receivers (which downconverts the observed frequencies to more digitally accessible intermediate frequencies) enables spectral sampling at resolutions of 30 kHz, equivalent to a velocity resolution of ~ 20 m s^{-1} at 340 GHz. This translates to an extraordinary resolving power of $R = \lambda/\Delta\lambda \sim 10^7$, a regime that is extremely demanding, if not unmatchable, at shorter observing wavelengths. The process of imaging spectral line data yields an image *cube*, rich with information that can be extracted in a variety of geometrical ways (see Figure 1.8).

These capabilities open the door to detailed studies of protoplanetary disk *kinematics*, through

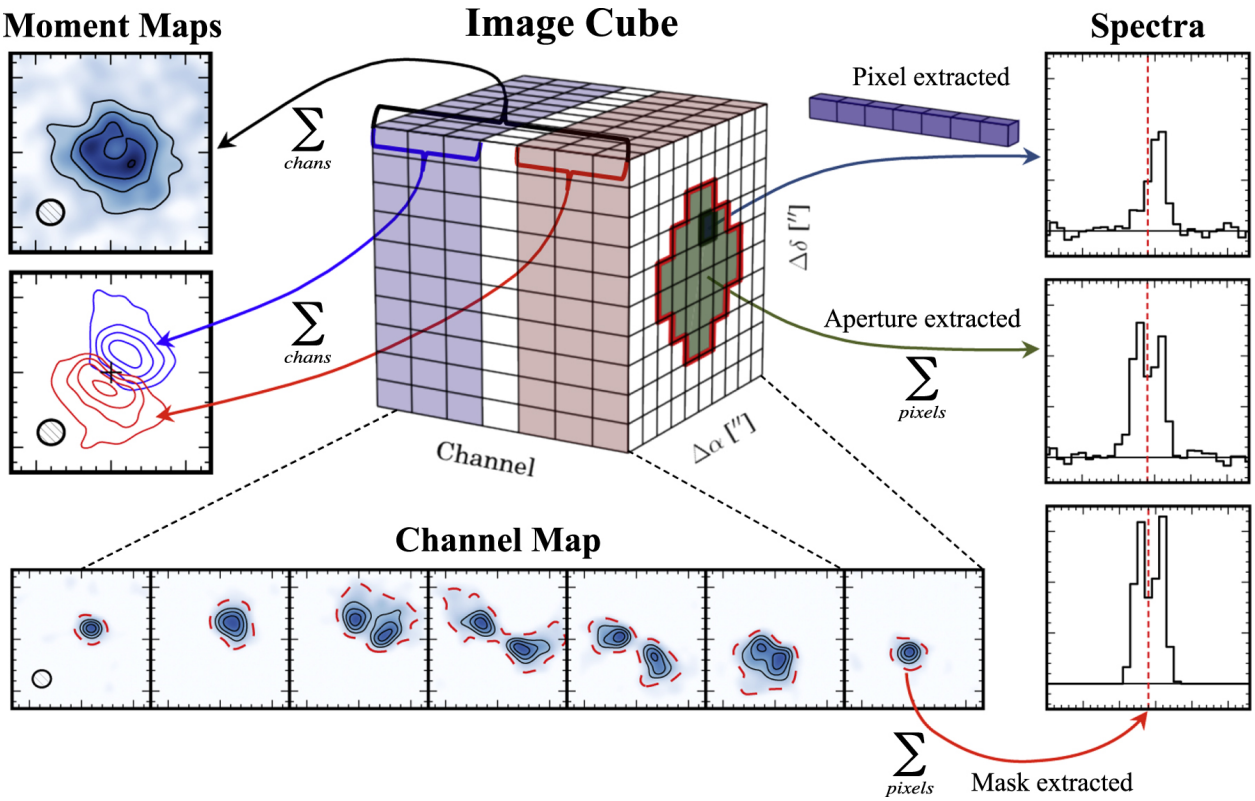

Figure 1.8: Illustration of an image cube, and the variety of ways its contents can be viewed or analyzed. Credits: Loomis et al. (2018).

the precise measurement of Doppler shifts in spatially resolved molecular emission lines. ALMA's high velocity resolution allows the intrinsic emission line widths —typically ~ 300 m s^{-1} and dominated by thermal broadening— to be easily resolved into many independent spectral elements. As a result, the line *center* can be precisely identified (e.g., Teague & Foreman-Mackey, 2018a), and offsets between the line center and the rest frequency can be robustly interpreted as the projected *line-of-sight velocity*, $v_{\rm los}$, of the emitting gas.

The (quasi)Keplerian rotation of the gas around the central star (c.f. §1.1.3) Doppler shifts the emission away from its rest frequency ν_0 by an amount $\Delta\nu = -v_{\rm los}(\nu_0/c)$. The line emission captured in any single $v_{\rm los}$ channel thus represents an isovelocity slice through the disk velocity field, modulated by the disk's inclination on the sky. The morphology of the emission captured within a velocity channel is nearly symmetric about the disk major axis, because a given $v_{\rm los}$ is achieved twice along a single orbit of a gas parcel. A pedagogical demonstration is given in Figure 1.9. The vertical structure of the disk (c.f. §1.1.3) can alter this symmetry through the projected height of the emission layer (e.g., Rosenfeld et al., 2013).

The last decade of disk observations from ALMA has facilitated many significant leaps in the field of planet formation. Measurements of the rotational velocity of the disk gas have shown that pressure maxima coincide with continuum rings (Teague et al., 2018b; Rosotti et al., 2020a; Stadler et al., 2025), providing direct evidence that dust grains are trapped in gas pressure maxima (c.f. §1.1.4). Novel methodologies have demonstrated how to ascertain the vertical heights of emission layers in mid-inclination disks (e.g., Pinte et al., 2018a; Kurtovic & Pinilla, 2024), and high angular resolution continuum observations have confirmed that millimeter-sized grains are subject to significant vertical settling to the midplane (c.f. §1.1.4; Villenave et al., 2020). Observations of *multiple* molecular tracers (different molecules or transitions, with different exci-

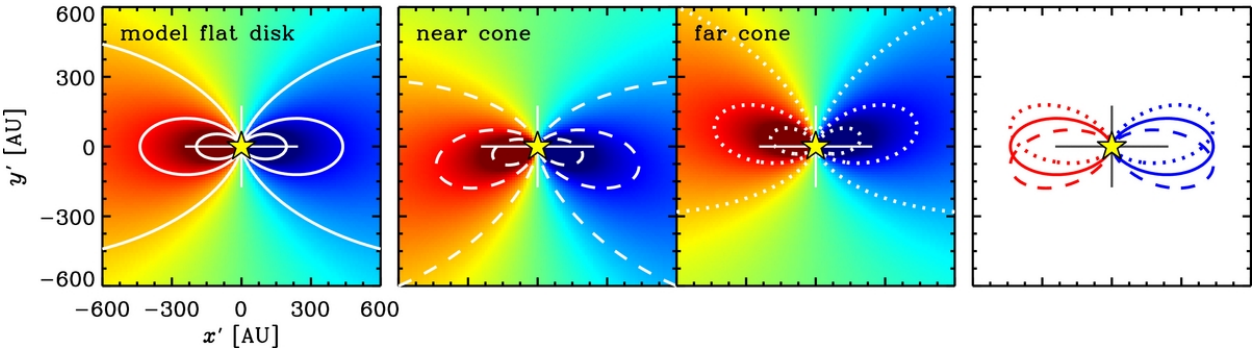

Figure 1.9: Projected line-of-sight velocity field of an inclined rotating disk, with flat and elevated emission surfaces. The white contours show isovelocity contours at $|v_{\rm los}| = 0.75$, 1.5 and 2.25 km s^{-1}, highlighting the nominal emission pattern that would be captured within a single velocity channel. The disk major axis is parallel to the x-axis in this case. Credits: Rosenfeld et al. (2013).

tation temperatures and abundances) have been used to study the vertical density and thermal structure (c.f. Figure 1.5; e.g., Law et al., 2021; Paneque-Carreño et al., 2022; Galloway-Sprietsma et al., 2025). Discovering the vertical snowline, we learned where irradiative heating becomes ineffective and gained invaluable knowledge of the temperature of the planet-forming midplane (e.g., Dullemond et al., 2020).

In all, the advent of ALMA has rendered planet formation a truly data-driven field. In the four observing cycles since the start of the pandemic, ALMA has logged 1,440 hours of observing programs in the science category of "Disks and planet formation" alone, speaking to ALMA's productivity in this community. This dissertation is based on approximately 80 hours of ALMA observing time.

1.3 The search for planets in formation

One of the core motivations of this dissertation is to detect the presence of young protoplanets embedded in their natal disks. Ultimately, revealing this population will arm us with the information necessary to confront the immensely diverse population of mature exoplanetary systems, and turn their evolution equation into an Initial Value Problem anchored with initial conditions.

The central challenge, by definition, is that these youngest protoplanets are *embedded*: a substantial column of material from the circumstellar —or circumplanetary— disk lies between us and them. Although a protoplanet's thermal or accretion-related (e.g. Hα) emission is expected to be sufficiently bright in the optical or near-infrared to allow for detection with ground- or space-based facilities, the enshrouding material can result in significant levels of attenuation to these photons (Pinte et al., 2019; Alarcón et al., 2024; Choksi & Chiang, 2025), and accordingly, extinct the prospect of their direct detection at these wavelengths.

In this sense, the few successful detections we have made of disk-embedded planets are literally breakthroughs. PDS 70 b and c (Keppler et al., 2018; Haffert et al., 2019) and HD 169142 b (Hammond et al., 2023) have been convincingly detected in multi-epoch direct imaging of near-infrared emission. These detections are thought to have been enabled in large part to the protoplanets' locations, lying in particular areas of their disks that are almost entirely devoid of attenuating material. The strong candidate in AB Aur (Currie et al., 2022) is an embodiment of the challenges when this is not the case.

These challenges have motivated explorations for protoplanets at (sub)millimeter wavelengths, where the enshrouding circum*planetary* material could serve instead as an illuminating target beacon. This was initially explored with models of circumplanetary disks in continuum (Zhu et al., 2018) and molecular emission (Cleeves et al., 2015; Perez et al., 2015). However, at the time of writing, the success of this approach on-sky is limited to the PDS 70 system (Isella et al., 2019; Benisty et al., 2021) and a candidate in AS 209 (Bae et al., 2022a). The limited success of this direct approach in the (sub)mm is attributable to the tininess, and faintness, of the circumplanetary signals (Andrews et al., 2021a, see also Chapter 6, §6.2).

In this context, we are compelled to develop *indirect techniques* to search for planets, and instead infer their presence through their influence on the larger circumstellar environment. While the enshrouding material may hide their emergent photons, it cannot hide the authoritative gravitational consequences of their mass — instead, it can reveal it. Casting our examining net more widely in this manner, we use the fact that protoplanets are embedded to our advantage. This is precisely the method of planet-hunting to which Chapters 2 and 3 of this

dissertation are dedicated.

The remainder of this section provides a primer on planet-disk interactions and indirect signatures of embedded planets (§1.3.1), followed by recent reports of such signatures in observations (§1.3.2).

1.3.1 Predicting the signatures of embedded planets

As soon as an embedded solid body grows large enough ($\gtrsim$ 10 km in size), its interactions with the disk are no longer aerodynamical (c.f. §1.1.4) but gravitational. Fundamental properties of fully formed planets —their mass, orbit, and compositional ingredients— are dictated by gravitational planet-disk interactions.

Figure 1.10 provides an overview of the current landscape of how an embedded planet is expected to modify the surrounding gas-scape. We duly note that these signatures can be non-axisymmetric (having localization or directionality inherent to the planet) or axisymmetric (where the position of the planet along its orbit is not relevant). It is also key to note that since these signatures manifest as perturbations to the disk's density and pressure structure, they necessarily give rise (c.f. §1.1.3) to perturbations in the disk's velocity structure. Below, we parse the myriad of observable signatures that arise from planet-disk interactions, synthesizing insights from analytic theory, numerical simulations, and discuss predictions for how these manifest in real observations.

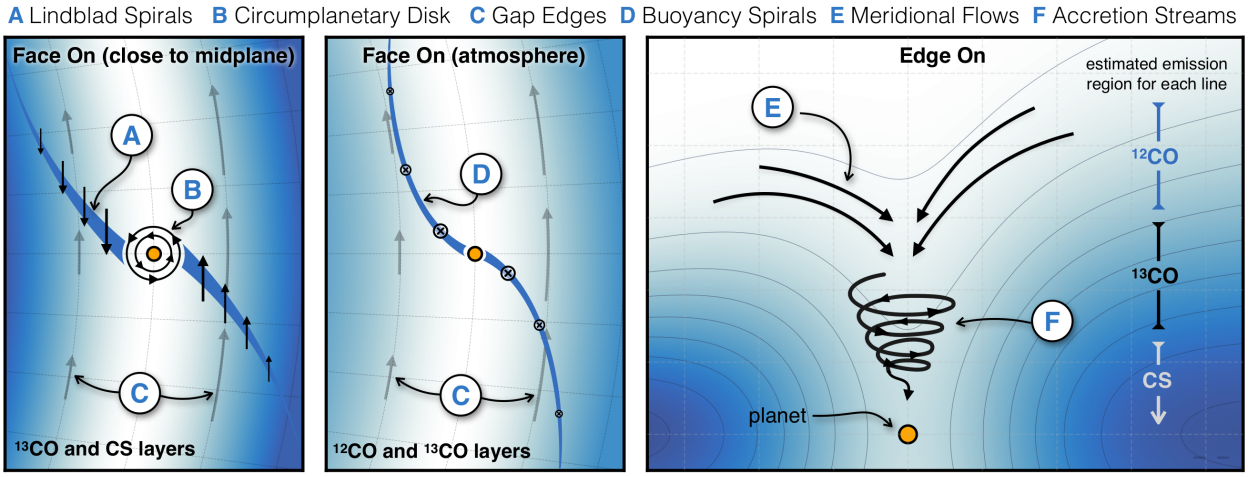

Figure 1.10: Schematic representation of the many ways an embedded planet influences its surrounding environment. Observable signatures are labeled. Panels present slices through the gas disk in the $r-\phi$ plane (left two panels) and in the $r-z$ plane (rightmost panel). Graphic credits: Richard Teague, exoALMA Collaboration (Teague et al., 2025).

Analytic Theory and Numerical Simulations

The theoretical groundwork for the study of planet-disk interactions was laid more than four decades ago (Goldreich & Tremaine, 1978). In the last two decades, theoretical advancements have been enabled by numerical simulations that allow inclusion of additional physical ingredients on a variety of geometrical domains in 2 and 3 dimensions.

Lindblad spirals. A planet embedded within a disk, orbiting the central star with a fixed angular frequency and circular radius r_p, gravitationally resonates with the epicyclic frequencies of the disk fluid located at its Lindblad resonances, $r_m^\pm = (1 \pm 1/m)^{2/3}\, r_\mathrm{p}$ (Goldreich & Tremaine, 1979a), where m is the azimuthal wavenumber of a single harmonic. The Lindblad resonances become the launching points of spiral density waves, which propagate away from the planet in both directions (Goldreich & Tremaine, 1978, 1980). In particular, the mth Fourier component planet's gravitational potential excites a set of m wave modes, evenly spaced in azimuth, at the mth inner and mth outer Lindblad resonance (Ogilvie & Lubow, 2002; Goodman & Rafikov, 2001). The constructive interference among wave modes having different m leads to the emergence of the primary Lindblad spiral arm (as well as possible secondary and tertiary spiral arms, for appropriate sets of wave modes; Bae & Zhu, 2018a,b).

Implicitly, the framework underlying the paragraph above is the *linear* theory of the excitation of spiral density waves, which works well when the planet mass M_p is much smaller than the thermal mass[4] M_th. In contrast, wave excitation by more massive planets ($M_\mathrm{p} \gtrsim M_\mathrm{th}$) involves significant non-linear effects that are challenging to treat analytically. Regardless of how the waves are excited though, their subsequent propagation inevitably becomes non-linear: this transition occurs almost immediately for $M_\mathrm{p} \gtrsim M_\mathrm{th}$, while for $M_\mathrm{p} \ll M_\mathrm{th}$ it occurs later, at distances up to $\sim 6\,H$ away from the planet (Goodman & Rafikov, 2001).

As Lindblad spirals are waves, it is intuitive that they imprint on the disk's velocity field in addition to its density structure. The spirals induce significant deviations from Keplerian rotation in the azimuthal velocity field (see Figure 1.11), accompanied by radial and, to a lesser extent, vertical flows along the wake. These multi-directional velocity perturbations can reach peak amplitudes of 5 – 10% the local Keplerian speed, depending on the background disk properties and the planet's mass (Teague et al., 2018a; Gyeol Yun et al., 2019; Pinte et al., 2019; Disk Dynamics Collaboration et al., 2020; Rabago & Zhu, 2021).

[4]The thermal mass is a unit defined as: $M_\mathrm{th} = (H/r)_\mathrm{p}^3\, M_\star = c_\mathrm{s}/(\Omega G)$ (Goodman & Rafikov, 2001). The Hill radius of a thermal mass planet is comparable to the gas pressure scale height H at its orbital radius.

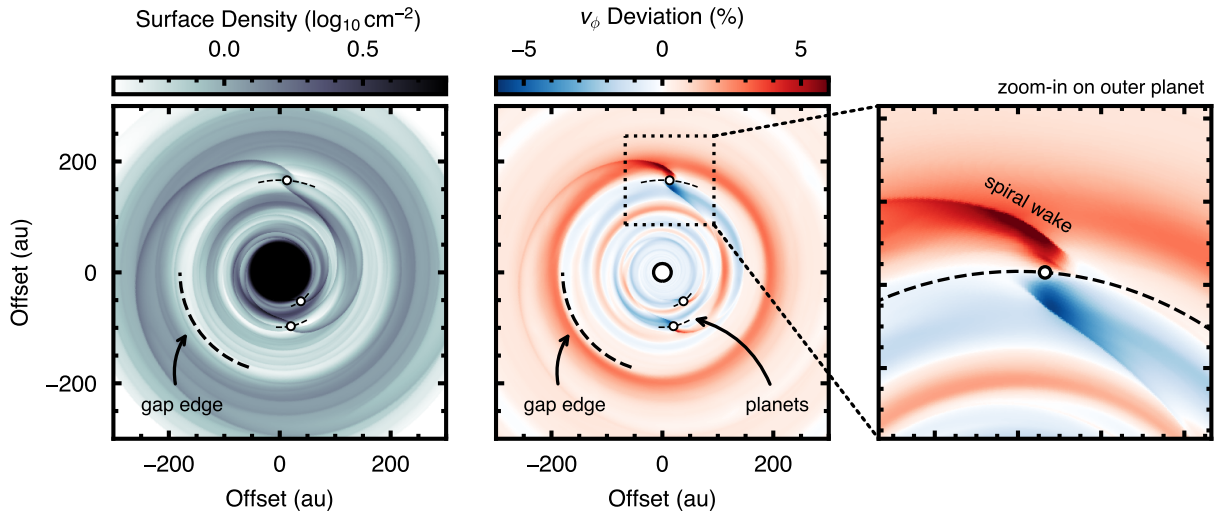

Figure 1.11: 3D hydrodynamic simulation illustrating the influence of three embedded planets on the disk surface density (left panel) and azimuthal velocity (two rightmost panels) as a %-deviation to the background Keplerian velocity. Credits: Disk Dynamics Collaboration et al. (2020).

Gaps. Each spiral density wave mode carries an m-dependent amount of angular momentum as it travels away from the planet. The inevitable non-linear propagation of spiral density waves means they eventually steepen into shocks — or in the case of super-thermal mass planets, shock essentially right upon launch (Goodman & Rafikov, 2001; Rafikov, 2002a). When a spiral wave steepens and shocks, it deposits angular momentum into the disk fluid. As the outer spiral shocks exert a positive torque, the gas exterior to the planet's orbit (at the outer Lindblad resonances or farther) flows outward, while the inner spirals exert a negative torque and the gas interior to the planet's orbit flows inward. A gap in the gas density consequently forms, centered on the planet's orbit. If a planet excites secondary or tertiary spiral arms, it can create multiple gaps at the shock fronts in the same fashion (Dong et al., 2017; Bae et al., 2017).

The gap cleared by a planet results in radially-localized pressure gradients, which in turn result in concentric deviations in the azimuthal velocity of the clearing gas (Kanagawa et al., 2015; Teague et al., 2018a). The mechanism is the same as we saw in Equation 1.1, where a radial pressure gradient acts as a radial force to maintain centrifugal balance. The negative pressure gradient interior to the planet's orbit behaves like an outward radial force, opposing the stellar gravity, inducing *sub*-Keplerian rotation at the inner edge of the gap. At the outer edge, the force of the positive pressure gradient is in the same direction as the star, and the gas orbits at *super*-Keplerian speeds. This is visualized in Figure 1.12.

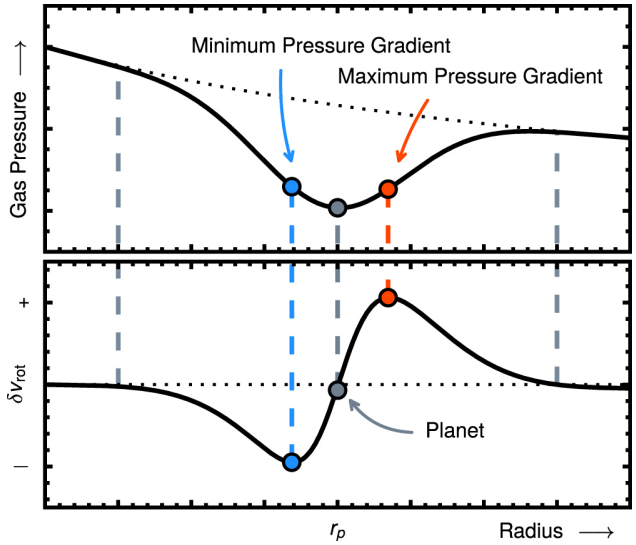

Figure 1.12: Visualization of the impact of a local gas pressure minimum (top panel) on the local azimuthal velocity (bottom panel). Credits: Teague et al. (2018a).

Meridional flows and accretion streams. Meridional circulation (motion in the $r-z$ plane) is another consequence of planetary gaps. It arises from the vertical stratification of planetary torques: the planet exerts the strongest torque near the midplane, forcing the gas at the gap edges high in the atmosphere to viscously cycle down through different altitudes to fill in the gap and maintain hydrostatic equilibrium (Kley et al., 2001; Crida et al., 2006). This circulation is expected at all gap azimuths. Meanwhile, at azimuths local to the planet, an additional system of complex vertical flows are expected: accretion streams. Using high resolution shearing-box simulations, Tanigawa et al. (2012) showed that up as much as ~ 90% of the gas is delivered to a planet through vertical streams, rather than radially through the midplane. This process in turn drives stronger meridional circulation local to the planet, over and above the azimuthal average (Szulágyi et al., 2014; Morbidelli et al., 2014; Fung & Chiang, 2016).

Buoyancy spirals. Planetary spirals are not restricted to those launched at Lindblad resonances. If the disk thermodynamics permit, another species of spiral is launched by the resonance of the planet's orbital frequency and the buoyancy frequency of the disk fluid: buoyancy spirals (Zhu et al., 2012b; Lubow & Zhu, 2014). Unlike Lindblad resonances, the buoyancy resonance does not excite propagating waves, and the resonance locations lie on tilted planes, radially extending much closer to the planet. Buoyancy spirals are very tightly wound compared to Lindblad spirals, and to develop in the disk atmosphere when the thermal relaxation timescale is slow (longer than the timescale of the buoyancy; Bae et al., 2021).

Predictions for Observations

As the above three pages described, an embedded planet influences its surrounding environment in myriad of ways, modifying both the density and velocity fields of the gas. Though they may seem diverse, all features stem from one cause: the planet's gravity. Gravitational torques launch Lindblad (and buoyancy) spirals, Lindblad spirals work to clear gaps, and gaps in turn induce meridional flows.

Several modeling efforts over the last decade have worked to predict how the density and velocity perturbations caused by a planet should appear in real observations with ALMA. Most pertinent to this dissertation are the predictions for how the Lindblad spiral wakes would appear in observations of molecular line emission. Some of the earliest seminal work on this front was done by Perez et al. (2015), who used 3D smooth particle hydrodynamic and radiative transfer simulations of embedded giant planets (1 and 5 Jupiter masses) to create mock intensity channel maps of ^{12}CO, ^{13}CO and C^{18}O emission, corrupted with realistic long baseline phase noise extracted from the recent Science Verification HL Tau ALMA data (ALMA Partnership et al., 2015b). The authors found a clear "twist" in the channel maps due to deviations in the local velocity of the gas along the planetary spiral wake, which would later go by the name of 'kink'. A reproduction of these maps is shown in Figure 1.13.

Following a similar methodology but extending the parameter space, Pérez et al. (2018b)

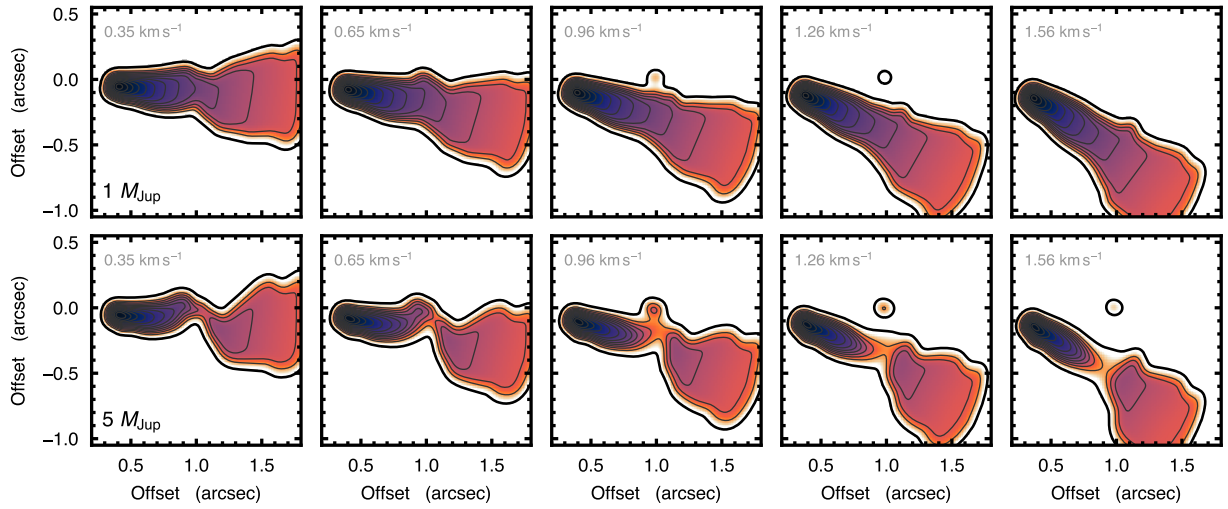

Figure 1.13: Synthetic ALMA channel maps of ^{13}CO emission from disks with an embedded $1\,M_{\rm Jup}$ planet (top row) and $5\,M_{\rm Jup}$ planet. The velocity 'kinks' are more pronounced for the more massive planet. Credits: Disk Dynamics Collaboration et al. (2020), using the simulations by Perez et al. (2015).

demonstrated that the kinematic perturbations from planets may also be detected over large areas of the disk, with the strongest kinks appearing near the planet.

A deeper understanding of the observational mechanics behind velocity kinks came with the development of complementary analytic theory a few years later. Bollati et al. (2021) extended the works of Goodman & Rafikov (2001) and Rafikov (2002a) to show how the projection of the radial and azimuthal velocity perturbation along a wake *Doppler shifts* the gas emission into adjacent spectral channels. Consequently, within a given channel, the observed emission pattern displays a small distortion, or kink, relative to the nominal Keplerian isovelocity curve. The authors further developed a semi-general theory relating observed velocity kink properties (namely the amplitude) to the properties of the planet responsible for them. This semi-analytic approach was particularly pedagogically informative, though it is only applicable at the disk midplane, and for low-mass planets ($M_{\rm p} \ll M_{\rm th}$).

The discerning reader may notice a piece of the puzzle is missing here: The observational predictions described above solely concern the gas. Detecting a planet's spiral wake in *continuum emission* would constitute compelling evidence for its presence, particularly considering the mm continuum probes the dense planet-forming midplane. How do planetary spiral wakes manifest in the *dust* component of the disk, and would they be observable with ALMA? Chapter 2 of this dissertation is dedicated to addressing these questions.

1.3.2 Observational revelations

The velocity kink phenomenon was reported for the first time by Pinte et al. (2018b) using ALMA observations of ^{12}CO toward HD 163296 from the DSHARP program (Andrews et al., 2018), establishing the precedent for the use of velocity kinks as powerful indicators of embedded planets (see Figure 1.14). The authors described that the observed velocity kink is located $\approx$ 260 au from the star, at an elevation of $\approx$ 70 au above the midplane, with the planet assumed to lie on the midplane directly below. By generating a grid of synthetic ^{12}CO channel maps from hydrodynamic and radiative transfer simulations with varying planet masses, they found that a $\approx 2\ M_{\rm Jup}$ planet best reproduced the apparent amplitude of the observed kink, which was estimated as a 15% deviation from Keplerian velocity.

The following year, high angular resolution observations of ^{13}CO toward HD 97048 revealed a second velocity kink, this time at an altitude of 17 au, and associated with a giant planet ($2-3\ M_{\rm Jup}$) whose inferred location at 130 au is co-spatial with a dust gap in the mm continuum (Pinte et al., 2019, see Figure 1.15). The authors noted that HD 97048 was observed with SPHERE on the VLT, obtaining a point source detection limit of $\approx 2\ M_{\rm Jup}$ at the inferred

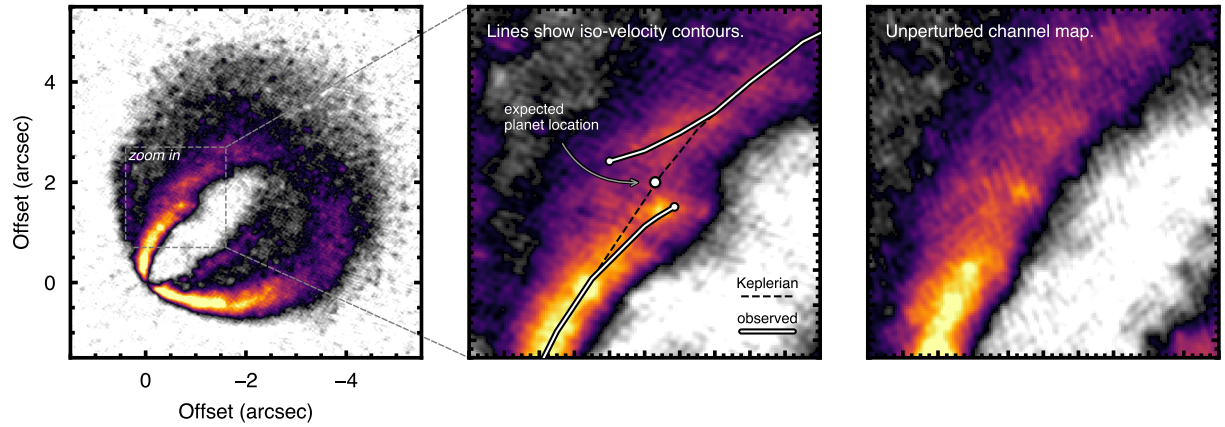

Figure 1.14: The first report of a velocity kink. The leftmost two panels show a single channel of ^{12}CO emission toward HD 163296, displaying a break in the isovelocity curve indicative of an embedded planet. The white dot represents the planet's location, projected upwards onto the ^{12}CO emission surface. The rightmost panel shows an unperturbed channel. Credits: Disk Dynamics Collaboration et al. (2020), adapted from (Pinte et al., 2018b).

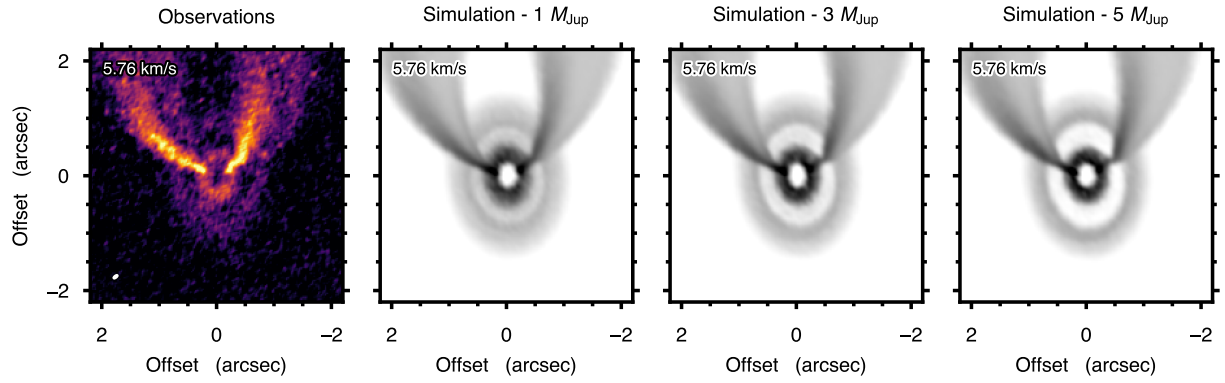

Figure 1.15: The second report of a velocity kink. The leftmost panel shows a single channel of ^{13}CO emission toward HD 97048, displaying a kink in the western emission lobe indicative of an embedded planet located within the continuum gap. The rightmost three panels show synthetic ^{13}CO channels from 3D hydrodynamic simulations with varying planet mass, labeled at the top of each column. Credits: Disk Dynamics Collaboration et al. (2020), adapted from (Pinte et al., 2019).

planet location. Using synthetic observations from hydrodynamic and radiative transfer simulations, they estimated that the material enshrouding the planet has an optical depth along our line-of-sight of $\tau \approx 0.5$ at 1.6 μm, such that the embedded planet's thermal or accretion-related emission would be extincted by a factor of two.

Pinte et al. (2020) carried out a larger search for the presence of velocity kinks within an additional 17 systems (18 re-counting HD 163296) observed by the DSHARP Large Program

in ^{12}CO, reporting the detections of velocity kinks in 7 new disks and a second velocity kink in HD 163296 at smaller orbital separations. Most recently, Pinte et al. (2025) found kinematic signatures in 6 of the 15 disks observed by the exoALMA Large Program in ^{12}CO pointing toward the presence of planets. Preliminary hydrodynamic and radiative transfer simulations were performed, and the planets responsible for the observed velocity kinks were estimated to have masses in the range of 1 to 5 $M_{\rm Jup}$, at orbital distances between 80 and 310 au.

Nearly all studies targeting the kinematic detection of planets have relied on observations of bright molecular tracers, ^{12}CO or ^{13}CO, in low rotational transitions ($J = 3-2$ or $J = 2-1$). The brightness of these lines helps achieve high signal-to-noise ratios (SNR) at narrow spectral resolutions (Δv) across the finite width of the emission line, without prohibitively long integration times (Δt), since SNR $\propto \sqrt{\Delta v \Delta t}$. Still, the observational demand remains high. For example, the exoALMA Large Program —a dedicated kinematic planet-hunting campaign targeting the $J = 3-2$ transition of CO isotopologues (Teague et al., 2025)— required 180 hours of observing time toward 15 disks to reach their goals.

At the same time, the torques exerted by embedded planets are strongest in the disk midplane, where the planets are expected to reside (c.f. §1.3.1). The velocity kinks observed in ^{12}CO or ^{13}CO trace the upper extensions of the planetary wake, which has propagated upward from the midplane to become expressed in these molecular emission surfaces.

In contrast to line emission, continuum emission is not confined to a finite spectral width. Continuum observations can be made over bandwidths many orders of magnitude broader than line emission, exploiting the full bandwidth of ALMA to achieve high SNR in much shorter integration times.

Detecting a planet's wake in the dust continuum, which probes the planet-forming midplane, would provide compelling evidence for its presence — particularly when supported by corresponding evidence for these wakes in the molecular layers. These considerations motivated the studies presented in Chapters 2 and 3.

1.4 The role of instabilities

While the first half of this dissertation is dedicated to searching for young planets (Chapters 2 & 3), the second half shifts focus toward understanding the physical processes involved in their formation (Chapters 4 & 5).

Instabilities play a key role in the formation of planets. Insofar as they appear at critical junctures along our theorized formation pathways, one may even argue that planet formation would not proceed in a disk without them. Fundamentally, instabilities are the mechanism by which minor perturbations within a disk can aggravate and intensify into major ones. They represent the difference between a smooth, stable environment and one with high dynamic range.

The full zoo of instabilities is a broad class of processes. Some instabilities are global in nature, influencing the disk on scales of hundreds of au, while other instabilities play out locally, at the scale of a pressure bump or eddy. Some manifest primarily in the gas component of the disk, and others through the interplay between the dust and gas. The essence of every instability, though, is the same: De-stabilizing effects prevail over stabilizing ones.

Instabilities can concentrate solids, encourage the formation of clumps, or trigger their gravitational collapse, in each case enabling progress between embryonic evolutionary stages that might otherwise stall. Instabilities are also essential to the secular evolution of disks, driving turbulence or large-scale structures, providing a means for mass and angular momentum to be redistributed (see §1.1.3). The activation of a given instability, however, is not necessarily guaranteed — each species requires certain conditions to be met in order to operate. This section briefly reviews the role of key instabilities in disk evolution (§1.4.1), and highlights the critical junctures in theorized pathways to planet formation where they appear (§1.4.2).

1.4.1 Disk evolution

As described in §1.1.3, the formation of circumstellar disks is a natural consequence of the conservation of angular momentum. Once formed, they remain subject to the same conservation law, such that their subsequent evolution and dispersal is a question of how the angular momentum can be redistributed, or lost. The processes responsible for the transport of angular momentum thus govern the disk lifetime, and determine the amount of time planet formation has to proceed (e.g., Manara et al., 2023). Broadly, two classes of transport mechanisms have been proposed: winds (of magneto-hydrodynamic origin), and turbulence (of magneto-, gravito-, thermo- or pure-hydrodynamic origin). We'll discuss the latter first.

For decades, turbulent stress has been modeled as an effective viscosity, following the seminal work of Shakura & Sunyaev (1973) and Lynden-Bell & Pringle (1974). The physical origin of the postulated turbulence was later identified as an instability: the magneto-rotational instability (MRI) by Balbus & Hawley (1991). The MRI operates efficiently in ionized regions of a differentially rotating disk (§1.2), where the gas is well coupled to a weak magnetic field that threads the disk vertically. Under these conditions, the differential rotation shears the magnetic field lines, generating a magnetic tension that acts to transport angular momentum outward —to annuli that already have more angular momentum— leading to an instability. Its nonlinear properties drive sustained turbulence and efficiently redistribute angular momentum. The degree of ionization of a disk is uncertain and spatially variable, however; in weakly ionized regions, the MRI may be suppressed (e.g., Turner et al., 2014).

A host of other (thermo-)hydrodynamic instabilities have been discovered in models and disk simulations which do not require an ionized disk, though are expected to produce weak to moderate turbulence (e.g., see Lesur et al., 2023, for a review). Some examples include the vertical shear instability (VSI), which operates when there are vertical gradients in rotational velocity due to thermal stratification (c.f. 1.1.3; Nelson et al., 2013), and the Rossby wave instability (RWI; Lovelace et al., 1999), where sufficiently sharp radial gradients in the curl of the velocity (vorticity) lead to long-lived anticyclonic vortices whose interactions transport angular momentum (Godon & Livio, 1999; Johnson & Gammie, 2005).

Importantly, *gravitational instability* (GI) drives vigorous turbulence. In disks that are sufficiently massive and/or cool, self-gravity can render the disk unstable to non-axisymmetric perturbations, leading to the formation of large-scale spiral arms (Kratter & Lodato, 2016a). These spiral arms transport angular momentum outward by gravitational torques, driving an inward flow of mass. The production of spirals can be sustained if the disk settles into a self-regulating state of marginal instability (Paczynski, 1978), where the dissipation of gravitational potential energy in turn heats the gas, acting as a stabilizing counterbalance to cooling and self-gravity (Durisen et al., 2007). In these conditions, GI-driven spiral waves can be strong sources of viscosity through gravito-turbulence — highly efficient at transporting angular momentum and shaping the disk's evolution (Lodato & Rice, 2004). Instances where the stabilizing feedback loop fails, or not, is highly pertinent to the formation of bound objects (see §1.4.2).

Finally, returning briefly to the former class of proposed angular momentum transport mechanism, magnetohydrodynamic (MHD) disk winds (Blandford & Payne, 1982) offer a complementary but distinct paradigm for disk evolution. In the presence of a large-scale poloidal magnetic field, angular momentum is extracted from the disk as ionized gas in the surface layers is launched from the disk, accelerated along open magnetic field lines (Lesur, 2021; Pascucci et al.,

2023). This magneto-centrifugal process brakes the disk's rotation and drives accretion onto the star (e.g., Moscadelli et al., 2022).

1.4.2 Pathways to planet assembly

Planet assembly bridges an extraordinary range of scales. If we consider a micron-sized dust grain as the starting point, and a gas giant planet as the end point, then the process of planet formation spans 12 orders of magnitude in size and 40 orders in mass. To conceptually navigate this vast range, the field tends to organize its thoughts around intermediate size regimes: (sub)micron-sized grains of the ISM, mm-sized aggregates, km-sized planetesimals, and, beyond that, terrestrial planets, whose size is similar to the cores of gas giants.

Currently, there are two theorized pathways to traverse these scales. In the *core accretion* scenario (Safronov, 1972; Lissauer, 1993), growth gradually proceeds from the bottom up, with solids progressing through the size bins to form a core that may go on to acquire a gaseous envelope. In contrast, the *gravitational instability* scenario (Boss, 1997) describes a more rapid top-down process, where unstable regions of the disk gravitationally collapse to form bound objects directly. The goal of this section is to highlight the critical junctures along both these pathways where instabilities play a key role.

Core accretion

From μm to mm. The initial stages of planet formation involve the growth of (sub)micron-sized dust grains into mm-sized particles. At these scales, growth is facilitated by pair-wise collisions that result in sticking, or coagulation (e.g., Dullemond & Dominik, 2005). Here, the role of instabilities (e.g., MRI) lies in the generation of turbulence, which encourages collisions. (Vertical settling and Brownian motion do too.)

From mm to km. Transitioning from mm-sized grains to km-sized planetesimals represents the first and perhaps most critical juncture in the core accretion pathway. There are two barriers to growth beyond mm-sizes. First, between $\sim$ 1 mm to $\sim$ 1 m, pair-wise collisions tend to occur at increasingly higher relative velocities, resulting in fragmentation rather than coagulation (e.g., Birnstiel et al., 2016; Brauer et al., 2008). This is known as the "fragmentation barrier". The second is the "meter-sized barrier" or radial drift problem (§1.1.4), where objects of this size are quickly lost out of the disk (Takeuchi & Lin, 2002).

At this critical juncture, two-fluid instabilities may provide a route to rapidly forming planetesimals in manner that bypasses the barriers of sequential growth through the meter-sized regime — by effectively skipping them. One prominent theory is the streaming instability (SI;

Youdin & Goodman, 2005; Johansen & Youdin, 2007), where mm-sized pebbles seek refuge from the headwind by collecting in each other's slipstream. As more pebbles join the peloton, they collectively exert a stronger backreaction on the gas, reducing their radial drift rate, capturing more pebbles, and eventually forming clumps on small spatial scales $\ll H$. If these pelotons of pebbles exceed the Roche density, they can gravitationally collapse to directly form planetesimals as large as 100 km in radius (Johansen et al., 2009; Youdin, 2011).

From planetesimals to planets. Beyond planetesimal sizes, pair-wise collisions become an efficient growth mechanism once more and instabilities take a back seat. In the classical core accretion model, the collisions are considered to be between planetesimals and other planetesimals, or at later stages, planetesimals and protoplanetary cores (Pollack et al., 1996). Here, the cross-section of the larger body is amplified by its gravity ("gravitational focusing", e.g., Kokubo & Ida, 2000). In the last few years, the theory of "pebble accretion" has emerged, which considers the accretion of mm-sized grains (Ormel & Klahr, 2010; Lambrechts & Johansen, 2012). Pebble accretion is aerodynamically assisted (unlike planetesimal accretion), and can be extremely efficient, given an initial seed above a Ceres mass ($\sim 5 \times 10^{-7}\ M_{\rm Jup}$). However, pebble accretion becomes extremely inefficient at disk radii of $\gtrsim 30$ au where the dynamical timescales are prohibitively large (Johansen & Lambrechts, 2017).

From cores to gas giants. The core accretion pathway to gas giant planet formation hinges on whether a solid core can grow to a critical mass before the gaseous disk dissipates (Pollack et al., 1996). If this is achieved, the core can trigger a hydrodynamic instability that leads to the rapid accretion of a massive gaseous envelope (Perri & Cameron, 1974; Mizuno, 1980).

Gravitational instability

The phenomenon of gravitational instability (GI) offers a more direct route to forming massive objects, particularly at large disk radii. In this picture, the parental protoplanetary disk breaks up through its own self-gravity into clumps that go on to collapse and contract into giant planets — effectively collapsing the sequence of intermediate size regimes that was described above into one single step. GI was put forward as a mode of planet formation by Boss (1997), whose numerical simulations suggested that GI can form giant planets (with rocky cores) faster than the core accretion mechanism can.

As described in §1.4.1, a disk's self-gravity renders it unstable to non-axisymmetric perturbation modes, which is opposed by two stabilizing forces: pressure (which stabilizes small scales) and shear (which stabilizes large scales). The formation of spiral arms is triggered in regions where the de-stabilizing forces prevail. The subsequent evolution of these spiral arms de-

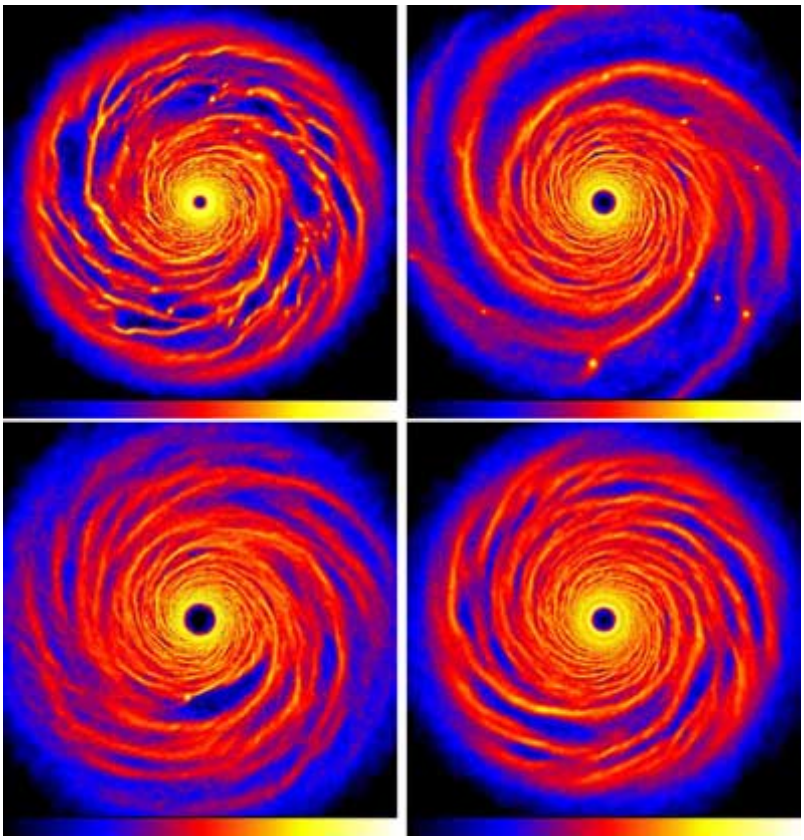

Figure 1.16: Surface density maps of massive disks undergoing gravitational instability, and in some cases, fragmentation. From left to right and top to bottom, the disks cool at rates of $3\times$, $5\times$, $6\times$ and $7\times$ the local dynamical time. The colorbar is logarithmic from 10 to 2×10^4 g cm^{-2}. Credits: Rice et al. (2005).

pends on self-gravity overwhelming the thermal pressure within them, and so thermodynamics becomes critical. If the gas cannot dissipate the increased stress —or cools too rapidly— to maintain a state of marginal instability (Paczynski, 1978), the spiral arms fragment into clumps (see Figure 1.16; Rice et al., 2005). Numerical simulations have shown that fragmentation occurs if the disk cools $\sim 3-6\times$ quicker than the local dynamical time (Gammie, 2001; Rice et al., 2003).

Recent works have highlighted an intriguing feature of the GI paradigm, showing how planet formation may proceed even without fragmentation. Instead, the dust layer embedded within the gaseous spiral arms —themselves sustained by slow cooling— may become unstable and collapse into planetary cores. This mechanism has been explored in detail in recent numerical simulations (Booth & Clarke, 2016; Longarini et al., 2023b,a; Rowther et al., 2024a). Considering gas fragmentation and dust fragmentation as viable pathways, GI may facilitate planet forma-

tion under both the rapidly cooling and slowly cooling regimes.

Connections to observations

Ultimately, we wish to confront our theorized pathways with observations. We can approach this from two directions:

First, through measurements of the fully mature exoplanet population. From the statistical properties of the growing number of detected exoplanets, core accretion has been demonstrated (with population synthesis models) to successfully account for most of the observed exoplanet population with small orbital radii ($\lesssim$few au; Benz et al., 2014). This is the population most readily accessible to our transit and radial velocity surveys. Direct imaging surveys, better equipped to detect the wide-orbit population (while still $\lesssim 300$ Myr old), have found that the overall occurrence rate of giant planets outside of $\gtrsim 30$ au is $0.6-8.6\%$ (Bowler, 2016; Vigan et al., 2017). This suggests that while GI is a less prolific pathway, it is crucial for explaining certain planetary systems.

Second, through observations of the disks around young stars where planet formation is actively unfolding. Many aspects of core accretion in action are inherently difficult to observe directly — the intermediate size regimes (planetesimals) have low opacity and the timescales involved are long. Gravitational instability, on the other hand, can leave observable imprints on the disk's global structure and dynamics while it is occurring (Hall et al., 2020). Chapters 4 and 5 of this dissertation are dedicated to discovering GI in action by examining the global dynamics of planet-forming disks with high velocity resolution ALMA observations.

1.5 This Dissertation

The dual goals of this dissertation are to explore how we can discover young planets through the gravitational signatures they imprint on their formation environment, and to assess what physical processes may be viable planet formation pathways through scrutinizing the global dynamics of these environments. The studies presented here are grounded in observations with the ALMA radio telescope, measuring continuum emission at wavelengths straddling 1.0 mm, as well as spectral line emission primarily from CO and its isotopologues. In many of the presented analyses, 2D or 3D numerical hydrodynamic simulations are performed, and synthetic data products are used to make predictions or provide insights into the observed features. Analytic theory is employed throughout as well, with analytic solutions traced onto the data in various scenarios to further aid in the interpretations. An overall breakdown of the contributions by chapter is as follows.

Chapter 2 begins by assessing ALMA's capability to detect the continuum emission pattern of spiral wakes launched by planets as they orbit within their host circumstellar disk. Detecting a planet's wake would constitute compelling evidence for its presence, particularly when observed in the dust continuum probing the dense planet-forming midplane. While these spiral wakes are incipiently launched in the gas, our hydrodynamic simulations with aerodynamic dust-gas interactions reveal that the wakes become expressed in the midplane dust layer of the host disk, and —in case of dust populations probed by ALMA— manifest with amplitudes and crest locations identical to that of the gas. Carrying out a suite of hydrodynamic simulations for a range of disk conditions, I generate 432 synthetic ALMA Band 7 continuum images under a wide variety of observing specifications. The brightness of the wake depends sensitively on the thermodynamical properties of the host disk, but in those most favorable, the wakes of giant planets can be recovered with observing times on the order of hours — similar to continuum programs commonly executed. The composite dataset of 432 synthetic images is made available[5] to the community.

After laying this groundwork, **Chapter 3** puts these predictions to the test with archival ALMA continuum observations in Band 6 and 7, to hunt for embedded planets in the midplane of 10 disks selected for exhibiting kinematic evidence of planetary spiral wakes in surficial CO emission. Unambiguous detections of spirals in the continuum were confirmed in only three disks (Elias 27, IM Lup and WaOph 6), in each case misaligned from the analytic model wake trajectories originating from the predicted planet location. These findings corroborate the ris-

[5] https://doi.org/10.6084/m9.figshare.19148912

ing notion that while the gravitational influence of planets can manifest as localized velocity kinks in intensity channels, not all kinks are unequivocally associated with planets.

Switching gears to address the second goal of this dissertation, **Chapter 4** scrutinizes the global dynamics of the disk around AB Aur, using high spectral resolution ALMA observations of ^{13}CO and C^{18}O molecular line emission in one of the longest programs toward a single protoplanetary disk to date. With a 3-pronged analysis combining molecular line data, 3D hydrodynamic simulations and analytic modeling, we discover compelling evidence for gravitational instability (GI) in this disk. I develop new analysis techniques to reveal the evidence for GI, including a flexible high-pass filter with a radially expanding convolution kernel[6] to expose global velocity perturbations and an architecture of spiral structure traced by the ^{13}CO line brightness and width. Working in position-velocity (PV) space enables us to morphologically identify GI-induced velocity wiggles, quantify their magnitude in units of m s^{-1}, and make quantitative estimates of the disk mass by comparisons with analytic models. These results suggest gravitational instabilities play a role in shaping the dynamical evolution of the largest circumstellar disks and the formation of wide-orbit giant planets at early stages.

The findings of the previous chapter opened new questions: How could a relatively evolved ($\sim$ 4 Myr old) system sustain, or gain, the necessary disk mass to trigger gravitational instability? **Chapter 5** presents a spatio-kinematic analysis of ^{12}CO molecular line data toward AB Aur from the same program. I cultivate a new approach, 'anti-Keplerian masking', to extract three disk-scale gas structures kinematically inconsistent with disk-like motion. Modeling their spatio-kinematic trajectories with an analytic infall model, I reproduce their three dimensional geometries and precisely pinpoint where they land within the disk. Coincident with this merging zone, we observe a brightness peak in sulphur monoxide emission indicative of localized heating by shocks. Together, Chapters 4 and 5 present a unified picture of late infall inducing replenishment of the disk, triggering gravitational instability, and modifying the conditions of forming planets. Just as vital, these studies provide a roadmap for the analysis of ever more complex systems revealed by such deep spectral line data.

Finally, **Chapter 6** summarizes these contributions in the wider context of the field, and highlights some of the ways they have already been used as a springboard for future investigations. This chapter also offers ideas and preliminary demonstrations of fresh approaches to planet-hunting, building on the techniques developed in this dissertation. These ideas are presented as part of an earnest gaze toward the exciting future for ground-based radio astronomy.

[6] https://github.com/jjspeedie/expanding_kernel

Chapter 2

Observing planet-driven dust spirals with ALMA

J. Speedie, R. A. Booth and R. Dong

The Astrophysical Journal, 930, 1, 40 (2022)

Abstract

ALMA continuum observations of thermal emission from the dust component of protoplanetary disks have revealed an abundance of substructures that may be interpreted as evidence for embedded planets, but planet-driven spiral arms –perhaps one of the most compelling lines of evidence– have proven comparatively elusive. In this work, we test the capabilities of ALMA to detect the planet-driven spiral signal in continuum emission. Carrying out hydrodynamic simulations and radiative transfer calculations, we present synthetic Band 7 continuum images for a wide range of disk and observing conditions. We show that thermal mass planets at tens of au typically drive spirals detectable within a few hours of integration time, and the detectable planet mass may be as low as ~Neptune mass ($0.3\,M_{th}$). The grains probed by ALMA form spirals morphologically identical to the underlying gas spiral. The temperature of the dust spiral is crucial in determining its contrast, and spirals are easier to detect in disks with an adiabatic equation of state and longer cooling times. Resolving the spiral is not necessary for its detection; with the help of residual maps, the optimal beam size is a few times the spiral width at a constant noise level. Finally, we show how the presence of gaps and rings can impair our ability to recognize co-located spirals. Our work demonstrates the planet-finding potential of the current design specification of ALMA, and suggests that observing capability is not the bottleneck in searching for spirals induced by thermal mass planets.

2.1 Introduction

Like the wake created by a boat as it moves through water, a planet drives a wake as it orbits in a disk (Ogilvie & Lubow, 2002). The wake then gets wound into a spiral by the disk's own Keplerian differential rotation (Arzamasskiy & Rafikov, 2018). Planet-driven spiral arms are a well understood natural consequence of the gravitational interaction between the planet and the disk; the analytical theory was established in the 1970's (Goldreich & Tremaine, 1978, 1979b, 1980) and has been repeatedly confirmed by hydrodynamical simulations (Dong et al., 2011a,b; Zhu et al., 2015; Bae & Zhu, 2018a,b; Miranda & Rafikov, 2019a). We therefore expect that within every planet-hosting protoplanetary disk, spiral wakes should also exist.

This theoretical expectation has not translated into an abundance of clear observational detections of planet-driven spirals, however. That statement particularly applies to continuum observations of (sub-)mm dust. High angular resolution ALMA continuum observations have shown that gaps and rings are common (e.g., Huang et al., 2018a), implying an abundance of planets forming in disks (Zhang et al., 2018), but to date we have only a handful of detections of continuum spirals. Elias 27, IM Lup and WaOph 6 (Huang et al., 2018b) exhibit large-scale $m = 2$ continuum spirals, but they are not co-located with a gap/cavity, and have not been decisively attributed to an embedded companion (Mawet et al., 2012; Meru et al., 2017; Paneque-Carreño et al., 2021a; Brown-Sevilla et al., 2021). A smaller scale, single continuum spiral has been observed in MWC 758 (Dong et al., 2018c); the motion of that disk's related $m = 2$ scattered light spirals have been reported as inconsistent with gravitational instability (Ren et al., 2020) but no associated point-source has yet been detected (Boccaletti et al., 2021). Tentative crescents or filaments in association with gaps/rings have been observed in continuum images of V1247 Ori (Kraus et al., 2017) and HD 135344B (Casassus et al., 2021) but haven't been confidently classified as spirals. Continuum spirals in disk systems with multiple stars, HD100453 (Rosotti et al., 2020b), AS 205 N and HT Lup A (Kurtovic et al., 2018) have been identified as induced by gravitational interaction with companions, but the companions are not of planetary mass.

Searches for planet-driven dust spirals in continuum observations, and recognizing the signatures that a spiral is planet-driven if it is found, would benefit from a clearer understanding of the following complexities:

(1) It is well understood how planets drive spirals in the gas, but it is not necessarily obvious how spirals manifest in the dust. The morphology (i.e., the amplitude, width, and azimuthal location) of dust spirals is determined by how quickly each particle responds to the drag forces exerted by the passing spiral wake (Sturm et al., 2020a). The response time of the dust depends on how well it is coupled to the gas, which in turn depends on the grain properties and local

gas density (the latter making it a function of radial location and height above the midplane, e.g. Eqn. 1 of Veronesi et al., 2019). For each observing wavelength and instrument, we need to understand what architecture of dust spiral we are looking for.

(2) Compounding this is the fact that planet-driven spirals are not dust traps. Since the gas spiral wake co-moves with the planet as it orbits the star, the dust experiences the spiral perturbation as a transient phenomenon. As a result, a dust spiral's density amplitude cannot exceed that of the gas. This is different to the case of dust rings, where dust can accumulate in a stationary (or at least, long-lived) pressure maximum over time (Whipple, 1972). In this way, a lower mass planet can still produce readily detectable dust gaps/rings (e.g., Rosotti et al., 2016; Bae et al., 2017; Dong et al., 2017, 2018a), but a lower mass planet drives proportionally lower amplitude spiral arms (Dong et al., 2011b; Bae & Zhu, 2018a; Miranda & Rafikov, 2019a). We need to understand what level of contrast a planet-driven spiral can achieve in the dust density for planets in the "still-forming" mass range.

(3) How we can actually observe the dust density distribution is, in the case of continuum observations, through its thermal emission – which then introduces the question of dust temperature and the rate at which the disk cools. The importance of using a realistic treatment of disk thermodynamics in simulations whose purpose is to interpret or predict planet-induced disk substructure is gaining recognition (Miranda & Rafikov, 2019b). One's choice of the equation of state has been shown to have significant consequences on the density wave dynamics (Miranda & Rafikov, 2020a). The rate of cooling, specifically, affects the angular momentum flux across the disk, which modifies the gas spiral density amplitude (Miranda & Rafikov, 2020b; Zhang & Zhu, 2020). The hydrodynamic $P\mathrm{d}V$ work done on the gas as the spiral pressure wave passes generates a rise in the temperature distribution, forming temperature spirals whose amplitudes can be observationally significant (Muley et al., 2021). For a given disk's thermodynamic properties (and optical depth), we need to understand how the density and temperature spirals combine into the observed quantity of intensity – for the dust.

(4) Finally, there is the practical consideration of the angular resolution and sensitivity at which we observe. Once we understand the dust spiral morphology and possible intensity contrast, we can establish which observing specifications, and which disks, give us the best chance of detecting planet-driven dust spirals.

In this work, we carry out this experiment for the case of sub-mm dust continuum observations with Band 7 of ALMA. Our purpose is to aid searches for planet-driven dust spirals in existing ALMA observations and to inform future observing proposals.

§2.2 describes our methodology. In §2.3 we present our results on the important physics: dust-gas coupling (Complexities 1 & 2) and thermodynamics (Complexity 3). In §2.4 (Com-

plexity 4) we present synthetic ALMA continuum observations of planet-driven dust spirals for a variety of disk and observing conditions. We discuss our results in §2.5 and summarize our findings in §2.6.

2.2 Methods

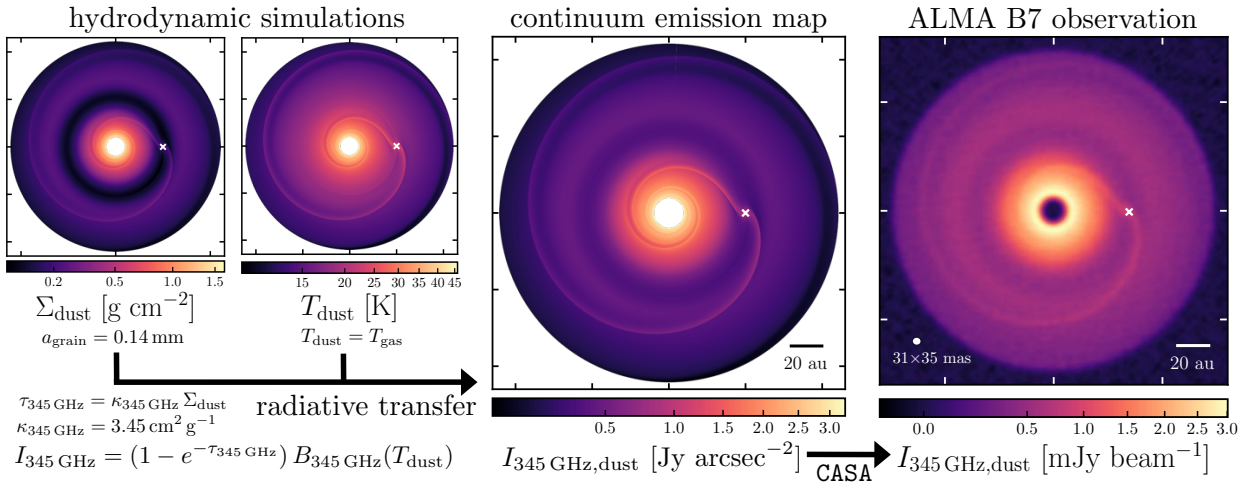

Figure 2.1: The procedure by which we generate synthetic ALMA continuum observations of planet-driven spiral arms. Dust surface density and temperature maps from our hydrodynamic simulations are combined via radiative transfer calculations to create model images of dust thermal emission (emergent intensity), with which we generate continuum observations using `CASA`. Shown here is the case of a $1\,{\rm M_{th}}$ planet embedded in an adiabatic ($\beta = 10$), marginally optically thick disk ($\tau_0 = 1.0$), observed with the C43-5 + C43-8 configuration pair and a combined 8.0 hrs of on-source time (measured rms noise $9.17\,\mu{\rm Jy\,bm^{-1}}$).

We run 2D gas + dust hydrodynamic simulations of disks with different cooling rates, optical depths and embedded planet masses to obtain the dust density and temperature distributions at the disk midplane (§2.2.1). The dust grain size is fixed to $a_{\rm grain} = 0.14\,{\rm mm}$ to correspond to Band 7 and the gas surface density is varied to achieve different dust optical depths assuming a fixed dust-to-gas mass ratio of 0.01. Next, we create synthetic continuum emission images of the resulting dust spirals via radiative transfer calculations (§2.2.2). With those we generate synthetic ALMA observations for a range of integration times and antenna configurations (§2.2.3). Figure 2.1 provides examples of the outputs after each step of our procedure.

2.2.1 Hydrodynamic Simulations

We perform 2D multi-fluid hydrodynamic simulations with a custom version of the FARGO3D code (Benítez-Llambay & Masset, 2016), modified to compute dust dynamics with the Eulerian implementation described in Rosotti et al. (2016), which uses the semi-implicit integrator introduced by Booth et al. (2015).

We run the simulations in a 2D cylindrical geometry (r, ϕ). The units are dimensionless, such that the orbital radius of the planet (r_p) is unity, the unit of time is the Keplerian angular velocity Ω_{Kep} at $r = r_p$, and the unit of mass is that of the central star. The domain extends from $0.1\,r_p$ to $3.0\,r_p$ in radius and from $-\pi$ to π in azimuth. The grid has a resolution of $N_r \times N_\phi = 1100 \times 2048$ cells, spaced logarithmically and linearly in the radial and azimuthal directions respectively, for approximately square cells. With this resolution, one scale height at r_p is resolved with 23 cells in both directions, and we resolve the spiral shock fronts.

The code solves the mass, momentum and energy equations of hydrodynamics:

$$\frac{\partial \Sigma_{gas}}{\partial t} + \nabla \cdot (\Sigma_{gas} \vec{v}_{gas}) = 0\,, \tag{2.1}$$

$$\frac{\partial \vec{v}_{gas}}{\partial t} + \vec{v}_{gas} \cdot \nabla \vec{v}_{gas} + \frac{\nabla P}{\Sigma_{gas}} = \vec{g}\,, \tag{2.2}$$

$$\frac{\partial E}{\partial t} + \vec{v}_{gas} \cdot \nabla E + \frac{P}{\Sigma_{gas}} \nabla \cdot \vec{v}_{gas} = 0\,, \tag{2.3}$$

where Σ_{gas}, $\vec{v}_{gas}$, P and E are the gas surface density, velocity, pressure, and internal energy per unit area, and $\vec{g}$ is the gravity term.

We solve the energy equation for the gas and simultaneously evolve the dust[7]. The dust is treated as a pressureless fluid and evolves according to linear drag forces from the gas, in addition to gravity and diffusion. The dust velocity is given by

$$\frac{d\vec{v}_{dust}}{dt} + \vec{v}_{dust} \cdot \nabla \vec{v}_{dust} = -\frac{1}{t_{stop}} \left(\vec{v}_{dust} - \vec{v}_{gas}(t) \right) + \vec{a}_{dust}\,, \tag{2.4}$$

where t_{stop} is the stopping time of the dust and $\vec{a}_{dust}$ is the non-drag acceleration. We focus on dust with dimensionless stopping time $t_{stop}\,\Omega_{Kep} \leq 1$, for which the fluid approximation is reasonable (Garaud et al., 2004). Throughout our simulations the dust-to-gas ratio never approaches unity, thus the back reaction from the dust onto the gas is unimportant and ignored. We include dust diffusion, and the Schmidt number (the ratio of the α-viscosity ν to the dust

[7] To our knowledge, ours is the first work using this custom version of FARGO3D to do so.

diffusion coefficient D) is set to $\mathrm{Sc} = \nu/D = 1$.

In order to explore the observability of planet-driven dust spirals in a diversity of disk conditions, we vary the gas equation of state to be locally isothermal or adiabatic. The relationship between the gas pressure, density and temperature naturally affects the gas spiral, which in turn we expect to affect the resultant dust spiral via dust-gas coupling.

The adiabatic equation of state is $P = (\gamma - 1)\,E$, and the gas temperature is

$$T_{\mathrm{gas,adi}} = \frac{\mu\, m_{\mathrm{p}}}{k_{\mathrm{B}}} \frac{(\gamma-1)\,E}{\Sigma_{\mathrm{gas}}}. \tag{2.5}$$

Here, $\mu = 2.3$ is the chemical potential for fully molecular gas of cosmic composition (mix of H and He), m_{p} is the mass of a proton, k_{B} is the Boltzmann constant and γ is the adiabatic index. In this work, we assume $\gamma = 5/3$, appropriate for a composition of H_2 at a low temperature (tens of Kelvin). We perform the adiabatic simulations with a simple cooling prescription, such that the gas temperature is relaxed towards its initial state on a timescale controlled by the parameter β:

$$\frac{dE(t)}{dt} = -\frac{\Omega}{\beta}\Big(E(t) - E_0\Big) \tag{2.6}$$

where Ω is the local angular velocity. Previous work has shown that simulations with an adiabatic equation of state and short cooling times ($\beta \lesssim 10^{-1}$) yield small planet-induced temperature perturbations and are very similar to simulations with an isothermal equation of state (Miranda & Rafikov, 2020b,a; Zhang & Zhu, 2020; Muley et al., 2021). Analytic expressions derived assuming conventional dust properties indicate that the cooling timescale can vary dramatically within a single disk at different radii, and typical values are $t_{\mathrm{cool}} = \beta\,\Omega^{-1}(r) \sim 20$ at $r = 10\,\mathrm{au}$ and $t_{\mathrm{cool}} \sim 0.02$ at $r = 100\,\mathrm{au}$ (Eqn. 39 of Zhang & Zhu, 2020). Thus in our experiments we explore β values of 0 (isothermal) and 10. We note that while the code does not add the energy dissipated via physical viscosity (e.g. α viscosity) to the internal energy of the gas, the heating due to the artificial viscosity (for handling shocks) has been included[8]. Viscous heating is likely unimportant for our purposes as we are modelling Class II disks with planets at tens of au.

We initialize the aspect ratio in the disk as

$$h(r) = H/r = h_{\mathrm{p}}\, r^{f}, \tag{2.7}$$

where we choose a flaring index of $f = 1/4$ and value of h at the location of the planet $h_{\mathrm{p}} = 0.07$

[8]Viscous heating is also missing in the public version of `FARGO3D` (Benítez-Llambay & Masset, 2016).

(see §2.2.2 for physical motivation). We use the α viscosity prescription of (Shakura & Sunyaev, 1973) and assume the conventional $\alpha = 10^{-3}$. Varying the viscosity does not impact the spiral arms (Dong & Fung, 2017a), while it makes an impact on the gap depth (Fung et al., 2014).

We tailor the setup of the dust component of our hydrodynamic simulations toward the end goal of ALMA Band 7 continuum observations by fixing the dust grain size. For the observing wavelength $\lambda_{\rm obs} = 0.87\,$mm (observing frequency $\nu_{\rm obs} = 345\,$GHz), we assume we probe thermal emission from dust particles of size (Kataoka et al., 2015a; Pavlyuchenkov et al., 2019)

$$a_{\rm grain} \approx \frac{\lambda_{\rm obs}}{2\pi}, \tag{2.8}$$

giving a dust grain size of $a_{\rm grain} = 0.14\,$mm. This means that the dust Stokes number,

$$\mathrm{St} = \mathrm{t_{stop}}\,\Omega_{\rm Kep} = \frac{\pi}{2}\,\frac{\mathrm{a_{grain}}\,\rho_{\rm dust}}{\Sigma_{\rm gas}}, \tag{2.9}$$

varies in space and time inversely to the gas surface density. We assume $\rho_{\rm dust} = 1.2\,\mathrm{g\,cm^{-3}}$ for the bulk grain density (in broad agreement with Birnstiel et al., 2018b). The initial gas surface density distribution is assumed to follow a power law

$$\Sigma_{\rm gas}(r) = \Sigma_0 \left(\frac{r}{r_{\rm p}}\right)^{-1}, \tag{2.10}$$

where Σ_0 is the initial gas surface density at $r = r_{\rm p}$. Since the simulations are scale-free and we ignore dust feedback, the normalization factor Σ_0 is arbitrary and we can use Σ_0 to scale our simulation results during post-processing to the physical $\Sigma_{\rm gas}$ and St that matches the $a_{\rm grain}$ we desire. More on this in §2.2.2.

We run our simulations with three different planet masses: $M_{\rm p} = 0.3$, 1.0 and 3.0 $\mathrm{M_{th}}$ (where the thermal mass is $\mathrm{M_{th}} = h^3 M_\star$), corresponding to planet-star mass ratios of $q = 1.03 \times 10^{-4}$, 3.43×10^{-4} and 1.03×10^{-3}. With an aspect ratio of $h_{\rm p} = 0.07$ and a stellar mass of $M_\star = 0.8\,\mathrm{M_\odot}$, those masses equate to $1.6\,\mathrm{M_{Nep}}$, $0.96\,\mathrm{M_{Sat}}$ and $0.86\,\mathrm{M_{Jup}}$ respectively. We keep the planet on a fixed circular orbit and include the indirect term that compensates for the displacement between the simulation grid origin and the star-planet center of mass. We simulate to 1500 orbits so that gaps and rings, a commonly observed category of disk substructure, have fully formed (e.g. Fig. 1, Fung & Chiang, 2016).

In addition to the simulations that we use to generate ALMA observations (presented in §2.4), we run a separate shorter set (15 orbits) for the purposes of deepening our understanding the effect of the cooling time and dust-gas coupling on the spiral's intrinsic properties (pre-

sented only in §2.3.1 and §2.3.2). In this set, we vary the cooling time from $\beta = 10^{-3}$ to 10^{2} in factors of 10. Following Sturm et al. (2020a), we evolve 40 species of dust with a spatially and temporally constant Stokes number logarithmically spaced between $\mathrm{St} = 10^{-4}$ and 1.0. Otherwise, the simulation setup is the same.

Boundary Conditions

For the gas component, we use closed boundaries where the surface density and azimuthal velocity fields are scaled using the closest active cell, the radial velocity field is mirrored, and the energy field is extrapolated symmetrically. For the dust component, we use open/inflow boundary conditions. Like Sturm et al. (2020a), we set the radial velocity at the boundaries to the radial drift velocity (an extrapolation based on Eqns. 23-26 of Takeuchi & Lin, 2002):

$$v_{r,\mathrm{dust}} = \frac{\eta\, v_{\mathrm{Kep}}}{\mathrm{St} + \mathrm{St}^{-1}} \propto \left(\frac{H}{r}\right)^2 v_{\mathrm{Kep}} \propto r^{2f-1/2} \tag{2.11}$$

where v_{Kep} is the Keplerian velocity and $\eta = \left(\frac{H}{r}\right)^2 \frac{d\log(P)}{d\log(r)}$. These radial velocity boundary conditions are desirable for us because they negate the effect of radial drift accumulating over time, meaning we avoid any dust pile-up at the inner boundary or depletion of dust in the outer disk that might impinge on the expression of the planet-driven spiral.

At the radial boundaries, we employ wave damping zones (de Val-Borro et al., 2006) to minimize wave reflections, where the damping zones' inner and outer edges have a Keplerian orbital frequency ratio of 2/3 (Eqns. A3 & A4 of McNally et al., 2019). For our domain, the inner and outer edges of the damping regions work out to $0.131\, r_{\mathrm{p}}$ and $2.289\, r_{\mathrm{p}}$. We apply damping to each of the density, azimuthal and radial velocity fields, with a local damping timescale of $1/[30\,\Omega_{\mathrm{Kep}}(r)]$.

2.2.2 Radiative Transfer Calculations

Prior to any post-processing, we radially truncate the disk to extend from $0.2\, r_{\mathrm{p}}$ to $2.2\, r_{\mathrm{p}}$ in order to remove the damped zones. We model our choice of physical disk parameters after the disks in the DSHARP survey, setting the stellar mass and stellar luminosity to the median of the sample, $M_\star = 0.8\,\mathrm{M}_\odot$ and $L_\star = 1.5\,\mathrm{L}_\odot$ (Table 1 of Andrews et al., 2018), and the orbital radius of the planet to be roughly coincident with the radial location where many of the DSHARP gaps and rings are found, $a_{\mathrm{p}} = 50\,\mathrm{au}$ (Fig. 7 of Huang et al., 2018a). The disk thus extends from 10 to 110 au. We place the disk at a distance of $d = 140\,\mathrm{pc}$ and assume it has zero inclination (i.e. is face-on), giving the disk diameter (220 au) an angular size of $1.57''$.

A key point we emphasize in this work is that both the dust surface density and dust temperature contribute to the emergent dust intensity, I_ν, the observed quantity in ALMA continuum images. We calculate I_ν as

$$I_\nu = B_\nu(T_{\rm dust}) \cdot (1 - e^{-\tau_\nu}), \tag{2.12}$$

where $B_\nu(T)$ is the Planck function, $T_{\rm dust}$ is the dust temperature, and τ_ν is the disk optical depth. Throughout, our observing frequency is $\nu = 345\,$GHz. The dust temperature contributes via the first factor, $B_\nu(T_{\rm dust})$, and the dust surface density via the second, $(1 - e^{-\tau_\nu})$.

In the first factor, $B_\nu(T_{\rm dust})$, we use a different dust temperature distribution for each equation of state. For the adiabatic simulations, we convert the FARGO3D output (gas) energy field into temperature in units of Kelvin, and assume thermal equilibrium between gas and dust such that $T_{\rm dust,adi} = T_{\rm gas}$. We justify this assumption in §2.B.

For the isothermal simulations (which don't solve the energy equation), we create an axisymmetric dust temperature map using Eqn. B2 of Dong et al. (2018b):

$$T_{\rm dust,iso} = 13.37 \left(\frac{r}{100\,{\rm au}}\right)^{-1/2} \tag{2.13}$$

which is the temperature profile consistent with disks heated by a central star of luminosity $L_\star = 1.5\,L_\odot$ and aspect ratio of Eqn. 2.7. At a radius of $a_{\rm p} = 50$ au, Eqn. 2.13 yields a temperature of 18.9 K, a sound speed of $0.26\,{\rm km\,s^{-1}}$, a physical scale height of 3.44 au and an aspect ratio just under 0.07 (hence our selection of $h_{\rm p} = 0.07$ in §2.2.1). A physical disk may have a vertical temperature gradient (e.g., Rosotti et al., 2020b), but (sub-)mm-sized grains are expected to settle to the disk midplane and adopt the temperature there.

In the second factor, $(1 - e^{-\tau_\nu})$, the disk optical depth is

$$\tau_\nu = \kappa_\nu \cdot \Sigma_{\rm dust}, \tag{2.14}$$

where $\Sigma_{\rm dust}$ is the dust surface density output from FARGO3D and $\kappa_{345\,{\rm GHz}} = 3.45\,{\rm cm^2\,g^{-1}}$ (Beckwith et al., 1990).

We vary the disk optical depth by initializing the hydro simulations with a fixed dust-to-gas ratio of 0.01 and different Σ_0 (Eqn. 2.10). The dust-to-gas ratio then evolves at each radii in the simulations. Throughout the paper, we use the term τ_0 to represent the optical depth at $\nu = 345\,$GHz and $r = r_{\rm p}$ at the beginning of our simulations, and we construct our simulation input parameters to give $\tau_0 = 0.1$, 0.3, 1.0, and 3.0. Of course, a particle of fixed grain size embedded in a higher density gas disk will be better coupled, and we account for this by setting up the initial dust Stokes number accordingly. For example, the dust in our $\tau_0 = 0.1$ disk has an initial Stokes

number of $\mathrm{St}(r_p) = 9\times10^{-3}$ via $\Sigma_0 = 2.89\,\mathrm{g\,cm^{-2}}$, and the optically thickest $\tau_0 = 3.0$ disk has initial $\mathrm{St}(r_p) = 3\times10^{-4}$ via $\Sigma_0 = 86.9\,\mathrm{g\,cm^{-2}}$. For a reference comparison between the $\tau_0 = 0.1$, 0.3, 1.0 and 3.0 disks, Figure 2.A.1 in §2.A provides radial profiles of Σ_{gas}, Σ_{dust}, St, T_{dust}, $\tau_{345\,\mathrm{GHz}}$ and $I_{345\,\mathrm{GHz}}$ for our adiabatic ($\beta = 10$) disk with a $1.0\,M_{\mathrm{th}}$ embedded planet.

2.2.3 Synthetic ALMA Observations

To explore ALMA's capability to detect planet-driven dust spirals, we generate synthetic Band 7 continuum observations for a range of integration times and antenna configurations with the `CASA` software package (McMullin et al., 2007a). Our choice of observing band strikes a balance between angular resolution (favouring shorter wavelengths), signal-to-noise ratio (favouring longer wavelengths), feasibility (disfavouring Bands 8-10), and popularity (favouring Bands 6 or 7).

We observe the disk with both a compact and extended 12m array configuration to simultaneously achieve a high angular resolution and a large maximum recoverable scale. We choose the configuration pairs C43-4 + C43-7, C43-5 + C43-8 and C43-6 + C43-9 following the Cycle 8 Proposer's Guides. The maximum recoverable scales of the compact configurations C43-4, C43-5 and C43-6 are $\theta_{\mathrm{MRS}} = 3.3''$, $1.9''$, and $1.2''$, respectively, so the C43-6 configuration does not quite cover emission on the angular scale of the disk, $\theta_{\mathrm{LAS}} = 1.57''$. Observing with a compact configuration in addition to an extended one requires $20-22\%$ more on-source time, but we found that doing so improves uv-sampling, reducing long baseline artifacts that exist with the high angular resolution configurations, giving the combined image overall higher quality; see Fig. 2.E.5 in §2.E for an illustration.

We set up the integration time to target a requested continuum sensitivity of 10, 15, 20, 25, 30 and $35\,\mu\mathrm{Jy\,bm^{-1}}$. As per the Sensitivity Calculator in the ALMA Cycle 8 OT, these requested sensitivities correspond to a combined on-source time (i.e., summed compact and extended configuration on-source time) of roughly 8.0 hrs, 3.5 hrs, 2.0 hrs, 1.3 hrs, 55 min, and 40 min, depending on the configuration pair. Table 2.E.1 in §2.E provides the individual and combined on-source times, as well as the total time including overheads, for each requested sensitivity and antenna configuration pair.

We generate measurement sets for the compact and extended configurations using the `simobserve` tool. The disk is assumed to have RA and Declination J2000 19h00m00 -40d00m00. We set the continuum bandwidth at 345 GHz to the full available 7.5 GHz, and adopt the default choices of a precipitable water vapour level of 0.913 mm and ambient ground temperature of 269 K. We concatenate the measurement sets from both configurations for each model and clean them

simultaneously with `tclean`, and then generate the noisy images with `simanalyze`. `CLEAN` images are created using a briggs weighting and a robust factor of 0.5. We clean to a threshold of 3× the requested sensitivity. After cleaning, the measured rms noise in all our images presented in §2.4 is ~80-95% of the requested sensitivity (with cleaning affecting those images with poorer uv-coverage more greatly).

2.3 Important Physics for the Observability of Planet-driven Dust spirals

We employ two different metrics to quantify the characteristics of planet-driven spirals: (1) "perturbation", and (2) "contrast". We calculate the perturbation in X disk quantity relative to an unperturbed disk as

$$\delta X / X_{\rm no\,planet} \equiv (X - X_{\rm no\,planet}) / X_{\rm no\,planet}\,, \tag{2.15}$$

where $X_{\rm no\,planet}$ is the state of an identical "no planet" simulation[9], at the same time snapshot. Our definition of perturbation is motivated from a theoretical perspective as it isolates the effect of the planet. Contrast is defined relative to the azimuthal average of the perturbed disk as

$$\text{contrast in } X \equiv (X - \overline{X}_\phi) / \overline{X}_\phi\,, \tag{2.16}$$

where $\overline{X}_\phi$ is the azimuthal average of the same disk, again at the same time. Our definition of contrast is motivated from an observational perspective, as an observer only has one disk to work with.

The hydrodynamic models presented in Figs. 2.2 & 2.3 of this section are our shorter (15 orbits) set, described at the end of §2.2.1, which we conducted with a $M_{\rm p} = 1.0\,{\rm M_{th}}$ planet and without a planet; Fig. 2.4 uses our radiative transfer models (1500 orbits).

2.3.1 Do dust spirals look different to gas spirals?

When a dust particle encounters the spiral wave, it experiences a temporary additional drag force due to the gas velocity perturbation and is disturbed from its near-Keplerian orbit. The degree of dust-gas coupling will determine the morphology of the resulting dust spiral. Through-

[9] Sturm et al. (2020a) also use an empty simulation as the unperturbed disk (private communication), but use notation X_0 instead of $X_{\rm no\,planet}$. Normalizing with an empty simulation instead of the initial state is an easy way to account for radial drift-induced perturbations in the dust.

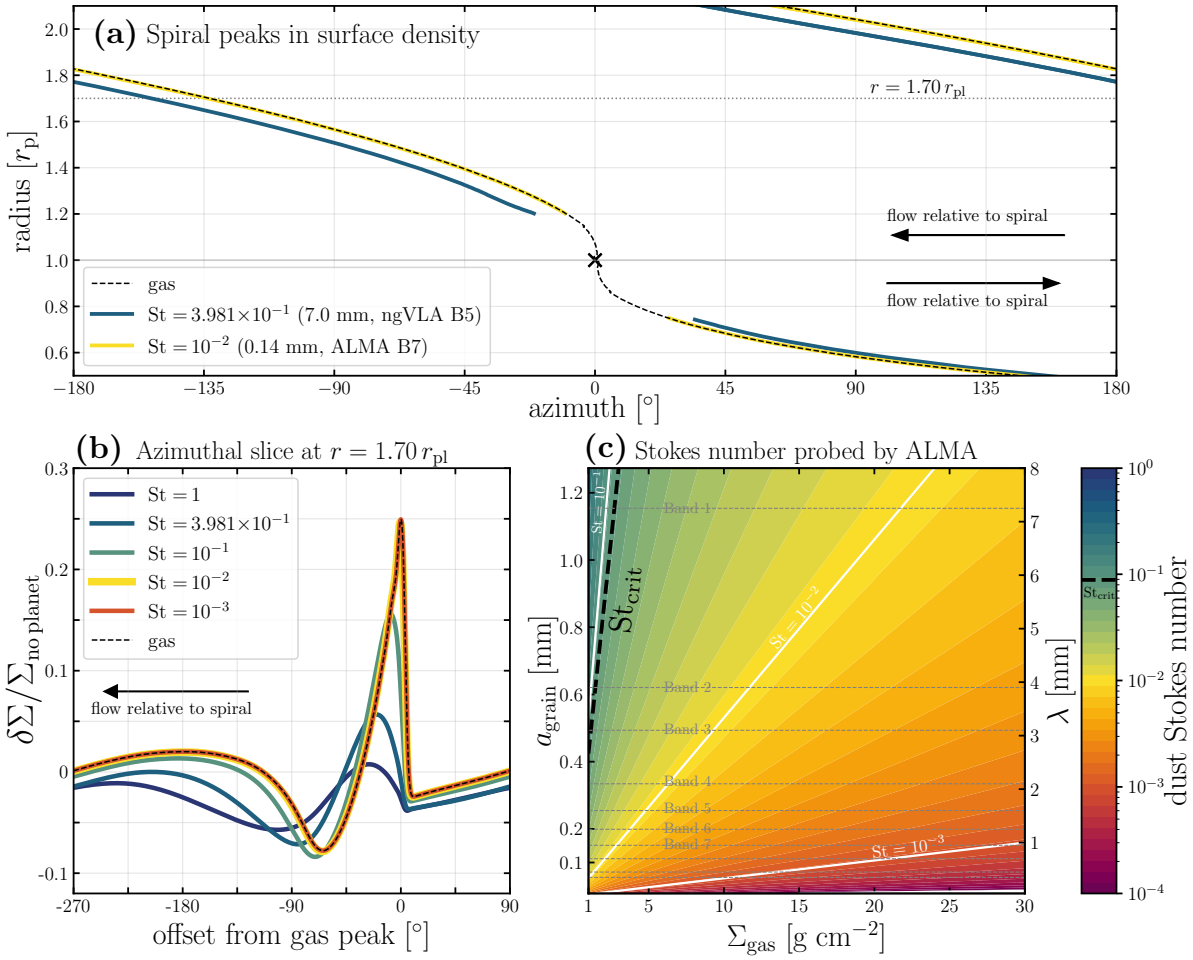

Figure 2.2: Spiral morphology in surface density, and expectations for ALMA observations. **(a)** The spine of the inner and outer primary spiral arm in the gas, one species of well-coupled dust ($\mathrm{St} = 10^{-2}$, or $a_{\rm grain} = 0.14\,\mathrm{mm}$ if $\Sigma_{\rm gas} = 3\,\mathrm{g\,cm^{-2}}$) and one of poorly coupled dust ($\mathrm{St} = 0.4$, $7.0\,\mathrm{mm}$), driven by a $1.0\,M_{\rm th}$ planet in an adiabatic ($\beta = 10$) disk. Poorly coupled dust ($\mathrm{St} > \mathrm{St_{crit}} = 0.089$, Eqn. 2.18) forms spirals whose peaks azimuthally lag behind the gas. **(b)** An azimuthal slice of the surface density perturbation far from the planet ($r = 1.7\,r_p$), for gas and 5 species of dust (two well-coupled, one marginal, two poorly-coupled). In addition to being azimuthally offset, $\mathrm{St} > \mathrm{St_{crit}}$ dust spirals have smaller amplitude. Note the yellow $\mathrm{St} = 10^{-2}$ curve has been made 2pts thicker to be visible behind the red $\mathrm{St} = 10^{-3}$ curve. **(c)** Stokes number calculated for a range of gas surface densities and ALMA dust grain sizes. For typical observing wavelengths of each ALMA band, we mark the dust grain size probed assuming (LH y-axis) $a_{\rm grain} = \lambda_{\rm obs}/2\pi$ (RH y-axis). In general, ALMA probes well-coupled dust spirals.

out this paper, we use the term "well-coupled" to describe dust that forms spirals morphologically identical their gas spiral counterparts, and "poorly-coupled" to refer to dust whose spirals are morphologically different. In this section we investigate the morphology of well-coupled and poorly-coupled dust spirals, and pinpoint the Stokes number that divides the two regimes.

Location of spiral peaks: In Figure 2.2(a), we trace the peaks of the spiral surface density perturbations (Eqn. 2.15) in the gas and two species of dust, St = 4×10^{-1} and St = 10^{-2}. In comparing them to the gas, we see that these two species represent examples of poorly-coupled and well-coupled dust, respectively. The spine of the well-coupled dust spiral overlaps with that of the gas spiral perfectly throughout the disk. On the other hand, the poorly-coupled dust spiral lags behind the gas; the azimuthal offset between the two at $r = 1.7\, r_p$ for example is 20.04 degrees.

Spiral amplitude: In Figure 2.2(b), we show an azimuthal cross section of the spiral surface density perturbation in the gas and five species of dust – two Stokes numbers representative of well-coupled dust (St = 10^{-3}, 10^{-2}), one marginal (St = 10^{-1}), and two poorly-coupled (St = 4×10^{-1}, 1). In addition to lagging behind the gas, the poorly-coupled dust spiral peaks are lower in amplitude. In contrast, the well-coupled dust spirals are indistinguishable from the gas. The marginal case suggests the de-coupling boundary occurs between St = 10^{-2} and St = 10^{-1}.

What is "well-coupled" dust in the context of planet-driven spirals? We can estimate the Stokes number that divides the well-coupled and poorly coupled regimes with a timescale argument, first described by Sturm et al. (2020a), where we compare the time it takes a dust particle to cross the gas spiral wake to the particle's intrinsic stopping time. First, we define $\Delta\phi_{\rm gas\,spiral}$ to be the azimuthal width of the gas spiral as a fraction of a full revolution, measuring it as the full width at half maximum (FWHM)[10] in the perturbed surface density (i.e. the "foot" is at $\delta\Sigma/\Sigma_{\rm no\,planet} = 0$ in the gas). Note that $\Delta\phi_{\rm gas\,spiral}$ is a function of, at a minimum, planet mass and radius. With that number, we calculate the gas spiral crossing time (Eqn. 5 of Sturm et al., 2020a):

$$t_{\rm cross} = \Delta\phi_{\rm gas\,spiral}\, \frac{t_{\rm dyn}}{(1 - \Omega_p\, t_{\rm dyn})}\,, \tag{2.17}$$

where $t_{\rm dyn} = 1/\Omega_{\rm Kep}$ is the dynamical time and Ω_p is the planet's (and therefore the gas spiral's) angular velocity. This equation assumes the dust moves at Keplerian velocity, and takes into account the additional time a particle spends in the spiral because the spiral moves in the same direction as the Keplerian flow.

Following Sturm et al. (2020a) we define the "critical" Stokes number –the boundary between what constitutes well-coupled and poorly-coupled dust– as the Stokes number for which $t_{\rm cross}$ and $t_{\rm stop}$ (Eqn. 2.9) are equal:

$$\mathrm{St}_{\rm crit} = \frac{\Delta\phi_{\rm gas\,spiral}}{(1 - \Omega_p\, t_{\rm dyn})}\,. \tag{2.18}$$

[10] In contrast to Sturm et al. (2020a), who estimate it using a Gaussian fit.

For the disk and planet parameters of Figure 2.2, we find $\Delta\phi_{\rm gas\,spiral} = 0.05$ and $\mathrm{St_{crit}} = 0.089$ at $r = 1.7r_{\rm p}$, in agreement with the results presented in the top and bottom left panels. The critical Stokes number offers an intuitive picture: Dust with Stokes number higher than $\mathrm{St_{crit}}$ takes longer to respond to the gas spiral drag forces than the amount of time those forces act on them, and so their spiral morphology is different.

What are the implications for ALMA observations? In Figure 2.2(c), we calculate the dust Stokes number for a range of gas surface densities $\Sigma_{\rm gas}$ and dust sizes $a_{\rm grain}$ (Eqn. 2.9). The horizontal lines mark the ALMA bands at which dust of a certain size is probed the best, assuming the median observing wavelength at each band $\lambda_{\rm obs} = 2\pi a_{\rm grain}$ (Eqn. 2.8). $\mathrm{St_{crit}} = 0.089$ (dashed black line) delineates the well-coupled and poorly-coupled regimes. This panel shows that, at almost all observing wavelengths and gas surface densities, ALMA probes well-coupled dust ($\mathrm{St} < \mathrm{St_{crit}}$). We therefore expect that planet-driven dust spirals observed by ALMA will be perfect tracers of their parent gas spirals at the disk midplane.

2.3.2 The Ingredients of Intensity: In what disks are dust spirals most prominent?

Both the surface density of the dust and its temperature contribute to the overall dust thermal emission that we detect with ALMA continuum observations. It is therefore relevant for the observability of planet-driven dust spirals to understand how the spirals manifest in both the dust surface density and temperature, and to disentangle each ingredient's contribution to the surface brightness of the spiral.

From top to bottom, Figure 2.3 shows the perturbations (Eqn. 2.15) in dust surface density, dust temperature, and the resultant dust intensity in the optically thin limit generated by a $1.0\,\mathrm{M_{th}}$ planet. As we are interested in ALMA observations, we focus on well-coupled dust ($\mathrm{St} \ll \mathrm{St_{crit}}$; §2.3.1). From left to right, we show these quantities in a locally isothermal disk and in disks with an adiabatic equation of state and different dimensionless cooling timescales. The dependence of these three perturbation quantities on the cooling rate is not always monotonic, and the five selected cases ($\beta = 10^{-2}$, 10^{-1}, 1, 10 and the isothermal EoS representing the limit $\beta \to 0$) represent the full range of behaviours for the thermodynamics we consider. Complementing this figure is Fig. 2.C.2 in §2.C.

Dust surface density: Consider first the surface density perturbation, shown in the top row of Figure 2.3. In the entire domain, the density spiral amplitude is strongest in the locally isothermal disk, while it drops by $\lesssim 10\%$ when β increases to 10^{-2}. At the other extreme, the density spiral amplitude in disks with $\beta \geq 10$ are $\sim 50\%$ as strong as the isothermal case near the planet

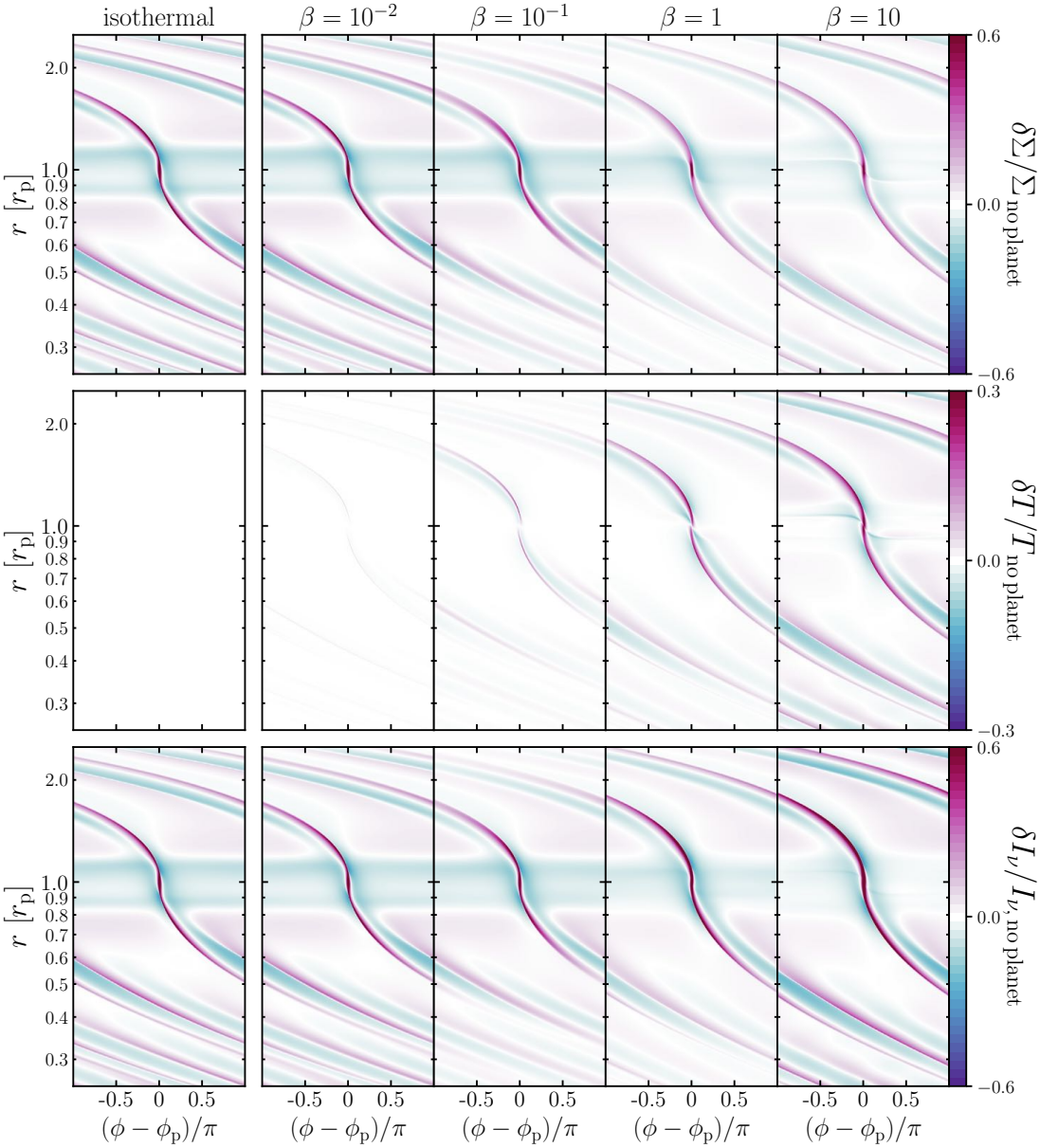

Figure 2.3: Planet-induced spiral perturbations (Eqn. 2.15) in disks with increasing cooling timescales β (**left to right**). The spiral dust surface density perturbation (**top**) is largest in isothermal disks, whereas the temperature perturbation (**middle**) is necessarily zero in isothermal disks and increases monotonically with the cooling time. As a result, the observable dust intensity perturbation (**bottom**), shown here in the optically thin limit ($I_\nu \propto \Sigma_\mathrm{dust} B_\nu(T_\mathrm{dust})$, where $\nu = 345\,\mathrm{GHz}$), is largest in adiabatic disks that cool slowly. See also Fig. 2.C.2 in §2.C. The planet mass is $M_\mathrm{p} = 1.0\,\mathrm{M_{th}}$. Note that the colourbar range in the temperature row is half the value in the other two rows.

$(0.6\,r_\mathrm{p} < r < 2.0\,r_\mathrm{p})$ but become more comparable further away. In the intermediate cases, $10^{-1} \leq \beta \leq 1$, the spiral density waves also start $\sim 50\%$ as strong as the isothermal case near

the planet, but are significantly damped as they propagate. These results agree with those presented in Miranda & Rafikov (2020b, their Fig. 1) and Zhang & Zhu (2020, their Fig. 9); efficient cooling leads to stronger compression. If we considered the well-coupled dust surface density alone, we might naively expect spirals to have higher contrasts, and thus be easier to detect given the same background disk surface brightness, in disks with short cooling timescales.

Dust temperature: In the middle row of Figure 2.3, we present the temperature perturbation. It is the strongest near the planet and decreases as the waves propagate in both directions. Here, the dependence on the cooling timescale is monotonic — the temperature spiral amplitude at all radii is an increasing function of β, as inefficient cooling results in larger temperature increase from adiabatic compression. The results are in agreement with Muley et al. (2021).

Dust intensity: The bottom row of Figure 2.3 shows the intensity perturbation in the optically thin limit, i.e., $I_{345\,\mathrm{GHz}} \propto \Sigma_{\mathrm{dust}}\, B_{345\,\mathrm{GHz}}(T_{\mathrm{dust}})$. In this way we demonstrate the effect of the temperature spiral without the added complication of disk optical depth, as a start. The surface density and temperature perturbations combine to give the intensity spiral amplitude a non-monotonic dependence on the dimensionless cooling timescale. It is largest in adiabatic disks with $\beta \geq 10$ at all disk radii. In other words, dust spirals are more prominent in slow cooling disks. The inner and outer primary spiral amplitude in the $\beta = 10$ case is uniformly $\sim 20\%$ higher than in the locally isothermal disk (Fig. 2.C.2 in §2.C).

A second crucial effect of the temperature spiral –or more fundamentally, the dimensionless cooling timescale– is to introduce a degeneracy between the intensity spiral amplitude and the planet mass. Comparing the two most different cases, the intensity perturbation amplitude at $r = 1.7\,r_{\mathrm{p}}$ is 0.13 for $\beta = 10^{-1}$ and 0.45 for $\beta = 10$. This is a factor of 3.5 different for the same $1.0\,\mathrm{M_{th}}$ planet.[11]

In Figure 2.4 we bring back the complication of disk optical depth by using the results of our radiative transfer calculations, and switch to our observationally-motivated metric to quantify the spiral, the "contrast" (Eqn. 2.16). Figure 2.4 shows the contrast traced along the inner and outer primary spiral arms in dust surface density, temperature and intensity, where intensity has now been calculated with the radiative transfer equation (Eqn. 2.12) for a range of disk optical depths. As per the first factor of Eqn. 2.12, we also plot the contrast in $B_{345\,\mathrm{GHz}}(T_{\mathrm{dust}})$. The driving planet has a mass $M_{\mathrm{p}} = 0.3\,\mathrm{M_{th}}$. We show the results for the locally isothermal disk and compare them to a disk with an adiabatic EoS and $\beta = 10$.

Comparing the spiral surface density contrast between the two disks first, we see again that the isothermal case exhibits the most prominent density spirals. The difference is most signifi-

[11] Fixing instead the cooling timescale to $\beta = 10$ and varying the planet mass by a factor of 10 (from $0.3\,\mathrm{M_{th}}$ to $3.0\,\mathrm{M_{th}}$), the amplitude difference is a factor of 2.4.

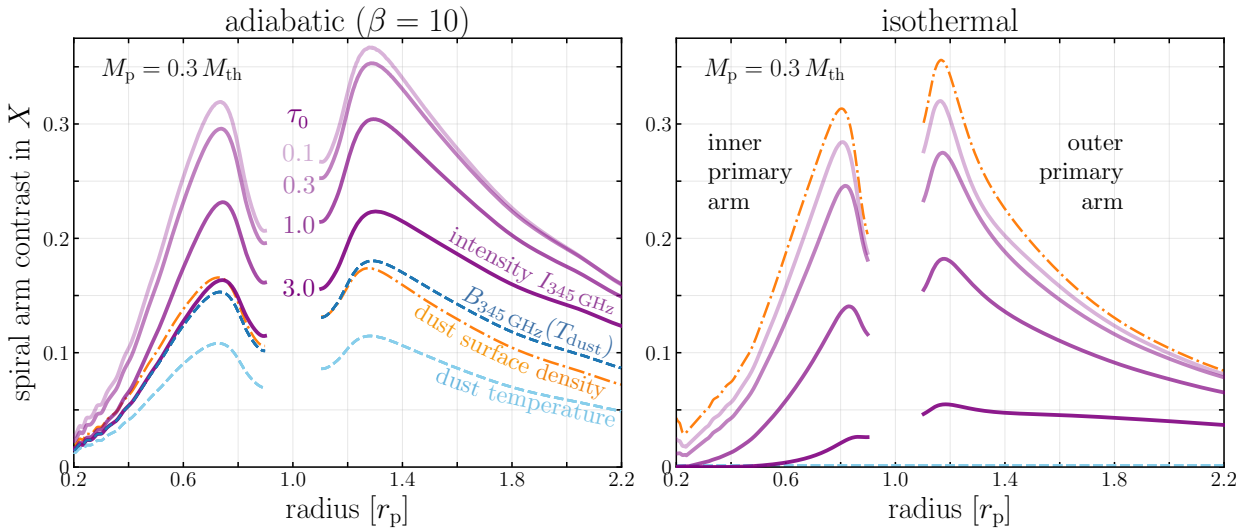

Figure 2.4: Spiral arm contrast (Eqn. 2.16) in dust surface density (**orange dot-dashed**), temperature (**light blue dashed**), $B_{345\,GHz}(T_{dust})$ (**dark blue dashed**) and intensity (**shades of solid purple**) traced along the inner and outer primary arms induced by a $0.3\,M_{th}$ planet. The shades of purple distinguish the dust intensity at different disk optical depths, from light (optically thin) to dark (optically thick); τ_0 is the initial optical depth at r_p. The dust surface density spiral contrast in the isothermal case (**right**) is higher than that in the adiabatic one (**left**), but the former represents the upper bound of an isothermal spiral's contrast in intensity. Due to the presence of a temperature spiral in the adiabatic disks, the adiabatic spiral intensity contrast can exceed its dust surface density contrast and be brighter than in isothermal disks – particularly at high τ.

cant (roughly a factor of 2) close to the planet (within $0.4\,r_p$ on either side). However, the spiral density contrast in the isothermal case constitutes an upper bound for how *bright* spirals can be in that disk. For any non-zero optical depth, the isothermal spiral intensity contrast is lower than its dust density contrast.

In adiabatic disks on the other hand, the spiral intensity contrast can be larger than the density contrast, depending on the significance of the temperature spiral. In the $\beta = 10$ case, the spiral temperature contrast is $\sim 70\%$ as strong as the density contrast, and is enhanced by the Planck function to give a contrast in $B_{345\,GHz}(T_{dust})$ that is $\sim 110\%$ as strong. This results in a spiral intensity contrast that not only exceeds its own density contrast, but that is also larger than the intensity contrast in the locally isothermal disk.

This difference between spirals in isothermal and adiabatic disks becomes more pronounced when the disk is optically thick. For an initial optical depth at the planet's orbital radius of $\tau_0 = 3.0$, the spiral intensity contrast in the adiabatic $\beta = 10$ disk is 3-4 times larger than in the isothermal disk. The temperature spiral in adiabatic disks represents a "floor" for the spiral intensity; as τ increases it takes on a greater fraction of the responsibility for making adiabatic

spirals brighter than isothermal ones, while isothermal spiral contrast disappears when $\tau \to \infty$.

Finally, we note that the outer spiral arm can have $10-40\%$ larger contrast in intensity than the inner arm at its peak at various optical depths. This, combined with that the outer spiral fades more slowly as it propagates away from the planet, makes the outer spiral easier to identify in observations.

2.4 Synthetic ALMA Observations: An Observer's Guide

In this section, we present synthetic ALMA B7 continuum observations and our method of highlighting the planet-driven spiral signal. We report trends in the amount of ALMA time needed under different disk and observing conditions (§2.4.1); we describe the impact of different ALMA antenna configurations (§2.4.2); we feature a successful recovery of the spiral driven by a low mass planet (§2.4.3); and we show the impact that gaps and rings could have on our ability to recognize co-located spiral arms (§2.4.4).

In Figure 2.5 we show a gallery of 16 synthetic ALMA continuum images, a representative selection from our full set[12], obtained with the C43-5 + C43-8 configuration pair (beam size 31×35 mas). This gallery demonstrates the outcomes under a variety of disk and observing conditions: two integration times (8 hours vs. 40 mins on-source), two equations of state (adiabatic with a cooling timescale $\beta = 10$ vs. isothermal), two disk optical depths (marginally optically thin $\tau_0 = 0.3$ vs. optically thick $\tau_0 = 3.0$) and two planet masses ($M_{\rm p} = 1.0\,{\rm M_{th}}$ or $3.0\,{\rm M_{th}}$). In panels (e), (f), (g), (h) and (p), the outer primary spiral arm is very clearly visible in the continuum image. In panels (f) and (h), the inner primary (and panel (h), the inner secondary) arm can also be seen. We have labelled the outer primary ("OP"), inner primary ("IP") and inner secondary ("IS") arms in panel (h).

In order to quantify the robustness of these detections, and in order to amplify the spiral signal in less conspicuous cases, we make residual maps for all our synthetic observations – in the image plane. We first transform the ALMA image in on-sky coordinates into polar (r,ϕ) coordinates[13], then average the observed intensity over the full azimuth to obtain an axisymmetric disk, $\overline{I_{{\rm obs}\phi}}$. We subtract that map from the observed image and normalize the difference by the observation's rms noise, such that the reported quantity in residual maps is ${\rm S/N} = (I_{\rm obs} - \overline{I_{{\rm obs}\phi}})/({\rm rms\,noise})$. Figure 2.6 presents such residual maps for the observations in

[12]The results from our full set (3 planet masses, ×4 disk optical thicknesses, ×2 equations of state, ×3 antenna configuration pairs, ×6 integration times = 432 model images and their residual maps) plus an additional set of inclined disk models are available at https://doi.org/10.6084/m9.figshare.19148912.

[13]We use the `polarTransform` python module: https://polartransform.readthedocs.io/en/latest/

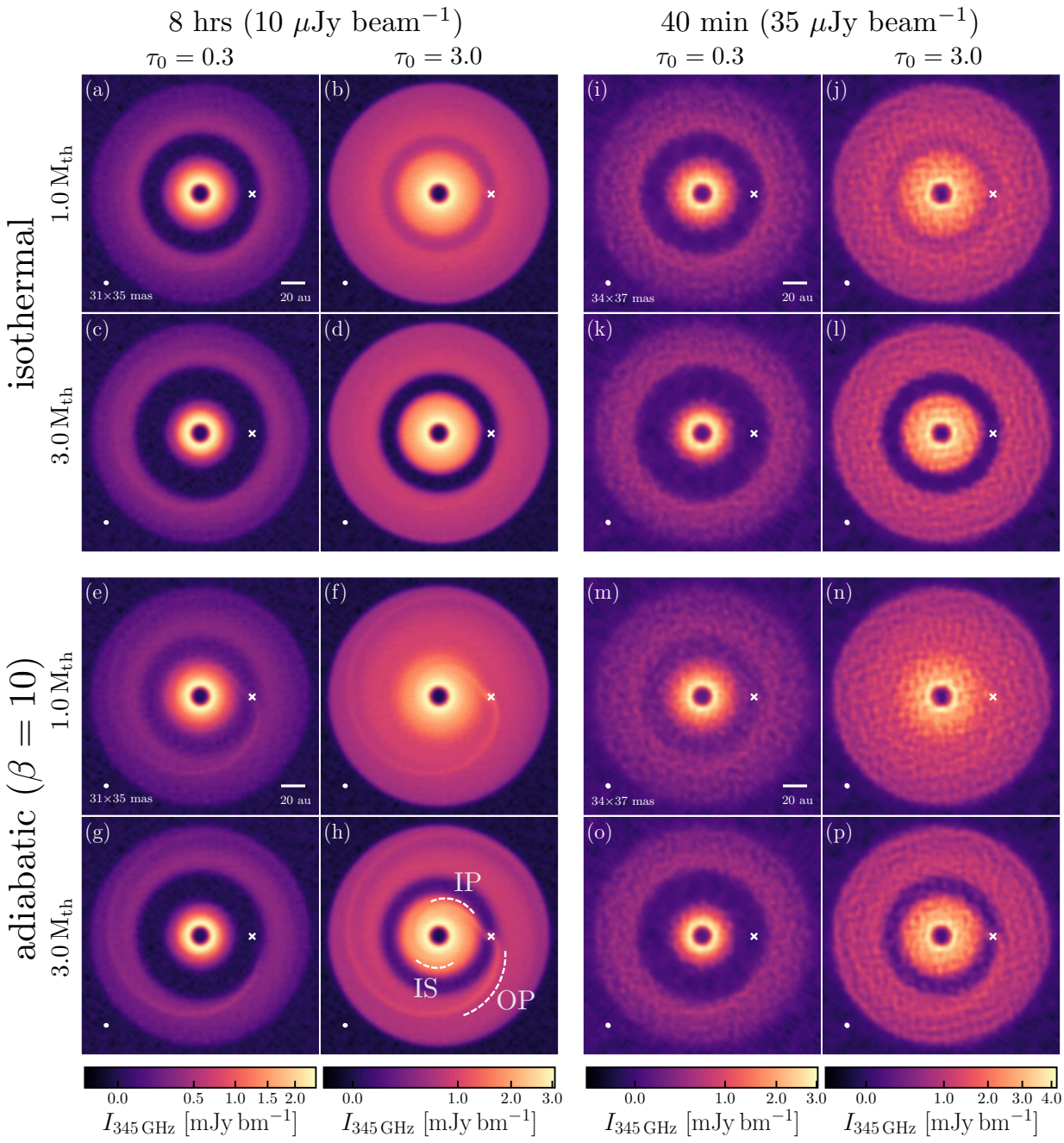

Figure 2.5: A selection of synthetic ALMA B7 continuum images with the C43-5 + C43-8 configuration pair, demonstrating trends with equation of state (**top** vs. **bottom**), combined on-source time (**left** vs. **right**), planet mass (**inner top** vs. **inner bottom**), and disk optical depth (**inner left** vs. **inner right**). The requested sensitivity (number in brackets, e.g. $10\,\mu\mathrm{Jy\,bm^{-1}}$) is what was used to determine the combined on-source time (e.g. 8 hrs). The synthesized beam is shown in the bottom left corner of each image, and each colourbar applies to the whole column. Images are shown with a $\frac{1}{2}$-powerlaw stretch. The full set of images is available at https://doi.org/10.6084/m9.figshare.19148912.

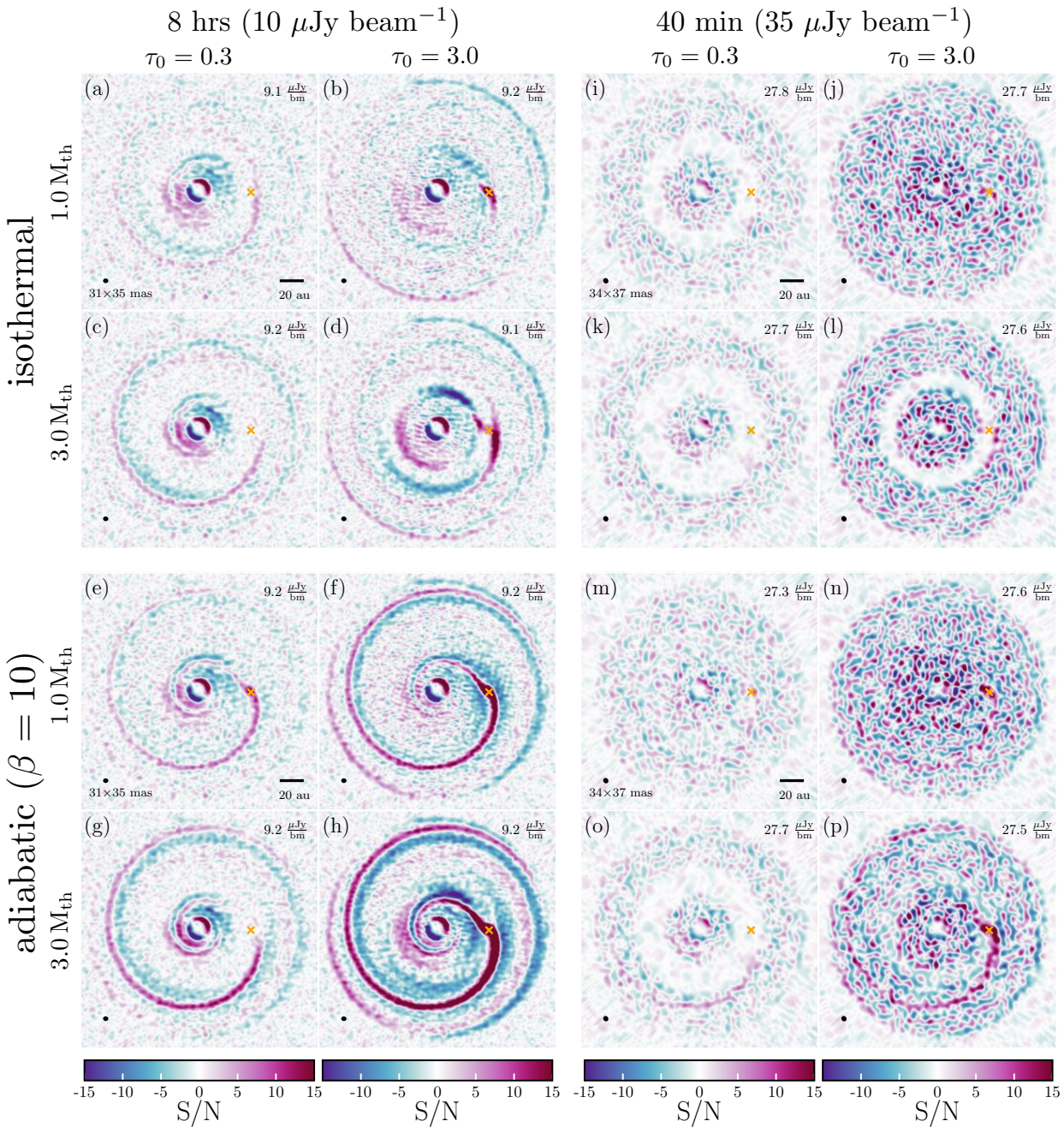

Figure 2.6: Residual maps of the observations in Figure 2.5. The signal to noise ratio is calculated as $S/N = (I_{obs} - \overline{I_{obs\phi}})/(\text{rms noise})$, where $\overline{I_{obs\phi}}$ is an axisymmetric disk obtained by azimuthally averaging in the image plane. The measured rms noise in each observation after cleaning is written in the top right corner of each panel, and in all cases is $\sim 10-20\%$ less than the requested sensitivity.

Figure 2.5.

The strongest dust spiral recovery in all our permutations of disk conditions is the one in

panel (h) of Figures 2.5 & 2.6: a $3.0\,M_{th}$ planet in an adiabatic ($\beta = 10$), optically thick ($\tau_0 = 3.0$) disk. Change the disk's equation of state to locally isothermal [panel (d)], and the spiral hardly appears in the residuals at all. Decreasing the planet mass to $1.0\,M_{th}$ [panel (f)] decreases the spiral signal in S/N, but it is still strong. Decrease the disk optical depth by a factor of 10 [panel (g)] and some parts of the inner primary arm are lost, but three spiral arms (outer primary, inner primary, inner secondary) are still visible in the residuals. The outer spiral driven by the planet in panel (h) is so significant that it is identifiable in the residuals of a 40 min observation [panel (p)].

From Figure 2.5 we conclude that the signal from planet-driven dust spirals in isothermal disks is very weak in comparison to those in adiabatic disks that cool slowly. We also see that even though spiral intensity contrasts are intrinsically larger in optically thin disks (Fig. 2.4), they are actually more difficult to observe due to the disk being dimmer overall.

Before moving on to permutations of observing conditions, a few remarks on residual maps. Firstly, we find that they are an excellent tool for probing spirals, though this comes with the caveat that they are easy to make for our face-on model disks and may not be as straightforward to make for real disk observations. Secondly, we emphasize the importance of plotting both the positive *and negative* residuals when searching for planet-driven spirals. Detecting both a spiral's peak and its associated trough can lend weight to the detection of the structure, as well as to the conclusion that it is companion-driven, because they are predicted together by density wave theory (e.g., Bae & Zhu, 2018a). We also tried making residual maps in the visibility plane using `frankenstein` (Jennings et al., 2020), which has been shown to produce accurate fits to real visibility data (e.g., Jennings et al., 2021), but with our models we found that the imaged `frank` visibility residuals showed the spiral less clearly (see Fig. 2.E.4 in §2.E).

2.4.1 How much ALMA time do you need?

It is *a priori* possible that observing planet-driven spirals requires very deep observations. To test this possibility, we created ALMA observations achieving requested sensitivities of 10, 15, 20, 25, 30, 35 μJy bm^{-1} with 0.7, 0.9, 1.3, 2.0, 3.5 and 8.0 hours of combined on-source time (totaling roughly 2, 2.5, 3.8, 5.0, 9.0 and 20 hours with overheads) and judged whether the spiral was detected in each case. For context, the DSHARP program had a median integration time of ~ 1.4 hours (Andrews et al., 2018), and the longest integration done on a single disk to date (achieving a sensitivity and beam size comparable to our models, $25.7\,\mu$Jy bm^{-1} and $\theta_{AR} = 24.6$ mas in B7) is 5.59 hours of on-source time toward HL Tau (2019.1.01051.S, currently in progress). Our maximum on-source time thus pushes the envelope by ~ 2.5 additional on-

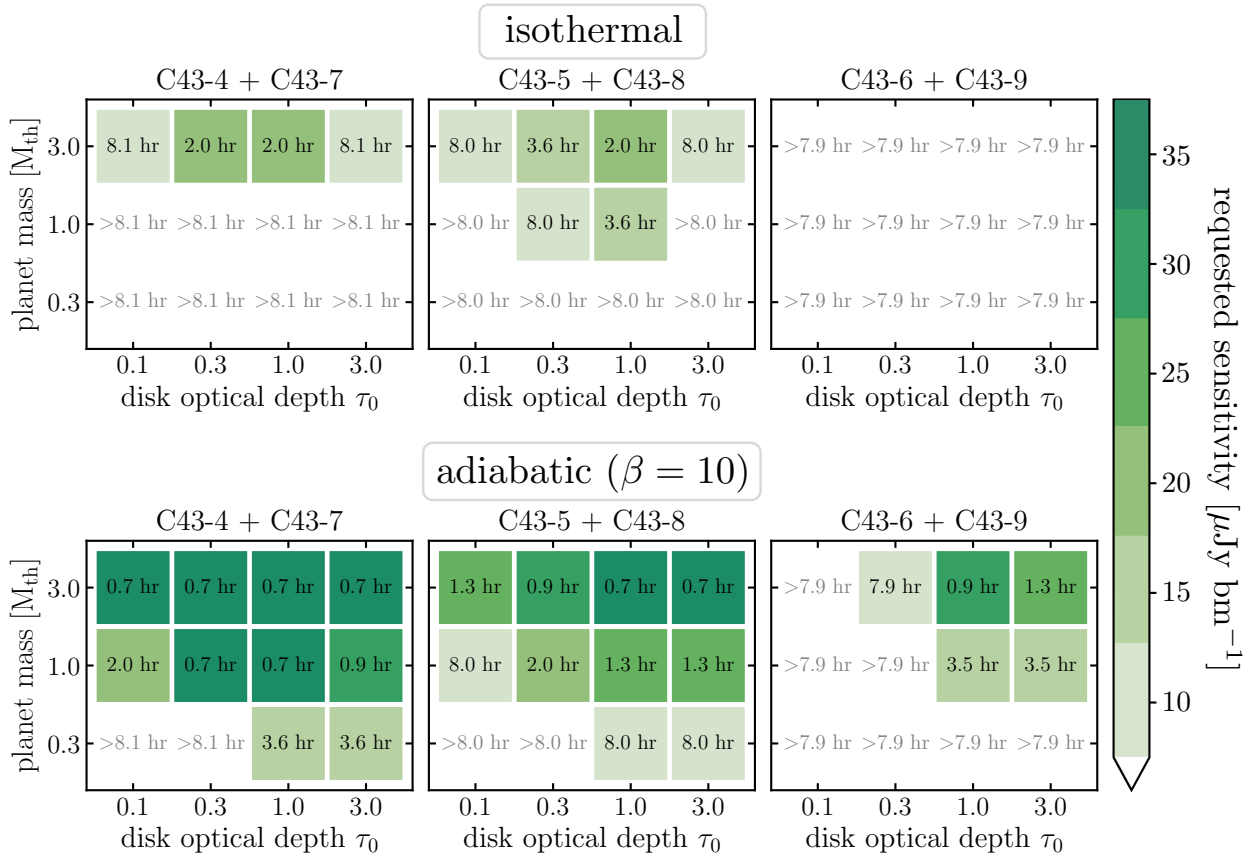

Figure 2.7: Amount of on-source time required to recover the planet's outer spiral arm in residuals of our B7 ALMA continuum images under the disk and observing conditions we explore in this work, coloured by the corresponding requested sensitivity. White indicates cases where we were not able to recover the spiral.

source hours.

To decide on a criterion for successful spiral recovery, we considered: *How does one recognize a spiral?* By definition, a spiral is a structure that extends some range in azimuth $\Delta\phi$ for each increment in radius Δr. The more azimuth $\Delta\phi$ we notice the structure spanning, the more confident we are that it is a spiral and not a segment of a circle, or an azimuthal asymmetry. Motivated by that concept, we set the criterion for a successful spiral recovery to be that we can trace the outer spiral arm in our residual maps with S/N = 5 contours over at least 90 degrees continuously in azimuth (not necessarily starting from the known planet location). We chose to focus on the outer primary spiral because it has a larger intrinsic contrast (Fig. 2.4) and was more often apparent in our residual maps (Fig. 2.6) than the inner primary arm. Structures at larger radii also naturally have larger angular extent.

Figure 2.7 is a visual table depicting the amount of on-source time required to recover the

outer spiral arm under our 72 permutations of disk and observing conditions (×2 EoS ×3 M_p ×4 τ_0 ×3 configuration pairs). We created this figure by identifying, for each permutation, the observation with the least on-source time that still recovered the spiral. That minimum on-source time is coloured by the corresponding ALMA OT requested sensitivity. White space (with grey text, e.g. "> 8.1 hr") indicates that we were not able to recover the spiral under those disk and observing conditions with our maximum tried on-source time.

Figure 2.7 shows that, if they are present, planet-driven dust spirals are easier to observe (i.e., require less integration time to detect) in adiabatic disks that cool slowly ($\beta \gtrsim 10$), that are marginally but not too optically thick ($\tau_0 \gtrsim 1.0$), and that host massive planets ($M_p \gtrsim 1.0\,M_{th}$). In such disks, spirals can be detected with integration times on the order of hours.

2.4.2 What angular resolution do you need?

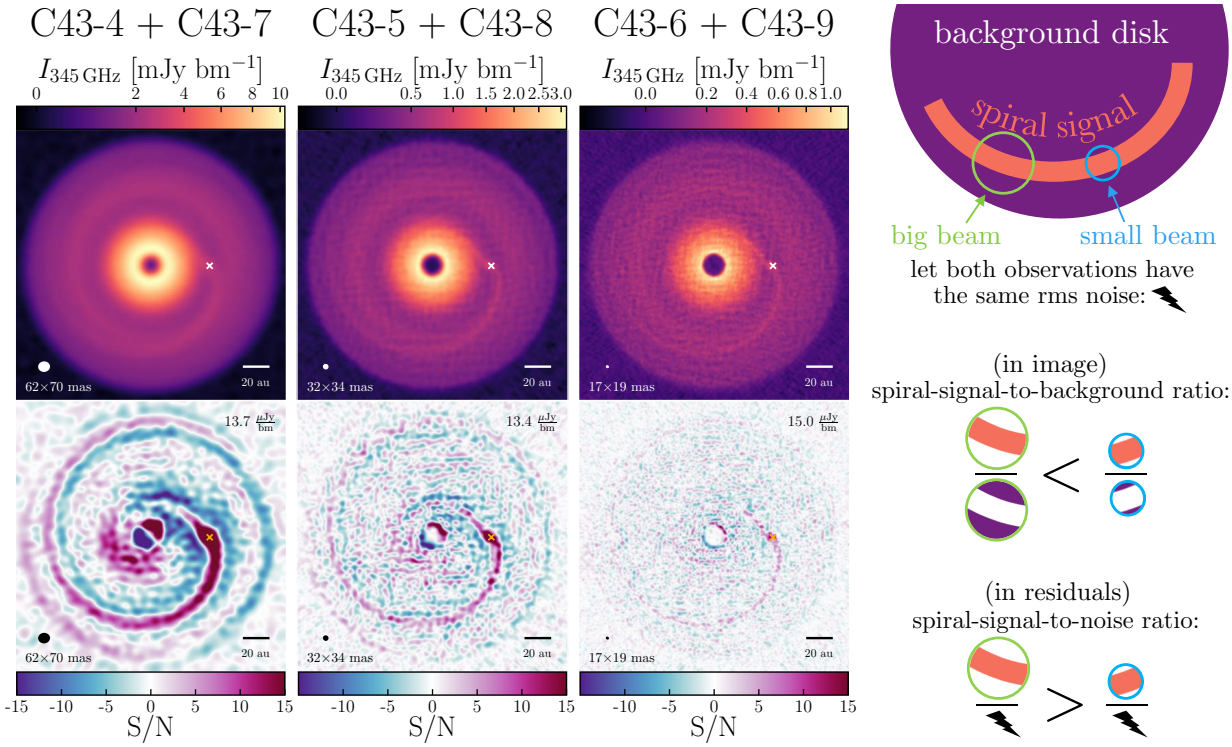

Figure 2.8: Synthetic ALMA B7 continuum images (**top**) and residuals (**bottom**) observed with different configuration pairs, shown from left to right in order of low to high angular resolution, for a $1\,M_{th}$ planet embedded in an adiabatic ($\beta = 10$), marginally optically thick ($\tau_0 = 1.0$) disk. In all observations, the measured rms noise (top right corner of residual panels) is very similar. The requested sensitivity is $15\,\mu$Jybm^{-1}, corresponding to a combined on-source time of 3.5 hrs. The schematic (**right**) shows that a lower angular resolution observation has a lower spiral-signal-to-background ratio (the spiral is "washed out") but actually has higher spiral-signal-to-noise ratio (detects the spiral with the highest S/N).

Planet-driven spiral arms are intrinsically fine structures with widths comparable to scale height (e.g. Fig. 2.3). As such, it is natural to think that high angular resolution observations –observations that *resolve* the spiral– are necessary in order to detect them. We find that the situation is more nuanced, and that high resolution doesn't necessarily lead to best detectability.

In Figure 2.8, we show ALMA continuum observations and residual maps obtained with three different antenna configuration pairs: C43-4 + C43-7 ($\theta_{\rm AR} = 0.061''$), C43-5 + C43-8 ($\theta_{\rm AR} = 0.028''$), and C43-6 + C43-9 ($\theta_{\rm AR} = 0.017''$), translating to 8.5 au, 3.9 au and 1.7 au at $d = 140$ pc, respectively. We achieve a measured sensitivity of ~13-15 Jy bm^{-1} with ~3.5 hrs of on-source time in all cases. The disk is adiabatic ($\beta = 10$), marginally optically thick ($\tau_0 = 1.0$) and contains a 1.0 $M_{\rm th}$ planet. If we approximate the spatial width of the spiral as $H(r_{\rm p}) = 3.5$ au, we see that the C43-7 configuration does not resolve the spiral, C43-8 is marginal, and C43-9 resolves the spiral with ~ 2 beams.

In the continuum images (top panels of Fig. 2.8), we find the intuitive result: the spiral signal is "washed out" in the lower angular resolution observation (left panel). In the higher angular resolution image (right panel), the outer spiral is easily seen directly in the image, and even the inner spiral arm is visible. The explanation is simply that what is captured by a smaller beam can be comprised of a greater proportion of spiral signal than background disk signal, in comparison to the proportion captured by a larger beam. In other words, when the spiral is not fully resolved, a higher angular resolution observation has a higher spiral-signal-to-background ratio.

The nuance is introduced when one considers the *robustness* of the spiral detection, i.e., the spiral-signal-to-*noise* ratio. In the residual maps (bottom panels of Fig. 2.8), we find that the lower angular resolution observation with C43-4 + C43-7 detects the spiral with the highest S/N: we can trace S/N = 5 contours over ~ 270 degrees, and S/N = 10 contours over ~ 90 degrees. On the other hand, the detection with the higher angular resolution observation (C43-6 + C43-9) is less robust; it did satisfy our recovery criterion (Fig. 2.7), but only just.

The explanation for this rests on two factors: (1) the observed intensity is in units of Jy bm^{-1}, not Jy arcsec^{-2}; and (2) the observations we are comparing have very similar levels of rms noise. The spiral signal in Jy bm^{-1} is larger for a larger beam (due to the beam's larger "area"). Therefore, if noise is independent of beam size, the low angular resolution detection has a higher spiral-signal-to-noise ratio. This holds at all sensitivities that we explored. Of course, there is a minimum angular resolution required for spiral detection; one would need to resolve the distance between the spirals (think: Rayleigh criterion), and ideally any background structures on scales larger than the spiral.

The utility of archival or future continuum observations of real disks done at high angular

resolution could be enhanced by uv-tapering to produce larger beam sizes, possibly improving the S/N and helping to identify the spiral signal in S/N space.

2.4.3 Detecting spirals from low mass planets?

Detecting a low mass planet embedded in a protoplanetary disk is an exciting prospect because if we believe planets grow in mass over some non-zero formation timescale, then "low mass" translates to "early stage", and probing lower mass planets probes closer to their birth. The challenge is linearly proportional to the reward, however, because the amplitude of planet-driven spirals (in the sub-thermal mass regime) is proportional to the planet mass (Dong et al., 2011b; Bae & Zhu, 2018a; Miranda & Rafikov, 2019a). We observe many dust gaps and rings, which we believe could be the birth-sites of planets, but as yet few co-located spirals. One possible explanation for the dearth of observed planet-driven spirals despite the abundance of observed gaps and rings could simply be that the spiral amplitude is too insignificant to be detected with ALMA. What is the lowest planet mass that drives a detectable dust spiral?

In Figure 2.9, we show a successful recovery of the outer spiral driven by our lowest mass planet, $0.3\,M_{th}$ ($0.1\,M_{Jup}$ or $1.6\,M_{Nep}$, $q = 1.03 \times 10^{-4}$). As shown in Figure 2.7, if the disk is adiabatic and cools slowly ($\beta = 10$), we can recover the outer spiral driven by this $0.3\,M_{th}$ planet in both the $\tau_0 = 1.0$ and 3.0 disks after 3.6 hours of on-source time with the C43-4 + C43-7 configuration pair, and after 8.0 hours of on-source time with the C43-5 + C43-8 pair. Figure 2.9 shows the former case with $\tau_0 = 1.0$. The contrast (as we've defined contrast, Eqn. 2.16) of the outer spiral driven by the $0.3\,M_{th}$ planet in the adiabatic, $\tau_0 = 1.0$ disk ranges from 0.15 to 0.3 (see left panel of Fig. 2.4).

The spiral is not clearly visible directly in the synthetic ALMA continuum image, but is recovered in the residuals at S/N ≥ 5 over ~ 160 degrees of the disk, underscoring the utility of residual maps. We caveat this successful recovery by noting that, although this planet had been living in our hydro simulations for 1500 orbits before we took its picture with ALMA, it created no observable gaps and rings, due to the modest viscosity adopted ($\alpha = 10^{-3}$). As we discuss in the following section, the smoothness of the background disk aids the recovery.

2.4.4 Can spirals be hiding in gaps and rings?

In this section, we explore another possible explanation for the dearth of observed planet-driven spirals despite the abundance of observed gaps and rings: Could the presence of the gaps and rings themselves be affecting the observability of the spirals? As discussed in §2.4.1, an observer's ability to recognize a spiral as a spiral requires seeing it unfurl over a sufficiently

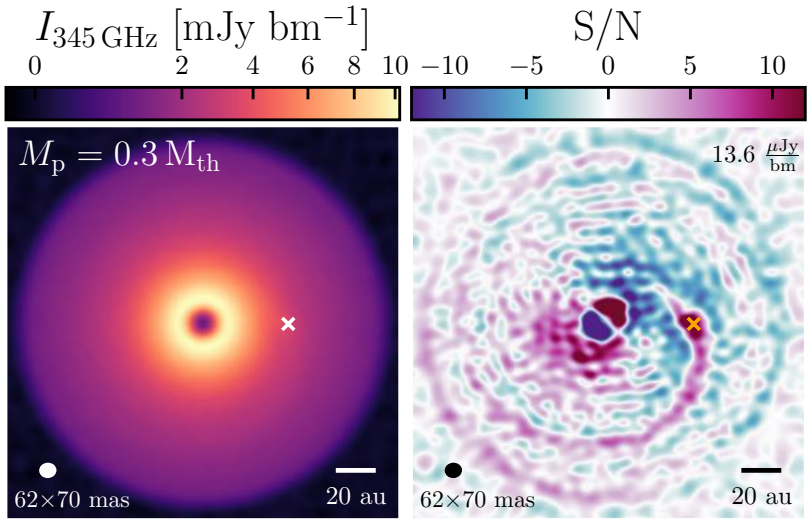

Figure 2.9: Spiral arm recovery for a low mass planet ($M_\mathrm{p} = 0.3\,\mathrm{M_{th}} = 1.6\,\mathrm{M_{Nep}}$) in a marginally optically thick disk ($\tau_0 = 1.0$) with an adiabatic equation of state ($\beta = 10$), obtained with the combined C43-4 + C43-7 antenna configuration and a combined on-source time of 3.6 hours. The measured rms noise is $13.6\,\mu\mathrm{Jy\,bm^{-1}}$.

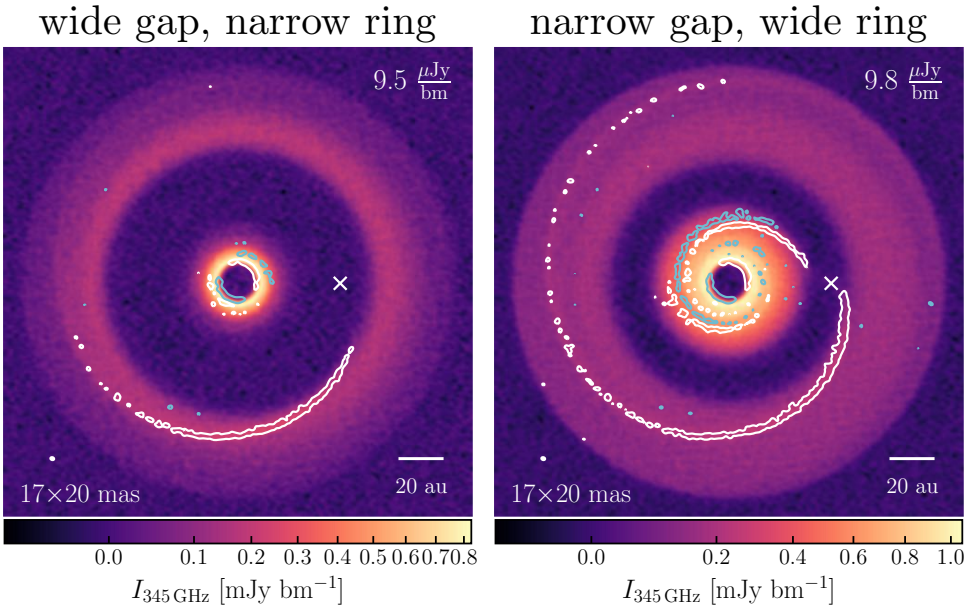

Figure 2.10: Synthetic ALMA B7 continuum observations exploring the effect of dust gaps and rings on the spiral observability. Both disks are adiabatic ($\beta = 10$) and contain a $3.0\,\mathrm{M_{th}} \approx 1.0\,\mathrm{M_{Jup}}$ planet; both observations were obtained with the C43-6 + C43-9 configuration pair and 8.0 hours of on-source time. The overlaid white and blue contours are S/N = +5 and S/N = −5 contours from the residual maps, respectively. The rms noise in each observation is written in the top right corner of the images and the beam size is marked at the lower left corner. Wide gaps and narrow outer rings reduce the amount of disk area over which the spiral can be traced.

large range of azimuth. To span more azimuth $\Delta\phi$, the spiral requires a larger radial breadth Δr of smooth background disk – and this can be affected by gaps and rings.

Figure 2.10 compares the observability of spirals in a disk with a wide planet-induced gap and narrow outer ring (left panel), to that of a spiral in a disk with a narrower gap and wider outer ring (right panel). To compare the effect of the dust distribution alone, we have re-scaled the underlying intensity maps such that the outer ring in the two disks are equally bright. The left is our optically thinnest ($\tau_0 = 0.1$) disk model and the right is our marginally optically thick ($\tau_0 = 1.0$) disk model, meaning their gas surface densities are different by a factor of 10; as a result the Stokes number of the $a_{\rm grain} = 0.14\,$mm dust within them is also different by a factor of 10, giving the two disks their different dust distributions. Both disks have an adiabatic EoS ($\beta = 10$) and embedded planet with mass $M_{\rm p} = 3.0\,{\rm M_{th}}$. We show observations made with the C43-6 + C43-9 configuration pair and a combined on-source time of 8.0 hours (achieving measured rms noise $\sim 9.5\,\mu{\rm Jy\,bm^{-1}}$) in order to investigate what might be considered a highly desirable observing scenario: high angular resolution and high sensitivity. Atop the observations we overlay S/N = $\pm$5 contours from the residual maps.

Comparing the two panels in Figure 2.10, we see that the presence of the wide gap and narrow ring renders a smaller fraction of the spiral visible in the contours. In the left panel, the outer spiral starts farther away from the planet and extends only $\sim$ 150 degrees in azimuth due to the small available radial area. In the right panel, the spiral contour starts closer to the planet and extends a full 270 degrees out to $\sim 2.2\,r_{\rm p}$. Similarly, in the inner disk, there is very little recognizable evidence of a spiral in the left panel, whereas in the right panel we can trace the inner primary arm, the inner secondary arm, and the trough between them.

Like Miranda & Rafikov (2019b), we find that a given planet mass carves shallower gaps in disks with an adiabatic equation of state than in a locally isothermal disk (and this translates to the well-coupled dust distribution, e.g. compare panels (a) vs. (e), (b) vs. (f), and (d) vs. (h) in Fig. 2.5). This is another way that the disk equation of state can affect the observability of spiral arms, in addition to regulating their contrast.

2.5 Discussion

Inclined disks. While most of our efforts were focused on face-on disks, we briefly experimented with inclined disks as well. Figure 2.D.3 in Appendix §2.D shows continuum images and deprojected residual maps for a demonstrative disk, inclined by 30°, 50° and 70°, along with its original face-on model for comparison. We find that the spiral visibility in the deprojected residual maps is not significantly affected if the disk inclination is low ($\leq 50°$), but becomes very

unclear when the inclination is high ($\geq 70°$). For a given target disk on the sky, the threshold inclination at which a spiral could no longer be as easily recovered in a deprojected residual map would depend on whether the beam resolves the structure along the disk's minor axis.

Multi-wavelength observations. Long-wavelength observations of dust spirals, for example with the ngVLA, may allow us to probe larger, poorly-coupled ($\mathrm{St} > \mathrm{St}_{\mathrm{crit}}$) dust grains. In Figure 2.11, we calculate the dust Stokes number of grain sizes relevant to the ngVLA ($a_{\mathrm{grain}} \sim 1-20\,\mathrm{mm}$) and overlay our estimate of the critical Stokes number, $\mathrm{St}_{\mathrm{crit}}$ (Eqn. 2.18), for a $1.0\,\mathrm{M}_{\mathrm{th}}$ planet at a disk radius $r = 1.7\,r_{\mathrm{p}}$, as found in §2.3.1. The ALMA equivalent of this figure is Figure 2.2(c). Comparing the spiral morphology in continuum observations of well-coupled vs. poorly-coupled dust opens new possibilities for future science.

Consider, for example, two observations of the same planet-driven dust spiral – one obtained with ALMA Band 7 ($a_{\mathrm{grain}} \approx 0.14\,\mathrm{mm}$) and the second with ngVLA Band 5 ($a_{\mathrm{grain}} \approx 7.0\,\mathrm{mm}$). Assuming a local gas surface density of $\sim 3.0\,\mathrm{g\,cm^{-2}}$, these two observations would probe $\mathrm{St} = 10^{-2}$ (well-coupled) and $\mathrm{St} = 0.4$ (poorly-coupled) dust, respectively. These two species are shown in Figure 2.2(a). At a distance of $0.7r_{\mathrm{p}}$ outside the planet, our hydrodynamic simulations predict an azimuthal offset between their spiral peaks in surface density of 20 degrees. This is a significant offset that could feasibly be measured in observations.

With a measurement of the azimuthal offset at a given disk radius, and with knowledge of its dependence on the Stokes number from fits to hydro simulations, one could estimate the underlying disk gas surface density, and subsequently measure the disk mass by repeating the exercise at different radii. This would be a direct evaluation of Σ_{gas} and M_{disk}, independent from other methods, and free from the usual uncertainties that stem from making assumptions about the dust-to-gas ratio or dust opacity. We note however that to do this in practice requires taking into account temperature effects, which we discuss in more detail in §2.B.

Equation of state. One of our main findings is that the observability of dust spirals depends heavily on how much the temperature spiral contributes to the overall spiral intensity, which in turn depends on the cooling timescale. It would therefore be helpful if we had an idea of how quickly we expect disks to cool. As discussed in §2.2.1, typical values of $t_{\mathrm{cool}} = \beta\,\Omega^{-1}(r)$ span a couple of orders of magnitude above and below unity at different radii within a single disk, and it is also likely that β varies between disks (due to different dust properties, for example). More work is needed to constrain the cooling rate of individual target objects.

In addition to affecting the spiral detectability, the cooling timescale also muddles our ability to deduce the mass of the driving object in an observation, because the spiral intensity contrast is degenerate in M_{p} and β (e.g. Fig. 2.3, 2.4 & 2.C.2). A good knowledge on the cooling timescale in specific disks may also help distinguish the two spiral arm excitation mechanisms

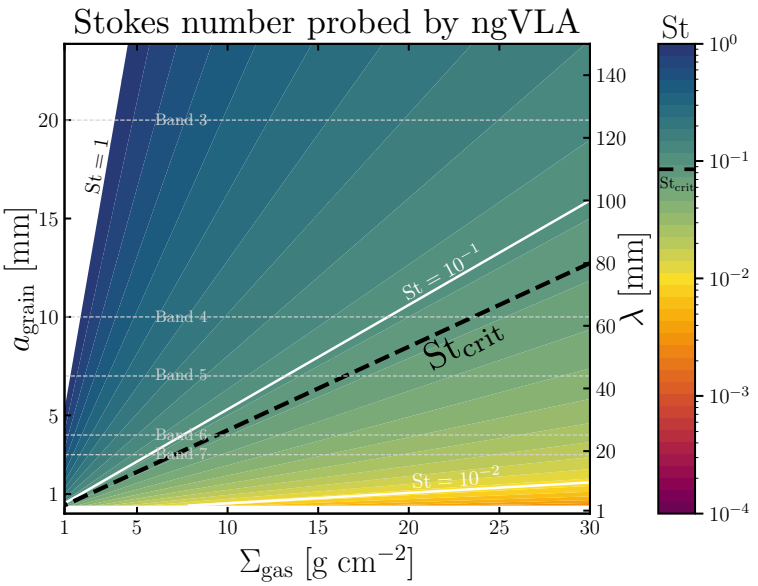

Figure 2.11: Dust Stokes number calculated for a range of gas surface densities and ngVLA dust grain sizes. For typical observing wavelengths of each ngVLA band, we mark the grain size probed assuming (LH y-axis) $a_{\mathrm{grain}} = \lambda_{\mathrm{obs}}/2\pi$ (RH y-axis). Long-wavelength observations with the ngVLA provide access to the $\mathrm{St} > \mathrm{St_{crit}}$ regime.

– we find planet-driven spirals to be more prominent in continuum observations at *longer* cooling timescales ($\beta \geq 10$), whereas GI-driven spirals have been found to express stronger velocity channel kinks at *shorter* cooling timescales ($\beta \leq 10$; Longarini et al., 2021b).

The planet-driven temperature spiral could also have consequences on the radial locations of icelines – again, depending on β. The icelines of common molecules have been found not to correlate with observed locations of gaps (van der Marel et al., 2019). Using radiative cooling, Ziampras et al. (2020) found that shock heating by the planet can raise the disk temperature high enough to displace the water iceline to larger radii. We find that a cooling rate of $\beta = 10^{-1}$ or more is required for a $1.0\,\mathrm{M_{th}}$ planet to drive a *spiral* whose peak temperature is transiently > 10% of the background (Fig. 2.C.2 in §2.C), but that to get an azimuthally averaged *ring* of 5% temperature enhancement over the background outside the planet, a $\beta = 10^2$ and a $3.0\,\mathrm{M_{th}}$ planet on a fixed orbit are needed (not shown).

Comparison to other published synthetic continuum images. To our knowledge no previous theoretical works have specifically targeted the observability of planet-driven dust spirals in the ALMA continuum, but a few have provided synthetic ALMA continuum images of planet-hosting disks for alternative purposes – and in some cases planet-driven dust spirals are visible in their results.

The image in Table 5 of Szulágyi et al. (2018) shows a model almost identical to one of our

runs: a Band 7 continuum observation with a $1.0\,M_{Jup}$ planet at 52 au and measured rms noise of $15\,\mu Jy\,bm^{-1}$, though with the C50-28 configuration (i.e., assuming future antennas). As in our case (e.g. Fig. 2.7), the outer primary spiral arm is directly visible in their image. They used the radiative 3D hydrodynamics code JUPITER (which includes heating by viscosity and adiabatic compression, and cooling by radiation and adiabatic expansion), and also emphasized that the temperature of one's target planet signature (in their case the CPD) influences its observability. They assumed, like us, $T_{dust} = T_{gas}$, and unlike us, obtained their dust surface density distribution by scaling the gas (though for ALMA B7 this is a valid assumption; see Fig. 2.2c).

Nazari et al. (2019) showed Band 7 observations achieving an rms noise of $18.5\,\mu Jy\,bm^{-1}$ for our medium angular resolution configuration pair, C43-5 + C43-8, of a disk with a low mass embedded planet ($30\,M_\oplus$, equivalent to 90% our $0.3\,M_{th}$ planet). They reported that no spirals were visible in their images. This agrees with our result in Fig. 2.9 (with a slightly better rms noise of $13.6\,\mu Jy\,bm^{-1}$), where we showed that a residual map is needed to detect the spiral.

In residual maps of Band 6 observations of disks with a locally isothermal equation of state, spatially and temporally constant Stokes number, and two embedded $\geq 2.5\,M_{th}$ planets, Veronesi et al. (2019) were able to detect the outer planet's inner primary and secondary spiral arm. In contrast to our parameter space, their outer planet was placed at 145 au.

Rowther et al. (2020) investigated the influence of a migrating planet embedded in a gravitationally unstable disk in which β varies radially with PHANTOM SPH simulations. They calculated their Band 6 ALMA continuum residuals using our same method, and found that spiral arms driven by an inwardly migrating $3.0\,M_{Jup}$ planet initially at 160 au were visible in both face-on and 40° inclined disks after > 1 hr of integration time. They too found that a lower angular resolution observation, with its higher S/N, allowed the planet-driven spirals to be seen more easily (see our Fig. 2.8), though there they were comparing the C43-6 and C43-7 configurations unpaired. We provide B7 images obtained with individual configurations in Fig. 2.E.5 in §2.E.

Caveats. Our work can benefit from a few improvements to incorporate more realistic physics. We have restricted the planet to be on the simplest orbit, i.e., circular, co-planar, and non-migrating. Relaxing these assumptions may affect the morphology of the gap(s) (Meru et al., 2019; Nazari et al., 2019; Pérez et al., 2019; Weber et al., 2019) and the spirals (Quillen et al., 2003; Duffell & Chiang, 2015), and impact the observability of spirals at a quantitative level. For example, Kanagawa et al. (2021) showed that the relative positions between the planet and the dust rings at gap edges depend on the migration rate of the planet. Meanwhile, the dust may be puffed up vertically in spirals (Krapp et al., 2021), which may result in detectable signatures in continuum observations (Doi & Kataoka, 2021). It is impossible to capture such effects in our 2D simulations. In addition, the presence of multiple planets, as in the case of PDS 70 (Haffert

et al., 2019), may also complicate the recognition of individual spirals.

We have ignored the effect of dust scattering, which can be important in optically thick disks (Kataoka et al., 2015a; Zhu et al., 2019; Liu, 2019). While we mainly focus on optically thin to marginally optically thick cases, scattering may cause an order unity correction to the overall disk brightness when $\tau \sim 1$ if the dust albedo is close to 1 (Fig. 1 in Sierra & Lizano, 2020), thus affecting the expected integration time to reach a desired S/N ratio. As a detailed sidenote, the increased dust surface density (thus τ) locally at the spirals would introduce another correction factor, but we expect its impact on the spiral contrast to also be minimal as the spiral $\Sigma_{\rm dust}$ enhancements are only on the order of 10%.

Finally, we adopt a single dust size most sensitively probed in observations with a fixed initial dust-to-gas mass ratio. In real systems, some dust mass is expected to be in grains of other sizes and thus does not contribute significantly to observations at a particular wavelength (Birnstiel et al., 2018b). As such, the disk brightness in our models might be taken as upper (more optimistic) limits for our assumed initial dust-to-gas mass ratio (0.01).

2.6 Summary & Conclusions

Detecting a planet's spiral wake would constitute compelling evidence for its presence in the disk – particularly if the inferred planet-spiral configuration is consistent with other signposts of the planet such as gaps/rings or local velocity kinks. In this work, we carry out 2D gas + dust hydrodynamic simulations and radiative transfer calculations. We produce synthetic Band 7 ALMA continuum observations of planet-driven dust spirals under a wide variety of disk and observing conditions. Our goal is to advise the search for planet-driven spirals in existing and future ALMA observations by identifying the most promising disk environments and observing specifications. We discuss the important physics underlying the observability of dust spirals in §2.3 before presenting our simulated observations in §2.4. Our conclusions are as follows.

- The "critical" Stokes number $\mathrm{St}_{\rm crit}$ dividing the well-coupled and poorly-coupled dust regimes can be estimated by equating the dust's intrinsic stopping time $t_{\rm stop}$ with the gas spiral wake crossing time $t_{\rm cross}$ (Eqn. 2.17). We find $\mathrm{St}_{\rm crit} \sim 0.05 - 0.1$ (Eqn. 2.18). Dust particles with $\mathrm{St} < \mathrm{St}_{\rm crit}$ form spirals identical to the driving gas spiral in morphology, while bigger particles azimuthally lag behind the gas peaks (Fig. 2.2a,b), echoing Sturm et al. (2020a). At almost all gas surface densities and observing wavelengths, ALMA probes well-coupled ($\mathrm{St} < \mathrm{St}_{\rm crit}$) dust. Therefore, barring inclination or geometrical offsets, we expect dust spirals observed with ALMA to be excellent tracers of gas spirals at

the midplane (Fig. 2.2c).

- While the surface density contrast of well-coupled dust spirals depends non-monotonically on the cooling timescale β and is the largest in locally isothermal disks, the strength of the temperature spiral formed in adiabatic disks increases monotonically with β. Adiabatic disks that cool slowly ($\beta \geq 10$) produce the hottest spirals with the largest contrast in surface brightness (Figs. 2.3 & 2.C.2).

- The difference in brightness between dust spirals in slowly cooling vs. locally isothermal disks is most pronounced when the disk is optically thick (Fig. 2.4).

- The signal of a spiral in a continuum image can be effectively highlighted in the residual map, enabling detections that otherwise may go unnoticed (Figs. 2.5 & 2.6).

- Planet-driven dust spirals are easiest to detect in adiabatic disks that cool slowly ($\beta \gtrsim 10$), that are marginally but not too optically thick ($\tau_0 \gtrsim 1.0$), and that host massive planets ($M_\mathrm{p} \gtrsim 1.0\,\mathrm{M_{th}}$). In such disks, spirals can be detected with integration times on the order of hours (Fig. 2.7).

- Detecting a spiral is not contingent on resolving it. Higher angular resolution observations (beam size $\approx 0.5\times$ the spiral width) have a higher spiral-signal-to-background ratio (they contain a greater proportion of spiral signal within each beam), but have a lower spiral-signal-to-*noise* ratio. Lower angular resolution observations (beam size $\approx 2\times$ the spiral width) "wash out" the spiral signal in the continuum image itself, but reveal the spiral with higher S/N in a residual map (Fig. 2.8).

- In a face-on, adiabatic ($\beta = 10$) marginally optically thick disk with a smooth dust surface density distribution exterior to the planet, we recover the outer spiral arm driven by a 1.6 Neptune mass planet ($0.3\,\mathrm{M_{th}}$) around a solar-type star at 50 au in the residuals of a Band 7 continuum observation obtained with an angular resolution of 62×70 mas and a measured rms noise of $13.6\,\mu\mathrm{Jy\,bm^{-1}}$, achievable with 3.6 hours of on-source time and a full continuum bandwidth of 7.5 GHz (Fig. 2.9).

- The presence of gaps and rings can impair the observability of co-located spirals, by reducing the amount of disk area over which the spiral can be traced (Fig. 2.10).

Future continuum observations with the ngVLA may provide access to the poorly-coupled ($\mathrm{St} > \mathrm{St_{crit}}$) dust spiral regime (Fig. 2.11). Comparing the azimuthal location of dust spiral peaks in

ALMA vs. ngVLA observations and measuring their offsets (Fig. 2.2a) may enable direct constraints on the gas surface density and disk mass.

Acknowledgements We are grateful to an anonymous referee for constructive suggestions that improved our paper. JS thanks: Pablo Benítez-Llambay and Leonardo Krapp for maintaining and monitoring the public `FARGO3D` Bitbucket, and Shangjia Zhang and Dhruv Muley for providing simulations – all of which aided in code comparisons; Ardjan Sturm for consultation where our works overlap; Jane Huang for helpful comments on an early version of the manuscript; Sarah Wood at the ALMA Help Desk and Nienke van der Marel for technical advice with the ALMA OT; Jeff Jennings and Brodie Norfolk for technical help on uvtables; and the Planet Formation Group at the University of Victoria for helpful discussions. Hydrodynamic simulations were performed on GPU computing nodes of Graham, Béluga and Cedar hosted by Compute Canada (www.computecanada.ca), as well as GASTRO hosted at McMaster University. RD and JS are supported by the Natural Sciences and Engineering Research Council of Canada (NSERC) and the Alfred P. Sloan Foundation. RAB was supported by a Royal Society University Research Fellowship, the STFC consolidated grant ST/S000623/1 and funding from the European Research Council (ERC) under the European Union's Horizon 2020 research and innovation programmes PEVAP (grant agreement number 853022) and DUSTBUSTERS (grant agreement number 823823). The National Radio Astronomy Observatory is a facility of the National Science Foundation operated under cooperative agreement by Associated Universities, Inc.

Software astropy (Astropy Collaboration et al., 2013, 2018), `CASA` (McMullin et al., 2007a), CMasher (van der Velden, 2020), matplotlib (Hunter, 2007), numpy (Harris et al., 2020), pandas (McKinney, 2011), scipy (Virtanen et al., 2020)

Data Availability Full set of synthetic ALMA observations and an image gallery are available at: https://doi.org/10.6084/m9.figshare.19148912.

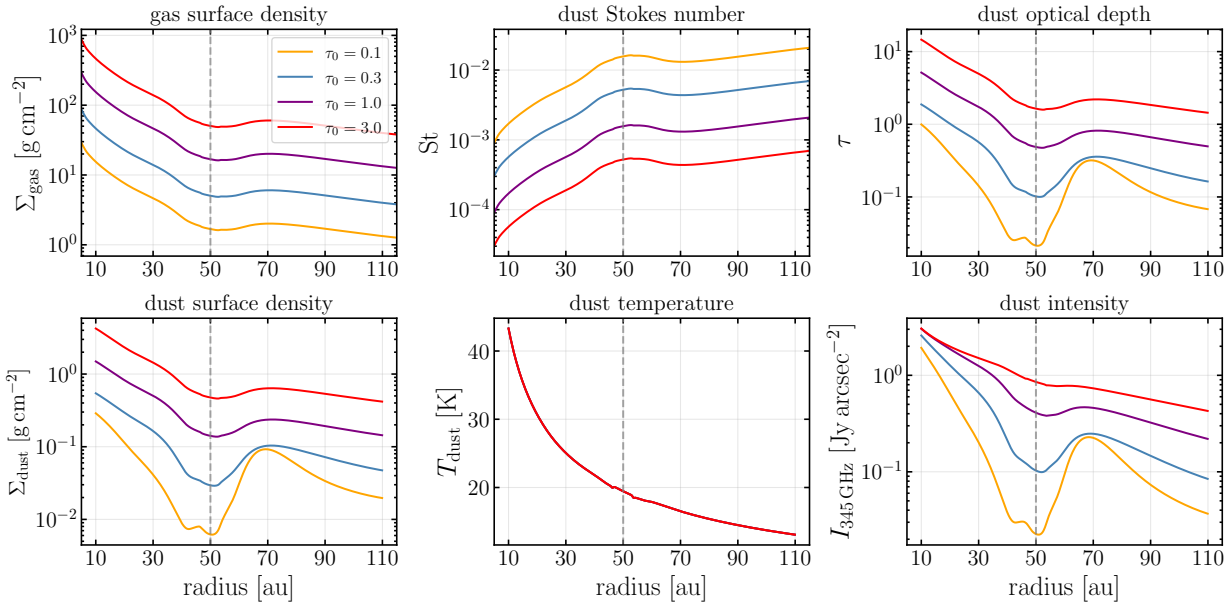

Figure 2.A.1: Azimuthally averaged radial profiles of important disk quantities for four of our models, demonstrating the construction of the optical depth parameter, τ_0. Shown is the adiabatic ($\beta = 10$) disk with a $1.0\,M_{\rm th}$ embedded planet.

Appendix

2.A Representative Disk Radial Profiles

Figure 2.A.1 illustrates the differences between our $\tau_0 = 0.1$, 0.3, 1.0, and 3.0 models by showing azimuthally averaged radial profiles of the relevant disk quantities (for one demonstrative permutation of EoS and $M_{\rm p}$). As described in §2.2.2, four hydrodynamic simulations are run and normalized individually such that the dust surface density (with an initial profile determined by a fixed dust-to-gas ratio of 0.01) gives an initial optical depth at $r_{\rm p}$ of 0.1, 0.3, 1.0, and 3.0. By fixing the grain size to $a_{\rm grain} = 0.14\,$mm, the Stokes number is different in each disk by the same factor as the gas surface density (§2.4.4).

2.B On assuming dust and gas thermal equilibrium at the midplane

As described in §2.2.2, we use the gas temperature output of our adiabatic `FARGO3D` hydrodynamic simulations as the dust temperature input for our radiative transfer calculations and

subsequent ALMA observations of planet-driven dust spirals in adiabatic disks. Below, we justify this assumption and describe considerations for observers interested in longer wavelength observations (see discussion around Fig. 2.11 in §2.5).

Under what conditions should the dust temperature $T_{\rm dust}$ be equal to the gas temperature $T_{\rm gas}$? The argument is simple: The temperature of a dust particle will be equal to that of its surroundings if it spends enough time in those surroundings to equilibrate. We will show that the time it takes a dust particle to respond thermally happens to be very similar to the time it takes to respond aerodynamically, $t_{\rm therm} \approx t_{\rm stop}$. Dust that is well coupled to the gas, as in our simulations, is therefore also well thermally coupled.

Consider a dust particle, with stopping time $t_{\rm stop}$ and thermal coupling time $t_{\rm therm}$, flowing through a gas spiral wake with crossing time $t_{\rm cross}$ (Eqn. 2.17). First, we express the particle's stopping time as

$$t_{\rm stop} = \frac{\rho_{\rm dust}\, a_{\rm grain}}{\rho_{\rm gas}\, v_{\rm th}}\,, \tag{2.B.1}$$

where $\rho_{\rm dust}$ and $\rho_{\rm gas}$ are the dust and gas volume densities, $a_{\rm grain}$ is the dust grain size and $v_{\rm th} = \sqrt{8 k_{\rm B} T_{\rm gas}/\pi\mu\, m_{\rm H}}$ is the mean thermal speed of the gas molecules. As the particle enters the spiral wake, the temperature of its surroundings changes (e.g. Fig. 2.3). The heating rate of a dust grain is given by (e.g., Burke & Hollenbach, 1983)

$$m_{\rm dust} C_{\rm dust} \frac{\partial T_{\rm dust}}{\partial t} = \pi a_{\rm grain}^2 n_{\rm gas} v_{\rm th} \alpha \left(2 k_{\rm B} T_{\rm gas} - 2 k_{\rm B} T_{\rm dust}\right), \tag{2.B.2}$$

where α is the accommodation coefficient, $m_{\rm dust}$ and $C_{\rm dust}$ are the mass and specific heat capacity of the particle, $n_{\rm gas}$ is the gas number density and $k_{\rm B}$ is Boltzmann's constant. This may be written as

$$\frac{\partial T_{\rm dust}}{\partial t} = \left[\frac{4\pi a_{\rm grain}^2}{3 m_{\rm dust}} \rho_{\rm gas} v_{\rm th}\right] \frac{3 k_{\rm B}}{2 C_{\rm dust}} \alpha \left(T_{\rm gas} - T_{\rm dust}\right). \tag{2.B.3}$$

Identifying the terms in square parentheses with $1/t_{\rm stop}$ we arrive at

$$\frac{\partial T_{\rm dust}}{\partial t} = \frac{1}{t_{\rm stop}} \frac{3 k_{\rm B}}{2 C_{\rm dust}} \alpha \left(T_{\rm gas} - T_{\rm dust}\right). \tag{2.B.4}$$

We may thus define the thermal coupling time as

$$t_{\rm therm} = t_{\rm stop} \times \frac{2 C_{\rm dust}}{3 k_{\rm B}} \alpha^{-1}. \tag{2.B.5}$$

Since $\alpha \approx 1$ (Burke & Hollenbach, 1983), the particle's thermal coupling time will be similar to its stopping time $t_{\rm stop} \approx t_{\rm therm}$ if the specific heat capacity of the dust and gas are similar.

Requiring enough time for a particle to come into thermal equilibrium with the gas inside the spiral wake, i.e. requiring $t_{\rm therm} < t_{\rm cross}$, is therefore equivalent to requiring $t_{\rm stop} < t_{\rm cross}$, which is our definition of being well coupled, ${\rm St} < {\rm St}_{\rm crit}$ (§2.3.1). In other words, small dust grains probed by ALMA will have the same temperature as the gas. Their temperature spirals, and their intensity spirals, will be co-located.

The temperature spiral peaks of gas and poorly-coupled (${\rm St} > {\rm St}_{\rm crit}$, and therefore $t_{\rm therm} > t_{\rm cross}$) dust will *not* be co-located. For observers interested in measuring the azimuthal offset between dust spirals in ALMA vs. ngVLA observations, this is a good thing; if the dust temperature peaks were aligned with that of the gas, the azimuthal offset between gas and large dust in the observed surface brightness would be reduced from that in surface density. Whether the poorly-coupled dust temperature spiral peaks align with *their own* surface density peaks requires future investigation, but it is promising that they are at least governed by similar timescales, $t_{\rm therm} \approx t_{\rm stop}$.

2.C An alternative visualization of Figure 3

Figure 2.C.2 is an alternative visualization of Figure 2.3, in which we trace the perturbation peaks in dust surface density, temperature and intensity (in the optically thin limit) along the inner and outer primary arms. We resolve the dependence of these quantities on the cooling timescale β with additional values not shown in Fig. 2.3. The amplitude of the perturbations varies substantially for the same $1.0\,{\rm M}_{\rm th}$ embedded planet.

2.D Synthetic observations of inclined disks

As a first start in informing observations of inclined disk systems, we generate an additional set of continuum images of tilted disks. The underlying dust surface density and temperature maps have been "squished" along the north-south axis by a factor of $\cos(i)$, and the dust surface density scaled by a factor of $1/\cos(i)$, before the emergent dust intensity was calculated. The optical depths of the inclined disks are thus different to their face-on counterparts, but we still use the τ_0 parameter to refer to them.

We also experimented with changing the position angle of the planet by 90 degrees (such that it was located on the north-south axis) and found that the spiral visibility in the deprojected residual maps was not greatly affected.

The images in Figure 2.D.3 depict a $M_{\rm p} = 1.0\,{\rm M}_{\rm th}$ planet embedded in an optically thin

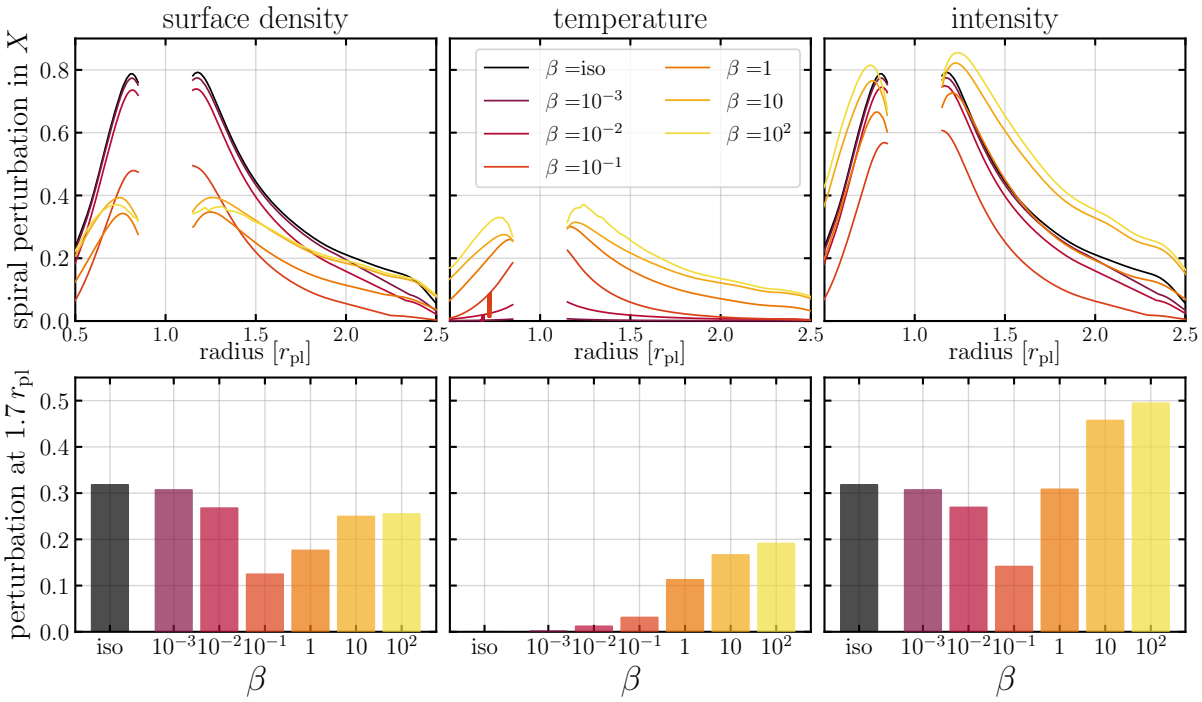

Figure 2.C.2: Like Figure 2.3, but with the perturbations in each disk quantity traced along the inner and outer primary arms (**top panels**), and showing additional cooling timescales β. To highlight the non-monotonic dependence of the dust surface density and intensity perturbations on β, as well as to emphasize the spread in the amplitude generated by a given planet mass under different β, we show the values at $1.7\,r_{\rm p}$ as a bar chart (**bottom panels**). In this case the planet mass is $1.0\,{\rm M_{th}}$.

(τ_0 = 0.1) disk with an adiabatic equation of state (β = 10), observed with the C43-5 + C43-8 configuration pair for a combined on-source time of 8.02 hours. The synthesized beam is shown in the bottom left corner of each image, and the measured rms noise is shown in the top left corner of the deprojected residual panels. View all our model permutations at https://doi.org/10.6084/m9.figshare.19148912.

2.E Considerations behind synthetic observations

In Table 2.E.1 we provide the individual and combined on-source (OS) times used in this work, which were specified by the ALMA Cycle 8 OT as what is needed to achieve each selected requested continuum sensitivity with each configuration pair at 345 GHz for a bandwidth of 7.5 GHz. For context, we also show the total observing time including overheads (OT), which does not scale linearly with the estimated time on source. Our highest sensitivity observation requires 8 SB executions.

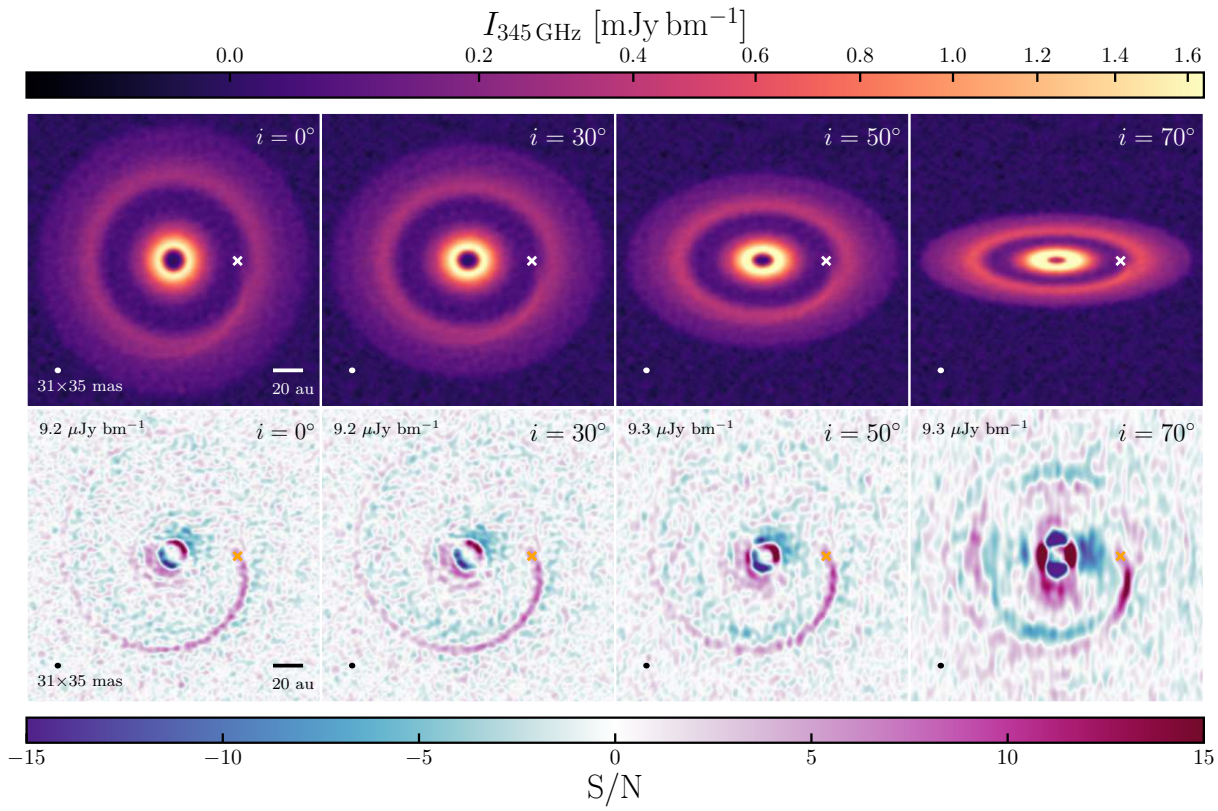

Figure 2.D.3: Synthetic ALMA B7 continuum images (**top**) and deprojected residuals (**bottom**) of a demonstrative model disk, inclined by 30°, 50° and 70° to compare spiral visibility under varying disk inclination. The effect of inclination is not significant unless the disk is very inclined (i.e. 70°, rightmost column).

As described in §2.4, we experimented with using `frank` (Jennings et al., 2020) to create residual maps and highlight the planet-driven spiral signal in our synthetic continuum observations. We fitted the observed visibilities with `frank` (exploring 16 permutations of the hyperparameters w_{smooth} and α and using the corrected weights), converted the residual uvtable into a measurement set, and imaged that measurement set with `tclean` in a way identical to as was done for the synthetic continuum observations, with the exception of setting the number of iterations to zero. Figure 2.E.4 provides a comparison between `frank` and our method of calculating residuals directly in the image plane (e.g. Fig. 2.6). We found that with the corrected weights, the visibility residuals were most similar to our image plane residuals, and were very insensitive to w_{smooth} and α. Figure shows 2.E.4 the results with parameters $w_{\mathrm{smooth}} = 1.01$, $\alpha = 1.05$ and $R_{\mathrm{max}} = 1.2''$.

In Figure 2.E.5 we show continuum observations made from the compact and extended configuration measurement sets that were concatenated to create the continuum images pre-

Table 2.E.1: ALMA observing time for requested sensitivities.

Requested Sensitivity (μJy/beam)	**Compact Configuration** (hr)	**Extended Configuration** (hr)	**Combined (on-source only)** (hr)	**Combined (on-source + overheads)** (hr)
	C43-4	**C43-7**		
10	1.51	6.57	8.08	18.51
15	0.67	2.92	3.59	8.35
20	0.38	1.64	2.02	4.63
25	0.24	1.05	1.29	3.15
30	0.17	0.73	0.90	2.09
35	0.12	0.53	0.66	1.62
	C43-5	**C43-8**		
10	1.45	6.57	8.02	21.94
15	0.64	2.92	3.56	10.08
20	0.36	1.64	2.00	5.49
25	0.23	1.05	1.28	4.03
30	0.16	0.73	0.89	2.52
35	0.12	0.53	0.65	2.08
	C43-6	**C43-9**		
10	1.38	6.57	7.95	18.21
15	0.61	2.92	3.53	8.22
20	0.34	1.64	1.98	4.55
25	0.22	1.05	1.27	3.10
30	0.15	0.73	0.88	2.06
35	0.11	0.53	0.65	1.60

Notes: Since the C43-6 + C43-9 configuration pair was not available in Cycle 8, the Cycle 7 ALMA OT was used to determine the observing times for that pair.

sented in the middle column of Figure 2.8. The individual measurement sets were imaged by the same procedure as was their combination. The residual maps of the extended configuration observation demonstrate the long baseline artifacts mentioned in §2.2.3. These artifacts can be generally characterized as repeating patterns of large regions on the sky with over- or under-intensity, in the rough shape of stripes, slices of pie, or wide spokes, depending on the configuration.

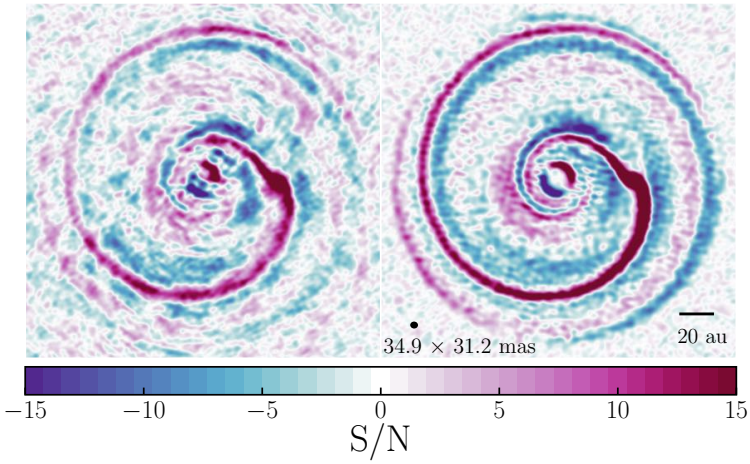

Figure 2.E.4: (**Left**) Imaged `frank` visibility residuals generated with parameters that best revealed the planet-driven spiral of the parameters that we explored. (**Right**) Residuals generated with the method used in this work. The measurement set shared between these two images corresponds to the model that was presented in panel (h) of Figs. 2.5 & 2.6 and represents one of the strongest spiral recoveries out of our full set of 432 model images.

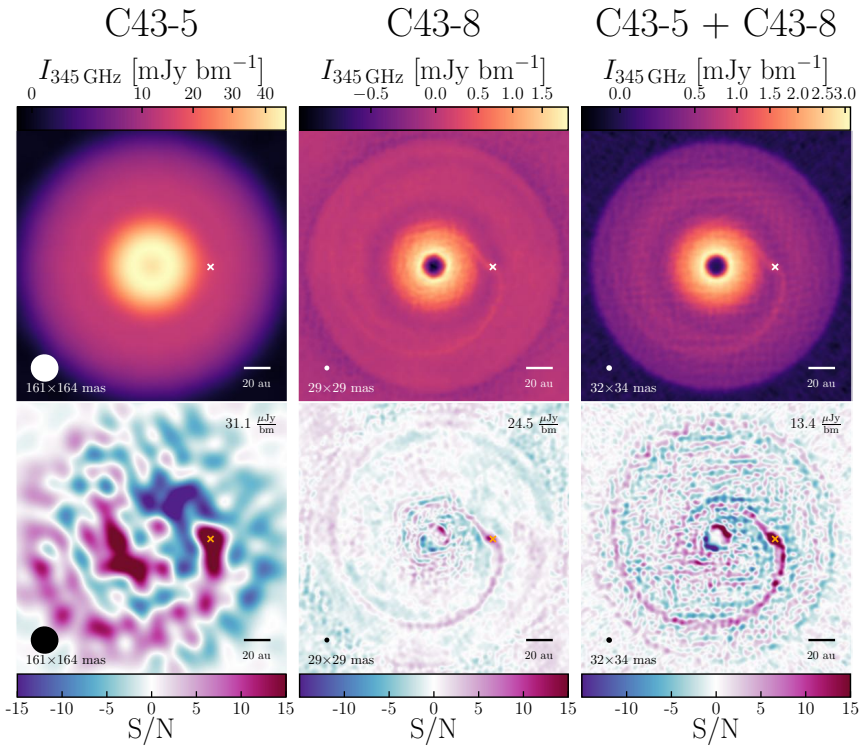

Figure 2.E.5: Synthetic ALMA B7 continuum observations with the compact and extended configurations that correspond to the pair shown in the middle column of Fig. 2.8. Following the Sensitivity Calculator in the ALMA OT, the combined on-source time of 3.56 hrs for this requested sensitivity of $15\,\mu\mathrm{Jy\,bm}^{-1}$ was distributed as 0.64 hrs with C43-5 and 2.92 hrs with C43-8 (see also Table 2.E.1). The measured rms noise in each observation is written in the top right corner of the residual maps.

Chapter 3

Testing velocity kinks as a planet-detection method: Do velocity kinks in surface gas emission trace planetary spiral wakes in the midplane continuum?

J. Speedie and R. Dong

The Astrophysical Journal Letters, 940, 2, L43 (2022)

Abstract

Spiral density waves generated by an embedded planet are understood to cause "kinks" in observed velocity channel maps of CO surface emission, by perturbing the gas motion within the spiral arms. If velocity kinks are a reliable probe of embedded planets, we should expect to see the planet-driven spiral arms in other observational tracers. We test this prediction by searching the dust continuum for the midplane counterparts of the spirals responsible for all of the velocity kink planet candidates reported to date, whose orbits lie inside the dust continuum disk. We find no clear detection of any spiral structure in current continuum observations for 6 of the 10 velocity kink planet candidates in our sample (DoAr 25, GW Lup, Sz 129, HD 163296 #2, P94, and HD 143006), despite the high planet masses inferred from the kink amplitude. The remaining 4 cases include 3 clear detections of two-armed dust spirals (Elias 27, IM Lup and WaOph 6) wherein neither spiral arm aligns with a wake originating from reported planet location, suggesting that under the planetary-origin hypothesis, an accurate method for inferring the location of the planet in the midplane may need to encompass vertical effects. The 10th case, HD 97048, is inconclusive with current knowledge of the disk geometry.

3.1 Introduction

The velocity "kink" kinematic signature has gained standing as a promising method for discovering embedded planets (Disk Dynamics Collaboration et al., 2020; Pinte et al., 2022). To date, 12 planet candidates have been reported based on velocity kink detections; in three cases, the planets have been ingested into the NASA or European exoplanet databases as *confirmed* planets[14] (Pinte et al., 2019; Izquierdo et al., 2022), and in one case, the candidate's circumplanetary disk has been observed co-located with the kink (AS 209, Bae et al., 2022b). Many more such detections of embedded planets are expected with the upcoming `exoALMA` Large Program[15].

Some loose ends exist, however, that motivate independent verification of the planetary origin of velocity kinks. Eleven of the 12 velocity kink detections were made in ^{12}CO emission, which is expected to originate above the midplane (e.g., Law et al., 2021), outside of where any analytic theory of velocity kinks has been achieved (Bollati et al., 2021). Ten of the 12 detections were made by visual inspection, without an assessment of the statistical significance of the kink signal (Pinte et al., 2018b, 2019, 2020), and in some cases the detections do not appear in independent datasets (Teague et al., 2021b). While the planet hypothesis is on the one hand supported by the inferred planet locations coinciding with dust gaps, the mass needed to generate kinks with the observed amplitudes is higher than the planet mass derived from the properties of the dust gaps by a factor of $4-100$ (e.g., Lodato et al., 2019; Zhang et al., 2018).

The velocity kink signal is understood to be generated by the embedded planet's spiral wakes. Along the spiral arms, the gas motion is perturbed relative to Keplerian rotation, which appears as an excess and absence of emission (i.e., a "kink") in the channel maps (e.g., Bollati et al., 2021). This understanding enables us to make a robust, testable prediction: *All instances of planet-driven velocity kinks should be concurrent with planet-driven spiral arms.* Recently, Calcino et al. (2022) demonstrated that the velocity kinks observed in ^{12}CO emission in HD 163296 map directly onto the theoretical curve for the spiral wake driven by planet c, projected up onto the emission surface. In this letter, we search the disk midplane for the spiral arms driven by 10 velocity kink planet candidates, using (sub-)mm continuum observations, under the usual assumption that the ~(sub)-mm-sized dust traced by such observations has settled to the disk midplane. Our goal is to provide an independent verification for the existence of the predicted planets, and thereby test the validity of velocity kinks as signposts of planets in disks.

[14] HD 97048 b; HD 163296 b; HD 163296 c (links embedded).
[15] 2021.1.01123.L; https://www.exoalma.com/

3.2 Data & Methods

3.2.1 Sample: Disks with Velocity Kinks

We compile all the disks with velocity kinks reported in the literature to date:

- 1 kink in HD 163296 ("HD 163296 #1") from Pinte et al. (2018b) (hereafter Pin18)
- 1 kink in HD 97048 from Pinte et al. (2019) (hereafter Pin19)
- 9 kinks (8 new) in 8 DSHARP disks: Elias 27, HD 143006, HD 163296 (a second kink in this disk: "HD 163296 #2"), IM Lup, DoAr 25, GW Lup, Sz 129 and WaOph 6, from Pinte et al. (2020) (heraftер Pin20)
- 2 kinks in HD 163296 (a third unique kink, "P94", and an independent re-detection of HD 163296 #1, dubbed "P261") from Izquierdo et al. (2022) (hereafter Izq22)
- and 1 kink in AS 209 co-located with a CPD candidate from Bae et al. (2022b) (hereafter Bae22).

In total, 12 velocity kinks have been reported in 10 disks. With the exception of P261 and P94 in HD 163296 (which were identified by `discminer`; Izq22), all the detections have been made by visual inspection of the channel maps, and the statistical significance of the detections has not been quantified. We list the disks and relevant properties of the kink detections in Table 3.2.1.

We then exclude from our sample the detections with inferred planet locations exterior to the outer edge of continuum emission. This eliminates HD 163296 #1 a.k.a P261 (Pin18; Izq22) and AS 209 (Bae22), leaving us with a total of 10 velocity kinks in 9 disks (where the repeat disk is HD 163296 containing Pin20's HD 163296 #2 kink and Izq22's P94 kink).

As a side note, velocity deviations attributed to a planet have also been reported in HD 100546 (Casassus & Pérez, 2019; Pérez et al., 2020) and TW Hya (Teague et al., 2022). We do not consider these detections in this work primarily[16] because we are concerned with detections based on kinks in velocity channel maps, whereas these were made based on Doppler flips in velocity residual maps.

[16]Additionally, the HD 100546 planet lies inside a continuum ring ($0.01\pm0.04''$, $0.21\pm0.04''$ on the sky; Casassus & Pérez, 2019), which is contrary to the classical paradigm that embedded planets carve gaps (though would support the scenario of Nayakshin et al., 2020). Since the initial discovery, the velocity deviations in HD 100546 have been explained as being due to an inner binary companion (Norfolk et al., 2022a), and due to disk eruptions driven by an embedded outflow (Casassus et al., 2022). The inferred planet location in TW Hya ($r_{\rm p} = 1.53''$ or 82 au, $\rm PA_p = 60°$) lies outside of the outer edge of continuum emission that is detected when observed at high angular resolution (~ 30 mas, Huang et al., 2018c), and the existing observations with sufficient sensitivity to detect continuum emission extending beyond 82 au are too low angular resolution for our purposes ($0.37''$, Ilee et al., 2022).

Planet location. The works reporting the velocity kinks in our sample provide the midplane location of the predicted planets. As we are testing this prediction, we adopt the given locations. For 9 of our 10 candidate planets (the exception being P94 in HD 163296; Izq22), the procedure that was used to determine the planet location is the following (Pin19; Pin20):

i) Identify the CO channel in which the velocity kink is most prominently detected, by visual inspection;

ii) Identify the center of the kink in that channel, by visual inspection;

iii) Measure the altitude of the CO emission surface at the center of the kink, using the method of Pinte et al. (2018a);

iv) Deproject that location onto the disk midplane.

In these 9 cases, the planet position is given in sky-coordinates (r_p, PA_p) without an estimate of spatial uncertainty.

The location of the P94 planet in HD 163296 is retrieved by `discminer`,[17] in disk-frame coordinates (R_p, ϕ_p), with an uncertainty in the radial and azimuthal directions of ±6 au and ±3 degrees, respectively (Izq22). However, due to `discminer`'s velocity centroid folding procedure,[18] the retrieved polar angle is degenerate about the disk minor axis and additional information or reasoning is needed to subsequently determine if the detection is on the redshifted or blueshifted side of the disk. The `discminer` velocity residuals of P94 were found to have a Doppler flip morphology, and by reasoning that the sub-Keplerian branch should be interior to the planet's orbit and the super-Keplerian branch should be exterior (Bollati et al., 2021), Izq22 report the planet on the redshifted side. We note that the "mirror kink" (i.e., the detection with opposite sign but equal significance, on the blueshifted side) is co-located with Pin20's HD 163296 #2 kink (Footnote 11, Izq22).

We list the reported locations of the candidate planets in our sample in Table 3.A.1. In all cases, the inferred location pinpoints the planet within a dust gap.

3.2.2 Dataset: Continuum Observations

The continuum data we present in this Letter are from the same ALMA program as the CO data in which the velocity kinks were detected. For the 8 Pin20 disks, we retrieve the publicly avail-

[17] We note that `discminer` assesses the significance of a deviation from Keplerian velocity, not whether the deviation matches the expected morphology of a planet-driven velocity deviation (as this has not yet been described analytically in 3 dimensions).

[18] A way of removing contributions to the velocity field that are symmetric about the disk minor axis, stemming from gas gaps and bulk disk rotation.

able, self-calibrated science-ready continuum images and fiducial (continuum-subtracted) ^{12}CO $J = 2-1$ image cubes from the DSHARP data repository.[19] For HD 97048, we obtain the self-calibrated continuum images and ^{13}CO $J = 3-2$ cube from Figshare.[20] Our analysis is only focused on the continuum images, and we do no new analysis on the CO cubes. Table 4.B.1 summarizes the observations and some basic properties of the data. For observational setup and data reduction details, we refer the reader to Pin19 for HD 97048, and to Andrews et al. (2018) for the 8 DSHARP disks in our sample. We measure the rms noise in the continuum images inside an annulus centered on the disk whose outer radius is the maximum allowed by the field of view and inner radius sufficiently larger than the source, following Andrews et al. (2018). For reference, we also measure the rms noise in the CO cubes, in the same annular area, throughout the first and last 5 channels.

3.2.3 Methods: Searching for Dust Spirals

Approach. Since spirals are perturbations in surface brightness above/below the background disk, our approach is to subtract an axisymmetric model for the background in order to extract the spiral signal. We create this axisymmetric background model in the image plane, by azimuthally averaging the continuum image.

We choose to do our analysis in the image plane, rather than the visibility domain, for two main reasons. Firstly, it yields similar results to uv-plane fitting in terms of both the morphology and sensitivity of the residuals, and is easily reproducible. We discuss this in more detail in Appendix §3.D.1. Secondly, the disk conditions (equation of state, optical depth, planet mass) and observing setups (angular resolution, sensitivity) under which the image plane method successfully retrieves the spiral signal has been quantified on synthetic continuum observations of planet-driven dust spirals in hydrodynamic simulations (Speedie et al., 2022). We therefore can form apples-to-apples expectations for the observability of the dust spirals, which we describe in detail in §3.2.4.

Disk geometry. Knowledge of the inclination and position angle of the continuum disk is needed to create the axisymmetric background model, and Table 3.A.3 provides the geometrical parameters we use for each disk. For 4 of the 8 DSHARP disks (HD 143006, HD 163296, GW Lup and Sz 129), we use the values found in Andrews et al. (2021b) (their Table 2) by the `frank` (Jennings et al., 2020) residual appearance method. We also tried the Huang et al. (2018a) geometries for these 4 disks and found that it had no effect on our results. For the other 4 not in

[19] https://almascience.eso.org/almadata/lp/DSHARP/
[20] DOI: https://doi.org/10.6084/m9.figshare.8266988.v1

Andrews et al. (2021b) (Elias 27, IM Lup, DoAr 25 and WaOph 6), we use the values found in Huang et al. (2018a) (their Table 2) by fitting ellipses to individual annular dust substructures. For HD 97048, no continuum-derived geometry has been published to our knowledge. We thus adopt two possible geometries, found by different methods: (i) fitting a Keplerian disk model to the velocity field from CO line data cubes (Table C.1, Bohn et al., 2022) using `eddy` (Teague, 2019a); (ii) fitting ellipses to rings and gaps in near-IR scattered light (Table 1, Ginski et al., 2016).

Disk rotation direction. We assume the predicted planet orbits in the same direction that the disk rotates. For HD 163296, DoAr 25 and HD 97048, it has been determined which side of the disk major axis is the near/far side with existing scattered light observations (see notes for Col. 10 in Table 3.A.3 for references), and we use that information in conjunction with knowing which side about the minor axis is the blue/redshifted side to deduce the direction that the disk rotates. For HD 143006 and GW Lup (low inclination disks), the near/far side determination not definitive (e.g., Benisty et al., 2018), but Pérez et al. (2018a) suggest HD 143006's west side is the near side, and Garufi et al. (2022a) posit GW Lup's northwest side is mostly likely the near side. This would mean HD 143006 rotates clockwise and GW Lup rotates anti-clockwise. In the former case this happens to be the opposite direction to the "low-level" tentative large-scale Archimedean spiral found by Andrews et al. (2021b) (see Appendix §3.D.1 for more discussion). For Sz 129, a relatively unstudied disk, no scattered light observations exist in the literature to our knowledge. Our results (Figs. 3.3.1 & 3.3.2) will show that the rotation direction of these 3 disks –HD 143006, GW Lup and Sz 129– is rendered irrelevant by the lack of spiral features in their continuum residual maps, but we still wish to show the tightness of the spiral winding. For that purpose, we assign clockwise for HD 143006 and anti-clockwise for GW Lup (motivated by the suggestions of Pérez et al., 2018a; Garufi et al., 2022a) and anti-clockwise Sz 129 (arbitrarily). For Elias 27, IM Lup and WaOph 6, we adopt the rotation direction found in Huang et al. (2018b) (their §3.2).

Table 3.2.1: Sample and summary of possibly planet-induced velocity kink detections to date.

Disk	Ref.	Method	Line	$v_{\rm res}$ (m/s)	$v_{\rm kink\,channel}$ (km/s)	Δv	$\sigma_{\rm kink}$	S/N$_{\rm CO}$	Gap	$M_{\rm p}$ ($M_{\rm Jup}$)
Kinks inside the continuum emission disk										
Elias 27	Pin20	VI	^{12}CO(2 – 1)	350	1.70	"?"	Firm	12	D69	1 – 3
HD 143006	Pin20	VI	^{12}CO(2 – 1)	320	8.84	$\approx 0.2\,v_{\rm Kep}$	Firm	10	D22	1 – 3
HD 163296 (P94)	Izq22	`discminer`	^{12}CO(2 – 1)	320	6.28	0.41 km/s	(19.4, 7.5)	...	D86	1 – 3
HD 163296 (#2)	Pin20	VI	^{12}CO(2 – 1)	320	3.40	$\approx 0.15\,v_{\rm Kep}$	Firm	36	D86	1 – 3
IM Lup	Pin20	VI	^{12}CO(2 – 1)	350	3.05	$< 0.24\,v_{\rm Kep}$	Firm	14	D117	1 – 3
DoAr 25	Pin20	VI	^{12}CO(2 – 1)	350	5.05	"?"	Tent.	7	D98	1 – 3
GW Lup	Pin20	VI	^{12}CO(2 – 1)	350	2.70	$< 0.3\,v_{\rm Kep}$	Tent.	12	D74	1 – 3
Sz 129	Pin20	VI	^{12}CO(2 – 1)	350	4.80	$< 0.2\,v_{\rm Kep}$	Tent.	11	D64	1 – 3
WaOph 6	Pin20	VI	^{12}CO(2 – 1)	350	2.10	"?"	Tent.	13	D79	1 – 3
HD 97048	Pin19	VI	^{13}CO(3 – 2)	120	5.76	...	...	...	130 au	2 – 3
Kinks outside the continuum emission disk										
HD 163296 (#1, P261)	Pin18	VI & `discminer`	^{12}CO(2 – 1)	110	1.00	0.40 km/s	(5.2, 4.6)[d]	...	N/A	2
AS 209	Bae22	VI	^{12}CO(2 – 1)	200	4.80	...	...	...	N/A	$1.3\cdot(\alpha/10^{-3})^{1/2}$

The last two rows are not in our sample, as the inferred planet location lies outside the continuum emission disk, but we include them for completeness. Column descriptions: (1) Name of disk. Name of kink or planet candidate in brackets, if applicable. (2) Paper first reporting the velocity kink. All values in the corresponding row are from this reference unless otherwise noted. (3) Method by which the velocity kink was detected. "VI" means visual inspection of the channel maps, and `discminer` is the quantitative tool of Izquierdo et al. (2021). (4) CO isotopologue and J transition in which the kink is reported. (5) Velocity (spectral) resolution of the CO cube in which the kink is reported. (6) Velocity (relative to Earth) of the channel in which the kink is most prominently detected, which is used to pinpoint the planet location (see Sec. 3.2.1). The two exceptions to this are: *(i)* Izq22 (row 3): the value in this entry is one of two channels in which the authors note the kink can be seen visually (caption of their Fig. 1), and `discminer` is used to pinpoint the planet location; *(ii)* Bae22 (row 12): the value in this entry is the channel in which the CPD candidate is most clearly detected in ^{13}CO, and is the central of three channels in which the ^{12}CO velocity kink is reported. (7) Amplitude of the velocity deviation. "?" is verbatim from the reporting paper, and '...' means not provided by the authors. For an independent velocity deviation prediction from 3D simulations for some of the DSHARP disks, see Rabago & Zhu (2021). (8) Either a qualitative classification as a "firm" or "tentative" kink detection by Pin20, or, the statistical significance (σ_r,σ_ϕ) of the deviation from Keplerian velocity from `discminer` (Izq22). (9) Signal to noise of CO emission at the location of the kink. (10) Dust gap associated with inferred planet location. Gap name designation from Huang et al. (2018a) for the DSHARP disks, and approximate gap radius in au for HD 97048 (Pin19). (11) Mass estimate of the candidate planet, inferred from the velocity kink amplitude. For the Pin18, Pin19 and Pin20 disks, this is from forward modeling with SPH simulations; for P94 it is from forward modeling with hydrodynamic simulations (Izq22); and for AS 209 (Bae22) it is from the Kanagawa et al. (2016) empirical relation between the gas gap width and planet mass. For mass estimates derived from the dust gap properties, see Zhang et al. (2018) and Lodato et al. (2019).

3.2.4 Expectations: Dust Spirals Driven by the Velocity Kink Planets

Midplane spiral morphology. We expect the embedded planets predicted by the velocity kink detections to drive spiral wakes in the gas at the midplane whose intrinsic morphology (amplitude, width and phase) is determined by the planet mass and location, as well as disk temperature.

As we are searching for these spirals in the (sub-)mm continuum and not the gas, the first question is whether we expect a difference between the dust spiral morphology and the morphology of the spiral in the gas. This depends on how quickly the dust responds to the change in aerodynamic drag forces exerted by the gas when the grains encounter the gas spiral perturbation, which in turn depends on the dust grain size and the local gas surface density. Sturm et al. (2020b) and Speedie et al. (2022) showed that for dust with Stokes number ($\mathrm{St} \propto a_{\mathrm{grain}}\,\Sigma_{\mathrm{gas}}^{-1}$, where a_{grain} is the dust grain size and Σ_{gas} is the local gas surface density) lower than the critical Stokes number, $\mathrm{St} \lesssim \mathrm{St}_{\mathrm{crit}} \approx 0.05 - 0.1$,[21] the dust responds quickly enough such that the resulting dust spiral is morphologically identical to the driving gas spiral at the midplane. We expect our continuum observations to be most sensitive to thermal emission from dust grains of size $a_{\mathrm{grain}} \approx \lambda_{\mathrm{obs}}/2\pi$ (Kataoka et al., 2015b; Pavlyuchenkov et al., 2019), which translates to $a_{\mathrm{grain}} \approx 0.14$ mm for HD 97048 (Band 7) and $a_{\mathrm{grain}} \approx 0.20$ mm for the 8 DSHARP disks (Band 6). For gas surface densities higher than just $\sim 0.2\,\mathrm{g\,cm^{-2}}$, these grain sizes correspond to Stokes numbers lower than $\mathrm{St}_{\mathrm{crit}}$ (see Fig. 2 of Speedie et al., 2022). Figure 7 of Dullemond et al. (2018) shows inferred gas surface densities for a subset of the DSHARP disks (including 3 in our sample) to range $0.1 \lesssim \Sigma_{\mathrm{gas}} \lesssim 50\,\mathrm{g\,cm^{-2}}$. To put it another way, assuming a gas surface density profile $\Sigma_{\mathrm{gas}} \sim 1/r$, then in order for Σ_{gas} to be lower than $0.2\,\mathrm{g\,cm^{-2}}$ at 50 au (typical location of inner arms in our sample), the total disk mass contained within 100 au would need to be lower than $6.7 \times 10^{-4}\,M_{\odot}$. We therefore expect no difference between the intrinsic morphology of the predicted midplane gas spiral and that of the dust spiral we aim to observe, and can use the literature knowledge of gas spirals to understand the morphology of the expected dust spirals.

The trajectory of a planet-driven spiral (i.e., the azimuthal location of the spine, or peak amplitude, as a function of radius) is the result of constructive interference among various spiral wave modes, each excited by a different Fourier component of the planet's gravitational potential (Bae & Zhu, 2018a,b). To predict where we expect to see positive residuals (emission above the axisymmetric background) in the continuum residual map for each planet in our sample,

[21] The critical Stokes number is the Stokes number for which the time it takes a dust grain to cross the spiral wake is equal to the grain's stopping time, and so this range is introduced by the azimuthal width of the wake, which changes with planet mass and distance from the planet (§3.2, Speedie et al., 2022).

we use the analytic phase equation of Bae & Zhu (2018a):[22]

$$\begin{aligned}\phi_{m,n}(R) = &- \phi_{\rm p} - \mathrm{sgn}(R - R_{\rm p})\frac{\pi}{4m} + 2\pi\frac{n}{m} \\ &- \int_{R_m^{\pm}}^{R} \frac{\Omega(R')}{c_s(R')}\left|\left(1 - \frac{R'^{3/2}}{R_{\rm p}^{3/2}}\right)^2 - \frac{1}{m^2}\right|^{1/2} \mathrm{d}R' ,\end{aligned} \tag{3.2.1}$$

where $(R_{\rm p}, \phi_{\rm p})$ are the midplane coordinates of the planet in the disk frame, $\Omega(R)$ is the angular velocity of the disk, $c_{\rm s}(R)$ is the sound speed of the gas, and m is the azimuthal wavenumber of the wave mode excited by the mth Fourier component of the planet's potential, which itself has a number of components indexed by n. The $n = 0$ components form the primary spiral arms, which are easier to recognize than e.g. secondary arms ($n = 1$ for $R < R_{\rm p}$, or $n = m - 1$ for $R > R_{\rm p}$) because: (i) they are launched relatively near to the planet, at Lindblad resonances $R_m^{\pm} = (1 \pm 1/m)^{2/3} R_{\rm p}$ (Goldreich & Tremaine, 1979b), and therefore the inner and outer primary arms always "point" to the planet, whereas the location of the additional arms (both the starting point and the azimuthal separation from the primary) varies with planet mass (Fung & Dong, 2015); and (ii) close to the planet, they have the highest amplitude (Bae & Zhu, 2018a). As such, we set $n = 0$.

The third term in Eqn. 3.2.1 is the only radially-varying term, and describes how tightly wound the spiral wave modes are as they propagate away from the planet. In addition to m, this term depends on the gas pressure scale height, $H(R) = c_{\rm s}/\Omega$. We calculate $\Omega(R)$ as the Keplerian angular velocity $\Omega(R) = (G M_\star / R^3)^{1/2}$, where R is the disk-frame radial coordinate and $M_\star$ is the stellar mass (Col. 3, Table 3.A.3). We calculate the gas sound speed as

$$c_{\rm s}(R) = \left(\frac{k_{\rm B}\, T_{\rm d}(R)}{\mu\, m_{\rm prot}}\right)^{1/2} , \tag{3.2.2}$$

where $k_{\rm B}$ is the Boltzmann constant, $\mu = 2.37$ is the mean molecular weight of the gas in atomic units, and $m_{\rm prot}$ is the proton mass. We thus need an analytic estimate for the disk temperature at the midplane $T_{\rm d}(R)$, for which we use the simple irradiated flaring disk recipe of Dullemond et al. (2018):

$$T_{\rm d}(R) = \left(\frac{\frac{1}{2}\varphi L_\star}{4\pi r^2 \sigma_{\rm SB}}\right)^{1/4} . \tag{3.2.3}$$

Here, $L_\star$ is the luminosity of the central star (Col. 4, Table 3.A.3), $\sigma_{\rm SB}$ is the Stefan-Boltzmann constant and φ is the flaring angle (e.g., Chiang & Goldreich, 1997; Dullemond et al., 2001).

[22] This equation assumes a circular orbit for the planet; see Zhu & Zhang (2022) and Fairbairn & Rafikov (2022) for semi-analytic linear theory of spiral density waves excited by planets on eccentric orbits.

A smaller flaring angle corresponds to a colder temperature profile and a more tightly wound spiral. We assign $\varphi = 0.02$ to be consistent with Dullemond et al. (2018) and Huang et al. (2018a).

Returning to the m dependence of the third term in Eqn. 3.2.1, we expect the phase of the spiral we see to follow that of the dominant azimuthal mode, $m_{\rm dom} = (\frac{1}{2})(H/r)_{\rm p}^{-1}$, in the case of low mass planets ($M_{\rm p} \lesssim 0.1\,M_{\rm th}$, where $M_{\rm th} = c_{\rm s}/\Omega G = (H/r)_{\rm p}^{3}\,M_{\star}$ is the unit of thermal mass; Bae & Zhu, 2018a,b). However, for higher mass planets, the wave modes propagate at faster speeds, and the resulting spiral arms are more open (Goodman & Rafikov, 2001) and should more closely follow lower ($m < m_{\rm dom}$) modes. In Col. 8 of Table 3.A.1, we convert the predicted masses of the embedded planets ($1-3\,M_{\rm Jup}$, Col. 8 of Table 3.2.1) into units of $M_{\rm th}$ using our estimation of $(H/r)_{\rm p}$ (Col. 7 of Table 3.A.1), and find $M_{\rm p} > 1.0\,M_{\rm th}$ in every case. For this reason, we consider azimuthal wave modes down to the lowest possible m ($m = 1$ in the outer disk and $m = 2$ in the inner disk). We also consider $m \to \infty$, corresponding to the linear limit of Rafikov (2002a) and the most tightly wound spirals (used in applications to observations by e.g., Muto et al., 2012; Casassus et al., 2021).

Observability. Using synthetic continuum observations, Speedie et al. (2022) found that the dust spirals driven by thermal mass planets at 50 au in a slowly cooling and moderately inclined ($i \lesssim 50°$) disk 140 pc away are detectable in continuum observations with sensitivity between $10-25\,\mu$Jy beam^{-1} and angular resolution $\sim 30-65$ mas. Dong & Fung (2017b) show that the amplitude of the spirals increases with planet mass for sub-thermal mass planets, and flattens out for super-thermal mass planets (their Fig. 1). In our sample, the inferred planet location is at a few tens to ~100 au, the mean beam size is $42 \pm 12 \times 54 \pm 17$ mas, the mean distance to the source is 144 ± 26 pc, the estimated continuum rms noises are all $\leq 22.6\,\mu$Jy beam^{-1} (except HD 97048), and only 2 disks are inclined by greater than 50°. We thus expect the current continuum observations to be sensitive to dust spirals driven by planets of thermal mass and above. Using the estimated $(H/r)_{\rm p}$ (Col. 7, Table 3.A.1) and known $M_{\star}$ (Col. 3, Table 3.A.3) for each candidate in our sample, this $1.0\,M_{\rm th}$ lower limit translates to Jupiter masses ranging between $0.15-0.96\,M_{\rm Jup}$ (with $0.15\,M_{\rm Jup}$ corresponding to HD 143006, and $0.96\,M_{\rm Jup}$ to HD 97048).

Note that gravitational instability may also produce spiral arms in continuum emission detectable in ALMA residual maps (Hall et al., 2019), and they may interfere with planet-induced spirals (Rowther et al., 2022). We do not account for this complication in this work.

3.3 Results & Discussion

We find non-detections of dust spirals for 6 of the 10 candidate planets in our sample: DoAr 25, GW Lup, Sz 129, HD 163296 #2, P94, and HD 143006 (Fig. 3.3.1 & 3.3.2, §3.3.1). In 3 cases (Elias

27, IM Lup and WaOph 6), dust spirals are detected but their locations do not agree with that of the predicted planet (Fig. 3.3.4, §3.3.3). For the 10th candidate planet, HD 97048, the result is inconclusive (Fig. 3.3.3, §3.3.2).

3.3.1 Non-detections

Of the 6 non-detections of dust spirals, 3 correspond to velocity kinks that were classified as "tentative" detections (DoAr 25, GW Lup, Sz 129; Pin20). In these disks, we find no significant non-axisymmetric continuum substructure (Fig. 3.3.1).

Of the latter 3 non-detections (Fig. 3.3.2), 2 correspond to "firm" kink detections (HD 163296 #2, HD 143006; Pin20), and 1 to a kink detection with a radial and azimuthal significance of $(\sigma_r, \sigma_\phi) = (19.4, 7.5)$ (P94; Izq22). We find some small-scale non-axisymmetric continuum substructures in these disks, but none that agree with the predicted spiral wakes.

The above results persisted in additional imaging efforts we performed with the calibrated measurement sets for DoAr 25, GW Lup, Sz 129, HD 163296 and HD 143006, varying the Briggs parameter to maximize the observing sensitivity (see Appendix §3.C).

If the planets are there, why don't we see the dust spirals? One possibility is that the disks cool quickly, such that the dust temperature perturbation along the spiral wake is small, and does not enhance the spiral's intensity contrast (Speedie et al. 2022, see also Miranda & Rafikov 2020b; Zhang & Zhu 2020). If that is the case, then we are mainly only probing the spiral *surface density* perturbation, which may be washed out at Band 6/7 wavelengths if the optical depth is sufficiently high. Follow-up at longer observing wavelengths may rule this possibility more or less likely. Additionally, in HD 163296 and HD 143006, the planet candidates are embedded in deep gaps and surrounded on either side by narrow rings. Only a small portion of the HD 163296 #2 and P94 spirals have the opportunity to be expressed upon the rings before they encounter the D48 gap or the outer edge of the continuum disk (Col. 4, Fig 3.3.2).

3.3.2 Inconclusive: HD 97048

We find strong and large-scale continuum residuals for the two assumed geometries (Cols. 7 & 8, Table 3.A.3) for HD 97048 (Fig. 3.3.3). Significant positive residuals in the inner disk align with the prediction for the inner spiral under both geometries, and the residuals show a portion of the outer spiral under the Ginski et al. (2016) geometry. It is unclear whether these matches support the planet hypothesis or are coincidental, because (a) the quality of the match depends on the geometry assumed, and (b) no matter what geometry we assume, there are significant residuals. Considering the possibility that these strong large-scale residuals indicate that an

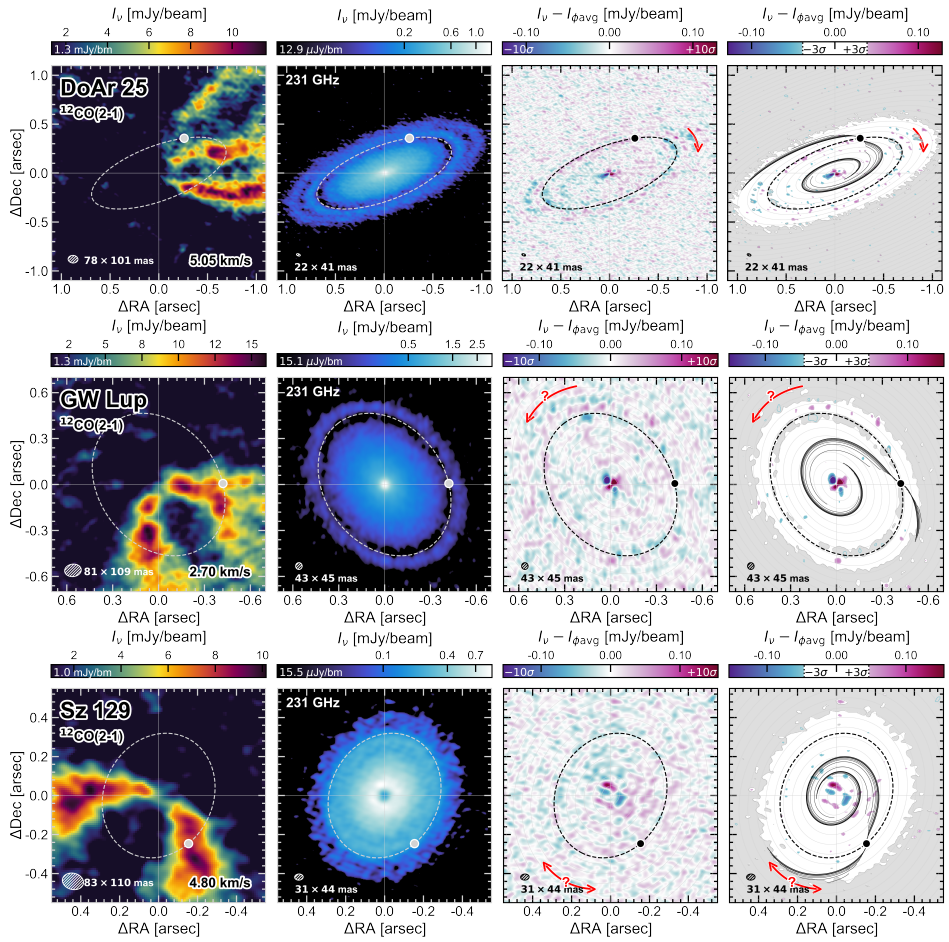

Figure 3.3.1: **No clear detections of the predicted dust spirals:** DoAr 25, GW Lup and Sz 129. In all columns, the grey or black point marks the reported planet location in the midplane, and the dashed grey or black line shows its circular orbit. **1st column:** The CO channel map in which the velocity kink is most prominently detected. The estimated rms noise in the cube is written in the colorbar, and the colormap starts at that value. **2nd column:** Continuum image showing where the planet lies relative to substructures in the dust distribution. The colormap starts at three times the rms noise (again written in the colorbar) and has a $\frac{1}{4}$-power law stretch. **3rd column:** Continuum residuals after subtracting the azimuthal average. Red arrows indicate the direction of rotation of the disk, and in all cases the arrow is located at the redshifted major axis. The colorbar spans $\pm 10\times$ the rms noise. **4th column:** Comparison between detected residual substructures stronger than $3\times$ the continuum rms noise, and the theoretical prediction for the midplane spiral wake driven by the candidate planet (Bae & Zhu, 2018a,b, our Eqn. 3.2.1). Light grey indicates where emission in the continuum image falls below this same threshold, helping to distinguish whether an absence of spiral-shaped residuals is due to the non-presence of spiral, or non-presence of emission (e.g. inside dust gaps or beyond the edge of the disk). Thin grey ellipses are projected concentric circles in radial steps of 1 beam major axis, helping to discern spirals from circular arcs under the angular resolution of the image.

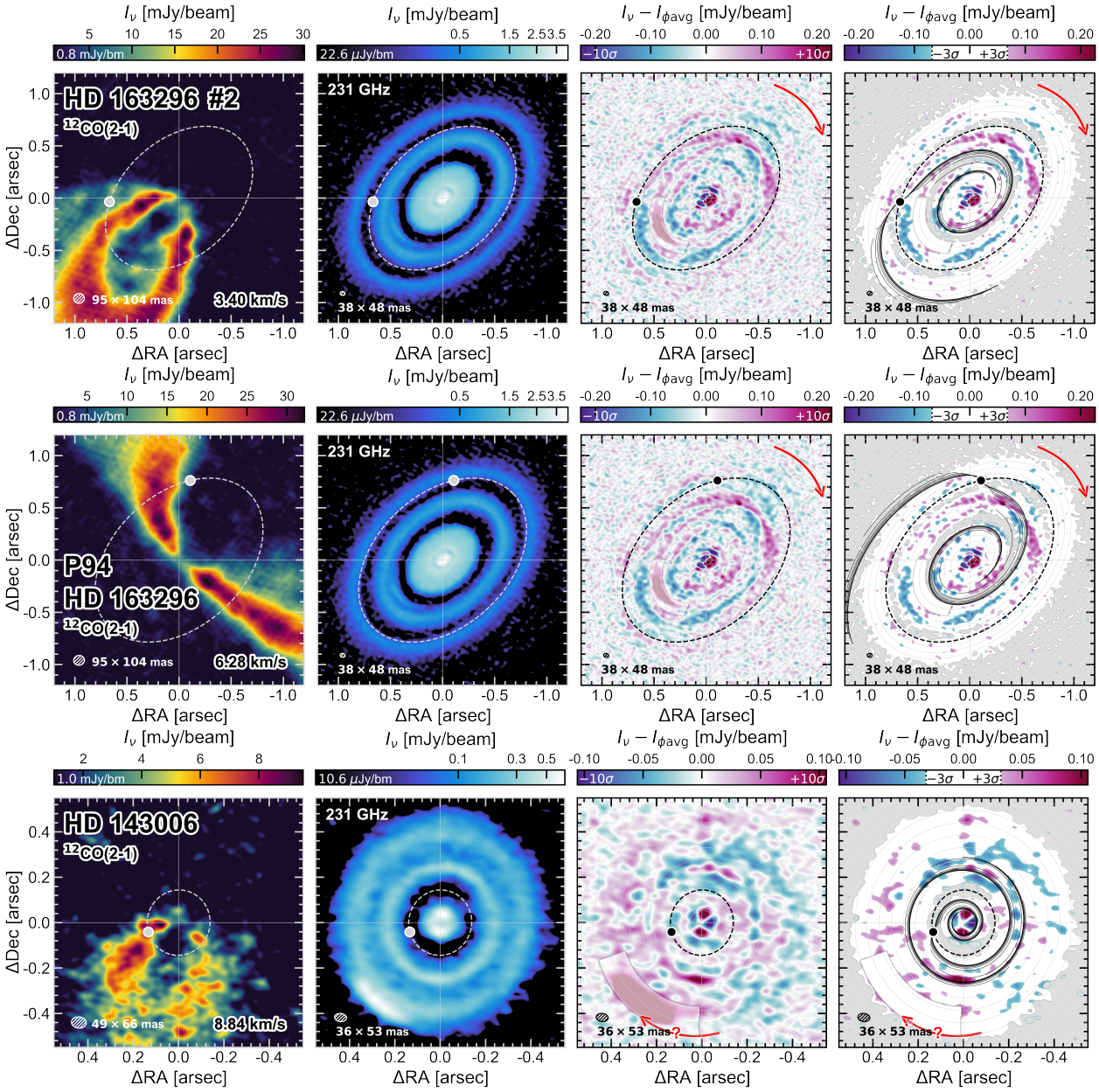

Figure 3.3.2: **No clear detections of the predicted dust spirals (continued):** HD 163296 #2, P94, and HD 143006. We mask the pronounced arc-like azimuthal asymmetries in these two disks to enhance the possibility of spiral detection (see Appendix Fig. 3.B.1). Additional figures showing the continuum residuals after re-imaging the calibrated measurement sets with different Briggs parameters are available for HD 163296, HD 143006, DoAr 25, GW Lup and Sz 129 at DOI: 10.6084/m9.figshare.21330426.

axisymmetric background model is not a good model, we attempt to find spiral residuals by a method that does not assume axisymmetry (Appendix Fig. 3.D.5), but come up empty-handed. We thus classify this case inconclusive.

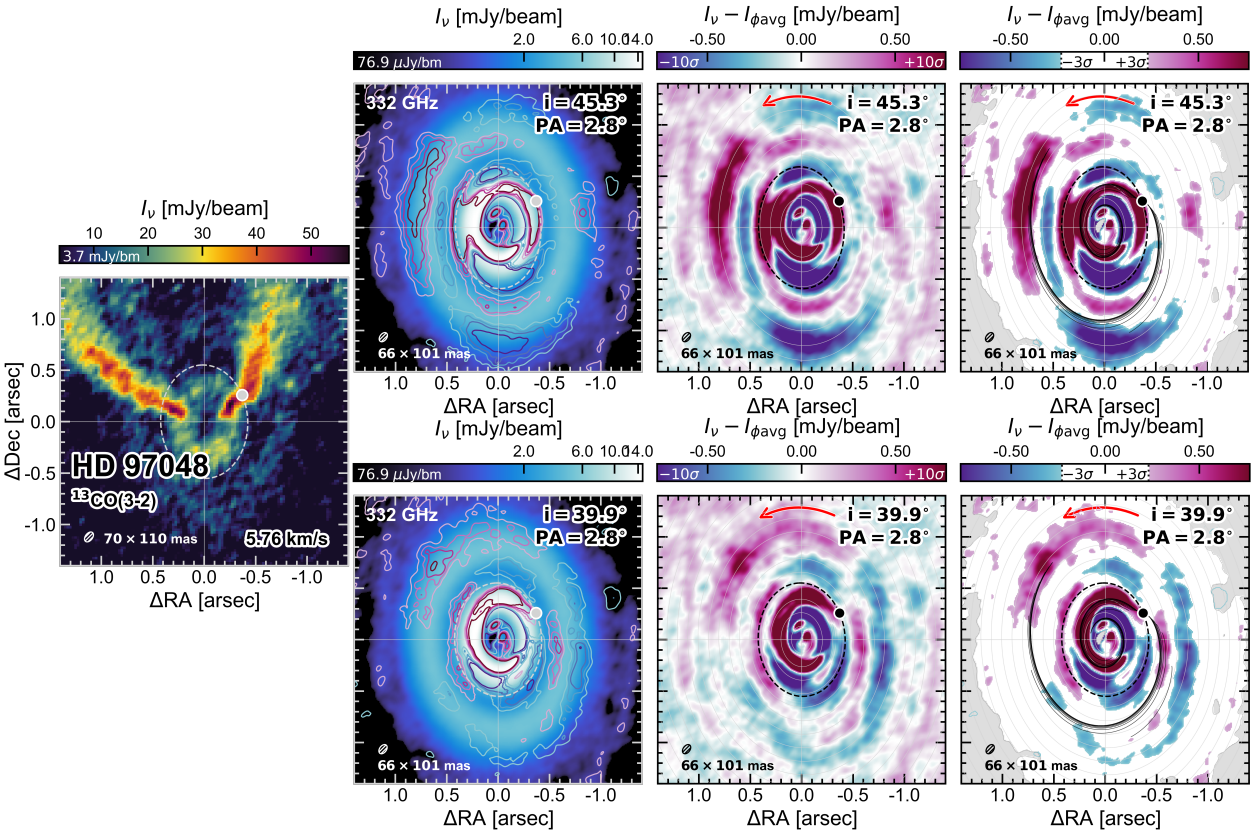

Figure 3.3.3: **Inconclusive case:** HD 97048. See §3.3.2 for details. Residual contours of $\pm 3, 5, 7, 10\times$ the continuum rms noise are overlaid in the 2nd column to help identify where residuals lie in relation to the gap and rings. **Top row:** Continuum residuals calculated assuming the disk geometry of Bohn et al. (2022). **Bottom row:** Continuum residuals calculated assuming the disk geometry of Ginski et al. (2016). Appendix Fig. 3.D.6 provides non-geometry-dependent residual maps for this disk.

3.3.3 Elias 27, IM Lup & WaOph 6

Of the 3 detections of dust spirals (Fig. 3.3.4), 2 correspond to velocity kinks that were classified as "firm" detections (Elias 27, IM Lup; Pin20), and 1 corresponds to a "tentative" kink detection (WaOph 6; Pin20). In all 3 cases, we see two spiral arms in the continuum residual maps, echoing Pérez et al. (2016) and Huang et al. (2018b).

Comparing the continuum residuals to the predicted spiral trajectories in Fig. 3.3.4, we find that the locations of the detected dust spirals in these 3 disks does not match with where we expect them to lie, given the predicted planet locations.

By comparing our estimation of $(H/r)_p$ and the reported estimates of the embedded planet masses (Cols. 7 & 8 of Table 3.A.1) to Figure 3 of Bae & Zhu (2018b), we see that the Elias 27, IM Lup and WaOph 6 planet candidates lie in a region of parameter space where we expect to see

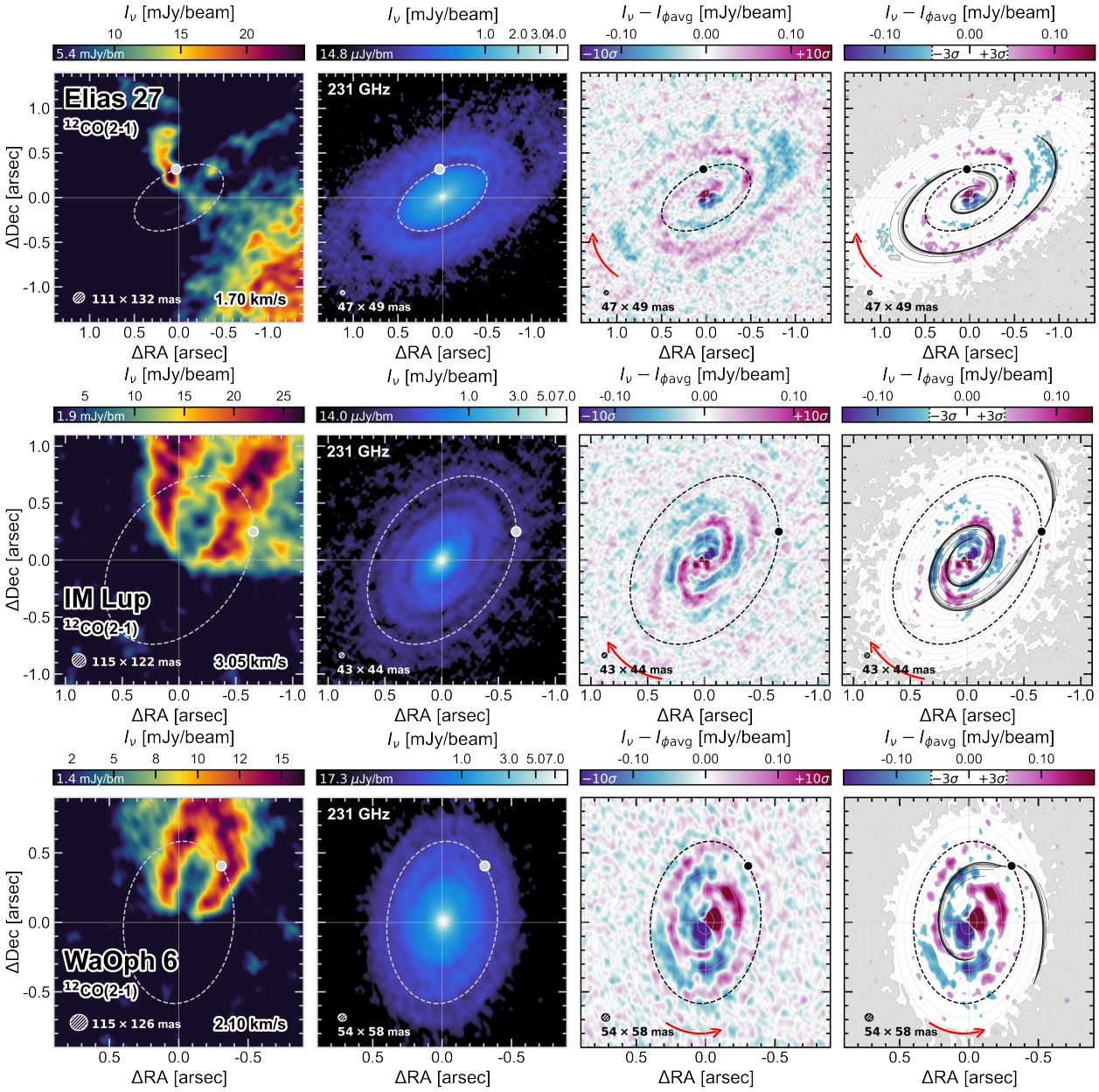

Figure 3.3.4: **Detections of dust spirals offset from the predicted planet location:** Elias 27, IM Lup and WaOph 6. The continuum spirals in these disks were first reported in Pérez et al. (2016) and Huang et al. (2018b).

both a primary and secondary spiral in the inner disk. This may support the hypothesis that the observed two-armed spirals are planet-driven.

However, the two arms in these 3 disks are roughly symmetric, and simulations have shown that a planet-to-star mass ratio of $q \sim 0.01$ (or larger) is required to make symmetric inner pri-

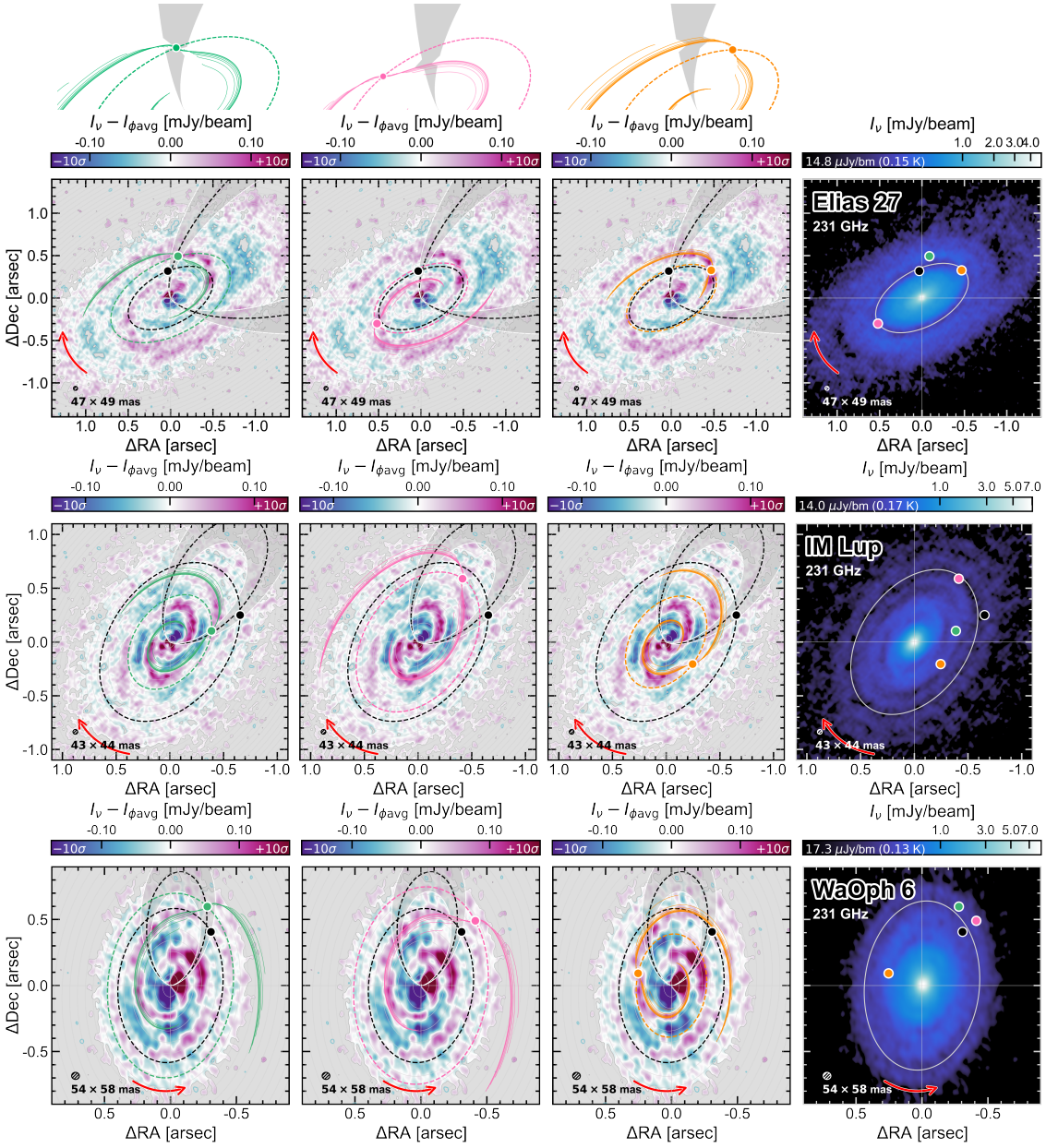

Figure 3.3.5: **Columns 1-3:** Alternative planet locations that achieve a better match to the observed continuum spiral residuals in Elias 27, IM Lup and WaOph 6, under three different restrictions (represented by the schematic at the top of each column; see §3.3.3 for details). The dashed black isovelocity contour is the velocity of the channel in which the kink is most prominently detected, and shaded grey regions demarcate ±0.5× the channel width. In all columns, the black dot marks the deprojected kink location (shown in previous figures as representing the reported planet). **Column 4:** Comparison between deprojected kink location and the alternative planet locations. The solid-line white ellipse is the DSHARP dust gap associated with the reported planet location (Col. 10 of Table 3.2.1).

mary and secondary spiral arms (Fig. 3, Fung & Dong, 2015). This is a point of mild tension with the masses inferred from the velocity kink amplitude ($q \in [0.001, 0.005]$ in these 3 cases). Gravitational instability may be a better explanation for symmetric two-armed spirals (e.g., for Elias 27, see Meru et al. 2017; Tomida et al. 2017; Paneque-Carreño et al. 2021b, and for such spirals in other disks, Dong et al. 2015).

As an alternative possibility that maintains the planetary-origin hypothesis, we contemplate the method used to determine the predicted planet locations (§3.2.1), which involves deprojecting the visually-identified kink center location from the estimated emission surface directly onto the midplane. Since the ^{12}CO emission surface is expected to be a few scale heights above the midplane (e.g., Pinte et al., 2018a; Law et al., 2021; Paneque-Carreño et al., 2021b), there may be room for error in translation. For example, Zhu et al. (2015) showed with 3D hydrodynamical simulations that spiral wakes are not perpendicular to the midplane, and instead curl towards the star at the disk surface. Vertical temperature gradients can introduce further complications, changing a spiral's pitch angle and misaligning the surface wakes from the midplane wakes (Juhász & Rosotti, 2018; Rosotti et al., 2020b). While Calcino et al. (2022) had success in matching ^{12}CO emission surface kinks around the full disk azimuth to the predicted spiral wake of HD 163296 #1 (P261), their simulations and analytic models assumed no vertical dependence in the velocity perturbations, and the location of this planet (which lies outside the continuum) has not been confirmed in midplane tracers. It's therefore conceivable that the method for pinpointing the planet may need to encompass vertical effects. Motivated by the possibility of leveraging the location of the midplane continuum spirals to inform the development of such a method, we assume the spirals in Elias 27, IM Lup and WaOph 6 are planet-driven, and explore alternative planet locations.

Considering alternative planet locations

In the following, we present 3 alternative planet locations (shown left to right in Fig. 3.3.5) in each of Elias 27, IM Lup and WaOph 6, under a set of 3 informative and gradually loosening restrictions. In all cases, the restrictions are based on *midplane* information: the dust continuum residuals, the deprojected kink location, midplane isovelocity contours, and the 2D velocity kink theory of Bollati et al. (2021). We calculate the midplane isovelocity contours using the 2D Keplerian velocity field $v_0(R,\phi) = v_{\rm Kep}(R)\sin(i)\cos(\phi) + v_{\rm LSR}$, where i is the disk inclination, R and ϕ are the disk frame coordinates (ϕ measured from the redshifted disk major axis), and $v_{\rm LSR}$ is the systemic velocity. For $v_{\rm LSR}$ values see caption of Table 3.A.4.

In the 1st column of Fig. 3.3.5, we shift the planet location to get a better alignment with the

detected dust spirals, under the restriction that the planet cannot lie outside the midplane area of the channel in which the velocity kink is most prominently detected. The motivation for this restriction is the idea that the velocity kink amplitude should be strongest close to the planet (e.g., Bollati et al., 2021; Calcino et al., 2022). We represent this area in grey, which spans a half channel width on either side of the velocity of the kink channel[23] (Col. 6, Table 3.2.1) in order to incorporate the spatial "uncertainty" introduced by the spectral resolution of the CO data. We are able to achieve more satisfactory alignments, but find that the necessary shift in radial and azimuthal position places the planets outside their DSHARP dust gap (white solid ellipse in the 4th column).

At the top of Fig. 3.3.5, we show a midplane schematic of how we may expect the planet location to affect the emission morphology in a given channel (a logic-extension of the results from Bollati et al., 2021): if the inner spiral wake shifts emission to lower velocity channels, and the outer wake shifts emission to higher velocity channels, then the channel centered on the planet may be left with an absence emission at the planet's location. The kink (specifically, emission present in a channel that is spatially offset from the rest) may then instead be most prominent in a channel where it coincides with the inner or outer spiral wake.

Thus, in the 2nd and 3rd columns of Fig. 3.3.5, we again shift the planet location to get a better alignment with the detected dust spirals, but this time while maintaining that the reported kink is probing a portion of the planet's inner spiral arm (2nd column) or outer spiral arm (3rd column), with the planet being as close to the deprojected kink location as possible. Under these two restrictions, we find some qualitative improvement in the match to the detected dust spiral, and in some cases (inner and outer wake scenario for Elias 27, inner wake scenario for IM Lup) we find that the resulting planet location lies inside the DSHARP dust gap. Important to note is that the *observed* midplane dust spiral residuals do not perfectly intersect with the deprojected kink location (and so the inner and outer wakes of our planet locations do not achieve perfect intersection either), suggesting a possible disjunction between midplane spirals and their expression on the disk surface.

We consider the 3 planet locations for each disk in Fig. 3.3.5 to be *possible* locations, in the sense that they plausibly satisfy the continuum spiral residuals. The main caveat is that we have not quantitatively assessed the agreement between the theoretical spiral trajectories and the continuum residuals, and obtained the planet locations by visual inspection / trial and error. We provide the locations in Table 3.A.4, and note that in some cases the planet in the midplane

[23] In the case of Elias 27, we infer from Table 2 and Fig. 1 of Pin20 that the kink is also detected in the two adjacent channels, though strong cloud contamination is present. In the case of Elias 27 and WaOph 6, it is unclear from their Table 2 whether the kink is detected in more than one channel. We thus opt to only consider the single channel.

lies far from the deprojected velocity kink in ^{12}CO surface emission. As mentioned above, our determination of these planet locations was done using midplane-based information, without consideration for any surface velocity evidence associated with the new locations, and how the planets can reproduce the strength of the detected kink signals in a distant channel is unclear. It may not be the case that the channel in which the kink is intrinsically most prominent has been correctly identified in Elias 27 and WaOph 6, though, as the ^{12}CO channel maps of these 2 disks suffer cloud contamination. This applies to almost the entire redshifted (south) half of Elias 27, and a large portion of WaOph 6 from the disk minor axis toward the blueshifted (north) side (see note *a* in Table 3.2.1 for affected velocities).

Our results emphasize the need for more theoretical and simulation work to understand the expected morphology of a planet-driven velocity kink, how the planet's spiral manifests at different heights in the disk, how the strength of the kink signal should vary with channel, and how we can use that information to successfully pinpoint the planet.

3.4 Summary

1. Despite the sufficiently high planet masses inferred from the reported velocity kink amplitudes, we are unsuccessful in detecting any dust spirals associated with 6 of the 10 velocity kink planet candidates reported to date whose orbits lie within the continuum disk, using current continuum observations (Figs. 3.3.1 & 3.3.2). We interpret this to mean that the full planet-finding potential of the velocity kink method may not be exemplified by this specific set of candidates. More kink detection efforts, including better quantification of the kink signal robustness and assessment for a planet-driven morphology, are needed.

2. Our search for dust spirals in the HD 97048 disk is inconclusive (Fig. 3.3.3). Observations with higher resolution and/or better sensitivity are needed to renew the search.

3. In the remaining 3 disks in our sample (Elias 27, IM Lup and WaOph 6), we re-detect clear and coherent dust spirals in the continuum residuals (Pérez et al., 2016; Huang et al., 2018b), but find that they do not align with the theoretical spiral trajectory originating at the candidate planet's reported location (Fig. 3.3.4). If these spirals are planet-driven, then this spatial offset may indicate that the method used to pinpoint the planet location from the kink detection in these disks (§3.2.1) is incomplete; a more successful method may need to encompass how a midplane spiral can be "morphed" during its upward propagation to be expressed on the disk surface (§3.3.3). We provide alternative midplane planet locations that are plausible from the dust spiral's perspective for these 3 planet

candidates in Fig. 3.3.5 and Table 3.A.4, which in some cases are far from the reported velocity kink (§3.3.3).

Acknowledgements We thank the anonymous referee for their thoughtful and constructive questions and suggestions. J.S. thanks Richard Booth, Cathie Clarke, Giovanni Rosotti, Richard Alexander, Richard Nelson, Brodie Norfolk, Rebecca Nealon, Sahl Rowther, Guilia Ballabio, Simon Casassus, Sebastián Pérez and Philipp Weber for insightful discussions that helped shape this work, and we thank Daniel Price for comments on the manuscript. J.S. also thanks the curator of the Catalog of Circumstellar Disks (www.circumstellardisks.org). R.D. and J.S. are supported by the Natural Sciences and Engineering Research Council of Canada (NSERC) and the Alfred P. Sloan Foundation.

We are grateful to Christophe Pinte and DSHARP Collaboration for making their data publicly available. This paper makes use of the following ALMA data: ADS/JAO.ALMA #2016.1.00484.L, ADS/JAO.ALMA #2016.1.00825.S. ALMA is a partnership of ESO (representing its member states), NSF (USA) and NINS (Japan), together with NRC (Canada), MOST and ASIAA (Taiwan), and KASI (Republic of Korea), in cooperation with the Republic of Chile. The Joint ALMA Observatory is operated by ESO, AUI/NRAO and NAOJ. The National Radio Astronomy Observatory is a facility of the National Science Foundation operated under cooperative agreement by Associated Universities, Inc. This work has made use of data from the European Space Agency (ESA) mission *Gaia* (`https://www.cosmos.esa.int/gaia`), processed by the *Gaia* Data Processing and Analysis Consortium (DPAC, `https://www.cosmos.esa.int/web/gaia/dpac/consortium`). Funding for the DPAC has been provided by national institutions, in particular the institutions participating in the *Gaia* Multilateral Agreement.

Facilities ALMA.

Software `astropy` (Astropy Collaboration et al., 2013, 2018), `cmasher` (van der Velden, 2020), `disksurf` (Teague et al., 2021a), `gofish` (Teague, 2019b), `matplotlib` (Hunter, 2007), `numpy` (Harris et al., 2020), `pandas` (The pandas development team, 2020), `scipy` (Virtanen et al., 2020).

Appendix

3.A Supporting Tables

Tables 3.A.1, 3.A.2, 3.A.3 and 3.A.4.

Table 3.A.1: Inferred midplane locations of planets detected by a velocity kink inside the continuum.

Disk	Ref.	Planet Sky Coordinates		Planet Disk Frame Coordinates		$(H/r)_p$	M_p
		r_p ($''$)	PA_{sky} (deg)	R_p (au)	ϕ_p (deg)		(M_{th})
Elias 27	Pin20	0.32 ± ...	6 ± ...	60 ± ...	-103 ± ...	0.087	3.0 – 8.9
HD 143006	Pin20	0.14 ± ...	107 ± ...	24 ± ...	-61 ± ...	0.043	6.5 – 19.6
HD 163296 (P94)	Izq22	0.77 ± 0.05	-8 ± 3	94 ± 6	50 ± 3	0.069	1.4 – 4.3
HD 163296 (#2)	Pin20	0.67 ± ...	93 ± ...	82 ± ...	129 ± ...	0.066	1.6 – 4.8
IM Lup	Pin20	0.70 ± ...	-69 ± ...	127 ± ...	136 ± ...	0.089	1.5 – 4.6
DoAr 25	Pin20	0.44 ± ...	-36 ± ...	101 ± ...	60 ± ...	0.071	2.8 – 8.3
GW Lup	Pin20	0.42 ± ...	-89 ± ...	78 ± ...	-119 ± ...	0.084	3.5 – 10.4
Sz 129	Pin20	0.29 ± ...	-148 ± ...	53 ± ...	63 ± ...	0.059	5.6 – 16.8
WaOph 6	Pin20	0.51 ± ...	-37 ± ...	72 ± ...	138 ± ...	0.089	2.0 – 6.0
HD 97048	Pin19	0.45 ± 0.10	-55 ± 10	109 ± 24	-66 ± 10	0.073	2.1 – 3.1

(1) Name of disk. Name of kink or planet candidate in brackets, if applicable.
(2) Reporting paper, as in Table 3.2.1.
(3-4) Coordinates of the planet as seen on the sky: Radial separation from the star (r_p), and position angle measured east of north (PA_p). The '...' indicates where authors gave no indication of uncertainty. Note that Pin20 (their Table 1) provides PA_p measured *west* of north.
(5-6) Coordinates of the planet in the disk frame: Radius in the deprojected midplane (R_p), and polar angle measured anti-clockwise from the disk's redshifted major axis (ϕ_p). Disk frame coordinates were calculated by this work, with the exception of row 3 (P94, Izq22), in which case we calculated the sky frame coordinates. Values of d used for arcsec↔au are in Table 3.A.3.
(6) Aspect ratio (H/r) evaluated at R_p, calculated by this work using Eqn. 3.2.3 and $L_\star$ in Table 3.A.3.
(7) Mass estimate of the planet in units of thermal mass M_{th}, calculated by this work using Column 6, $M_\star$ in Table 3.A.3, and the M_p range in units of M_{Jup} from the reporting paper (Column 11 of Table 3.2.1).

Table 3.A.2: Summary of observations used in this work.

Disk	**Origin**	**CO**		**Continuum**	
		rms noise (mJy/bm)	$\theta_{\rm beam}$ (mas)	rms noise (μJy/bm)	$\theta_{\rm beam}$ (mas)
(1)	(2)	(3)	(4)	(5)	(6)
Elias 27	DDR	1.6	111×132	14.8	47×49
HD 143006	DDR	1.0	49×66	10.7	36×53
HD 163296	DDR	0.8	95×104	22.6	38×48
IM Lup	DDR	1.9	115×122	14.0	43×44
DoAr 25	DDR	1.3	78×101	12.9	22×41
GW Lup	DDR	1.3	81×109	15.1	43×45
Sz 129	DDR	1.0	83×110	15.5	31×44
WaOph 6	DDR	1.4	115×126	17.3	54×58
HD 97048	FS	3.7	70×110	76.9	66×101

(1) Name of source.
(2) DDR: DSHARP Data Repository (Program ID: 2016.1.00484.L), FS: Figshare (Program ID: 2016.1.00825.S).
(3) Measured rms noise in the cube.
(4) Synthesized beam FWHM of the cube.
(5) Measured rms noise in the image. The values in Column 3 & 5 are almost identical to those of Andrews et al. (2018) (Table 4 & 5) and Pinte et al. (2019).
(6) Synthesized beam FWHM of the continuum image.

Table 3.A.3: Stellar properties and disk geometries.

Disk	d	$M_\star$	$L_\star$	Disk geometry					Rotation
				Δx	Δy	i	PA	Method	
	(pc)	($M_\odot$)	($L_\odot$)	(mas)	(mas)	(deg)	(deg)		
(1)	(2)	(3)	(4)	(5)	(6)	(7)	(8)	(9)	(10)
Elias 27	110.1 ± 10.3	$0.49^{+0.20}_{-0.11}$	$0.91^{+0.64}_{-0.37}$	-5 ± 5	-8 ± 3	56.2 ± 0.8	118.8 ± 0.7	E	CW
HD 143006	167.3 ± 0.5	$1.78^{+0.22}_{-0.30}$	$3.8^{+1.6}_{-1.1}$	-6 ± ~2	23 ± ~2	16 ± ~2	167 ± ~2	FRANK	CW?
HD 163296	101.0 ± 0.4	$2.04^{+0.25}_{-0.13}$	$17.0^{+17}_{-8.5}$	-3.5 ± ~2	4 ± ~2	47 ± ~2	313 ± ~2	FRANK	CW
IM Lup	155.8 ± 0.5	$0.89^{+0.21}_{-0.23}$	$2.6^{+1.5}_{-0.95}$	-1.5 ± 2	1 ± 2	47.5 ± 0.3	144.5 ± 0.5	E	CW
DoAr 25	138.2 ± 0.8	$0.95^{+0.10}_{-0.33}$	$1.0^{+0.56}_{-0.35}$	38 ± 2	-494 ± 2	67.4 ± 0.2	290.6 ± 0.2	E	CW
GW Lup	155.2 ± 0.4	$0.46^{+0.12}_{-0.15}$	$0.33^{+0.19}_{-0.12}$	0.5 ± ~2	-0.5 ± ~2	39 ± ~2	37 ± ~2	FRANK	ACW?
Sz 129	160.1 ± 0.4	$0.83^{+0.06}_{-0.24}$	$0.44^{+0.26}_{-0.16}$	5 ± ~2	6 ± ~2	32 ± ~2	153 ± ~2	FRANK	?
WaOph 6	122.5 ± 0.4	$0.68^{+0.32}_{-0.13}$	$2.9^{+1.7}_{-1.0}$	-244 ± 3	-361 ± 3	47.3 ± 0.7	174.2 ± 0.8	E	ACW
HD 97048	184.4 ± 0.8	2.36 ± 0.19	36.6 ± 20.03	0	0	45.3 ± 2.55	2.84 ± 2.55	Velocity Field	ACW
				0	0	39.9 ± 1.8	2.8 ± 1.6	Scattered Light	

(1) Name of source.
(2) Distance to the source, from *Gaia* DR3 (Gaia Collaboration et al., 2016a, 2022) as $d = 1/\varpi$.
(3) Stellar mass.
(4) Stellar luminosity. Values for $L_\star$, and $M_\star$ are from Andrews et al. (2018) except HD 97048, in which case $L_\star$ and $M_\star$ are from Bohn et al. (2022).
(5) R.A. offset of disk center from phase center (in the datasets we use; see Table 4.B.1).
(6) Decl. offset of disk center from phase center.
(7) Disk inclination.
(8) Disk position angle, measured anti-clockwise (i.e., east of north) to the red-shifted major axis.
(9) Method used to estimate disk P.A., inclination, and offset from phase center in the work from which we source the values: "E" indicates that the values were derived by fitting ellipses to continuum annular substructures (Table 2, Huang et al., 2018a); "FRANK" indicates the `frank` residual appearance method of Andrews et al. (2021b) (their Table 2); "Velocity Field" indicates the results of fitting a Keplerian disk model to the velocity field from CO line data cubes (Table C.1, Bohn et al., 2022) with `eddy` (Teague, 2019a); and "Scattered Light" indicates the results of fitting ellipses to gaps and rings observed in near-IR scattered light by SPHERE (Table 1, Ginski et al., 2016).
(10) Direction in which the disk rotates. "CW" means clockwise (west of north) and "ACW" means anti-clockwise. Rotation direction for Elias 27 and WaOph 6 were taken from Huang et al. (2018b); the remaining disk rotations were determined by this work based on scattered light observations in the following works: Elias 27 (Huang et al., 2018b), HD 143006 (Benisty et al., 2018; Pérez et al., 2018a), HD 163296 (Monnier et al., 2017; Muro-Arena et al., 2018), IM Lup (Avenhaus et al., 2018; Huang et al., 2018b), DoAr 25 (Andrews et al., 2008; Garufi et al., 2020), GW Lup (Garufi et al., 2022a), Sz 129 (none to our knowledge), WaOph 6 (Huang et al., 2018b), HD 97048 (Ginski et al., 2016). "?" indicates cases where the near/far side is uncertain or unknown in scattered light images in the literature to date (note the low inclination of those 3 disks).

Table 3.A.4: Coordinates of the alternative planet locations presented in Fig. 3.3.5.

Disk	Column	Sky Coordinates		Disk Frame Coords.		v_p
		r_p ($''$)	PA_p (deg)	R_p (au)	ϕ_p (deg)	(km/s)
(1)	(2)	(3)	(4)	(5)	(6)	(7)
Elias 27	1	0.50	-10	85	-114	1.65
	2	0.60	120	66	2	4.48
	3	0.57	-55	64	191	0.31
IM Lup	1	0.40	-75	76	129	2.99
	2	0.72	-35	112	-179	2.51
	3	0.32	-130	74	87	4.57
WaOph 6	1	0.66	-25	86	153	2.13
	2	0.64	-40	92	135	2.53
	3	0.27	70	48	-100	3.40

(1) Name of disk.
(2) Column of Fig. 3.3.5 showing the planet whose coordinates are given, numbered 1 to 3, left to right.
(3-4) Coordinates of the planet as seen on the sky: Radial separation from the star (r_p), and position angle measured east of north (PA_p).
(5-6) Coordinates of the planet in the disk frame: Radius in the deprojected midplane (R_p), and polar angle measured anti-clockwise from the disk's redshifted major axis (ϕ_p). Values of d used for arcsec↔au are in Table 3.A.3.
(7) Velocity coordinate of the planet, relative to Earth. Systemic velocities used to find these values were estimated from the morphology of emission in the channel maps (thus having uncertainty v_{sys}, Col. 5 of Table 3.2.1), and are: $v_{LSR} = 2.40$ km/s for Elias 27, $v_{LSR} = 4.45$ km/s for IM Lup and $v_{LSR} = 3.85$ km/s for WaOph 6.

3.B Treatment of Confined Azimuthal Asymmetries

The strong emission from the confined arc-like features in HD 163296 and HD 143006 will, of course, raise the azimuthal average emission within the radial region that they occupy, therefore making it more difficult to detect any dust spirals above the (overly-positive) average background in that radial region. This is particularly relevant for our search in HD 163296, as the inner spiral wake of both the HD 163296 #2 and P94 planets would be expressed upon the B67 ring, which is contaminated by the arc-like feature. It is less important for our search in HD 143006, because the candidate planet's spiral wake is tightly wound and unlikely to "reach" the radial region occupied by the crescent. In HD 163296, we omit from the calculation of the azimuthal average the emission lying within $135° \leq \phi \leq 220°$ between $R = 0.49''$ and $R = 0.63''$, where R and ϕ are disk frame coordinates (ϕ measured anti-clockwise from the redshifted disk

major axis). In HD 143006, we omit the emission lying within $-58° \leq \phi \leq 12°$ between $R = 0.37''$ and $R = 0.5''$.

Figure 3.B.1 shows the continuum residual maps in HD 163296 and HD 143006 with and without including the confined arc-like features in the azimuthal average. In HD 163296, excluding the arc-like feature modifies the residuals in a way that is more relevant for the HD 163296 #2 planet candidate than for P94 (hence why it is plotted in Figure 3.B.1 instead of P94) – some disconnected positive residuals are introduced in the northeast portion of the radial region (where HD 163296 #2's inner spiral would lie), though they do not appear to be a segment of a spiral. In HD 143006, excluding the arc-like feature removes the strongly negative residuals in the west half of the disk, but doesn't affect the residuals near the planet candidate.

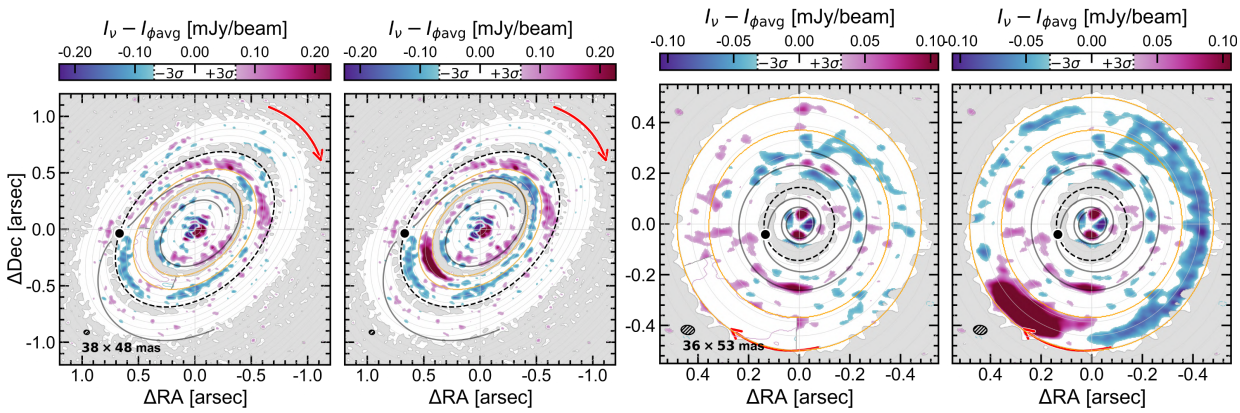

Figure 3.B.1: **Treatment of crescents in HD 163296 and HD 143006:** Detected residual substrctures stronger than 3× the continuum rms noise in HD 163296 (left two panels) and HD 143006 (right two panels) when either including or excluding the confined arc-like azimuthal asymmetries. The two orange ellipses guide the eye to the radial region affected (i.e., the residual maps are identical outside of this region). A 3σ contour of the arc-like feature is shown under the mask to demonstrate how the mask covers the feature.

3.C Re-imaging the continuum visibilities to achieve higher sensitivity

Speedie et al. (2022) argued that a beam size ~2 times larger than the width of the spiral can yield a higher signal-to-noise detection in a residual map than a higher angular resolution image. Motivated by this, we re-imaged the publicly available DSHARP calibrated measurement sets of the 5 disks whose fiducial images yielded non-detections (DoAr 25, GW Lup, Sz 129, HD 163296 and HD 143006), varying the Briggs parameter to explore the full available range of angular

resolutions and achievable sensitivities. We show an example of the results in Figure 3.C.2. The full set is available at DOI: 10.6084/m9.figshare.21330426.

3.D Methods for Detecting Dust Spirals

3.D.1 Comparison with `frank`

All 8 of the DSHARP disks in our sample were analyzed in uv-space with `frank` by Jennings et al. (2022a), and 4 of them also by Andrews et al. (2021b). Those works did not report detections of dust spirals in the `frank` residual maps of DoAr 25, GW Lup, Sz 129 and HD 163296, a result echoed by this letter. Side-by-side comparisons between the imaged `frank` residuals and our image-plane residuals shows the techniques give nearly identical results.

Andrews et al. (2021b) report a "low-level" tentative large-scale Archimedian spiral in HD 143006 (their Figure 4). In our Figure 3.D.3, we re-present the continuum residuals we obtained for HD 143006 (the exact same map as appears in the main text in the bottom right panel of Figure 3.3.2), on the same colour scale as Andrews et al. (2021b), to more clearly demonstrate the extent to which our azimuthal average technique recovers this tentative spiral. The basic result is similar, and our method recovers the spotty residual features along the Andrews et al. (2021b) spiral. In this case, some differences in the residuals can be attributed to the differing treatments of the confined azimuthal asymmetries. We note that the direction of this spiral (assuming it is trailing) implies counter-clockwise rotation for the HD 143006 disk, opposite to the clockwise rotation suggested by Pérez et al. (2018a).

3.D.2 Additional Searches with the Unsharp Masking Method

One of the most significant challenges to using the azimuthal average as a background model is that it makes assumptions on the disk geometry – namely, that the dust disk is inherently axisymmetric and planar, and that one has accurate knowledge of the disk inclination and position angle. Artificial residuals can be introduced if one uses the incorrect disk geometry. Creating residual maps with `frank` (Jennings et al., 2020) involves the same challenges (e.g., Appendix A of both Jennings et al., 2022b; Andrews et al., 2021b).

In this section we explore an alternative technique that makes no assumptions on the disk geometry, and apply it to the disks that exhibited small- or large-scale azimuthal average residuals: HD 163296, HD 143006, and HD 97048. The technique has been referred to as "unsharp masking" (e.g., Pérez et al., 2016; Meru et al., 2017), and involves convolving the observation

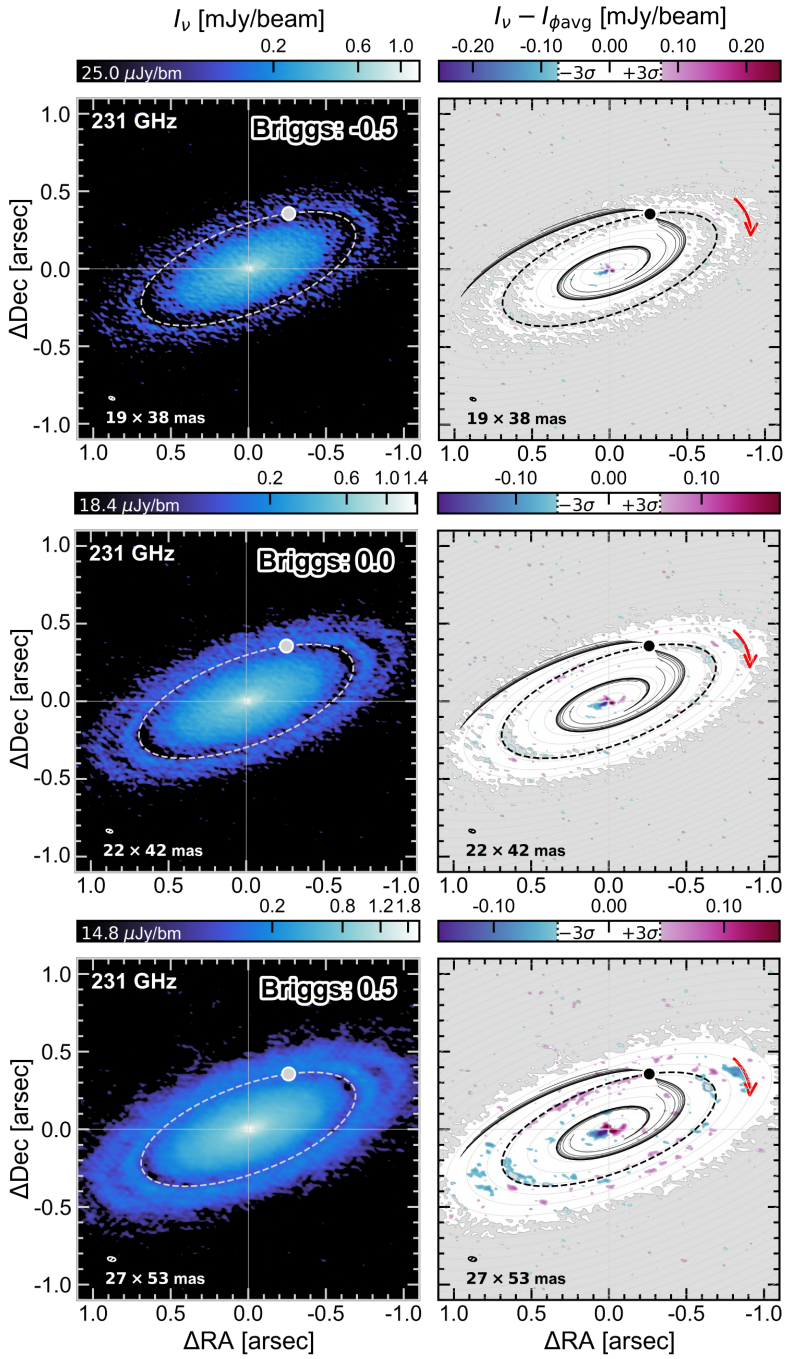

Figure 3.C.2: Subset of our re-imaging efforts with higher Briggs parameters to increase the beam width and sensitivity, showing the disk DoAr 25 as an example. The full set of images for DoAr 25, Sz 129, GW Lup, HD 163296 and HD 143006 for Briggs parameters $\in [-1, -0.5, -0.3, 0, 0.3, 0.5, 1, 2]$ is available at: DOI: 10.6084/m9.figshare.21330426.

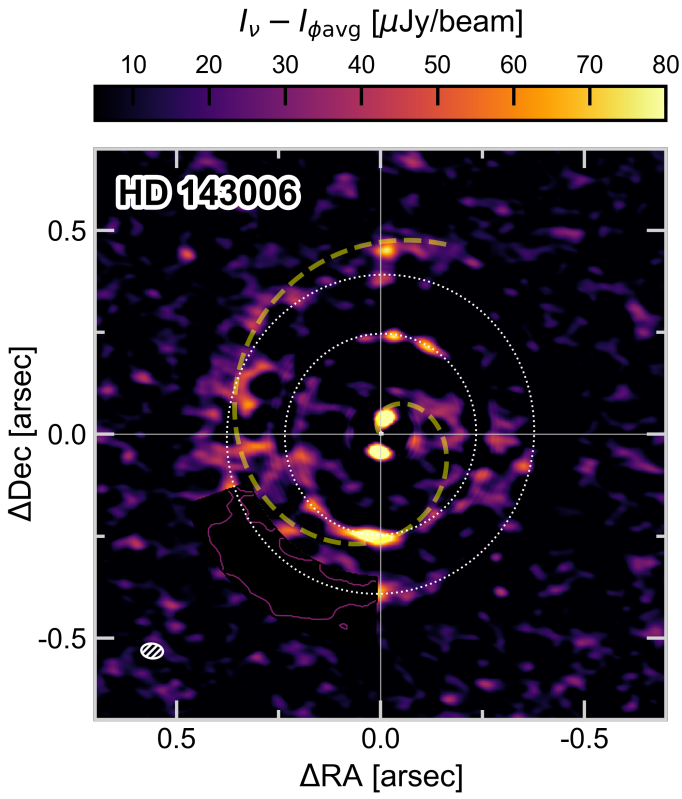

Figure 3.D.3: A re-presentation of our azimuthal average continuum residual map for HD 143006, for comparison to Figure 4 of Andrews et al. (2021b). The dashed yellow curve is their (visually tuned, not fit) Archimedian spiral overlay, described in disk-frame coordinates by $R_{\text{spiral}} = 0.170 + 0.067\phi$ [arcsec]. The two dotted white ellipses mark the DSHARP-identified rings, B41 and B65.

with a normalized 2D Gaussian of HWFM $\sigma_{x,y}$ and subtracting the result from the original image. It is mathematically equivalent to the "high-pass filtering" technique (e.g., Rosotti et al., 2020b; Norfolk et al., 2022a) which involves suppressing large-scale spatial (angular) frequencies by convolution with a 1D Gaussian of HWFM σ_ν in the Fourier domain. We confirmed both give identical residual maps with the appropriately-scaled Gaussian kernels ($\sigma_\nu = 2\pi/\sigma_{x,y}$), but only show the former here so as to consistently work in the image plane.

Figure 3.D.4 compares the efficacy of the residual-making method we use in the main body of the paper to that of the unsharp masking method, using a synthetic continuum observation model[24] from Speedie et al. (2022). To produce the unsharp masking residual map, we convolve the model image (I_ν, 1st panel) with a 2D Gaussian of HWFM $\sigma_{x,y} = 30$ mas (I_{conv}, 4th panel)

[24] Downloadable from Figshare: 10.6084/m9.figshare.19148912. This model contains a 1.0 Mth mass planet at 50 au in an adiabatic, slowly cooling ($\beta = 10$), marginally optically thin ($\tau_0 = 0.3$) disk at a distance of 140 pc, observed with the C5+C8 ALMA configuration pair for an on-source time of 3.56 hours.

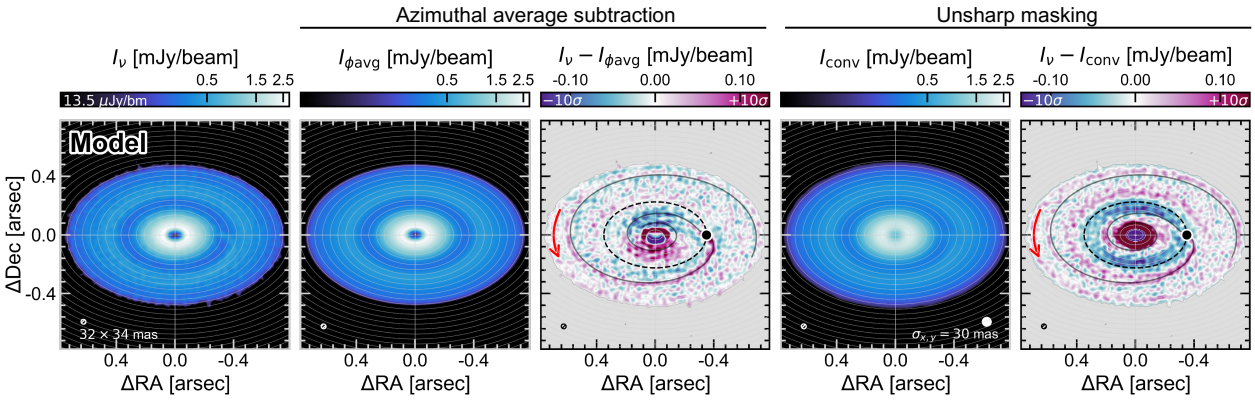

Figure 3.D.4: **Comparing methods for detecting planet-driven dust spirals:** Azimuthal average subtraction vs. unsharp masking. **1st panel:** Synthetic continuum observation, I_ν. **2nd panel:** Background disk model $I_{\phi\rm avg}$ obtained by azimuthally averaging I_ν, using knowledge of the disk inclination, position angle and phase offset. **3rd panel:** Residual map as the difference between I_ν and $I_{\phi\rm avg}$. **4th panel:** Background disk model $I_{\rm conv}$ obtained by convolving I_ν with a 2D Gaussian kernel of HWFM $\sigma_{x,y}$, making no assumptions on the disk geometry. Filled white circle represents the Gaussian kernel. **5th panel:** Residual map as the difference between I_ν and $I_{\rm conv}$. In the residual maps, we overlay the theoretical prediction for the midplane spiral wake driven by the model planet (Bae & Zhu, 2018a,b, our Eqn. 3.2.1), whose mass is $M_{\rm p} = 1.0\,M_{\rm th}$. Only the dominant azimuthal mode ($m_{\rm dom} = (\frac{1}{2})(H/r)_{\rm p}^{-1}$) is shown, and the planet's outer spiral wake becomes more open than the predicted trajectory with distance from the planet.

using `scipy.ndimage.gaussian_filter`. The residuals resulting from different kernel sizes will vary in morphology, as different kernels sequentially highlight different spatial scales of the image structures, and in practise we strongly encourage the observer to view the results for a range of $\sigma_{x,y}$. Here, we show the results for a select $\sigma_{x,y}$, chosen such that $I_{\rm conv}$ is smoothed of blobs but still contains the radial structure present in I_ν. This figure shows that the unsharp masking method can be effective, though it is prone to accentuating gaps and rings.

Nonetheless, for its main benefit of not requiring assumptions on the disk geometry, we apply it to the continuum observations of HD 163296, HD 143006 and HD 97048 in Figs. 3.D.5 & 3.D.6. In the resulting residual maps for HD 163296 and HD 143006 (5th column of Figure 3.D.5), we detect only ring and gap structures and no spirals, consistent with the azimuthal average method in the main text. In HD 97048 (Figure 3.D.6), we find that a single 2D Gaussian kernel does not highlight substructure in both the inner and outer ring simultaneously, and so we show the results for both a $\sigma_{x,y} = 60$ mas kernel and a $\sigma_{x,y} = 30$ mas kernel. The residual map produced with the larger kernel (2nd panel, Figure 3.D.6) shows no spiral structure in the outer ring. The residual map produced with the smaller kernel (3rd panel, Figure 3.D.6) reveals a double-ring structure over $\sim 270^\circ$ of the inner ring, but no residuals that consistently follow the

predicted trajectory for the planet's inner spiral arm.

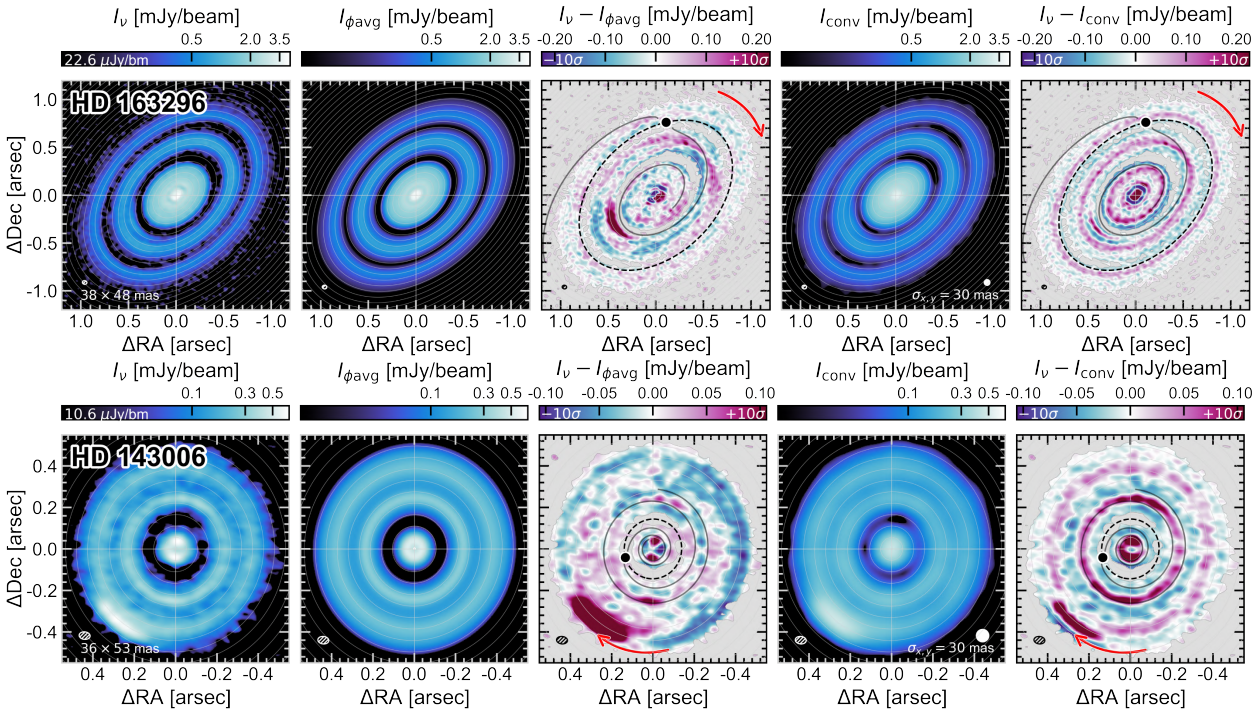

Figure 3.D.5: **Additional searches for the predicted dust spirals:** HD 163296 and HD 143006. Panel layout similar to Figure 3.D.4.

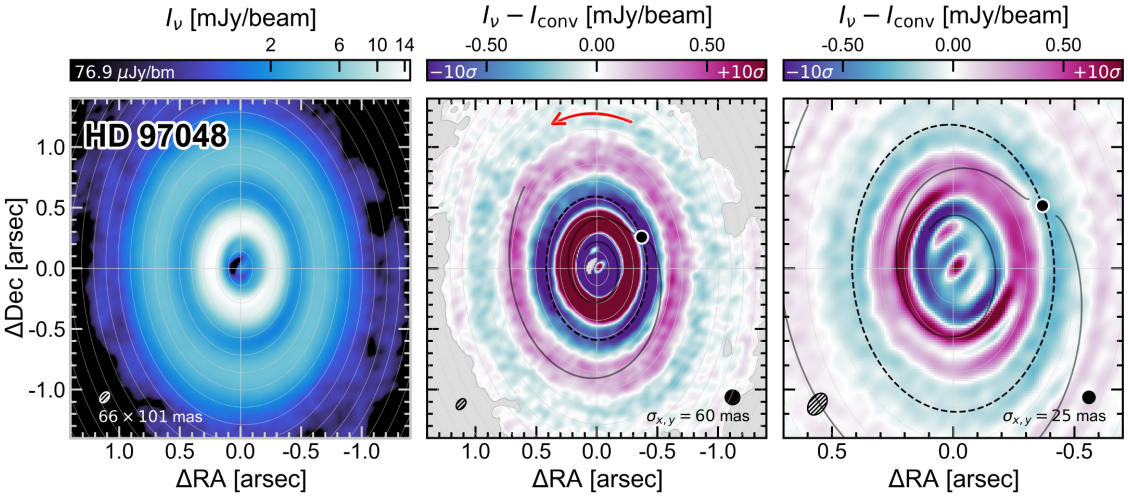

Figure 3.D.6: **Additional searches for the predicted dust spirals:** HD 97048. Unsharp masking residuals produced with two 2D Gaussian kernels of different sizes to highlight substructure in the outer ring (**2nd panel**) and inner ring (**3rd panel**).

Chapter 4

Gravitational instability in a planet-forming disk

J. Speedie, R. Dong, C. Hall, C. Longarini, T. Paneque-Carreño,
B. Veronesi, G. Lodato, Y. Tang, R. Teague and J. Hashimoto

Nature, 633, 8028 (2024)

Summary

The canonical theory for planet formation in circumstellar disks proposes that planets are grown from initially much smaller seeds (Chiang & Youdin, 2010; Johansen & Lambrechts, 2017; Ormel, 2017; Liu & Ji, 2020; Drążkowska et al., 2023). The long-considered alternative theory proposes that giant protoplanets can be formed directly from collapsing fragments of vast spiral arms (Boss, 1997; Gammie, 2001; Rice et al., 2003; Zhu et al., 2012a; Deng et al., 2021; Cadman et al., 2021) induced by gravitational instability (GI; Lodato & Rice, 2004; Cossins et al., 2009; Dipierro et al., 2014) – *if* the disk is gravitationally unstable. For this to be possible, the disk must be massive compared to the central star: a disk-to-star mass ratio of 1/10 is widely held as the rough threshold for triggering GI, inciting significant non-Keplerian dynamics and generating prominent spiral arms (Kratter & Lodato, 2016b; Dong et al., 2015; Hall et al., 2016, 2019). While estimating disk masses has historically been challenging (Paneque-Carreño et al., 2021b; Veronesi et al., 2021; Stapper et al., 2023), the motion of the gas can reveal the presence of GI through its effect on the disk velocity structure (Hall et al., 2020; Longarini et al., 2021a; Terry et al., 2022). Here we present kinematic evidence of gravitational instability in the disk around AB Aurigae, using deep observations of ^{13}CO and C^{18}O line emission with the Atacama Large Millimeter/submillimeter Array (ALMA). The observed kinematic signals strongly resemble predictions from simulations and analytic modeling. From quantitative comparisons, we infer a disk mass of up to 1/3 the stellar mass enclosed within 1″ to 5″ on the sky.

4.1 Main Text

We targeted the disk around AB Aurigae (AB Aur), a 2.5 – 4.4 Myr old (van den Ancker et al., 1997; DeWarf et al., 2003; Beck & Bary, 2019; Garufi et al., 2024) Herbig Ae (Rodríguez et al., 2014) star of intermediate mass ($M_\star = 2.4\,M_\odot$; DeWarf et al., 2003; Beck & Bary, 2019; Guzmán-Díaz et al., 2021) at a distance of 155.9 ± 0.9 pc (Gaia Collaboration et al., 2023). AB Aur is at a relatively late stage of protostellar evolution, classified as a Class II Young Stellar Object (YSO; Henning et al., 1998; Bouwman et al., 2000). To probe the velocity structure of the disk, we obtained deep ALMA Band 6 observations of molecular emission lines ^{13}CO ($J = 2 - 1$) and C^{18}O ($J = 2 - 1$) with high velocity resolution (channel widths of $v_{\rm chan}$ = 42 m/s and 84 m/s respectively). The observations were taken in two array configurations with baselines ranging 14 to 2,216 m, reaching a total on-source integration time of 5.75 hours. Imaging with a Briggs robust value of 0.5 provided image cubes with a spatial resolution or beam size of $0.237'' \times 0.175''$ (beam position angle, PA = 1.2°) equivalent to 37 × 27 au. We collapse the 3D image cubes into 2D moment maps to expose the velocity-integrated intensity (moment 0), intensity-weighted line-of-sight velocity ($v_{\rm los}$, moment 1) and emission line width (moment 2). This collection is shown in Extended Data Figure 4.D.2.

To reveal the spiral arms in the disk, we apply a high-pass filter (see Methods; Pérez et al., 2016) to the ALMA ^{13}CO moment maps (Figure 4.1.1bcd). In the filtered line-of-sight velocity (moment 1) map, we observe spiral-shaped disturbances in the gas velocity field throughout the disk (Figure 4.1.1b). With the filtered velocity-integrated intensity (moment 0) and line width (moment 2) maps, we visually highlight regions of peak density and temperature (Figure 4.1.1cd). Compression and shock-heating are expected to lead to temperature enhancements (and thus localized line broadening) within GI-induced density spirals in self-regulating disks (Cossins et al., 2009; Longarini et al., 2021a). The VLT/SPHERE H-band scattered light image of AB Aur originally presented in Boccaletti et al. (2020) is shown for comparison (Figure 4.1.1a). Scattered light comes from the disk surface, probing the distribution of (sub-)micron-sized dust usually well-coupled with the gas. Previous simulations have shown that GI-induced density spirals are prominent in scattered light (Dong et al., 2015, 2016b). At least seven spiral structures (S1-S7) have been previously identified in the H-band image (Hashimoto et al., 2011; Boccaletti et al., 2020), though not all occupy the same radial region and some may be branches of adjacent arms (Fukagawa et al., 2004). The disk rotates counter-clockwise (the spiral arms are trailing), and the south side is the near side, tilted toward us (Fukagawa et al., 2004; Lin et al., 2006; Perrin et al., 2009).

To provide a qualitative comparison to the ALMA observations, we run 3D smoothed-particle

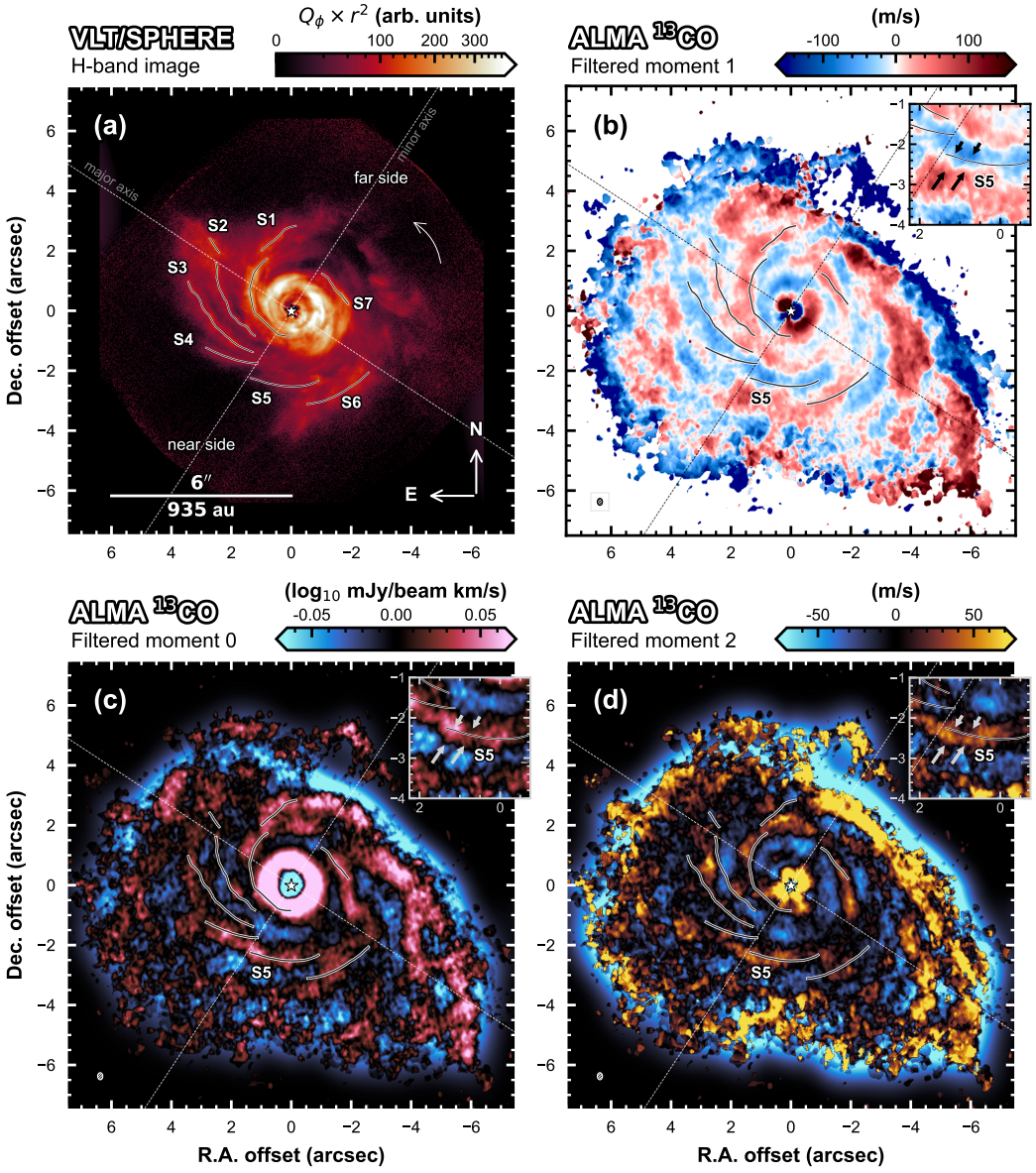

Figure 4.1.1: **Global spirals in the AB Aur disk. (a)** VLT/SPHERE H-band scattered light image of the AB Aur disk (Boccaletti et al., 2020) tracing spiral structure in (sub-)micron-sized dust grains. The labelled spirals S1-S7 are taken from previous works (Fukagawa et al., 2004; Hashimoto et al., 2011). **(b)** Filtered ALMA ^{13}CO intensity-weighted mean velocity (moment 1) map, revealing residual gas motion within the bulk flow. The synthesised beam is shown in the bottom left corner as an ellipse. The inset zooms into the region around where S5 crosses the minor axis, highlighting converging flows on the two sides of S5 indicated by arrows. **(c)** Filtered ALMA ^{13}CO integrated intensity (moment 0) map, highlighting peaks in the gas density and/or temperature. **(d)** Filtered ALMA ^{13}CO emission line width (moment 2) map, showing localized line broadening within the spiral arms. Insets in panels (c,d) zoom into the same region as panel (b) inset, showing enhanced gas density/temperature caused by the radially converging flows around S5.

hydrodynamic (SPH) simulations of a gravitationally unstable disk (see Methods). The simulations were post-processed with radiative transfer and then further processed to have the same viewing angle, sensitivity, spectral and angular resolution as the AB Aur data. To place the disk comfortably within the gravitationally unstable regime ($M_{\rm disk}/M_\star \gtrsim 0.1$), we set the total gas mass to 0.3× the mass of the star. For sustained spiral arms, we set the cooling timescale to 10× the local dynamical timescale ($\beta = 10$). The simulated GI disk shows spiral structures in all three moment maps, resembling those in the AB Aur disk (Extended Data Figures 4.D.2 and 4.F.3). Overall, the AB Aur disk hosts a global architecture of spiral arms at 100 to 1,000 au scales across all azimuths in multi-wavelength observations tracing different disk components and quantities, strongly indicating ongoing gravitational instability.

One characteristic kinematic feature in the AB Aur disk can be found in the isovelocity curve at the systemic velocity $v_{\rm sys}$ in the moment 1 map — Figure 4.1.2a shows a sinusoidal pattern at $v_{\rm los} = v_{\rm sys}$ (along the minor axis; white color), more prominent towards the south. This signature, known as a "minor axis GI wiggle" (Hall et al., 2020), has been predicted in hydrodynamic simulations (Hall et al., 2020; Terry et al., 2022) and analytic theory (Longarini et al., 2021a) as a clear kinematic signature of gravitational instability (Figure 4.1.2bc). It is one of a global set of GI wiggles in isovelocity curves we observe throughout the AB Aur disk (Extended Data Figure 4.G.5). These wiggles are generated by self-gravitating spiral arms, which constitute local minima in the gravitational potential field and induce corresponding oscillations in the gas velocity field. The synthetic moment 1 map of the SPH GI disk simulation shows a minor axis GI wiggle with similar morphology as the observed one (Figure 4.1.2c), completely distinct from the linear pattern found in a disk undergoing Keplerian rotation with no radial motions (Figure 4.1.2bc insets).

Among all GI wiggles, the minor axis GI wiggle has been known and targeted in past studies for its convenience in quantitative analysis (Longarini et al., 2021a; Terry et al., 2022). Due to projection effects, only the radial and vertical components of the disk velocity field (v_r or v_z) contribute to $v_{\rm los}$ at the systemic velocity traced by this wiggle. In the case of GI-induced velocity perturbations, the v_r contribution is expected to dominate (Hall et al., 2020). As we show with 2D analytic calculations of gravitationally unstable disks (see Methods), a self-gravitating spiral arm induces radial motion convergent on itself, appearing as a wiggle in the moment 1 map at $v_{\rm sys}$ where the spiral crosses the minor axis (c.f. Extended Data Figure 4.G.4). The filtered moment 1 map in Figure 4.1.1b displays red- and blue-shift patterns corresponding to convergent flows toward spiral S5 (visible in both scattered light and ^{13}CO moment 0 and 2; Figure 4.1.1acd), supporting the interpretation that the GI wiggle along the southern minor axis in Figure 4.1.2a is generated by a self-gravitating spiral arm.

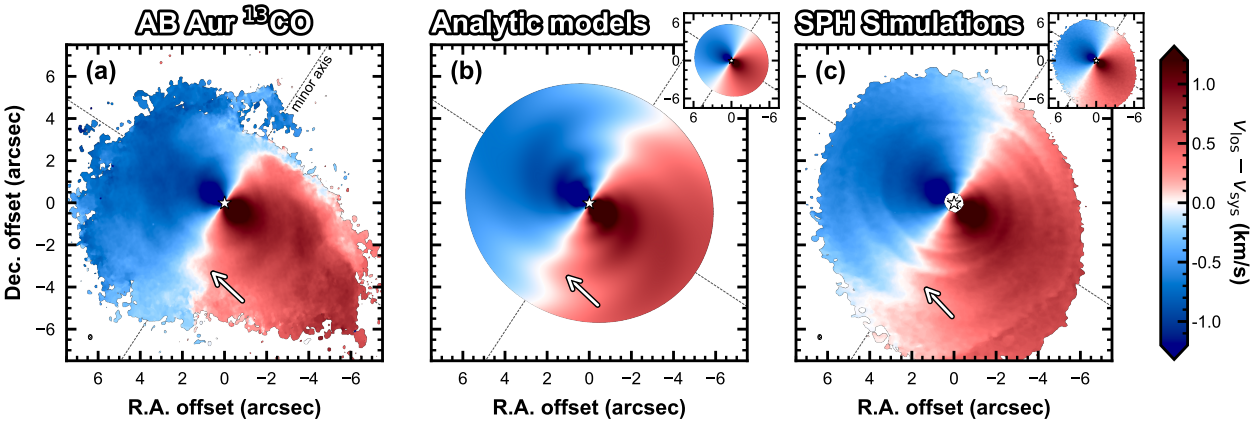

Figure 4.1.2: **Detection of the GI wiggle in the AB Aur disk. (a)** ALMA ^{13}CO intensity-weighted mean velocity (moment 1) map showing line-of-sight velocity ($v_{\rm los}$) of gas in the AB Aur disk. The observations display the "GI wiggle" along the minor axis (arrow) predicted by Hall et al. (2020) as a clear kinematic signature of gravitational instability. **(b)** $v_{\rm los}$ map of a gravitationally unstable disk at the inclination and position angle of the AB Aur disk, computed with 2D analytic modeling (Longarini et al., 2021a). Self-gravitating spiral arms crossing the minor axis induce radial motion that appears as a wiggle (arrow). **(c)** Synthetic ALMA ^{13}CO moment 1 map of the 3D SPH GI disk simulation, revealing the same GI wiggle signature (arrow). The insets in panels (b) and (c) show corresponding images for Keplerian disks with no radial gas motion, where the isovelocity curve at the systematic velocity appears as a straight line along the minor axis.

Having identified evidence of gravitational instability in disk kinematics and in the detections of spirals across multiple tracers and moment maps, we now quantitatively analyze the GI wiggle along the southern minor axis to constrain the disk mass. We extract the ^{13}CO and C^{18}O emission spectra along the southern disk minor axis (Figure 4.1.3ab) and detect the wiggle in position-velocity space (hereafter referred to as the "PV wiggle"), which is a different view of the position-position wiggle in Figure 4.1.2a. Slicing the 3D image cubes this way more comprehensively exposes the gas velocity structure and enables us to quantify the perturbation in units of velocity. We measure the emission line centers by performing a quadratic fit to the spectrum in each spatial pixel of the image cube (Teague & Foreman-Mackey, 2018a). This method achieves sub-spectral resolution precision on the line center and yields statistically meaningful and robust uncertainties (Teague, 2019c). We find remarkably similar sinusoidal morphology between the PV wiggles in ^{13}CO and C^{18}O emission (Figure 4.1.4a).

Theoretical studies have shown that the dynamical response of a disk to its own self-gravity is sensitive to the disk-to-star mass ratio and the cooling rate (Longarini et al., 2021a; Terry et al., 2022). Specifically, the amplitude of the induced radial velocity perturbations is proportional to $(M_{\rm disk}/M_\star)^2$ and $\beta^{-1/2}$ (Eqns. 4.E.11 & 4.J.18 in Methods). This allows us to use the observed minor axis PV wiggle to infer the disk mass once we make assumptions on the disk cooling rates.

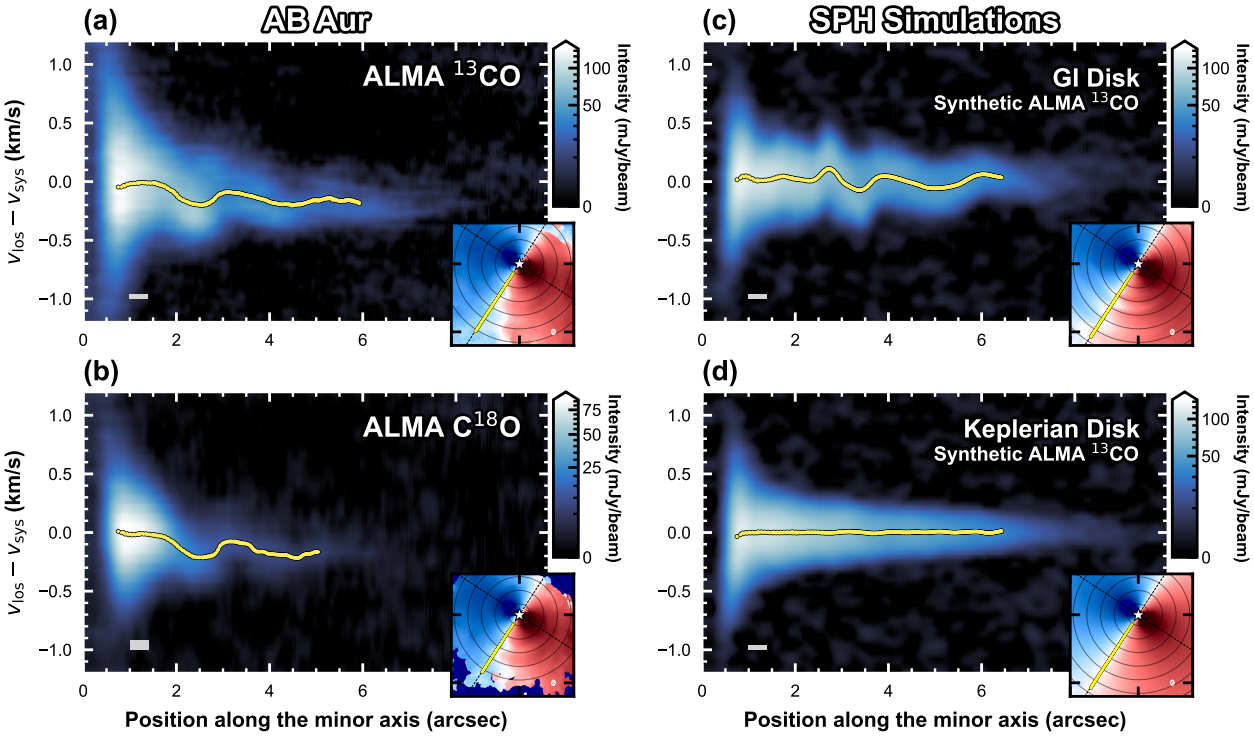

Figure 4.1.3: **The GI wiggle in position-velocity space, or PV wiggle.** Emission spectra (intensity as a function of velocity) extracted along the southern minor axis of the disk, plotted with distance from the star. The line centers are shown as yellow points. The insets at the bottom right of each panel show the corresponding line center map, with black circles delineating 1″ radial increments. The yellow line along the southern minor axis is the narrow (0.5°-wide) wedge-shaped mask within which the spectra and line centers are extracted. In all PV diagram panels, the grey box in the bottom left corner has horizontal width equal to the beam major axis and vertical height equal to the channel width. **(a)** ALMA observations of the AB Aur disk in ^{13}CO and **(b)** in C^{18}O. **(c,d)** Synthetic ALMA ^{13}CO observations generated from 3D SPH simulations of a gravitationally unstable disk with a disk-to-star mass ratio of 0.3 and a cooling rate described by $\beta = 10$. In **(d)**, the simulated disk has its velocity structure artificially post-processed to be Keplerian.

Following Longarini et al. (2021a), we employ a statistical metric to quantify the 'magnitude' of the minor axis PV wiggle, defined as the standard deviation of the line center velocities over a radial range. Bounded by the inner central cavity and outer edge of recovered C^{18}O emission, our radial range spans 1″ to 5″ (155 to 780 au). We find a magnitude of 37.4 ± 2.9 m/s for the southern minor axis PV wiggle in ^{13}CO and 44.2 ± 1.3 m/s in C^{18}O (Figure 4.1.4b). For comparison, the gravitationally unstable disk in the SPH simulation has a southern minor axis PV wiggle in ^{13}CO emission with quantitatively similar amplitude and sinusoidal morphology (Figure 4.1.3c), and a magnitude of 39.1 ± 1.8 m/s (Extended Data Figure 4.I.8a).

Quantifying the minor axis PV wiggle magnitude as above, we perform comparisons against analytic models to identify the combinations of disk mass ($M_{\rm disk}/M_\star$) and cooling timescale (β)

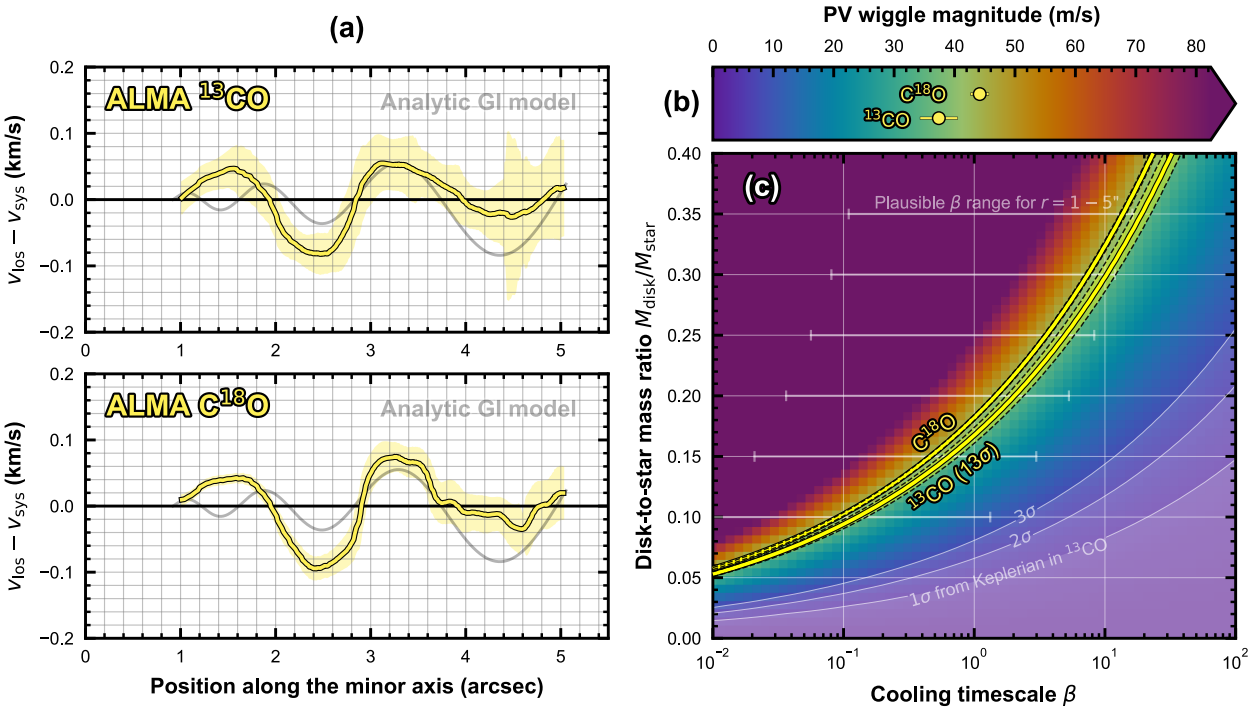

Figure 4.1.4: **PV wiggle mophology, magnitude, and constraints on the AB Aur disk mass.** **(a)** The ALMA ^{13}CO and C^{18}O line centers along the southern minor axis from Figure 4.1.3ab, after quadratic detrending (Methods). Uncertainties on the line centers are shown by yellow shaded regions. For qualitative comparison, the minor axis PV wiggle of the analytic GI model disk from Figure 4.1.2b is shown in the background in light grey. **(b)** The magnitude of the southern minor axis PV wiggle in AB Aur is measured to be 37.4 ± 2.9 m/s in ^{13}CO and 44.2 ± 1.3 m/s in C^{18}O. **(c)** A map of the minor axis PV wiggle magnitude of 3600 analytic GI model disks, calculated for a 60×60 grid of disk-to-star mass ratios and cooling timescales. Each cell in the map represents the minor axis PV wiggle magnitude from a different model. A yellow contour is drawn at each of the AB Aur ^{13}CO and C^{18}O measured magnitude values, and dashed lines represent the quoted uncertainties. White shaded regions denote 1σ, 2σ and 3σ departures from a Keplerian signal in ^{13}CO (c.f. Fig. 4.1.3d). White horizontal bars indicate independently derived β ranges at a selection of $M_{\rm disk}/M_\star$ values (Methods).

that satisfy the AB Aur observations. A proof of concept of this technique with the SPH simulation is shown in Extended Data Figure 4.I.8b. Using the analytic modeling code `giggle`[25] of Longarini et al. (2021a) (Methods), we calculate the minor axis PV wiggle magnitude in gravitationally unstable disk models for 60×60 combinations of $M_{\rm disk}/M_\star$ and β, letting each vary within the ranges $0.0 \leq M_{\rm disk}/M_\star \leq 0.4$ and $10^{-2} \leq \beta \leq 10^2$. A demonstrative analytic curve for the minor axis PV wiggle from the same model shown in Figure 4.1.2b is underlaid in Figure 4.1.4a for qualitative comparison. Figure 4.1.4c shows the resulting map of 60×60 analytic minor axis PV wiggle magnitudes. Overlaying contours in this map at the magnitude val-

[25] http://doi.org/10.5281/zenodo.10205110

ues measured for the AB Aur ^{13}CO and C^{18}O southern minor axis PV wiggles, we find a disk mass in the gravitationally unstable regime with $0.1 \lesssim M_{\rm disk}/M_\star \lesssim 0.3$ for a cooling timescale of $0.1 < \beta < 10$. This result is robust to plausible variations in the analytic model parameter choices (Extended Data Figure Figure 4.J.9). This disk mass range is broadly consistent with the observed spiral morphology — a lower disk mass may result in a large number of more tightly wound spirals than we observe, and vice versa (Lodato & Rice, 2004, 2005). To demonstrate that the implied cooling timescales are compatible with the constrained disk mass values, Figure 4.1.4c also displays ranges of β derived from independent radiative cooling prescriptions (see Methods).

The detection of GI in the disk around AB Aur, a Class II YSO (Henning et al., 1998; Bouwman et al., 2000), demonstrates that gravitational instability can take place during later evolutionary stages. This result, together with previous reports of multiple protoplanet candidates in and amongst spiral arms in the system (Extended Data Figure 4.G.6 Oppenheimer et al., 2008; Tang et al., 2017; Boccaletti et al., 2020; Currie et al., 2022), provides a direct observational connection between gravitational instability and planet formation. Looking forward, the AB Aur system can be an ideal testbed for understanding how planet formation is facilitated by GI-induced spiral arms – whether by fragmentation into gas clumps enabled by rapid cooling, $\beta \lesssim 3$ (Gammie, 2001; Rice et al., 2003; Zhu et al., 2012a; Deng et al., 2021), or by dust collapse of solids concentrated within spiral arms sustained by slow cooling, $\beta \gtrsim 5$ (Rice et al., 2004; Longarini et al., 2023a; Booth & Clarke, 2016; Rowther et al., 2024a).

Methods and Extended Data

4.A Additional information on the source

AB Aur is accreting from the disk at a rate $\dot{M} \sim 10^{-7} M_\odot$ yr^{-1} (Salyk et al., 2013), within the range expected for modest GI-driven accretion ($10^{-7} - 10^{-6} M_\odot$ yr^{-1} Rice & Armitage, 2009). This accretion rate, taken together with the current age $t_0 = 2.5 - 4.4$ Myr (van den Ancker et al., 1997; DeWarf et al., 2003; Beck & Bary, 2019; Garufi et al., 2024), implies a high "latent disk mass": $M_{\rm disk}^{\rm latent} = \dot{M}(t_0) \times t_0 = 0.25 - 0.44 M_\odot$, or $M_{\rm disk}^{\rm latent}/M_{\rm star} \sim 0.1 - 0.2$. $M_{\rm disk}^{\rm latent}$ provides an accretion rate-based assessment of disk mass, assuming a constant stellar accretion rate $\dot{M}$ and we are observing the system mid-way through the disk's lifetime (Hartmann et al., 1998; Dong et al., 2018b). This is a conservative estimate as the accretion rate at earlier epochs is likely higher (Sicilia-Aguilar et al., 2010). In millimeter continuum observations, the disk shows a dust ring at $\sim 1''$ and a cavity inside (Tang et al., 2012), likely caused by the trapping of millimeter-sized dust at a pressure bump. The dust ring is located inside the main spirals in both the scattered light and gas emission. Late infall from above or below the main disk plane (Nakajima & Golimowski, 1995; Grady et al., 1999; Tang et al., 2012; Rivière-Marichalar et al., 2020) is likely encouraging GI by providing a source of mass to maintain a high $M_{\rm disk}/M_\star$ value (Fukagawa et al., 2004; Hall et al., 2019).

4.B ALMA observations

We observed AB Aur with ALMA in April, May and September 2022 under ALMA program ID 2021.1.00690.S (PI: R. Dong). Measurements were taken with the Band 6 receivers (Ediss et al., 2004) in array configurations C-3 (2 execution blocks) and C-6 (6 execution blocks). In total, the 8 execution blocks reached an on-source integration time of 5.75 hours, making this the longest fine-kinematics ($v_{\rm chan} < 100$ m/s) program toward a single protoplanetary disk to date. Extended Data Table 4.B.1 provides details of the observations. We centered one spectral window (SPW) at the ^{13}CO $J = 2 - 1$ molecular emission line transition rest frequency (220.3986 GHz), covering a bandwidth of 58.594 MHz with 1920 channels, resulting in the highest achievable spectral resolution of 41.510 m/s after default spectral averaging with $N = 2$ by Hanning smoothing within the correlator data processor. A second SPW was centered at the C^{18}O $J = 2-1$ rest frequency (219.5603 GHz) covering the same bandwidth with half as many channels (960 channels; due to sharing a baseband with another SPW), achieving a 83.336 m/s spectral resolution. To enable self-calibration, our correlator setup sampled the continuum in another SPW

centered at 233.012 GHz with 128 channels each 15.625 MHz in width, obtaining the full available 2.0 GHz bandwidth. Using the continuum data, all execution blocks were aligned to a common phase center in the *uv*-plane. We performed a series of phase-only self-calibration iterations, and avoided combining by SPW in the first two rounds to remove any potential per-SPW phase offsets. We also carried out one round of amplitude and phase self-calibration. Finally, we applied the phase center realignments and calibration gain tables (that we generated with the continuum data) to the line data. We performed continuum subtraction in the *uv*-plane using the `uvcontsub` task.

Extended Data Table 4.B.1: Details of the ALMA Band 6 observations.

UTC Date	**Time on source** [a] (min)	$N_{\rm ant}$	**Baselines** (m)	**pwv** (mm)	**Calibrators** Bandpass	Flux	Phase
2022-04-19	41	41	14-500	0.74	J0510+1800	J0510+1800	J0438+3004
2022-05-15	32.4	45	15-680	0.69	J0510+1800	J0510+1800	J0438+3004
2022-07-17 [b]	47.4	41	15-2617	0.24	J0510+1800	J0510+1800	J0438+3004
2022-07-19	47.4	42	15-2617	1.49	J0510+1800	J0510+1800	J0438+3004
2022-07-20	34.8	44	15-2617	2.85	J0510+1800	J0510+1800	J0438+3004
2022-07-21	47.4	42	15-2617	2.37	J0510+1800	J0510+1800	J0438+3004
2022-07-22	47.3	44	15-2617	0.84	J0510+1800	J0510+1800	J0438+3004
2022-07-22	47.4	41	15-2617	0.63	J0510+1800	J0510+1800	J0438+3004

[a] Total time on source: 5.75 hours (4.53 hours in C-6 and 1.22 hours in C-3).

[b] This execution block was used as the reference for phase alignment during post-processing.

All imaging was performed with the CASA `tclean` task. We used the multiscale deconvolution algorithm (Cornwell, 2008) with Gaussian deconvolution scales [0.02″, 0.1″, 0.3″, 0.6″, 1.0″]. We did not image with a Keplerian mask so as not to restrict our ability to observe non-Keplerian emission. After experimentation with CASA's auto-multithresh masking algorithm (Kepley et al., 2020), we adopted an imaging strategy similar to PHANGS-ALMA (Leroy et al., 2021), in which we clean conservatively, with a broad mask (`usemask='pb'` and `pbmask=0.2`), forcing frequent major cycles[26]. To achieve frequent major cycles we set the maximum number of minor cycle iterations per channel to `cycleniter=80`, the minor cycle threshold to `max_psf_sidelobe_lev` and `minpsffraction=0.5`, and the maximum assigned clean component to `gain=0.02` times the peak residual. We adopted a Briggs robust weighting scheme, and generated two sets of image cubes; one with a robust value of 0.5 and a second with robust 1.5. The corresponding beam sizes for ^{13}CO are 237 × 175 mas, 1.2° for robust 0.5 and 390 × 274 mas, −1.4° for robust 1.5. We imaged with a FOV out to the primary beam FWHM (38″) with 0.02″ pixels (9 or 12

[26]The ^{13}CO robust 0.5 cube underwent 198 major cycles and the C^{18}O cube underwent 76.

pixels per synthesized beam minor or major axis, respectively). We imaged in LSRK velocity channels at 42 m/s for ^{13}CO and 84 m/s for C^{18}O respectively (nearly native channel spacing). The `CLEAN` threshold was set to 5× the rms noise measured in 20 line-free channels of the dirty image cube. We applied JvM correction (Jorsater & van Moorsel, 1995; Czekala et al., 2021) and primary beam correction. The rms noise in the resulting ^{13}CO cubes imaged with robust 0.5 and robust 1.5 is 2.0 mJy/beam and 1.2 mJy/beam respectively, and 0.6 mJy/beam in the C^{18}O cube imaged with robust 1.5.

We used the robust 0.5 image cubes for our position-position analysis (moment maps; Figures 4.1.1 & 4.1.2) and the robust 1.5 cubes for our position-velocity analysis (PV diagrams and line centers; Figures 4.1.3 & 4.1.4). We made the moment 0, 1 and 2 maps using the `bettermoments` (Teague & Foreman-Mackey, 2018b,a) methods `collapse_zeroth`, `collapse_first`, and `collapse_percent` respectively. We note that we calculate our "moment 2" maps as the average of the red- and blue-shifted line widths about the intensity-weighted median line center (i.e., as the average of the `wpdVr` and `wpdVb` maps). Mathematically this is a different approach to find the line width than the classic moment 2 approach, though in our case we find the two yield nearly identical outcomes. We applied sigma-clipping at 5× the rms noise and performed no spectral smoothing.

4.C Geometric properties

We used the Python package `eddy` (Teague, 2019a) to infer geometric properties of the disk, namely to constrain the disk center x_0, y_0, the disk inclination i, the position angle PA, the systemic velocity $v_{\rm sys}$, and the dynamical stellar mass $M_\star$. We performed an MCMC to fit the C^{18}O moment 1 map (Extended Data Figure 4.C.1) with a geometrically thin Keplerian disk rotation profile:

$$v_0 = \sqrt{\frac{G\,M_\star}{r}} \cdot \sin i \cdot \cos\phi + v_{\rm sys}\,, \tag{4.C.1}$$

where r is the disk radius, ϕ is the azimuthal angle around the disk, and G is the gravitational constant. Following convention, we fix the inclination to the value found from fitting the continuum, $i = 23.2°$ (Tang et al., 2012, 2017), and the distance to 155.9 pc (Gaia DR3; Gaia Collaboration et al., 2016b, 2023). We assumed flat priors for all values and spatially downsampled the rotation map to the beam FWHM prior to the likelihood calculation so that only spatially independent pixels were considered. The calculation of the posterior distributions was run with 128 walkers and an initial burn-in period of 10,000 steps before the posterior distributions were sampled for additional 10,000 steps. The resulting posterior distributions were $x_0 = -5 \pm 7$ mas,

$y_0 = -17 \pm 7$ mas, PA $= 236.7 \pm 0.3°$, $M_\star = 2.23 \pm 0.02\,M_\odot$, and $v_{\rm sys} = 5858 \pm 5$ m/s, where we report the uncertainties represented by the 16th and 84th percentiles about the median value. The latter three values are consistent with constraints from previous observations (Beck & Bary, 2019; Tang et al., 2017; Piétu et al., 2005; DeWarf et al., 2003; Tang et al., 2012).

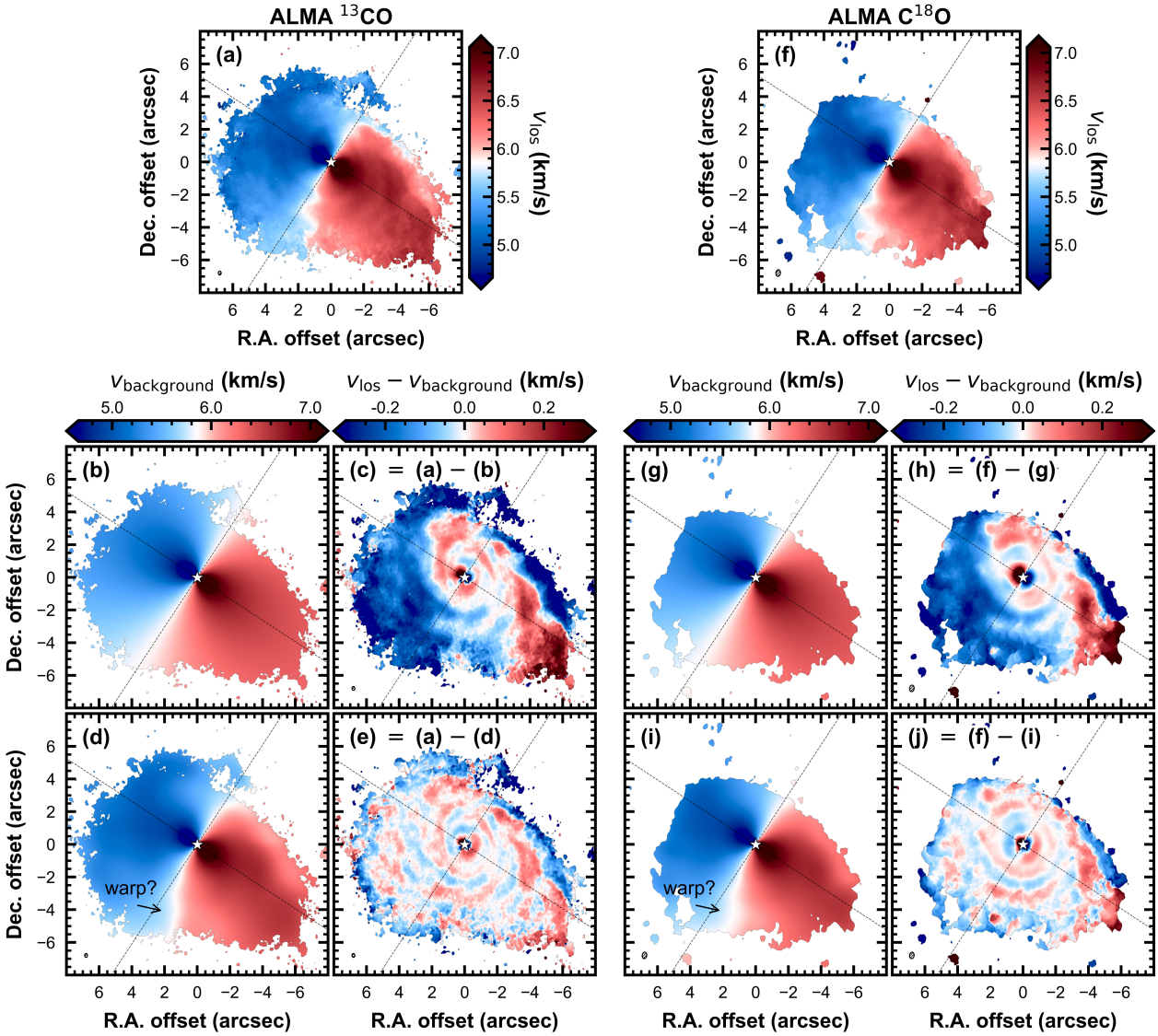

Extended Data Figure 4.C.1: **Obtaining velocity residuals in the AB Aur disk.** **(a)** ALMA ^{13}CO moment 1 map, imaged with robust 0.5, as shown in Figure 4.1.2a. **(b)** Background model made with a Keplerian rotation profile, assuming a geometrically thin axisymmetric disk (Eqn. 4.C.1). **(c)** Velocity residuals after subtracting the model in panel (b). Global spiral substructure is visible, but unevenly so. The model does not capture the non-axisymmetric emission surface morphology and/or super-Keplerian rotation. **(d)** Background model made with the expanding kernel filter (Eqn. 4.F.15). **(e)** Velocity residuals after subtracting the model in panel (d), as shown in Figure 4.1.1b. **(f-j)** Like (a-e) but with the ALMA C^{18}O moment 1 map, imaged with robust 1.5.

4.D Hydrodynamic simulations and synthetic ALMA observations

We performed 3D global smoothed-particle hydrodynamic (SPH) simulations with the PHANTOM code (Price et al., 2018) using 1 million SPH particles. We assumed a central star mass of $2.4\,M_\odot$ (DeWarf et al., 2003; Beck & Bary, 2019), represented by a sink particle (Bate et al., 1995) with accretion radius set to 60 au. The initial inner and outer disk radii were set to $r_{\rm in,SPH} = 80$ au and $r_{\rm out,SPH} = 500$ au, respectively. We set the initial gas mass to $0.7\,M_\odot$, corresponding to $M_{\rm disk}/M_\star = 0.29$. The surface density profile follows $\Sigma \propto r^{-p}$ (where the power-law index $p = 1.0$), and the sound speed profile follows $c_{\rm s} \propto r^{-q}$ (where $q = 0.25$). The initial disk aspect ratio was set to $H/r = 0.05$ at 80 au. We set $\alpha_{\rm SPH}$ such that $\alpha_{\rm min} \leq \alpha_{\rm SPH} \leq \alpha_{\rm max}$, with $\alpha_{\rm min} = 0.001$ and $\alpha_{\rm max} = 1.0$, with the value of $\alpha_{\rm SPH}$ set by the Cullen & Dehnen (2010) switch that increases viscosity only in the case of converging flows. This results in a Shakura-Sunyaev viscosity of $\alpha_{\rm SS} \approx 0.01$ throughout the disk.

We assumed an adiabatic equation of state, with heating from compressional $P\,{\rm d}V$ work and shock heating. The disk cools by Gammie cooling (a.k.a. β-cooling; Gammie, 2001) where the cooling timescale is proportional to the local dynamical time by the factor β, such that $t_{\rm cool}(r) = \beta\,\Omega^{-1}(r)$, where $\Omega(r) = (G\,M_\star/r^3)^{1/2}$ is the Keplerian frequency. We set $\beta = 10$, a typical value used or found in simulations (Hall et al., 2020; Terry et al., 2022; Longarini et al., 2021a; Paneque-Carreño et al., 2021b). We let the simulation evolve for five orbital periods of the outermost particle, at which point the disk settles into a state in which the Toomre Q parameter is between 1 and 2 from $r_{\rm in,SPH}$ to $1.1\,r_{\rm out,SPH}$.

We computed the disk thermal structure and ^{13}CO ($J = 2-1$) model line cubes using the Monte Carlo radiative transfer code MCFOST (Pinte et al., 2006, 2009). We assumed the ^{13}CO molecule is in local thermodynamic equilibrium (LTE) with its surroundings and that the dust is in thermal equilibrium with the gas ($T_{\rm gas} = T_{\rm dust}$). We set the $^{13}{\rm CO}/{\rm H_2}$ abundance to 7×10^{-7} (**?**Hall et al., 2020) and we used $\approx 10^7$ photon packets to calculate $T_{\rm dust}$. Voronoi tesselation was performed on 990,972 SPH particles which corresponded to 99% of the mass in the simulation. We set the total dust mass to 1% of the total SPH gas mass and used a dust grain population with 50 logarithmic bins ranging in size from $0.1\,\mu$m to 3.0 mm. The dust optical properties are computed using Mie theory. The central star was represented as a sphere of radius $2.5\,R_\odot$ radiating isotropically at an effective temperature $T_{\rm eff} = 9770$ K, set to match AB Aur (Li et al., 2016; Hillenbrand et al., 1992; Natta et al., 2001; Currie et al., 2022). The disk was given an inclination of 23.2°, a position angle of 236.7° (where PA is measured east of north to the red-shifted major axis), and placed at a distance of 155.9 pc, all consistent with the AB Aur system.

We used the same PHANTOM simulation to create both the GI and Keplerian model line cubes shown in Figure 4.1.2c and 4.1.3. We created the Keplerian counterpart with MCFOST, using the flags `-no_vr` and `-no_vz` to force the radial and vertical velocities to be zero, and `-vphi_Kep` to force the azimuthal velocities to be Keplerian. Both ^{13}CO model line cubes were generated with MCFOST, binned at the observed spectral resolution of 42 m/s, and gridded in the image plane to have 2048×2048 pixels of size $0.02''$. We assumed a turbulent velocity of 0.05 km/s.

We generated synthetic ALMA image cubes from the ^{13}CO model line cubes using `syndisk`[27] to match the properties of the observed AB Aur ^{13}CO image cubes (robust 0.5 and 1.5). In the latter case the model line cube was convolved with a beam of size $0.390'' \times 0.274''$ and PA $-1.4°$. Correlated noise was added with an rms of 1.2 mJy/beam. The model data were then smoothed with a Hanning spectral response function with a resolution of 42 m/s. Effects associated with interferometric or spatial filtering are not captured by this process, and our synthetic ALMA image cubes are effectively fully-sampled in the uv-plane. The synthetic cubes were collapsed into moment maps following the same procedure as the AB Aur data (Extended Data Figure 4.D.2).

4.E Analytic modeling

We analytically compute the velocity fields of gravitationally unstable disks using the `giggle`[28] package developed by Longarini et al. (2021a). Working in 2D polar coordinates (r, ϕ), `giggle` considers a geometrically thin disk with surface density profile $\Sigma_0 \propto r^{-p}$ and inclination i, centered on a star of mass $M_\star$. It computes the projected line-of-sight velocity field as

$$v_{\rm los} = (v_r \sin\phi + v_\phi \cos\phi) \sin i + v_{\rm sys}\,, \tag{4.E.2}$$

where v_r and v_ϕ are the radial and azimuthal components of the disk velocity field. The basic state of the disk (i.e., considering only the gravitational potential contribution from the central star) is assumed to be Keplerian: $v_r = 0$ and $v_\phi = v_{\rm Kep}$. The scheme of the model is to determine the perturbations in v_r and v_ϕ generated by gravitational instability by taking into account the additional gravitational contribution from the disk, which is initialized as marginally unstable and imprinted with global spiral density perturbations. The model computes the velocity field under the assumption that the disc is self-regulated. This state is imposed by assuming a balance between heating (by compression and shocks within the spiral arms) and cooling (by

[27] https://github.com/richteague/syndisk
[28] http://doi.org/10.5281/zenodo.10205110

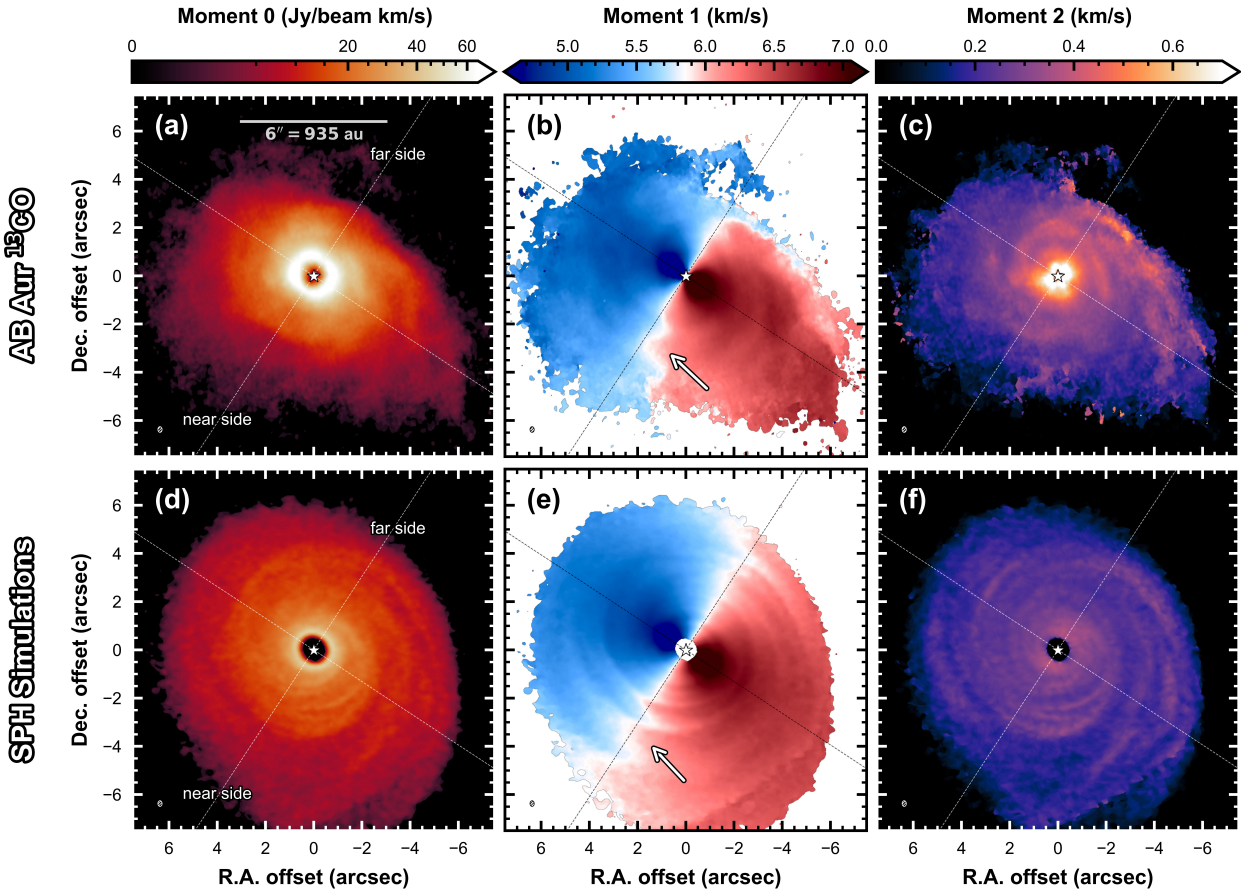

Extended Data Figure 4.D.2: **Moment maps: AB Aur observations and GI disk simulations. (a-c)** Integrated intensity (moment 0), intensity-weighted mean velocity (moment 1), and intensity-weighted line width (moment 2) maps for the ALMA ^{13}CO observations toward AB Aur. Panel (b) appears in the main text as Figure 4.1.2a. **(d-f)** Moment 0, 1, and 2 maps for the synthetic ALMA ^{13}CO observations of the SPH GI disk simulation. Like the AB Aur observations, the simulated GI disk displays a prominent GI wiggle along the southern minor axis (indicated by white arrows).

radiative processes). As such, the amplitude of the spiral density perturbations $A_{\Sigma_{\rm spir}}/\Sigma_0$ saturated to a finite value proportional to the cooling timescale β (Lodato, 2008; Cossins et al., 2009):

$$\frac{A_{\Sigma_{\rm spir}}}{\Sigma_0} = \chi \beta^{-1/2}, \tag{4.E.3}$$

where the proportionality factor χ is of order unity (Longarini et al., 2021a; Cossins et al., 2009). The imprinted spiral density perturbation is assumed to be small relative to the background surface density, so that all the relevant quantities (density Σ, gravitational potential Φ, velocities

v_r and v_ϕ, and enthalpy h) can be written as a linear sum of the basic state and the perturbation:

$$X(r,\phi) = X_0(r) + X_{\rm spir}(r,\phi)\,. \tag{4.E.4}$$

The spiral perturbation in density is given the form

$$\Sigma_{\rm spir}(r,\phi) = \Re\big[A_{\Sigma_{\rm spir}}\, e^{j(m\phi+\psi(r))}\big]\,, \tag{4.E.5}$$

where $j=\sqrt{-1}$ (as we are using i to represent the disk inclination), and m is the azimuthal wavenumber. The "shape function" $\psi(r)$ is described by m and the spiral pitch angle $\alpha_{\rm pitch}$ as:

$$\psi(r) = \frac{m}{\tan\alpha_{\rm pitch}}\log r\,, \tag{4.E.6}$$

which is related to the radial wavenumber k by $d\psi/dr = k$. The spiral density perturbation necessarily introduces a corresponding perturbation to the gravitational potential:

$$\Phi_{\rm spir}(r,\phi) = -\frac{2\pi G}{|k|}\,\Sigma_{\rm spir}(r,\phi)\,. \tag{4.E.7}$$

The negative proportionality $\Phi_{\rm spir} \propto -\Sigma_{\rm spir}$ is the definition of self-gravitating spiral arms. As a result, corresponding perturbations in the azimuthal and radial velocities are driven:

$$v_r(r,\phi) = \Re\big[A_{v_r}(r)\cdot e^{j(m\phi+\psi(r))}\big]\,, \tag{4.E.8}$$

$$v_\phi(r,\phi) = \Re\big[A_{v_\phi}(r)\cdot e^{j(m\phi+\psi(r))}\big] + r\Omega\,, \tag{4.E.9}$$

where we note $r\Omega \neq v_{\rm Kep}$ because the angular frequency Ω includes super-Keplerian rotation from the disk mass contribution:

$$\Omega^2 = \frac{GM_\star}{r^3} + \frac{1}{r}\frac{\partial\Phi_{\rm disk}}{\partial r}\,. \tag{4.E.10}$$

By assuming the disk is marginally unstable, and by maintaining the self-regulated state condition, the amplitude of the radial and azimuthal velocity perturbations $A_{v_r}(r)$ and $A_{v_\phi}(r)$ are determined (Longarini et al., 2021a):

$$A_{v_r}(r) = 2jm\chi\beta^{-1/2}\Big(\frac{M_{\rm disk}(r)}{M_\star}\Big)^2 v_{\rm Kep}(r)\,, \tag{4.E.11}$$

$$A_{v_\phi}(r) = -\frac{1}{2}j\chi\beta^{-1/2}\Big(\frac{M_{\rm disk}(r)}{M_\star}\Big) v_{\rm Kep}(r)\,, \tag{4.E.12}$$

where $M_{\rm disk}(r)$ is the disk mass enclosed within radius r. With a surface density profile $\Sigma_0(r) \propto r^{-p}$, then $M_{\rm disk}(r) \propto r^{-p+2}$, and the amplitude of the radial perturbation is described by $A_{v_r}(r) \propto r^{-2p+7/2}$. For $p < 7/4$, $A_{v_r}(r)$ is an increasing function of radius. The factor of imaginary number j in Eqn. 4.E.11 has important physical consequences: when the real component of $A_{v_r}(r)$ is taken (Eqn. 4.E.8), the radial velocity perturbation is $\pi/2$ out of phase with the spiral density perturbation (Eqn. 4.E.5), and convergent at the locations where $\Sigma_{\rm spir}$ takes a maximum. Explicitly,

$$v_r(r,\phi)\Big|_{\phi=\pi/2} \propto -\sin\left(m\frac{\pi}{2}+\psi(r)\right), \tag{4.E.13}$$

$$\Sigma_{\rm spir}(r,\phi)\Big|_{\phi=\pi/2} \propto \cos\left(m\frac{\pi}{2}+\psi(r)\right). \tag{4.E.14}$$

For qualitative visual comparison with the AB Aur moment 1 map in Figure 4.1.2a, we compute the projected line-of-sight velocity field of a gravitationally unstable disk with $\beta = 10$ and $M_{\rm disk}/M_\star = 0.3$ in Figure 4.1.2b. We set $m = 3$ and $\alpha_{\rm pitch} = 15°$ to approximately match the ^{13}CO spirals in the AB Aur disk (Figure 4.1.1), and assume $p = 1.0$ and $\chi = 1.0$ (Cossins et al., 2009). The dominant azimuthal wavenumber is expected to be inversely related to the disk-to-star mass ratio q, roughly obeying $m \sim 1/q$ (Lodato & Rice, 2004; Cossins et al., 2009; Dong et al., 2015), so our choice of $m = 3$ is consistent with $M_{\rm disk}/M_\star \approx 0.3$.

4.F Revealing global spiral structure

We obtain the residual moment maps shown in Figure 4.1.1 using a variation on the conventional high-pass filtering (a.k.a. unsharp masking) technique. The conventional method is to convolve the image with a Gaussian kernel and subtract the blurred image from the original. It is a common technique to increase the visual contrast of variations in an image and has been used successfully to reveal spiral structure disks (e.g., Boccaletti et al., 2020; Rosotti et al., 2020b; Pérez et al., 2016; Meru et al., 2017; Zhang et al., 2023; Norfolk et al., 2022b; Garufi et al., 2024). Here, we perform the convolution with a radially expanding kernel[29] – that is, with a Gaussian kernel whose FWHM, w, increases with radial distance from the image center (i.e., with disk radius) with a simple power-law dependence:

$$w(r) = w_0 \cdot (r/r_0)^\gamma, \tag{4.F.15}$$

[29] https://github.com/jjspeedie/expanding_kernel

where w_0 is the kernel width at $r_0 = 1''$. A radially expanding kernel provides a way to highlight variations more evenly throughout the disk, given the spatial scales of the variations –which are expected to track with the local scale height and increase with radius– and the dynamical range of the variations, which fall with radius. After experimentation we adopt $w_0 = 0.3''$ and $\gamma = 0.25$, though we emphasize this is a qualitative choice and the key spiral features, such as their locations, are robust against a variety of choices in kernel parameters. The high-pass filter technique is also flexible to the disk emission surface morphology, and can capture global scale deviations from Keplerian rotation in the background disk. Extended Data Figure 4.C.1 compares the residual moment 1 maps in ^{13}CO and C^{18}O obtained after subtracting the axisymmetric geometrically thin Keplerian model (Eqn. 4.C.1) vs. after subtracting a blurred version of the moment 1 map made with the expanding kernel filter. The Keplerian residuals (panels c and h) show signs of global scale deviation from Keplerian: the east (west) side is generally blueshifted (red-shifted), hinting at super-Keplerian rotation, signatures of disk mass contributing to the total mass of the system. While spiral structure is indeed also visible in the Keplerian residuals, the expanding kernel residuals (panels e and j) reveal the underlying spiral structure in a spatially even manner, indicating that the expanding kernel background model (panels d and i) more successfully captures the quasi-local background disk velocity. We note that this background model is non-axisymmetric; it displays excess blueshifted velocity in the southeast quadrant of the disk such that the contour of $v_{\rm los} = v_{\rm sys}$ diverges westward from the minor axis south of the star, possibly indicative of a global disk warp. This is what necessitates a detrending of the line centers to isolate the sinusoidal component of the southern minor axis PV wiggle in Figure 4.1.4a (see section "Measuring the magnitude of AB Aur's minor axis PV wiggle"). Filtered moment maps for the synthetic ALMA observations of the simulated SPH GI disk are shown in Extended Data Figure 4.F.3.

4.G Global kinematics of self-gravitating spiral arms

Radially convergent motion (as in Figure 4.1.1bcd insets) serves as a kinematic signature for the location of self-gravitating spiral arms at disk azimuths where the radial velocity perturbation contributes sufficiently strongly to the observed velocity field, and thus cannot be a fully unambiguous locator at disk azimuths away from the minor axis. Extended Data Figure 4.G.4c and g provide maps of velocity residuals from Keplerian for the 2D analytic GI disk model and the SPH GI disk simulation. The convergent motion toward the spiral spines is visible for a range of azimuths around the minor axis, but becomes progressively less clear moving toward the major axis as the azimuthal velocity –super-Keplerian rotation– contributes progressively more to

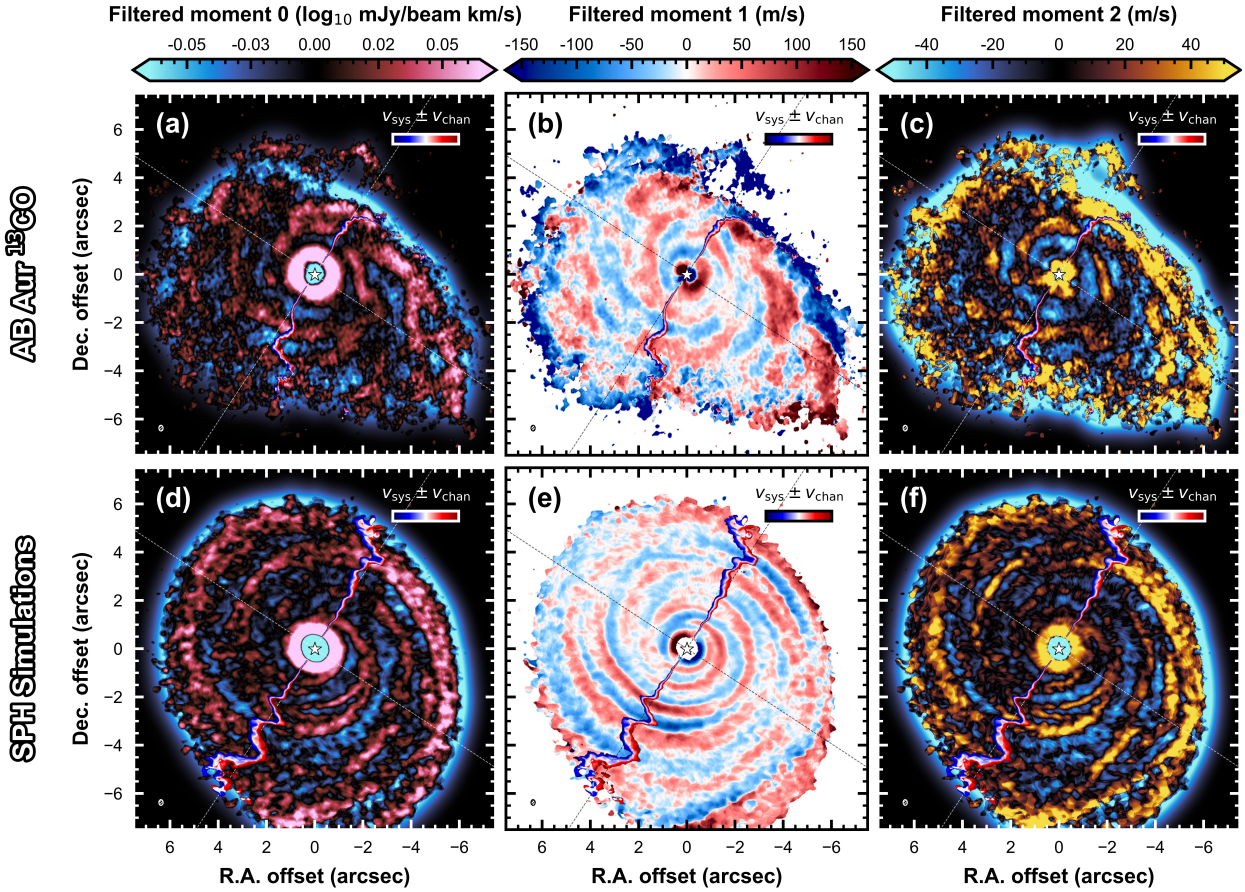

Extended Data Figure 4.F.3: **Filtered moment maps: AB Aur observations and GI disk simulations.** Expanding kernel filter residuals of the maps shown in Extended Data Figure 4.D.2, highlighting global spirals and velocity disturbances generated by GI. Panels (a-c) appear in the main text as Figure 4.1.1b-d. The minor axis GI wiggle indicated by white arrows in Extended Data Figure 4.D.2b and e is shown here as an isovelocity contour at $v_{\rm los} = v_{\rm sys} \pm v_{\rm chan}$ in all panels.

the line-of-sight. However, high-pass filtering (panel h) captures and removes the background super-Keplerian rotation, leaving a residual map that resembles the isolated radial component (panel d). Extended Data Figure 4.G.4i-l overlays the locations of ^{13}CO spirals in the AB Aur disk (from filtered moment 0/2; Figure 4.1.1cd) onto the filtered moment 1 maps, in order to illustrate where convergent motion does or does not serve as a locator throughout the disk. Ambiguity occurs around the major axis, which is a location of transition in the sign of $v_r \sin i \sin\phi$ (first term of Eqn. 4.E.2), and when two spirals are not well separated and their motions superimpose. Three of the seven spiral structures in VLT/SPHERE scattered light appear to be spatially associable with those in ^{13}CO (S1, S5, S7; panel l inset). Offsets in the southeast quadrant of the disk (S2, S3, S4) may be further indication of a disk warp (Extended Data Figure 4.C.1di), or other non-trivial phenomena (e.g., vertical density and temperature gradients, projection

effects; Ginski et al., 2016).

The kinematic signatures observed in the present ALMA dataset –probing disk scales ~100 to 1,000 au– are recognizably different from what is expected for planet-driven perturbations. Planetary wakes are dampened and become nearly circular as they propagate away from the planet (Goodman & Rafikov, 2001; Rafikov, 2002b; Ogilvie & Lubow, 2002), whereas GI-driven spirals maintain their modest pitch angles with radius and the amplitude of the induced velocity perturbations depends on the enclosed disk mass (Eqns. 4.E.11 & 4.E.12). In the planetary case, the density and radial velocity perturbations are in phase (their peaks spatially coincide), and the pattern of motion within an arm along a radial cross-section is divergent (Bollati et al., 2021; Hilder et al., 2023). Overall, the essential characteristic of GI-induced spirals is that they occur globally (c.f. Figure 4.1.1, Extended Data Figures 4.F.3, 4.G.5 & 4.G.4; Hall et al., 2020; Longarini et al., 2021a). In previous datasets probing smaller spatial scales –within the AB Aur disk's central cavity– planetary candidates P1/f1 (Tang et al., 2017; Boccaletti et al., 2020), P2/b (Tang et al., 2017; Currie et al., 2022; Zhou et al., 2023; Biddle et al., 2024; Currie, 2024), and f2 (Boccaletti et al., 2020) are known to be associated with –or driving– spiral arms, as observed in VLT/SPHERE scattered light and/or ALMA ^{12}CO emission. As shown in Extended Data Figure 4.G.6, due to their small separations ($\lesssim 0.7''$), kinematic signatures from these candidates are inaccessible to our ALMA observations. Clump-like signals 'c' and 'd' seen by HST/STIS (Currie et al., 2022) at wide separations ($\sim 2.75''$ and $\sim 3.72''$ respectively) are in locations tentatively suggestive of constituting spiral arm fragments and may warrant further investigation.

4.H Position-velocity analysis

We use the robust 1.5 image cubes for our position velocity analysis to maximize the recovery of emission at large disk radii. Owing to the clear association with a self-gravitating spiral arm (Figure 4.1.1bcd insets), we target the wiggle on the southern minor axis. A clear spiral arm in moment 0/2 crossing the northern minor axis is also observed, but at the outer edge of the recovered ^{13}CO and C^{18}O emission ($\sim 3''$; c.f. Extended Data Figure 4.G.4kl). We obtain the position-velocity diagrams shown in Figure 4.1.3 using `eddy` (Teague, 2019a) to extract spectra from pixels within a 0.5°-wide wedge-shaped mask oriented 90° clockwise of the red-shifted major axis (shown in Figure 4.1.3 insets). Our quantitative analysis of the minor axis PV wiggles is performed with maps of the line centers made using the quadratic method of `bettermoments` (Teague & Foreman-Mackey, 2018b,a), which fits a quadratic curve to the spectrum in each pixel of the cube:

$$I(v) = a_0 + a_1(v - v_{\rm peak}) + a_2(v - v_{\rm peak})^2\,, \tag{4.H.16}$$

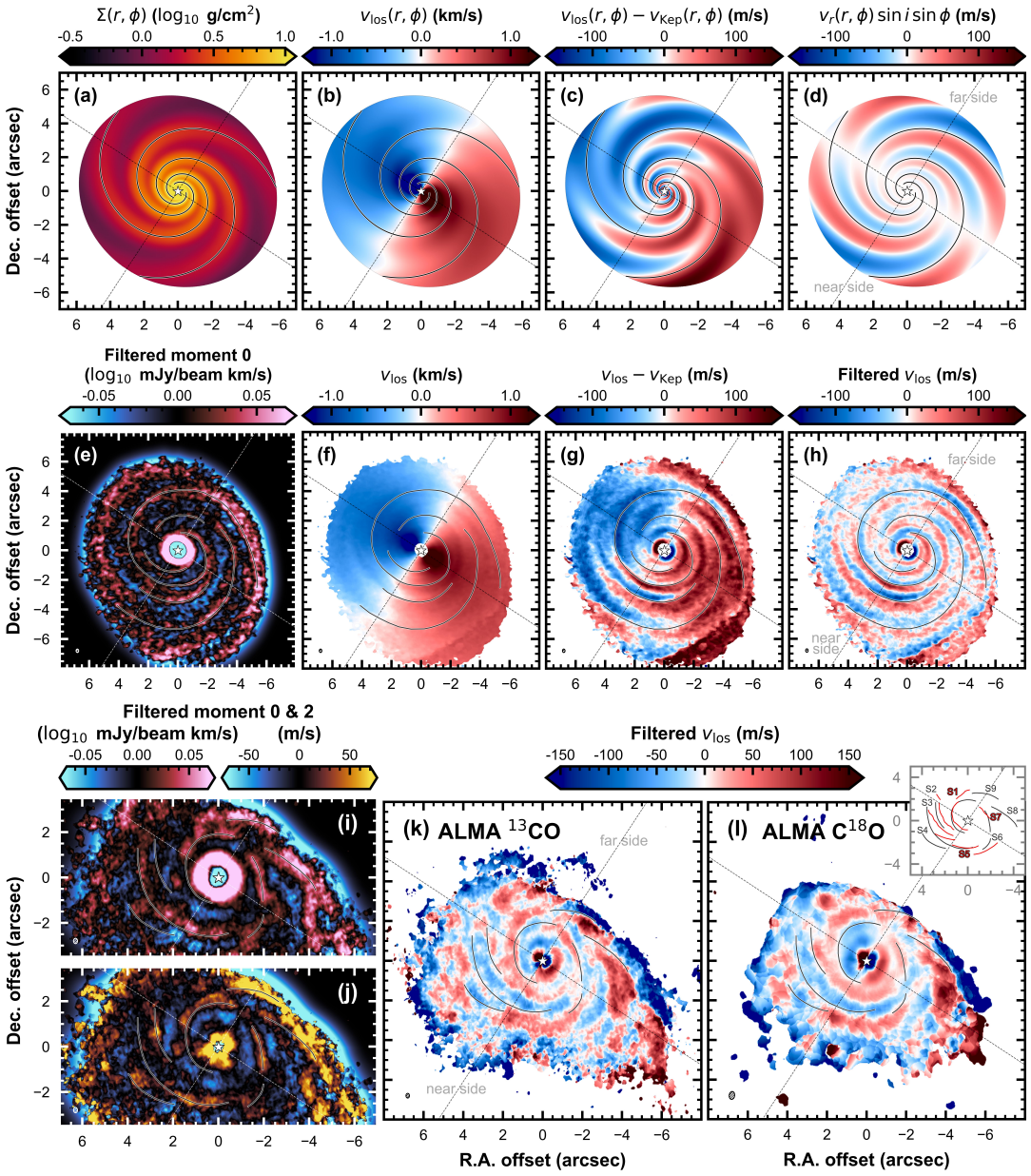

Extended Data Figure 4.G.4: **Kinematics of GI-driven spiral arms.** **(a-d)** 2D analytic modeling (Longarini et al., 2021a). **(e-h)** Synthetic ALMA ^{13}CO observations of the 3D SPH GI disk simulation. **(i-l)** ALMA observations of the AB Aur disk. **(a)** Disk surface density (Eqn. 4.E.4 & 4.E.5). **(b)** Line-of-sight velocity (Eqn. 4.E.2), as in Figure 4.1.2b. **(c)** Velocity residuals from Keplerian (i.e., subtracting Figure 4.1.2b inset). **(d)** Line-of-sight component of the radial velocity (first term of Eqn. 4.E.2). **(e)** Filtered moment 0. **(f)** Moment 1. **(g)** Moment 1 residuals from Keplerian. **(h)** Filtered moment 1. **(i)** ALMA ^{13}CO filtered moment 0. **(j)** ALMA ^{13}CO filtered moment 2. **(k)** ALMA ^{13}CO filtered moment 1. **(l)** ALMA C^{18}O filtered moment 1 (robust 1.5). Panel (l) inset overlays the VLT/SPHERE H-band scattered light spirals S1-S7 (Hashimoto et al., 2011; Fukagawa et al., 2004) in red, and ^{13}CO spirals S1-S9 we identify in black.

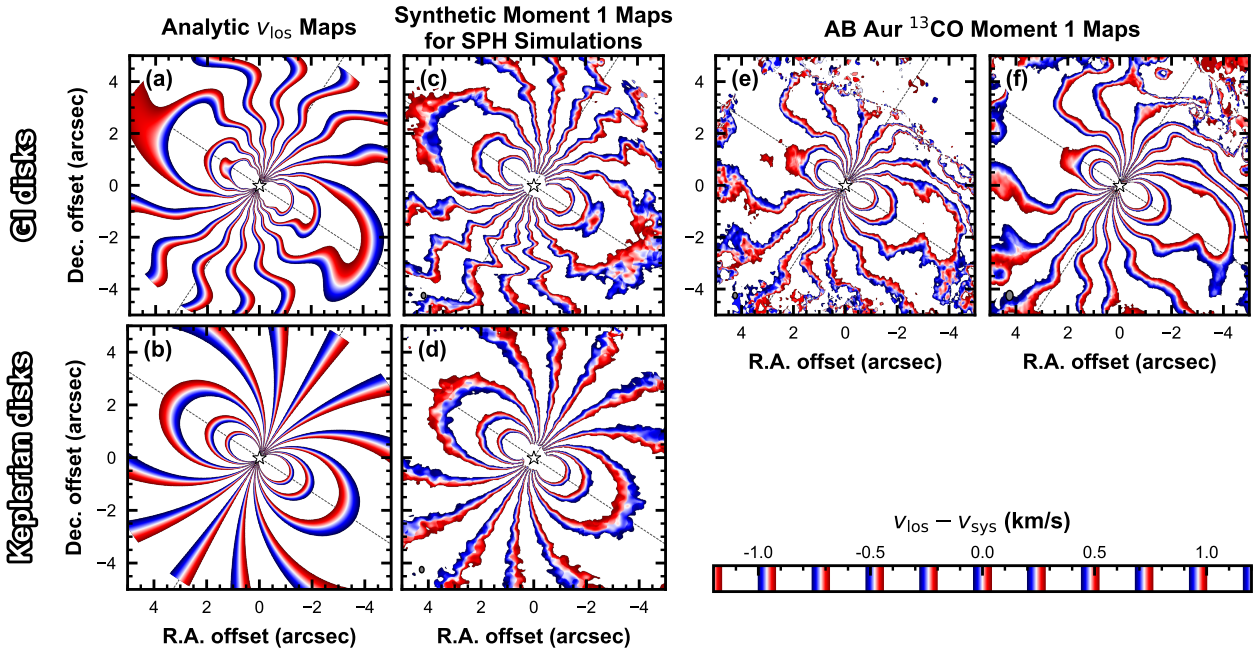

Extended Data Figure 4.G.5: **Global GI wiggles in analytic models, SPH simulations, and the AB Aur disk.** Isovelocity contours in line-of-sight velocity maps at the velocity values indicated by the colour bar. **(a)** $v_{\rm los}$ map of the 2D analytic GI disk model (shown in Figure 4.1.2b). **(b)** $v_{\rm los}$ map of the 2D analytic Keplerian disk model (shown in Figure 4.1.2b inset). **(c)** Synthetic ALMA ^{13}CO moment 1 map for the 3D SPH GI disk simulation (shown in Figure 4.1.2c). **(d)** Synthetic ALMA ^{13}CO moment 1 map for the 3D SPH Keplerian disk simulation (shown in Figure 4.1.2c inset). **(e)** Observed ALMA ^{13}CO moment 1 map for the AB Aur disk, imaged with robust 0.5 (shown in Figure 4.1.2a). **(f)** Like (e), but imaged with robust 1.5.

where $v_{\rm peak}$ is the channel of peak intensity in the spectrum. We select this approach over the traditional intensity-weighted mean velocity (moment 1) method specifically for its ability to provide well characterized, statistically meaningful uncertainties on the line center, $\sigma_{v\rm los}$ (Teague & Foreman-Mackey, 2018a). The statistical uncertainty on each line center is computed as:

$$\sigma_{v\rm los} = \sqrt{\frac{\sigma_I^2}{8}\left(\frac{3}{{a_2}^2} + \frac{{a_1}^2}{{a_2}^4}\right)}, \tag{4.H.17}$$

where σ_I is the rms noise of the intensities (see Teague & Foreman-Mackey, 2018a, for a derivation). The quadratic method also has the advantage of being unaffected by sigma-clipping and of automatically distinguishing the front side of the disk from the back side (Teague & Foreman-Mackey, 2018a). Prior to the quadratic fitting we spectrally smooth the data with a Savitzky-Golay filter of polynomial order 1 and filter window length of 10 channels (420 m/s) in the case of ^{13}CO and 3 channels (252 m/s) in the case of C^{18}O. The former was also applied to the two synthetic ALMA ^{13}CO image cubes generated from the SPH simulations. We extract the values

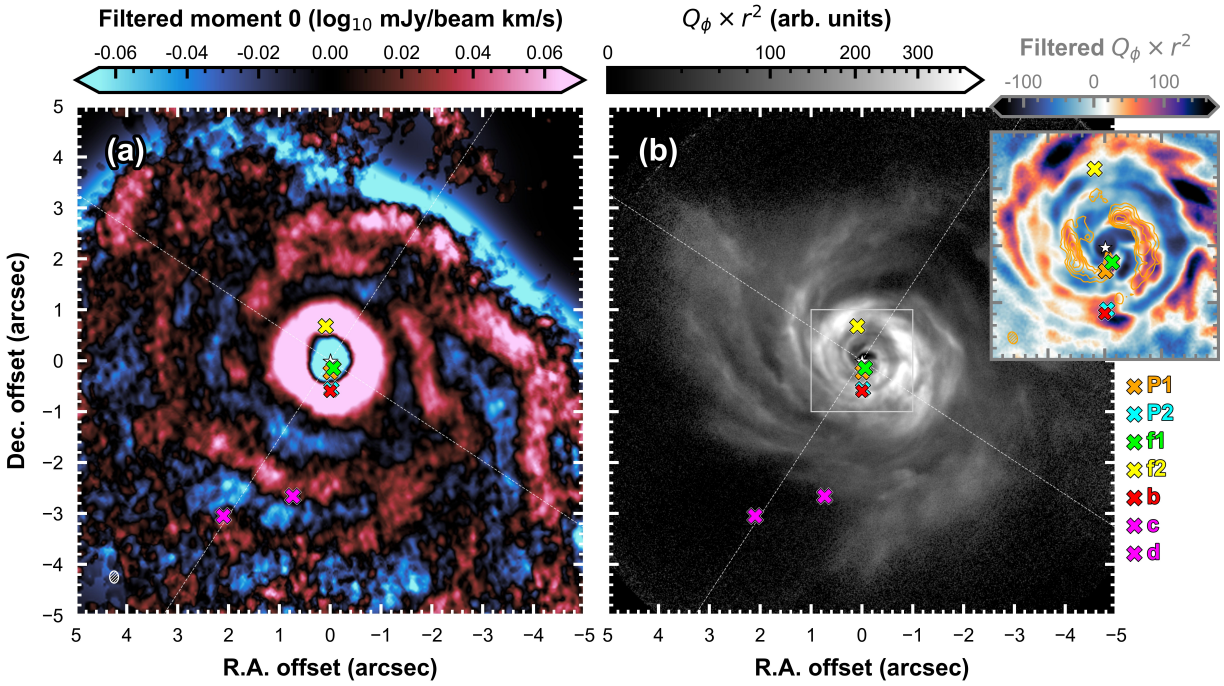

Extended Data Figure 4.G.6: **Candidate sites of planet formation.** Coloured ×'s mark the locations of candidate protoplanets reported in the literature (Tang et al., 2017; Boccaletti et al., 2020; Currie et al., 2022). A table providing the candidates' coordinates on the sky, estimated masses and the reporting references is available as **source data**. **(a)** Filtered ALMA ^{13}CO moment 0 map, as in Figure 4.1.1c. **(b)** VLT/SPHERE H-band scattered light image (Boccaletti et al., 2020), as in Figure 4.1.1a. The inset zooms into the central $2'' \times 2''$ region to show the spiral structures in different tracers at spatial scales unresolved by the present ALMA observations. The H-band scattered light image is shown after high-pass filtering, and orange contours show the two spirals identified in ALMA ^{12}CO $J = 2-1$ moment 0 (Tang et al., 2017) at levels from 25 to 50 mJy/beam km/s in increments of 5 mJy/beam km/s.

from the resulting line center and line uncertainty maps within the same wedge mask described above. The extracted line center values are shown as yellow points in Figure 4.1.3 and the uncertainties are shown as yellow shaded regions in Figure 4.1.4a.

4.I Measuring the magnitude of the minor axis PV wiggle

Following Longarini et al. (2021a), we measure the 'magnitude' of a minor axis PV wiggle as the standard deviation of the line center values over a radial range. Bounded by the inner central cavity and the outer edge of C^{18}O emission, we adopt a radial range of 1.0″ to 5.0″. We estimate the uncertainty on the magnitude measurement using a resampling procedure: we take 10,000 draws from Gaussian distributions centered on the observed line centers with standard deviation $\sigma_{v\mathrm{los}}$ (Eqn. 4.H.17) to create 10,000 instances of the minor axis PV wiggle; we compute

their magnitudes; and then report the uncertainty as the standard deviation of those 10,000 magnitude estimates.

In addition to the wiggle, the ^{13}CO and C^{18}O emission on the southern disk minor axis also exhibit an underlying monotonic blueward trend with disk radius, seen in Figure 4.1.3ab as a subtle downward bend with radius of the line centers, or equivalently in Figure 4.1.2a as a westward or clockwise shift in the contour of $v_{\rm los} = v_{\rm sys}$. We earmark this feature as a possible disk warp (Extended Data Figure 4.C.1di), and adopt a least-squares fitting approach to isolate the sinusoidal component of the PV wiggle. This approach yields the background trendline that minimizes the standard deviation of the residuals, thus providing the most conservative estimate for the magnitude of the detrended PV wiggle. We fit a quadratic trendline (Extended Data Figure 4.I.7a) as it more closely resembles the high-pass filter background curve than a linear one (Extended Data Figure 4.I.7bc). We show the quadratically-detrended PV wiggles in Figure 4.1.4a and report their magnitudes in Figure 4.1.4b. We find very similar magnitudes for both the ^{13}CO and C^{18}O wiggles, despite C^{18}O likely tracing lower optical depths in the AB Aur disk. This empirically substantiates comparisons with the 2D analytic model (next section).

Performing the same procedure outlined above on the synthetic ^{13}CO minor axis PV wiggle of the GI disk in the SPH simulation, we find a wiggle magnitude of 39.1 ± 1.9 m/s (Extended Data Figure 4.I.8).

4.J Constraining disk mass with quantitative comparisons to analytic models

We perform quantitative comparisons between the observed ^{13}CO and C^{18}O minor axis PV wiggles and the projected radial velocity component in our analytic model, $v_r \sin i$ (Longarini et al., 2021a). From Eqns. 4.E.8 and 4.E.11, the projected radial velocity on the minor axis ($\phi = \pi/2$) is:

$$v_r(r,\phi)\Big|_{\phi=\pi/2} \cdot \sin i = -2m\chi\beta^{-1/2}\left(\frac{M_{\rm disk}(r)}{M_\star}\right)^2 v_{\rm Kep}(r)\,\sin\left(m\frac{\pi}{2} + \psi(r)\right)\cdot \sin i\,. \tag{4.J.18}$$

This curve reflects the disk mass enclosed within the inner and outer radii of the model, which we set to span the same projected radial range as the observed PV wiggles (1″ to 5″). We compute 3600 of these curves for a 60×60 grid of models with (total enclosed) $M_{\rm disk}/M_\star$ linearly spaced $\in [0.0, 0.4]$ and β logarithmically spaced $\in [10^{-2}, 10^2]$. Again we set $m = 3$ and $\alpha_{\rm pitch} = 15°$ to match the AB Aur disk, and assume $p = 1.0$ and $\chi = 1.0$ (Cossins et al., 2009). For qualitative comparison, we plot an example analytic minor axis PV wiggle behind the data in Figure 4.1.4a;

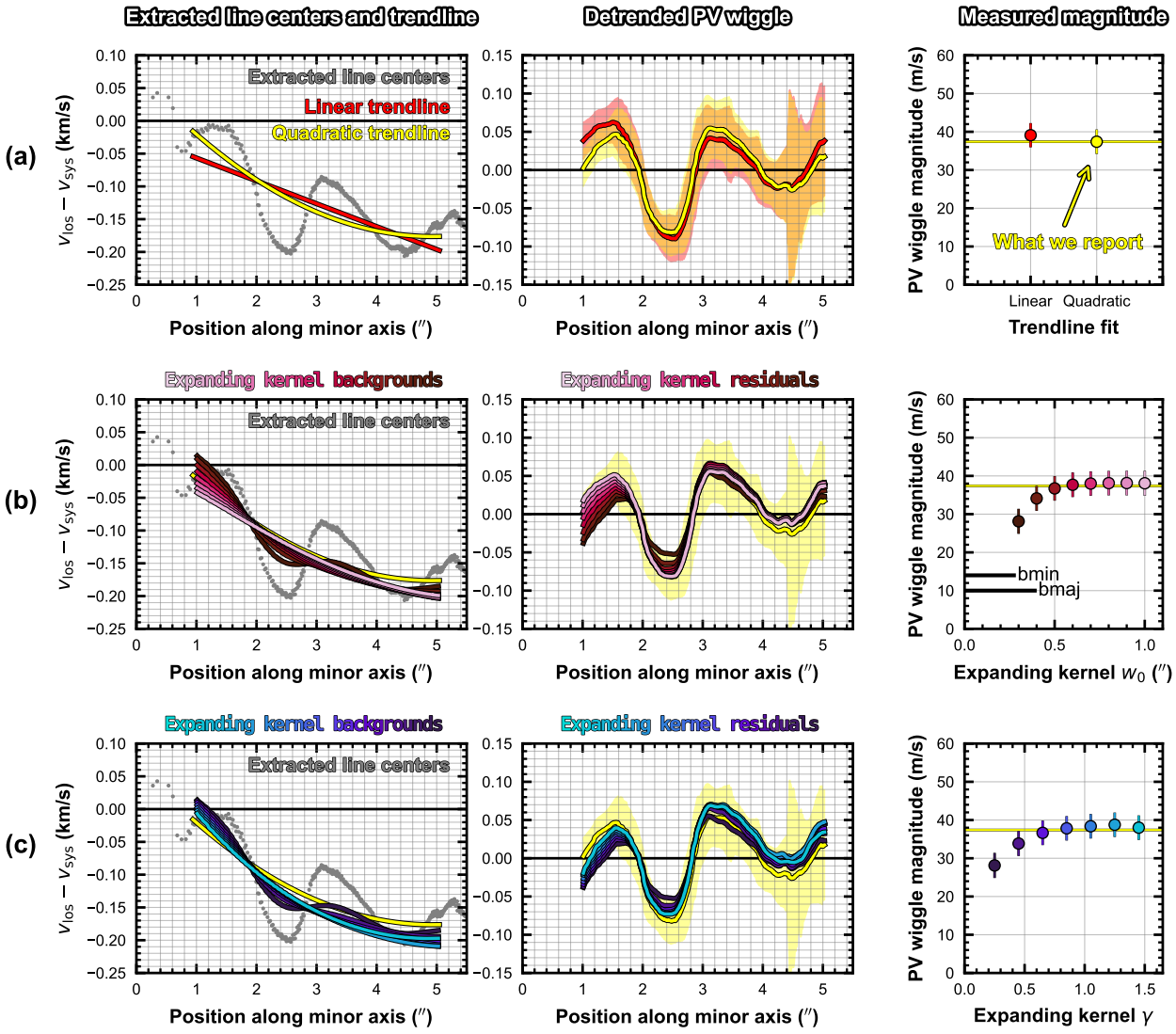

Extended Data Figure 4.I.7: **Methods for isolating the sinusoidal component of the southern minor axis PV wiggle in the AB Aur disk. (a)** Detrending the ALMA ^{13}CO line centers from Figure 4.1.3a with linear and quadratic trendlines found by a least-squares fit. **(b)** Detrending with the expanding kernel high-pass filter, varying the kernel width parameter w_0 and keeping the kernel radial power-law index fixed to $\gamma = 0.25$ (Equation 4.F.15). We find the background trendlines by extracting the velocity values from the high-pass filter background map (e.g. Extended Data Figure 4.C.1d) within the same 0.5°-wide wedge-shaped mask as we do for the line centers, positioned along the southern disk minor axis. **(c)** Like (b), but varying γ and keeping w_0 fixed to $w_0 = 0.30''$. The high-pass filter detrending approach converges to the same measured PV wiggle magnitude as the quadratic fit approach.

the model has $\beta = 10$ and $M_{\rm disk}/M_\star = 0.3$. We show in Extended Data Figure Figure 4.J.9 that $m = 3$ reproduces the observed wiggles better than other choices, and that $p = 1.5$ could also provide a satisfying match, while $p = 2.0$ is too steep. Since the wiggle amplitude is indepen-

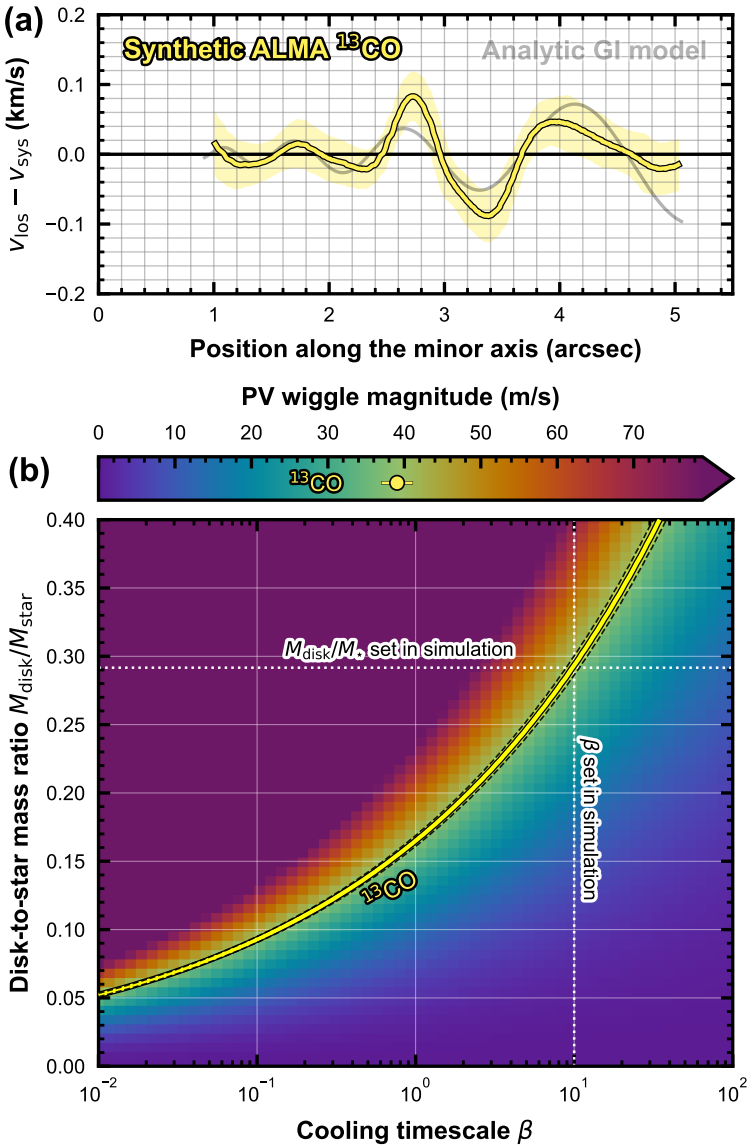

Extended Data Figure 4.I.8: **PV wiggle morphology, magnitude, and disk mass recovery in the SPH GI disk simulation.** Like Figure 4.1.4, but for the synthetic ALMA observations of the SPH GI disk simulation. **(a)** The synthetic ALMA ^{13}CO line centers along the southern minor axis from Figure 4.1.3c, after quadratic detrending. Uncertainties on the line centers are shown by yellow shaded regions. The magnitude of this PV wiggle is measured to be 39.1 ± 1.9 m/s. The analytic model shown in the background for qualitative comparison has the same parameters as the underlying SPH simulation ($M_{\rm disk}/M_\star = 0.29$ and $\beta = 10$) and its PV wiggle magnitude is 39.0 m/s. **(b)** As in Figure 4.1.4c, a map of the minor axis PV wiggle magnitude of 60×60 analytic models on a grid of disk-to-star mass ratios and cooling timescales. A contour is drawn at the measured magnitude of the synthetic ^{13}CO PV wiggle in panel (a), and dashed lines represent the quoted uncertainties. The technique successfully recovers the disk mass set in the SPH simulation.

dent of $\alpha_{\rm pitch}$ (Eqn. 4.E.11), the magnitude is constant with $\alpha_{\rm pitch}$ when sampled over the same range in phase (not shown).

We measure the minor axis PV wiggle magnitude of the 3600 models and present the resulting magnitude map in Figure 4.1.4c. By drawing contours in the Figure 4.1.4c map at the magnitude values measured for AB Aur (37.4 ± 2.9 m/s in ^{13}CO and 44.2 ± 1.3 m/s in C^{18}O), we find every combination of $M_{\rm disk}/M_\star$ and β that satisfy the observations. Repeating this procedure with our synthetic ALMA observations of the SPH GI disk simulation shown in Figure 4.1.3c, we find that this technique successfully recovers the disk mass set in the underlying SPH simulation (Extended Data Figure 4.I.8).

For independent physical estimates of plausible β values between $1''$ to $5''$ (155 to 780 au), we rely on radiative cooling prescriptions (Zhu et al., 2015; Zhang & Zhu, 2020). From Equation 39 of Zhang & Zhu (2020), β is a function of r and depends on $M_{\rm disk}$ through the surface density Σ. We assume $T = (\frac{\phi L_\star}{8\pi r^2 \sigma_{SB}})^{1/4}$, where σ_{SB} is the Stefan-Boltzmann constant, $L_\star = 59\,L_\odot$ is the stellar luminosity of AB Aur (Currie et al., 2022), and $\phi = 0.02$ represents the flaring angle (Dullemond et al., 2018). We use the DSHARP Rosseland mean opacity (Birnstiel et al., 2018b) $\kappa_{\rm R} = \kappa_{\rm R}(T, a_{\rm max})$ for a power-law grain size distribution truncated at $a_{\rm max}$. We set $a_{\rm max}$ to 0.1 mm and the dust-to-gas mass ratio to $f = 0.1\%$, based on radial drift arguments and lack of (sub-)mm emission at these large radii. We compute a $\beta(r)$ profile for each $M_{\rm disk}/M_\star \in [0.0, 0.4]$ and extract the values at $1''$ and $5''$. We overlay the resulting $\beta(M_{\rm disk}/M_\star)$ ranges as white shaded regions in Extended Data Figure 4.J.9 (where the dependence on p arises from the dependence on Σ), and in Figure 4.1.4 as white horizontal bars at a selection of $M_{\rm disk}/M_\star$ values. For example, for $M_{\rm disk}/M_\star = 0.2$ and $p = 1.0$, we find $\beta(1'') = 5.3$ and $\beta(5'') = 3.6 \times 10^{-2}$. While knowledge of cooling in disks is very limited, these estimates help to emphasize that not all values of β are equally likely.

Acknowledgements We thank our referees for their careful and insightful comments that improved the manuscript. We thank Kaitlin Kratter for enlightening discussions and valuable suggestions. J.S. thanks Ryan Loomis, Sarah Wood and Tristan Ashton at the North American ALMA Science Center (NAASC) for providing science support and technical guidance on the ALMA data as part of a Data Reduction Visit to the NAASC, which was funded by the NAASC. The reduction and imaging of the ALMA data was performed on NAASC computing facilities. J.S. thanks Christophe Pinte, Daniel Price and Josh Calcino for support with MCFOST, Luke Keyte and Francesco Zagaria for discussions on self-calibrating ALMA data, and Chris White for sharing perceptually uniform colormaps. J.S. acknowledges financial support from the Natural

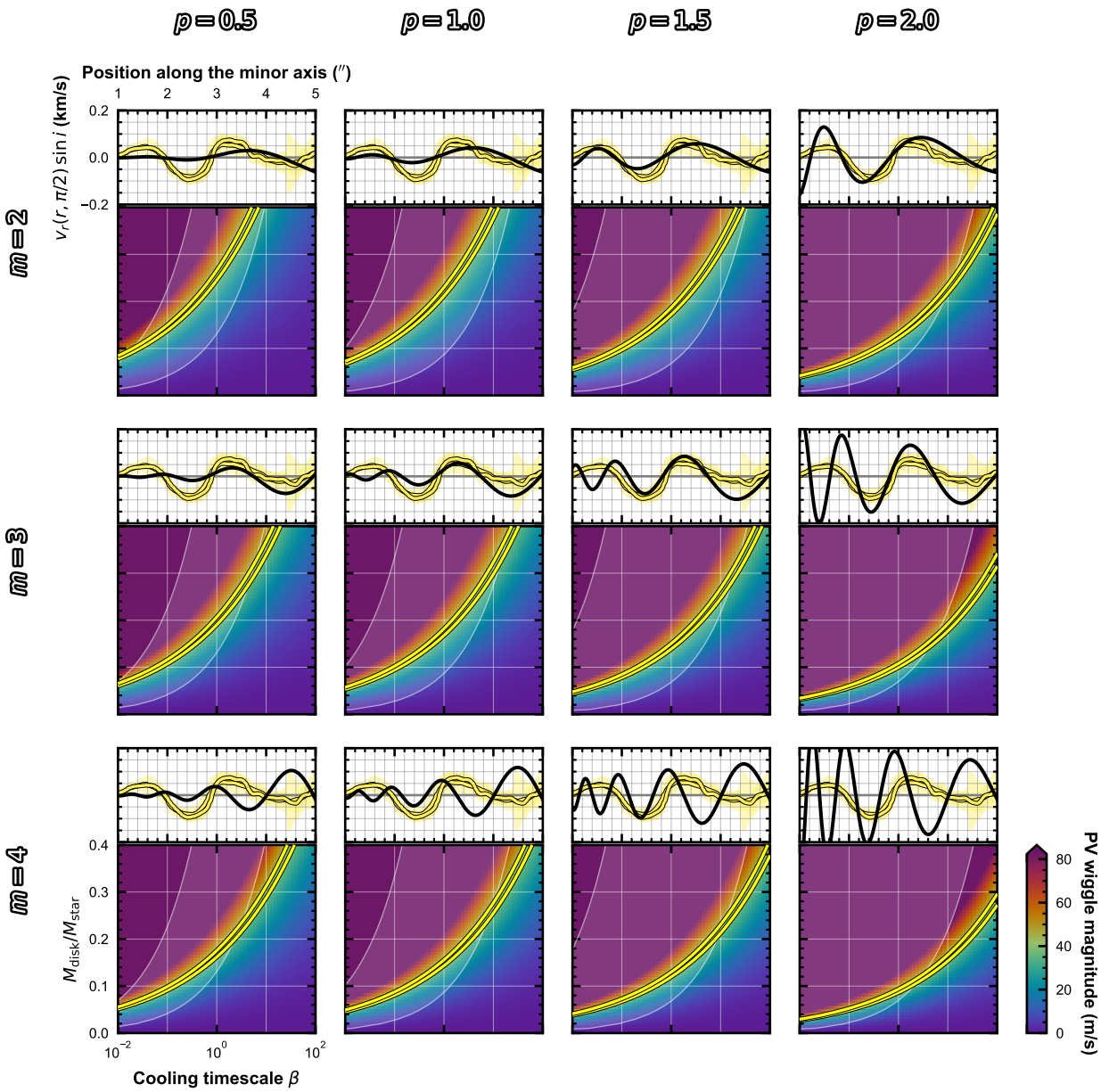

Extended Data Figure 4.J.9: **Comparisons to additional sets of analytic models.** Like Figure 4.1.4, but varying the azimuthal wavenumber m and surface density power-law index p in the comparison grid of analytic GI model disks. Each upper subpanel shows the quadratically detrended ^{13}CO and C^{18}O line centers (yellow) behind a demonstrative analytic PV wiggle (black) computed with the combination of m and p indicated by the row and column labels (keeping $M_{\rm disk}/M_\star = 0.3$ and $\beta = 10$ fixed). Each lower subpanel shows the corresponding map of PV wiggle magnitude computed for a 60×60 grid of analytic models in $M_{\rm disk}/M_\star$ and β, again with the combination of m and p indicated by the row and column labels. The two yellow contours are drawn at the magnitude values measured for the observed AB Aur ^{13}CO and C^{18}O southern minor axis PV wiggles. The white shaded region between two white curves represents plausible β ranges from $r = 1-5''$. The combination shown in Figure 4.1.4c is $m = 3$, $p = 1.0$.

Sciences and Engineering Research Council of Canada (NSERC) through the Canada Graduate Scholarships Doctoral (CGS D) program. R.D. acknowledges financial support provided by the Natural Sciences and Engineering Research Council of Canada through a Discovery Grant, as well as the Alfred P. Sloan Foundation through a Sloan Research Fellowship. C.L. and G.L. acknowledge funding from the European Union's Horizon 2020 research and innovation programme under the Marie Sklodowska-Curie grant agreement # 823823 (RISE DUSTBUSTERS project). C.L. acknowledges funding from UK Science and Technology research Council (STFC) via the consolidated grant ST/W000997/1. B.V. acknowledges funding from the ERC CoG project PODCAST No 864965. Y.W.T. acknowledges support through NSTC grant 111-2112-M-001-064- and 112-2112-M-001-066-. J.H. was supported by JSPS KAKENHI Grant Numbers 21H00059, 22H01274, 23K03463. This paper makes use of the following ALMA data: ADS/JAO.ALMA#2021.1.00690.S. ALMA is a partnership of ESO (representing its member states), NSF (USA) and NINS (Japan), together with NRC (Canada), MOST and ASIAA (Taiwan), and KASI (Republic of Korea), in cooperation with the Republic of Chile. The Joint ALMA Observatory is operated by ESO, AUI/NRAO and NAOJ. The National Radio Astronomy Observatory is a facility of the National Science Foundation operated under cooperative agreement by Associated Universities, Inc. This work has made use of data from the European Space Agency (ESA) mission *Gaia* (https://www.cosmos.esa.int/gaia), processed by the *Gaia* Data Processing and Analysis Consortium (DPAC, https://www.cosmos.esa.int/web/gaia/dpac/consortium). Funding for the DPAC has been provided by national institutions, in particular the institutions participating in the *Gaia* Multilateral Agreement. Based on data products created from observations collected at the European Organisation for Astronomical Research in the Southern Hemisphere under ESO programme 0104.C-0157(B). This work has made use of the SPHERE Data Centre, jointly operated by OSUG/IPAG (Grenoble), PYTHEAS/LAM/CESAM (Marseille), OCA/Lagrange (Nice), Observatoire de Paris/LESIA (Paris), and Observatoire de Lyon. This research used the Canadian Advanced Network For Astronomy Research (CANFAR) operated in partnership by the Canadian Astronomy Data Centre and The Digital Research Alliance of Canada with support from the National Research Council of Canada the Canadian Space Agency, CANARIE and the Canadian Foundation for Innovation.

Author Contributions R.D. led the ALMA proposal. J.S. processed the ALMA data. J.H. processed the VLT/SPHERE data. C.H. performed the SPH simulations. J.S. performed the radiative transfer calculations. C.L. and G.L. developed the analytic model. J.S. performed all presented analyses. J.S. and R.D. wrote the manuscript. All co-authors provided input to the ALMA proposal and/or the manuscript.

Competing Interests The authors declare that they have no competing financial interests.

Correspondence Correspondence and requests for materials should be addressed to: J.S. (email: jspeedie@uvic.ca), R.D. (email: rbdong@uvic.ca).

Data availability All observational data products presented in this work are available through the CANFAR Data Publication Service at https://doi.org/10.11570/24.0087. This includes final reduced and calibrated ALMA measurement sets, image cubes and moment maps, and processed SPHERE data. All simulated data products including hydrodynamic simulations and synthetic ALMA data are available at https://doi.org/10.5281/zenodo.11668694. The raw ALMA data are publicly available via the ALMA archive https://almascience.nrao.edu/aq/ under project ID 2021.1.00690.S. The raw VLT/SPHERE data are publicly available via the ESO Science Archive Facility https://archive.eso.org/eso/eso_archive_main.html under programme 0104.C-0157(B).

Code availability ALMA data reduction and imaging scripts are available at https://jjspeedie.github.io/guide.2021.1.00690.S. The Python packages used in this work are available: `bettermoments` (https://github.com/richteague/bettermoments), `eddy` (https://github.com/richteague/eddy), `giggle` v0 (http://doi.org/10.5281/zenodo.10205110), PHANTOM (https://github.com/danieljprice/phantom), MCFOST (https://github.com/cpinte/mcfost).

Chapter 5

Mapping the merging zone of late infall in the AB Aur planet-forming system

J. Speedie, R. Dong, R. Teague, D. Segura-Cox, J. E. Pineda,
J. Calcino, C. Longarini, C. Hall, Y. Tang, J. Hashimoto,
T. Paneque-Carreño and G. Lodato

The Astrophysical Journal Letters, 981, 2, L30 (2025)

Abstract

Late infall events challenge the traditional view that planet formation occurs without external influence. Here we present deep ALMA ^{12}CO $J = 2-1$ and SO $J_N = 5_6 - 4_5$ observations toward AB Aurigae, a Class II disk system with strong signs of gravitational instability and ongoing planet formation. By applying Keplerian and anti-Keplerian masks, we separate disk-like and non-disk-like motions of ^{12}CO, considering the two outputs as the 'disk' and 'exo-disk' (out of disk) emission components, respectively. The disk component of ^{12}CO extends to $\sim$1600 au in radius and exhibits a stunningly rich architecture of global spiral structure. The exo-disk emission consists predominantly of three spiral structures –S1, S2 and S3– whose projections are co-spatial with the disk. We successfully reproduce their trajectories with a ballistic accretion flow model, finding that S1 and S2 (both redshifted) are infalling toward the disk from in front, and S3 (blueshifted) is infalling from behind. Where the terminal ends of S1 and S2 become indistinguishable from the disk, we observe a brightness peak in SO emission 2.5× the azimuthal average of a background SO ring. This merging zone lies within a relatively confined region $15^\circ - 100^\circ$ east of north, and between $\sim 150 - 300$ au from the star, at scales relevant to where planet candidates have been previously identified. The AB Aur system provides a unified picture of late infall inducing replenishment of the disk, triggering gravitational instability, and modifying the conditions of forming planets.

5.1 Introduction

Recent scattered light and molecular observations are revealing more and more instances of large-scale narrow accretion filaments –'streamers'– delivering material to circumstellar disks, a process referred to as 'late-stage infall' in the case of Class II disks (e.g., Ginski et al., 2021; Huang et al., 2021; Garufi et al., 2022b; Harada et al., 2023; Pineda et al., 2023; Huang et al., 2024; Gupta et al., 2024). Modeling studies have shown that infalling material can have radical consequences for the disk chemistry and structure, including localized shock heating, the formation of pressure bumps, vortices or spiral arms, and disk warps or misalignments (e.g., Hennebelle et al., 2017; van Gelder et al., 2021; Kuffmeier et al., 2021; Kuznetsova et al., 2022; Calcino et al., 2024). Late infall in older Class II disks undergoing planet formation is thus highly relevant to the local conditions of forming planets.

AB Aurigae (AB Aur) is a 3.9 - 4.4 Myr old (DeWarf et al., 2003; Beck & Bary, 2019; Garufi et al., 2024) Class II young stellar object (YSO; Henning et al., 1998; Bouwman et al., 2000) at a distance of 155.9 ± 0.9 pc (Gaia Collaboration et al., 2023). Several candidate protoplanets have been identified or predicted amongst the disk's spiral arms (Dong et al., 2016a; Tang et al., 2017; Boccaletti et al., 2020; Currie et al., 2022; Zhou et al., 2023; Biddle et al., 2024; Currie, 2024), suggesting planet formation is underway. Optical and (sub)mm observations of the local environment have led numerous studies to propose that the AB Aur system is currently experiencing infall from its surroundings (Nakajima & Golimowski, 1995; Grady et al., 1999; Tang et al., 2012; Dullemond et al., 2019; Rivière-Marichalar et al., 2020; Kuffmeier et al., 2020; Gupta et al., 2023). The disk itself has long been suspected to be gravitationally unstable (Fukagawa et al., 2004), and recently found to exhibit the predicted kinematic markers of gravitational instability (Hall et al., 2020; Longarini et al., 2021a) in observations of ^{13}CO and C^{18}O emission with the Atacama Large Millimeter/submillimeter Array (ALMA; Speedie et al., 2024).

In this letter, we use high spectral resolution ALMA observations of ^{12}CO $J = 2-1$ and SO $J_N = 5_6 - 4_5$ emission to investigate the hypothesis that late infall is inciting gravitational instability (GI) in this relatively evolved system. Unlike other systems fed by single-streamers observed on spatial scales that dwarf their end destination (e.g., Pineda et al., 2020; Valdivia-Mena et al., 2022, 2023; Flores et al., 2023; Cacciapuoti et al., 2024; Gupta et al., 2024), the AB Aur system hosts *multiple* 'out-of-plane' spiral arms *on disk scales*, detected in previous ^{12}CO observations (Tang et al., 2012). In the 2D sky plane, these structures appear co-spatial with the disk, necessitating new techniques for isolating their emission and presenting a unique opportunity to study the interface between the disk and infalling material in detail.

5.2 Observations

We observed AB Aur with ALMA in Cycle 8 under program ID 2021.1.00690.S (PI: R. Dong). Here we present the ^{12}CO $J = 2-1$ ($\nu_{\rm rest}$ = 230.538 GHz, $E_{\rm up}$ = 16.6 K) and SO $J_N = 5_6 - 4_5$ ($\nu_{\rm rest}$ = 219.949 GHz, $E_{\rm up}$ = 35.0 K) molecular emission line components from this program, which were reduced and imaged concurrently with the ^{13}CO $J = 2-1$ and C^{18}O $J = 2-1$ components presented in Speedie et al. (2024). We refer the reader to that work for data processing details, and briefly reproduce the key aspects below[30].

5.2.1 Calibration

Measurements were taken in a short-baseline configuration C-3 (2 execution blocks) and a long-baseline configuration C-6 (6 execution blocks), using the Band 6 receivers (Ediss et al., 2004). We configured two spectral windows to target the ^{12}CO $J = 2-1$ and SO $J_N = 5_6 - 4_5$ lines, and dedicated a single 2.0 GHz spectral window to sampling the continuum, centered at 233.012 GHz. Using the continuum data, we aligned the eight execution blocks to a common phase center in the *uv*-plane (employing the EXOALMA alignment script; Loomis et al. submitted). Manual self-calibration was first performed on the short-baseline continuum data, starting with 6 rounds of phase-only calibration down to a solution interval of 18 s, followed by 1 round of amplitude+phase calibration on the interval of a scan length, resulting in a SNR increase by a factor of 2.2. Self-calibration subsequently continued on the concatenated short- and long-baseline continuum data, undergoing 4 rounds of phase-only calibration down to 60 s followed by 1 round of amplitude+phase calibration on the interval of a scan length, yielding a SNR increase by a factor of 1.5. Finally, the phase center shifts and self-calibration solutions acquired with the continuum data were applied to the line data, and continuum subtraction was done in the *uv*-plane.

5.2.2 Imaging

Imaging was undertaken with the CASA `tclean` task. The ^{12}CO data immediately presented two challenges: (i) the presence of large-scale diffuse emission with non-Keplerian morphologies, for which generating the optimal CLEAN mask became a protracted and nebulous goal; and (ii) the presence of negative bowling (Braun & Walterbos, 1985; Holdaway, 1999), particularly in central channels. Negative bowling, where the recovered (positive) emission appears to

[30] An online guide to the reduction and imaging for the full program is available at https://jjspeedie.github.io/guide.2021.1.00690.S

Table 5.2.1: Molecular lines and properties of the imaged ALMA data cubes (program ID 2021.1.00690.S).

Molecular Transition	Rest Frequency (GHz)	Channel Width (m/s)	`robust` Value	Beam Size ($''\times''$, deg)	rms Noise (mJy/beam)	JvM ϵ Factor
^{12}CO $J=2-1$	230.538	42.0	0.5	$0.23\times0.17,\ 0.2$	1.55	0.49
SO $J_N=5_6-4_5$	219.949	84.0	1.5	$0.39\times0.28,\ 171.2$	0.63	0.34

sit in a bowl of negative flux (e.g. Fig. 7 of Faridani et al., 2018), is a fundamental interferometer image artifact caused by the presence of emission on spatial scales larger than the reciprocal of the shortest measured baselines (known as the Maximum Recoverable Scale, MRS) and can only be solved by obtaining additional observations sampling the visibility function at smaller uv-spacings. Animated ^{12}CO channel maps illustrating the negative bowling are available (Figure 5.C.3) in the online article. The MRS of our short-baseline configuration, C-3, is $\sim 7''$ at 230 GHz (Remijan et al., 2019).

We adopted the following strategies in response to both of the above two issues: First, we cleaned with a broad mask[31] encompassing all emission within the field of view (FOV), and accordingly, we cleaned conservatively (to a threshold of 5× the rms noise measured in 20 line-free channels of the dirty cube). Second, we forced frequent major cycles[32] to repeatedly repopulate the uv-plane and interpolate into the missing short uv-spacings. These strategies borrowed from the philosophy of PHANGS-ALMA (Leroy et al., 2021). We used the multiscale deconvolution algorithm (Cornwell, 2008) with Gaussian deconvolution scales [0.02″, 0.1″, 0.3″, 0.6″, 1.0″], with an additional largest scale of 2.0″ appended for ^{12}CO. We adopted a Briggs robust weighting scheme, and imaged in LSRK velocity channels at 42 m/s for ^{12}CO and 84 m/s for SO. Unless otherwise specified, the images presented in this work use `robust=0.5` for ^{12}CO and `robust=1.5` for SO, and are JvM corrected (Jorsater & van Moorsel, 1995; Czekala et al., 2021) and primary beam corrected. Table 5.2.1 lists details for each image cube. The rms noise is measured within an annulus of 4″ inner radius and 8″ outer radius over the first and last 5 channels of the cube.

We used the `bettermoments` package (Teague & Foreman-Mackey, 2018b,a) to generate maps of peak intensity, velocity-integrated intensity (moment 0), and intensity-weighted velocity (moment 1) throughout this work. We applied σ-clipping at 5× the rms noise for ^{12}CO and 3× the rms noise for SO.

[31] We used the `tclean` arguments `usemask='pb'` and `pbmask=0.2`, which sets a cleaning mask extending to where the 12m antenna primary beam gain reaches the 20% level, which is usually considered the edge of the FOV.

[32] The ^{12}CO cube with `robust=0.5` underwent 282 major cycles.

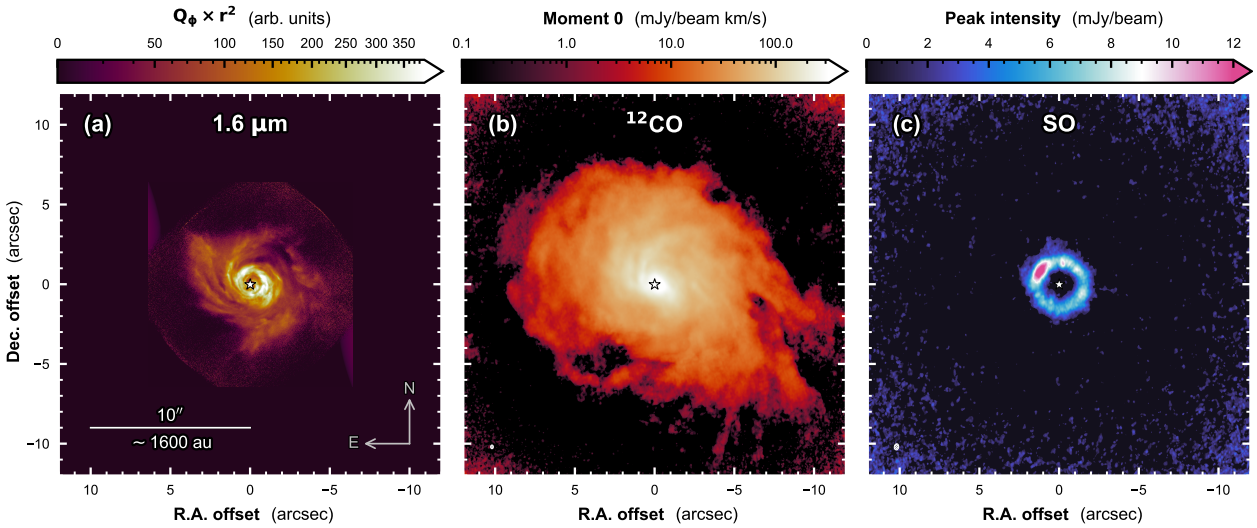

Figure 5.2.1: **Introducing our ALMA observations. (a)** VLT/SPHERE H-band scattered light image at 1.6 μm (Boccaletti et al., 2020), shown for scale. **(b)** ALMA ^{12}CO $J = 2-1$ integrated intensity map, collapsed uniformly over line-of-sight velocities ±6 km/s about $v_{\rm sys}$. Emission extends $\sim 20''$ (~ 3200 au) in diameter, roughly half the diameter of the 12m-antenna field of view in Band 6. **(c)** ALMA SO $J_N = 5_6 - 4_5$ peak intensity map. The ring takes a brightness peak in the northeast.

5.2.3 Overview with Standard Moment Maps

Figure 5.2.1 introduces our ALMA observations of the AB Aur disk. For scale, the VLT/SPHERE H-band scattered light image at 1.6 μm is shown in Figure 5.2.1a (Boccaletti et al., 2020; Speedie et al., 2024 reduction). Figure 5.2.1b presents our ALMA ^{12}CO $J = 2-1$ integrated intensity map, collapsed uniformly over velocities ±6 km/s about the systemic velocity ($v_{\rm sys} = 5.85$ km/s; Tang et al., 2012; Speedie et al., 2024). We find that the disk extends to $r \sim 10''$ ($r \sim 1600$ au) in ^{12}CO emission, placing it among the largest protoplanetary disks known both physically and on the sky (e.g., Berghea et al., 2024; Monsch et al., 2024). Spiral structure at all radii and azimuth is visible directly in the integrated intensity map. The ratio of the disk emission extent ($\sim 20''$) to the synthesized ALMA beam ($\sim 0.2''$) is ~ 100.

Figure 5.2.1c shows our SO $5_6 - 4_5$ peak intensity map, generated over a velocity range ±2.5 km/s about $v_{\rm sys}$. We observe a ring of SO emission between $r = 1.0'' - 2.0''$ on the sky. The ring exhibits substructure, namely a brightness peak in the northeast. Measuring the azimuthal extent of the brightness peak as the region where the peak intensity is above 10 mJy/beam (70% of the maximum), we find a position angle range of $32° - 82°$ east of north. The maximum SO intensity inside this region is 14.5 mJy/beam, which is a relative increase of 150% from the azimuthal average intensity of 5.7 mJy/beam measured throughout the rest of the ring. We confirmed that this brightness peak is not an artifact of continuum subtraction (see Figure 5.A.1

in Appendix 5.A).

5.3 The Disk and Exo-Disk Components of ^{12}CO

In this section and §5.4, we present a position-velocity (PV) analysis of the ^{12}CO $J = 2-1$ and SO $J_N = 5_6 - 4_5$ emission. We begin in §5.3.1 with radial PV diagrams to reveal the complexity in the ^{12}CO data. In §5.3.2 we kinematically disentangle the ^{12}CO into its disk-like and non-disk-like components, in preparation to model the latter component as infall in §5.4.

5.3.1 Radial Position-Velocity Diagrams

Figure 5.3.2 presents radial PV diagrams of ^{12}CO $J = 2-1$ and SO $J_N = 5_6 - 4_5$ emission extracted along the disk's major and minor axes. The SO is plotted over the ^{12}CO as filled contours. The PV slices are taken assuming a geometrically thin disk with inclination $i = 23.2°$ (from the continuum; Tang et al., 2012, 2017) and position angle P.A. = 236.7° (where P.A. is measured east of north to the redshifted major axis; Speedie et al., 2024). We used `pvextractor` (Robitaille et al., 2018) for all PV slicing throughout this work.

Along the major axis (top row of Figure 5.3.2), the projection of the disk's rotation is maximized, and we observe substantial excess ^{12}CO emission cleanly distinct in velocity from the bulk rotating component. For comparison, we overlay dashed orange curves of Keplerian rotation in a razor thin disk, following $v_{\rm LOS} - v_{\rm sys} = v_{\rm Kep} \sin i \cos\phi$, where $v_{\rm Kep} = (GM_\star / r)^{1/2}$, the stellar mass $M_\star = 2.23\,M_\odot$, the systemic velocity $v_{\rm sys} = 5.86$ km/s (Speedie et al., 2024), and $\cos\phi = 1$ on the redshifted major axis.

Three strong 'blobs' are identifiable within the excess ^{12}CO emission in the top row of Figure 5.3.2 (labeled S1 to S3). They correspond to radial cross sections through three "out-of-plane" spiral structures first identified by Tang et al. (2012) in ^{12}CO $J = 2-1$ observations with the Plateau de Bure interferometer (PdBI). Following Tang et al. (2012), we hereafter refer to them as S1, S2, and S3. They have additionally been observed in the same transition with NOEMA by Rivière-Marichalar et al. (2020). To our knowledge, we present the first ALMA detection.

Note that the Keplerian rotation curves do not account for the disk's contribution to the gravitational potential. The disk component of ^{12}CO emission shows substantial apparent super-Keplerian rotation at large radii in the major axis PV diagrams, indicative of significant self-gravity and a high disk-to-star mass ratio. We keep to qualitative statements here because these major axis slices were taken along a straight line, which is equivalent to assuming the ^{12}CO

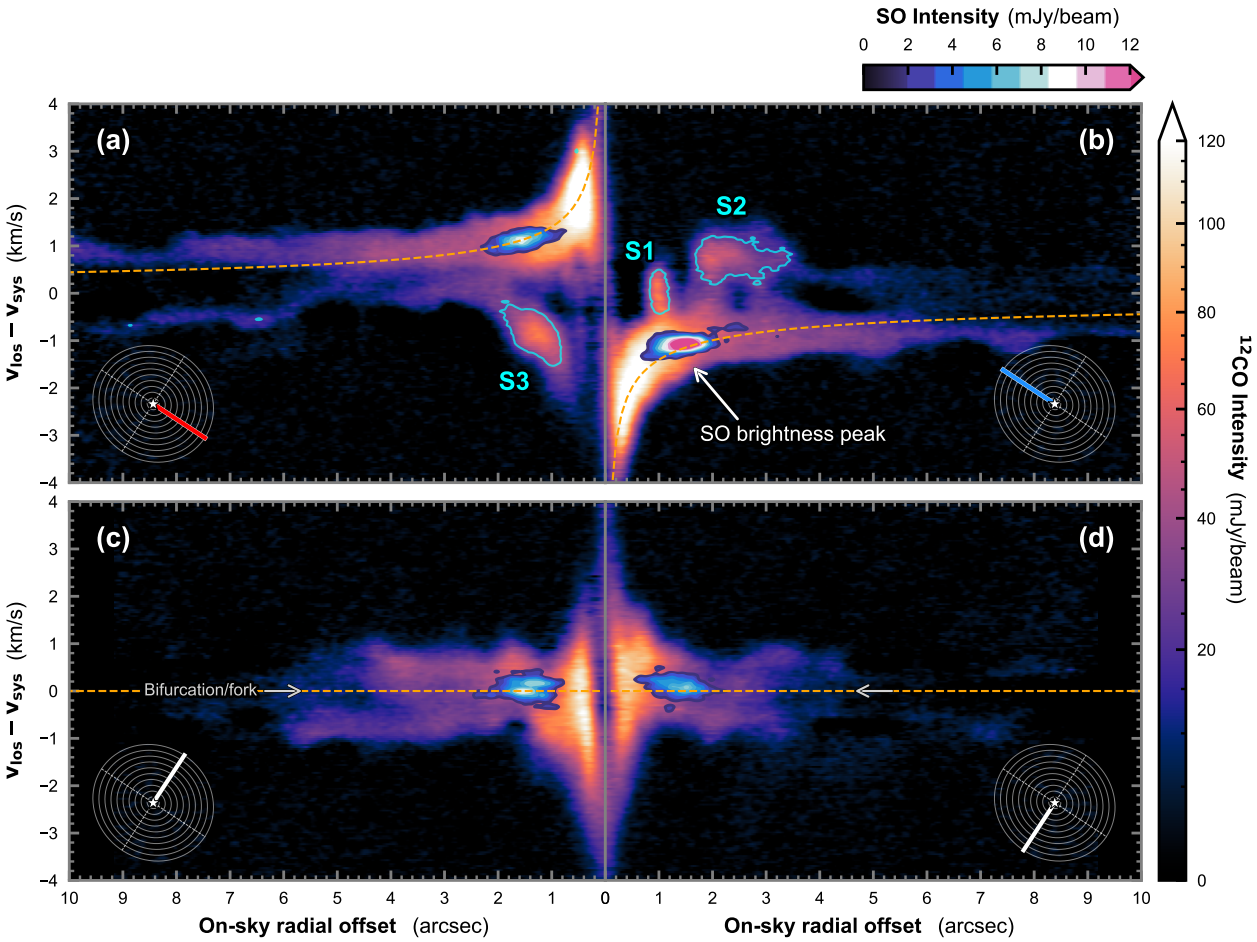

Figure 5.3.2: **Position-velocity (PV) slices in ALMA ^{12}CO $J = 2-1$ emission along the disk major and minor axes.** PV slices in the ALMA SO $J_N = 5_6 - 4_5$ emission are overplotted as filled contours in increments of 2σ starting at 3σ, where $\sigma = 0.63$ mJy/beam. The orientation of each slice is indicated in the bottom corner of each panel: **(a)** Redshifted (west) major axis. **(b)** Blueshifted (east) major axis. **(c)** Northern minor axis. **(d)** Southern minor axis. Keplerian rotation is denoted by orange dashed lines, accounting for the mass of the central star only. 'Out-of-plane' spiral arms S1, S2 and S3 identified by Tang et al. (2012) are labeled, and encircled by cyan contours from the anti-Keplerian weighted ^{12}CO cube (see next figures). In panels (c) and (d), grey arrows point to a bifurcation pattern we attribute to interferometric filtering (§5.2). An animation of radial position-velocity slices in ALMA ^{12}CO $J = 2-1$ and SO $J_N = 5_6 - 4_5$ emission is available in the online Journal. The animation sequence pans through all azimuthal angles in 0.5° steps following the rotation direction of the disk.

emission surface is the disk midplane. For now we note that the surface is almost certainly elevated, and thus the slices are likely sampling slightly away from the loci of $v_{\rm LOS}$ maxima. A quantitative kinematic analysis to fit for the disk mass should be done (e.g. Veronesi et al., 2021; **?**; Martire et al., 2024; Andrews et al., 2024), though complexities in the ^{12}CO emission, the non-axisymmetric nature of the disk and its low inclination complicate the extraction of a

^{12}CO emission layer. We tender that challenge to future work.

Along the minor axis (bottom row of Figure 5.3.2), we notice how the ^{12}CO emission appears to bifurcate (or fork) into two bands above and below the horizontal line of $v_{\rm LOS} - v_{\rm sys} = 0$ at large offsets, starting around $r \gtrsim 3.5''$. We understand this to be a result of interferometric spatial filtering in the central channels (§5.2).

5.3.2 Keplerian & Anti-Keplerian Masking

Next, we disentangle the bulk rotating component of ^{12}CO emission from all its non-disk-like emission, in a fashion similar to Huang et al. (2021, see their Appendix C). We generate a Keplerian mask (Teague, 2020) to kinematically encompass the disk, and an "anti-Keplerian" mask with opposite Boolean values to encompass any emission kinematically inconsistent with the disk. We additionally spectrally smooth each mask, i.e., convolve the top hat spectrum in each spatial pixel with a Gaussian, to mitigate edge artifacts (c.f. Figure 17 of Huang et al., 2021), which also introduces some overlap in their spectra. Two new versions of the ^{12}CO $J = 2-1$ ALMA image cube are then generated by multiplication with each of the Keplerian and anti-Keplerian masks. In this way, the masks serve effectively as 3D weighting functions. Further details are provided in Appendix 5.B and Figure 5.B.2. In the remainder of this letter, we refer to the emission in the Keplerian-weighted and anti-Keplerian-weighted ^{12}CO cubes as the "disk" and "exo-disk"[33] components, respectively.

Figure 5.3.3 shows moment maps collapsed from the Keplerian and anti-Keplerian ^{12}CO $J = 2-1$ image cubes. We emphasize that the masking process is not perfect, but is meaningfully effective considering the complexity of the ^{12}CO emission (Fig. 5.3.2). Beginning with the left column, Figure 5.3.3a shows the integrated intensity map of the map of the Keplerian-weighted ^{12}CO, or disk component. The inset panel shows the corresponding intensity-weighted velocity map, demonstrating that the emission isolated by the Keplerian mask is at least broadly recognizable as disk-like, with a redshifted and blueshifted side (compare to Figure 3 of Rivière-Marichalar et al., 2020). Figure 5.3.3c shows a high-pass filtered version of Figure 5.3.3a, made with a radially expanding Gaussian kernel[34] using the same parameter setting as Speedie et al. (2024). A rich architecture of spiral structure exists in the disk component, consistent with ongoing gravitational instability (e.g., Dipierro et al., 2014; Hall et al., 2019).

In the right column of Figure 5.3.3, we show moment maps of the anti-Keplerian-weighted ^{12}CO cube, or exo-disk component. Figure 5.3.3b presents the integrated intensity map, where

[33] As in 'outside of disk', in the same sense as 'exo-terrestrial' or 'exo-solar planet'.

[34] github.com/jjspeedie/expanding_kernel

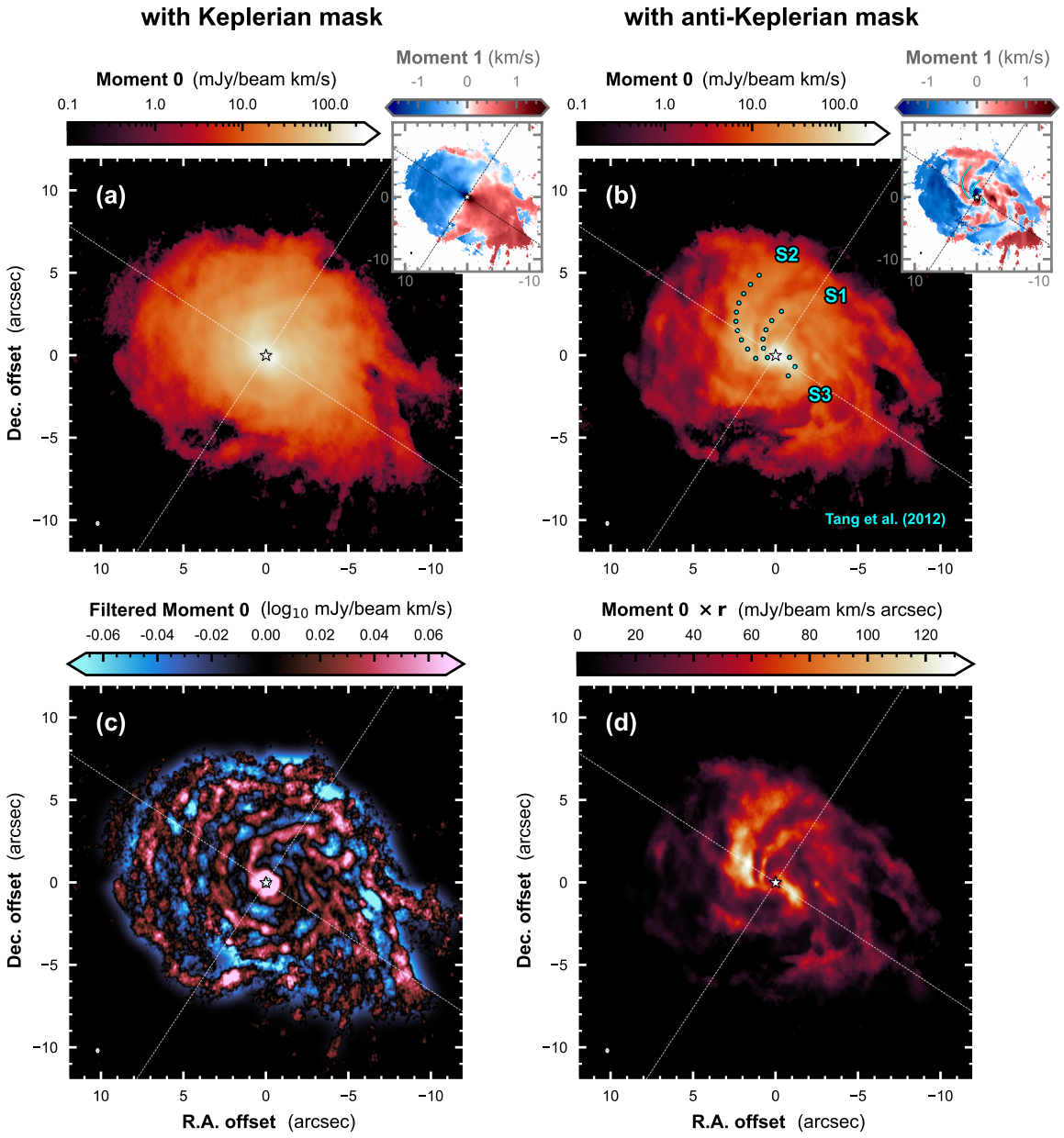

Figure 5.3.3: **ALMA ^{12}CO $J = 2-1$ moment maps after disentangling the disk and exo-disk emission.** **(a)** Integrated intensity map of ^{12}CO after weighting with a spectrally-smoothed Keplerian mask. **(b)** The same, but after weighting with an anti-Keplerian mask generated with opposite Boolean values prior to spectral smoothing. Views of the masks are provided in Appendix Figure 5.B.2. The cyan points trace S1, S2 and S3 from Table 4 of Tang et al. (2012). Panels (a) and (b) are shown on a $\log_{10}$ colorscale to compare with Figure 5.2.1b. Intensity-weighted velocity maps are shown in the insets. **(c)** High-pass filtered integrated intensity map of the Keplerian-weighted ^{12}CO cube in panel (a), highlighting the architecture of spiral structure within the disk. **(d)** The same as panel (b), but scaled by r (on-sky) and presented on a linear colorscale.

points along the spiral structures S1, S2, and S3 placed by Tang et al. (2012, their Table 4) are overplotted in cyan for reference. Figure 5.3.3d shows the integrated intensity map r-scaled with a linear colorbar. The exo-disk component is comprised predominantly of coherent spirals S1, S2 and S3, with additional 'whisps' of emission (particularly in the west and south). The corresponding intensity-weighted velocity map (Figure 5.3.3b inset) is markedly non-disk-like, with regions of emission at 'opposite' line-of-sight velocity to the disk.

We note that the imprint of S1 is visible in the *disk* component (compare Figure 5.3.3c and d). In other words, some of its emission remains within the Keplerian mask. As we'll discuss in the next section, this is because emission from S1 is not sufficiently offset in line-of-sight velocity from the disk component *along its entire* trajectory (not just at the major axis as we glimpsed in Figure 5.3.2b). On the other hand, S2 and S3 are kinematically distinct from the disk at almost all their spanned azimuths.

5.4 Modeling the Exo-disk Component as Infall

We focus on the coherent exo-disk spiral structures S1, S2, and S3, and show that their trajectories (in both RA-Dec and PV space) can be reproduced with the analytic accretion flow model of Mendoza et al. (2009), using the numerical implementation by Pineda et al. (2020). Interpreting the exo-disk emission as infall is well motivated: observations of AB Aur's kilo-au environment are highly suggestive of interaction with surrounding material (e.g., Grady et al., 1999). See more details in Figure 5.C.3 of Appendix 5.C. The next subsection outlines the scheme of the model, with our results presented in §5.4.2.

5.4.1 The Pineda Implementation of the Mendoza Streamline Model (PIMS)

The Mendoza et al. (2009) model considers a steady-state ballistic accretion flow from a rigidly rotating sphere of finite radius r_0 (representing the inner edge of a giant molecular cloud) toward a central object with mass M, located at the origin of coordinates. The angular frequency of the sphere's rigid-body rotation is Ω. In spherical coordinates, a fluid 'particle' is initiated on the sphere at an azimuthal angle ϕ_0 and a polar angle θ_0 (where $\theta = 90^\circ$ defines the equatorial plane). It can also be given an initial radial velocity, $v_{r,0}$. The particle has specific angular momentum h about the origin inherited from its initial location, where h is distributed on the sphere according to $h = h_0 \sin\theta$ assuming $h_0 = r_0^2\,\Omega$. The particle's specific energy E is the sum

of its specific kinetic energy, centrifugal potential energy, and gravitational potential energy:

$$E = \frac{1}{2}v_r^2 + \frac{1}{2}\frac{h^2}{r^2} - \frac{GM}{r} = \frac{1}{2}v_{r,0}^2 + \frac{1}{2}\frac{h_0^2 \sin^2\theta_0}{r_0^2} - \frac{GM}{r_0}. \tag{5.4.1}$$

The quantities h and E are contants of motion along each particular trajectory.

The trajectory of each particle (hereafter a 'streamline') is a solution to Kepler's problem (Newton, 1687), and therefore a segment of a conic section with the origin at one of the foci. This means each streamline is contained in a plane, and we will later refer to this as the plane 'of' a streamline. The whole system is cylindrically symmetric, such that each streamline 'collides' with its reflection counterpart at the equatorial plane. An important fundamental property of the model is that a streamline cannot spiral infinitely – it *must* hit the equatorial plane after traveling an azimuthal distance of $< 90°$ from its initial azimuthal location ϕ_0. It comes closest to subtending this maximum azimuthal distance when initialized close to the equatorial plane ($\cos(\phi - \phi_0) = \tan\theta_0 / \tan\theta$; Equation 8 of Mendoza et al., 2009).

With the Pineda et al. (2020) Implementation of the Mendoza et al. (2009) Streamline Model (PIMS[35]), we have 6-dimensional information –3 spatial coordinates and 3 velocity coordinates– at every point along the streamline. Two rotational transformations are then applied to the coordinates to project the system onto the sky: a first to give the streamline's equatorial plane some inclination, and a second to give the ascending node some position angle[36]. This yields 3D spatial coordinates $\langle \mathrm{RA}, \mathrm{Dec}, \mathrm{LOS} \rangle$ and 3D velocity components $\langle v_{\mathrm{RA}}, v_{\mathrm{Dec}}, v_{\mathrm{LOS}} \rangle$ at every point on the streamline. We further compute the projected radial coordinate, r_{proj}, as the hypotenuse of the RA and Dec coordinates. When we compare streamlines to the AB Aur data, we do so in the RA-Dec plane and the r_{proj}-v_{LOS} (PV) plane.

We obtained streamline solutions for each of S1, S2 and S3 by first exploring their trajectories in radial and azimuthal PV cross sections to build an understanding of their v_{LOS} behaviour as a function of ϕ and r. A selection of such cross sections is shown in Figure 5.D.4 of Appendix 5.D, with animated versions available in the online article. We then identified, by manual experimentation, the region of model parameter space where streamlines follow a broadly similar track in the PV plane. This procedure leverages the fact that the infall model trajectories in the r_{proj}-v_{LOS} plane only take one of a few basic shapes (e.g. see Thieme et al., 2022; Mori et al., 2024, for examples). From there, we iteratively fine-tuned the parameters until the match between the streamlines and the observed trajectories in the RA-Dec and PV planes were visually

[35] github.com/jjspeedie/pims

[36] We note that the line-of-sight velocity, v_{LOS}, is invariant under this transformation (v_{LOS} is independent of the position angle).

satisfactory. The only parameter we did not let vary in these experiments is M, which we set to $M = 2.90\,M_\odot = M_\star \times 130\%$ to represent both the central star and the disk (Speedie et al., 2024).

In the following subsection, we present one streamline solution for each of S1, S2 and S3. The PIMS parameters describing streamlines are provided in Table 5.E.2 of Appendix 5.E. We note that for each of S1 and S2, our procedure easily yielded a family of streamlines that are satisfactory matches. We confirmed each family describes a structure physically coherent in 3D spatial coordinates, ⟨RA, Dec, LOS⟩ (see Figure 5.E.5 in Appendix 5.E), and selected one solution to show in the main text. Satisfactory solutions for S3, on the other hand, were not so easily found; we nonetheless present our single best solution for S3 for discussion and for reference with Tang et al. (2012).

5.4.2 Streamline Solutions for S1, S2 and S3

Figure 5.4.4 presents our infall modeling results for each of S1, S2 and S3. In Figure 5.4.4a, we overlay the three PIMS streamline RA-Dec trajectories onto the ^{12}CO anti-Keplerian moment 1 map (from Figure 5.3.3b inset). The streamlines fall from large radii to small radii, and are coloured by their line-of-sight velocity, $v_{\rm LOS}$. The S1 and S2 streamlines are predominantly redshifted (where the AB Aur disk is blueshifted) and lie in front of the disk, falling toward the disk away from us. The plane of S1 is approximately 20° inclined with respect to the AB Aur disk midplane, and the plane of S2 is inclined by approximately 35°. S3 is blueshifted (where the disk is redshifted) and lies behind the disk, falling toward us, on a plane inclined by approximately 45° to the AB Aur disk midplane. See Figure 5.E.5 for a 3D rendering and animation of the system geometry.

In Figure 5.4.4bcd, we overlay each of the streamline $r_{\rm proj}$-$v_{\rm LOS}$ trajectories onto PV diagrams from the ^{12}CO image cube, where the PV slices were taken in the data cube along each of the streamlines' RA-Dec trajectories for completely consistent comparison (see Figure 9 of Huang et al., 2021, for another example of this). To help visually discern the disk and exo-disk components of the ^{12}CO emission in this space, the same slices were taken through each of the Keplerian- and anti-Keplerian weighted ^{12}CO image cubes, and overplotted with orange and cyan contours, respectively. Finally, we take the same slices through the SO $J_N = 5_6 - 4_5$ cube, and overplot the SO emission as filled contours as well (like Figure 5.3.2).

We find that both S1 and S2 –the observed structures– follow a 'flatline-then-dip' trajectory in the $r_{\rm proj}$-$v_{\rm LOS}$ plane as they accelerate toward the star. We identify the 'merging zone' of S1 and S2 as the region where their emission in ^{12}CO becomes indistinguishable from the emission from the disk, which is also where the terminal ends of our model streamlines intersect with the

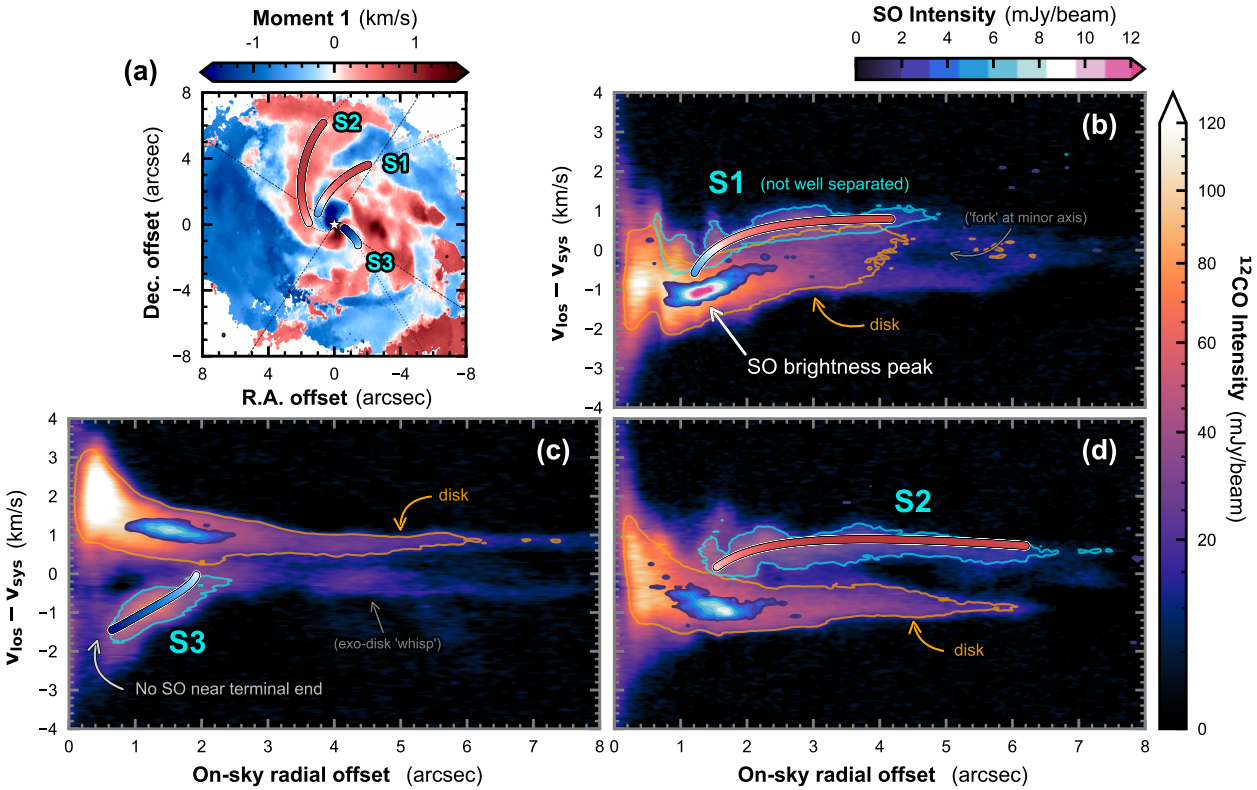

Figure 5.4.4: **Modeling S1, S2 and S3 as infall. (a)** Intensity-weighted velocity map of the anti-Keplerian weighted ^{12}CO $J = 2-1$ image cube (as in Figure 5.3.3b inset). We overlay RA-Dec trajectories of three streamlines matching S1, S2 and S3, computed with the analytic accretion flow model of Mendoza et al. (2009) implemented in (Pineda et al., 2020). The colorbar for velocity applies to both the background velocity map and the model streamlines. **(b,c,d)** PV slices taken *along the RA-Dec trajectory* of each streamline for completely consistent comparison between model and data (one panel per streamline). Within a panel, multiple cubes have been sliced: the full unweighted ^{12}CO cube (colormap), the Keplerian weighted ^{12}CO cube (orange contours), and the anti-Keplerian weighted ^{12}CO cube (cyan contours). PV slices in the SO $J_N = 5_6 - 4_5$ image cube are overplotted as filled contours in increments of 2σ starting at 3σ. We concatenate arbitrary extensions to the slice paths so that the PV diagrams span $r = 0'' - 8''$ in on-sky radial offset, shown as dotted gray lines extending from both ends of the streamline trajectories. Radial and azimuthal PV cross sections providing additional visualizations of S1 and S2 merging with the disk are available in Appendix Figure 5.D.4.

disk midplane in 3D spatial coordinates (Figure 5.E.5). Figure 5.4.4b and d show this from the perspective of PV slices along the streamlines themselves, and Appendix Figure 5.D.4 shows this from the perspective of PV slices in radius and azimuth. The merging occurs at radii $r \sim 1'' - 2''$ from the star and between position angles $15° - 100°$ east of north on the sky. SO $J_N = 5_6 - 4_5$ emission is observed at these same radii, peaking within this position angle range (§5.2.3), and at line-of-sight velocities consistent with Keplerian, indicating localized heating within the disk (discussed further in §5.5.3).

We note that, as mentioned in §5.3.2, emission from S1 is not well separated in line-of-sight velocity from the disk component along its entire trajectory (see Figure 5.4.4b), while emission from S2 is kinematically distinct from the disk at all its spanned azimuths leading up to the merging zone (Figure 5.4.4d). This can be explained as a projection effect: Both are observed at redshifted line-of-sight velocities within roughly $0-1$ km/s above $v_{\rm sys}$, but S1 is spatially nearer to the minor axis (particularly at large radii), where the disk emission already occupies these line-of-sight velocities. Away from the minor axis (looking east), rotation projects the disk blueward of $v_{\rm sys}$, such that emission from S2 is separated in line-of-sight velocity over the course of its approach.

Turning to Figure 5.4.4c, S3 is observed in ^{12}CO at blueshifted line-of-sight velocities within roughly $0-2$ km/s below $v_{\rm sys}$. Lying spatially near the western major axis, it is well separated from the disk's redshifted emission. We found that the analytic infall model cannot produce a streamline that simultaneously (i) is blueshifted, (ii) is located on the redshifted side of the disk, (iii) is oriented in a counter-clockwise sense on the sky, and (iv) takes a concave-down trajectory in the $r_{\rm proj}$-$v_{\rm LOS}$ plane. We present a streamline that violates solely attribute (iv). The terminal end of the model streamline lies on the redshifted major axis at $r\sim0.5''$, both spatially and kinematically offset from the observed SO emission.

5.5 Discussion

Figure 5.5.5 provides a summary of our main result. We have applied a simple ballistic accretion flow model (used by previous works to analyze streamers on cloud or envelope scales, e.g., Pineda et al., 2020; Valdivia-Mena et al., 2022; Garufi et al., 2022b; Valdivia-Mena et al., 2023; Flores et al., 2023) onto *disk-scales*, in a system with multiple infalling disk-scale streamers and several embedded planet candidates. Figure 5.5.5c shows that S1 and S2 are seen in 0.57 μm HST/STIS imaging (Grady et al., 1999), consistent with being in front of the disk. We identify the 'merging zone' of S1 and S2 as the region where their emission in ^{12}CO becomes indistinguishable from the emission from the disk (Figure 5.4.4 & 5.D.4), which is also where our model streamlines intersect with the disk midplane in 3D spatial coordinates (Figure 5.E.5). In this same region, we observe a brightness peak in SO $J_N = 5_6 - 4_5$ emission. We highlight that the merging zone is in close proximity to candidate sites of planet formation.

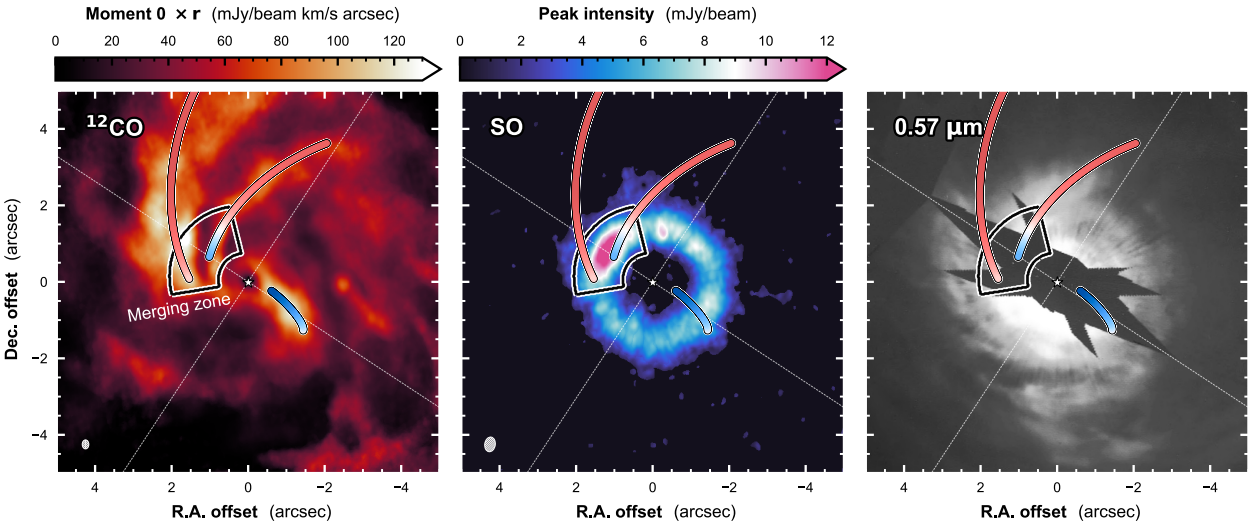

Figure 5.5.5: **The merging zone of late infall in the AB Aur disk.** The streamline trajectories for S1, S2 and S3 from Figure 5.4.4 are overlaid onto the exo-disk ^{12}CO $J = 2-1$ integrated intensity map (as in Figure 5.3.3d), the SO $J_N = 5_6 - 4_5$ peak intensity map (as in Figure 5.2.1c) and HST/STIS scattered light image at $\lambda = 0.57\,\mu$m (Figure 3 of Grady et al., 1999, reproduced with permission). The terminal ends of S1 and S2 coincide with the SO $J_N = 5_6 - 4_5$ brightness peak. A rendering of the disk+streamline geometry in 3-dimensional space is available in Appendix Figure 5.E.5.

5.5.1 What are the origins of late infall in the AB Aur system?

Late-stage infall events may be the result of low-velocity cloud fragments being gravitationally captured by the star, and accreted through a Bondi-Hoyle Lyttleton (BHL) type process (Bondi, 1952; Edgar, 2004). Zooming out to AB Aur's kilo-au environment, optical images with the University of Hawaii 2.2 m Telescope show an arc-shaped structure or "reflection nebula" surrounding AB Aur from the east to the south (Grady et al., 1999; Nakajima & Golimowski, 1995). This arc structure is hypothesized to be part of a cloudlet unrelated to the early protostellar collapse phase – specifically, a part that was *not* captured by the gravity of AB Aur, and instead was bent during a flyby encounter onto an arc-shaped (hyperbolic) trajectory (Dullemond et al., 2019; Kuffmeier et al., 2020; Gupta et al., 2023). Such a scenario, but playing out around DG Tau, was recently demonstrated with hydrodynamic simulations by Hanawa et al. (2024).

In Figure 5.C.3 (Appendix 5.C) we report new but very tentative evidence supporting this hypothesis in AB Aur. The closest projected separation of the reflection nebula, ~ 1500 au or ~ 10″, falls within the field of view of our ALMA observations (38″ × 38″). In ^{12}CO emission, we observe a faint 'tail-like' emission structure extending from the disk to the south, bridging the disk to a source outside the primary beam FOV. The tail appears co-spatial with the reflection nebula on the sky, hinting to a physical connection and suggesting that some part of the cloudlet has been

gravitationally captured. Further notes on the tail structure are provided in Appendix 5.C. We stress this detection is tentative as the relative response of the ALMA 12m antenna sensitivity tapers to the 20% level at the edge of our imaged FOV (§5.2). Follow-up kinematic observations probing a larger region of sky and with sensitivity to those larger spatial scales are needed. The connection, if any, between the 'tail-like' emission at the southern edge of the FOV and the streamers observed *within* the confines of the disk –S1, S2 and S3– is unclear.

5.5.2 What are the consequences of late infall in the AB Aur system?

The consequences of infall are fundamental and wide-reaching (e.g., Kuffmeier et al., 2023; Pelkonen et al., 2024; Winter et al., 2024). In this section we focus our lens on angular momentum transport and disk substructure.

Material infalling into a pre-existing disk must trigger some form of angular momentum redistribution for the new mass to be 'assimilated' into the disk (e.g., Krapp et al., 2021). Numerical simulations have shown gravitational instabilities to be triggered and/or spiral structure to be formed as a consequence of infall (e.g., Harsono et al., 2011; Lesur et al., 2015; Hennebelle et al., 2017; Kuffmeier et al., 2018). Indeed, infall has been previously proposed to trigger GI in Elias 2-27 (Paneque-Carreño et al., 2021b). In an evolved system like AB Aur, an influx of mass may have been necessary to acquire and maintain a high disk-to-star mass ratio (Fukagawa et al., 2004; Hall et al., 2019). If gravitationally unstable disks only exhibit prominent spiral structure for a limited time after the onset of GI, as suggested by recent numerical simulations (Rowther et al., 2024b), then we may infer that gravitational instability must have been triggered –e.g. by infall– relatively recently.

In addition to gravitational instabilities, simulations have shown infall to launch the Rossby wave instability (RWI), resulting in the ready formation of vortices and pressure bumps where material is deposited (Bae et al., 2015; Kuznetsova et al., 2022). This expectation appears to be borne out in the AB Aur system, which displays a ring and azimuthal asymmetry in mm continuum emission at $r \sim 1''$ (e.g., Figure 5.A.1, Tang et al., 2017), just interior to the merging zone identified here.

The sheer size of the AB Aur disk ($r \sim 1600$ au in ^{12}CO; §5.2.3) may also be ascribed to late infall, as extraordinarily large disks are statistically more likely to have experienced infall with high angular momentum (Kuffmeier et al., 2023). Misalignment between the angular momentum vector of infalling material and that of the inheriting disk can induce warping (Sai et al., 2020; Kuffmeier et al., 2021; Dullemond et al., 2022; Kuffmeier et al., 2024), with a severity that depends on the mass ratio of the two. Some degree of warping appears to be present in the AB

Aur disk, based on the non-axisymmetry of the background velocity field traced by ^{13}CO and C^{18}O (Speedie et al., 2024).

5.5.3 How do we interpret the SO emission morphology?

SO emission in the AB Aur system has been observed in five transitions with three facilities to date: SO $3_4 - 2_3$ and $5_6 - 4_5$ with the IRAM 30m telescope (Fuente et al., 2010, not spatially resolved); SO $5_6 - 4_5$ with NOEMA in CD configuration (Pacheco-Vázquez et al., 2016, spatially resolved for the first time); SO $5_5 - 4_4$ and $5_6 - 4_5$ with NOEMA in AC configuration (Rivière-Marichalar et al., 2020); and SO $5_6 - 4_5$, $6_5 - 5_4$ and $6_7 - 5_6$ with ALMA (Dutrey et al., 2024). In the latter three works, where SO $5_6 - 4_5$ is spatially resolved, a brightness peak within a ring of emission is found in the same location reported here. In this section, we discuss its production and survival.

The merging of S1 and S2 will be accompanied by shock waves if the infalling flow is supersonic. This is typically the case in infall, with the speed of sound being $\lesssim 0.2$ km/s at $r \gtrsim 100$ au. While we only measure line-of-sight velocities of S1 and S2 in the data (Figure 5.4.4), we can estimate their incident velocity using the known velocity components of the model streamlines, which are listed in Appendix Table 5.E.2. Their three velocity components (inward, clockwise, and toward the midplane) range 0.7 – 4.1 km/s, consistent with 'low-velocity' (usually quoted to mean 2 km/s) shocks.

Within shocks, the kinetic energy of the infalling material is converted into thermal energy. Dust grains are heated by conduction from the shocked gas, and by increased aerodynamic drag if the gas is decelerated by pressure forces (e.g., Miura et al., 2017). If the resulting dust temperature is sufficiently high (of order 40 – 70 K), SO can be produced directly via thermal sublimation of SO ice mantles (e.g., van Gelder et al., 2021). Within the SO ring in the AB Aur system, Rivière-Marichalar et al. (2020) and Pacheco-Vázquez et al. (2016) estimate an average gas kinematic temperature of ~ 39 K from H_2CO and SO multi-transition analysis. If aerodynamic heating operates alongside conductive heating, the gas kinematic temperature may represent a lower bound for the dust temperature.

Thermal sublimation is most efficient for small grains ($< 0.1\,\mu$m) because they are more significantly heated, due to their lower emissivities (Miura et al., 2017). They also likely represent the largest contribution to the dust-grain surface area (e.g. Mathis et al., 1977). HST/STIS imaging of AB Aur at $0.57\,\mu$m wavelengths (tracing grain sizes $\lambda/2\pi \sim 0.09\mu$m, e.g., Kruegel, 2003) confirms such small grains are present high in the disk atmosphere, and with a surface brightness distribution following S1 and S2 (Figure 5.5.5c; Grady et al., 1999).

Gas-phase formation of SO after the sputtering of s-CH_4 and s-H_2S may be an alternative possibility, in which case we should observe H_2CO and SH emission coincident with SO (van Gelder et al., 2021). Indeed, the former has been seen by Pacheco-Vázquez et al. (2016) and Rivière-Marichalar et al. (2020). On the other hand, sputtering has been found to only become relevant at larger shock velocities (> 10 km/s; Aota et al., 2015).

Regardless of which production mechanism, if SO *is* produced at the merging zone of S1 and S2, it would need to survive (only) ~ 3500 years to be circularized, based on the orbital period timescale, $P = r^{3/2} M_\star^{-1/2}$, at the outermost radius of the SO ring ($r \sim 300$ au). Chemical modeling of the AB Aur system by Pacheco-Vázquez et al. (2016) suggests SO molecules are depleted in less than 0.1 Myr (at densities > 10^7 cm^{-3} and assuming a fixed dust temperature of 45 K), which is a ~ 30× longer timescale. Looking toward other systems, there are cases where SO emission associated with the merging zone of infall has been observed as only a clump, rather than a ring, despite shorter circularization timescales: for example, DR Tau (Huang et al., 2024, 350 years), DG Tau and HL Tau (Garufi et al., 2022b, 600 – 1200 years). We may conclude there are different physical conditions in these systems, or deeper observations may help to further illuminate the SO emission morphologies.

5.6 Conclusions

We have presented deep and high spectral resolution ALMA observations (ID: 2021.1.00690.S) of ^{12}CO $J = 2-1$ and SO $J_N = 5_6 - 4_5$ emission toward the Class II YSO AB Aur. In ^{12}CO, we mapped three infalling 'streamers' spatially coincident with the disk, constrained their physical 3D geometries, and showed they can be modeled down to where they merge with the disk. A summary of our approach and findings is as follows.

- Using a combination of Keplerian and anti-Keplerian masking, we isolate the disk-like ^{12}CO emission from non-disk-like emission, which we term the 'exo-disk' component (§5.3.2).
- The disk emission of ^{12}CO extends up to ~ 1600 au in radius, and exhibits global spiral structure consistent with gravitational instability (Figure 5.3.3).
- Within the exo-disk emission, we re-detect the three ^{12}CO spiral structures S1, S2 and S3, first observed by Tang et al. (2012) with the PdBI. Using the ballistic accretion flow model of Mendoza et al. (2009) and Pineda et al. (2020), we reproduce the on-sky and position-velocity trajectories of S1, S2 and S3 in detail (Figure 5.4.4).

- Our modeling results indicate that S1 and S2 are infalling onto the disk from in front (Appendix Figure 5.E.5), consistent with their traces in HST/STIS imaging of 0.57 μm scattered light (Figure 5.5.5).
- We identify the 'merging zone' of S1 and S2 as the region where their emission becomes indistinguishable with that of the disk in PV space (Figure 5.4.4 & 5.D.4), and where their model streamlines intersect with the disk midplane (Figure 5.E.5).
- The merging zone of S1 and S2 lies 15° – 100° east of north and 150 – 300 au in radius on the sky, coincident with where a ring of SO emission exhibits a brightness asymmetry peaking at 2.5× its azimuthal average level (Figure 5.5.5).

We consider infall to be a strong explanation for the observed gravitational instability and implied high disk mass in the AB Aur system (§5.5.2; Speedie et al., 2024). The origin of the infalling material in this system remains an open question (§5.5.1), though kinematic observations probing larger spatial scales may affirm the cloudlet capture hypothesis (Appendix Figure 5.C.3; Dullemond et al., 2019). Detailed kinematic investigations of how late-stage infall interfaces with the disk should be undertaken in a larger number of planet-forming systems to understand its influence on disk structure and the local planet formation environment.

Acknowledgements We thank our referee for providing a helpful review of the manuscript, including thoughtful suggestions and questions. We are grateful to Michael Kuffmeier, Álvaro Ribas, Adele Plunkett, Andrew Winter, Myriam Benisty, Pablo Rivière-Marichalar, Asunción Fuente, Takayuki Muto, Yifan Zhou and Sahl Rowther for enlightening discussions, and to Giulia Perotti for valuable comments on the manuscript. J.S. thanks Ryan Loomis, Sarah Wood and Tristan Ashton at the North American ALMA Science Center (NAASC) for providing science support and technical guidance on the ALMA data as part of a Data Reduction Visit to the NAASC, which was funded by the NAASC. The reduction and imaging of the ALMA data was performed on NAASC computing facilities.

J.S. acknowledges financial support from the Natural Sciences and Engineering Research Council of Canada (NSERC) through the Canada Graduate Scholarships Doctoral (CGS D) program. R.D. acknowledges financial support provided by the Natural Sciences and Engineering Research Council of Canada through a Discovery Grant, as well as the Alfred P. Sloan Foundation through a Sloan Research Fellowship. C.L. and G.L. acknowledge funding from the European Union's Horizon 2020 research and innovation programme under the Marie Sklodowska-Curie grant agreement # 823823 (RISE DUSTBUSTERS project). C.L. acknowledges funding from UK

Science and Technology research Council (STFC) via the consolidated grant ST/W000997/1. B.V. acknowledges funding from the ERC CoG project PODCAST No 864965. Y.W.T. acknowledges support through NSTC grant 111-2112-M-001-064- and 112-2112-M-001-066-. J.H. was supported by JSPS KAKENHI Grant Numbers 21H00059, 22H01274, 23K03463. J.C. acknowledges support from the National Natural Science Foundation of China under grant No. 12233004 and 12250610189. D.S.-C. is supported by an NSF Astronomy and Astrophysics Postdoctoral Fellowship under award AST-2102405.

This paper makes use of the following ALMA data: ADS/JAO.ALMA#2021.1.00690.S. ALMA is a partnership of ESO (representing its member states), NSF (USA) and NINS (Japan), together with NRC (Canada), MOST and ASIAA (Taiwan), and KASI (Republic of Korea), in cooperation with the Republic of Chile. The Joint ALMA Observatory is operated by ESO, AUI/NRAO and NAOJ. The National Radio Astronomy Observatory is a facility of the National Science Foundation operated under cooperative agreement by Associated Universities, Inc.

Based on data products created from observations collected at the European Organisation for Astronomical Research in the Southern Hemisphere under ESO programme 0104.C-0157(B). This work has made use of the SPHERE Data Centre, jointly operated by OSUG/IPAG (Grenoble), PYTHEAS/LAM/CESAM (Marseille), OCA/Lagrange (Nice), Observatoire de Paris/LESIA (Paris), and Observatoire de Lyon.

This research used the Canadian Advanced Network For Astronomy Research (CANFAR) operated in partnership by the Canadian Astronomy Data Centre and The Digital Research Alliance of Canada with support from the National Research Council of Canada the Canadian Space Agency, CANARIE and the Canadian Foundation for Innovation.

Based on observations made with the NASA/ESA Hubble Space Telescope, obtained from the Data Archive at the Space Telescope Science Institute, which is operated by the Association of Universities for Research in Astronomy, Inc., under NASA contract NAS5-26555. These observations are associated with program #8065.

Herschel is an ESA space observatory with science instruments provided by European-led Principal Investigator consortia and with important participation from NASA. PACS has been developed by a consortium of institutes led by MPE (Germany) and including UVIE (Austria); KU Leuven, CSL, IMEC (Belgium); CEA, LAM (France); MPIA (Germany); INAF-IFSI/OAA/OAP/OAT, LENS, SISSA (Italy); IAC (Spain). This development has been supported by the funding agencies BMVIT (Austria), ESA-PRODEX (Belgium), CEA/CNES (France), DLR (Germany), ASI/INAF (Italy), and CICYT/MCYT (Spain). SPIRE has been developed by a consortium of institutes led by Cardiff University (UK) and including Univ. Lethbridge (Canada); NAOC (China); CEA, LAM (France); IFSI, Univ. Padua (Italy); IAC (Spain); Stockholm Observatory (Sweden); Im-

perial College London, RAL, UCL-MSSL, UKATC, Univ. Sussex (UK); and Caltech, JPL, NHSC, Univ. Colorado (USA). This development has been supported by national funding agencies: CSA (Canada); NAOC (China); CEA, CNES, CNRS (France); ASI (Italy); MCINN (Spain); SNSB (Sweden); STFC, UKSA (UK); and NASA (USA).

Facilities ALMA, VLT, Herschel, HST

Software `astropy` (Astropy Collaboration et al., 2013, 2018), `bettermoments` (Teague & Foreman-Mackey, 2018b,a), `CASA` (McMullin et al., 2007b), `CMasher` (van der Velden, 2020), `gofish` (Teague, 2019b), `keplerian_mask` (Teague, 2020), `matplotlib` (Hunter, 2007), `numpy` (Harris et al., 2020), `pandas` (McKinney, 2011), `pvextractor` (Robitaille et al., 2018), `pyvista` (Sullivan & Kaszynski, 2019), `scipy` (Virtanen et al., 2020).

Data Availability All ALMA data products presented in this work are available through the CANFAR Data Publication Service at `https://doi.org/10.11570/24.0098`. This includes final reduced and calibrated ALMA measurement sets, image cubes, masks and moment maps. The raw ALMA data are publicly available via the ALMA archive `https://almascience.nrao.edu/aq/` under project ID 2021.1.00690.S. Animations of Figures 5.3.2, 5.B.2, 5.C.3, 5.D.4, and 5.E.5 are available in the online Journal and on FigShare: `https://doi.org/10.6084/m9.figshare.28205066.v1`.

Appendix

5.A Robustness of SO brightness peak to continuum subtraction

Figure 5.A.1 presents our ALMA continuum image at 1.3 mm alongside peak intensity and integrated intensity maps of SO $J_N = 5_6 - 4_5$ imaged with and without continuum subtraction. The SO ring peaks exterior to, but still overlaps with, the continuum ring (c.f. Fig. 2 of Dutrey et al., 2024). As seen in previous works (e.g., Tang et al., 2017; van der Marel et al., 2021; Rivière-Marichalar et al., 2024), the continuum ring exhibits an azimuthal asymmetry, concentrated on nearly the opposite side of the disk to the brightness peak in SO. We re-imaged the SO data without continuum subtraction to confirm the SO brightness peak is not the gas counterpart

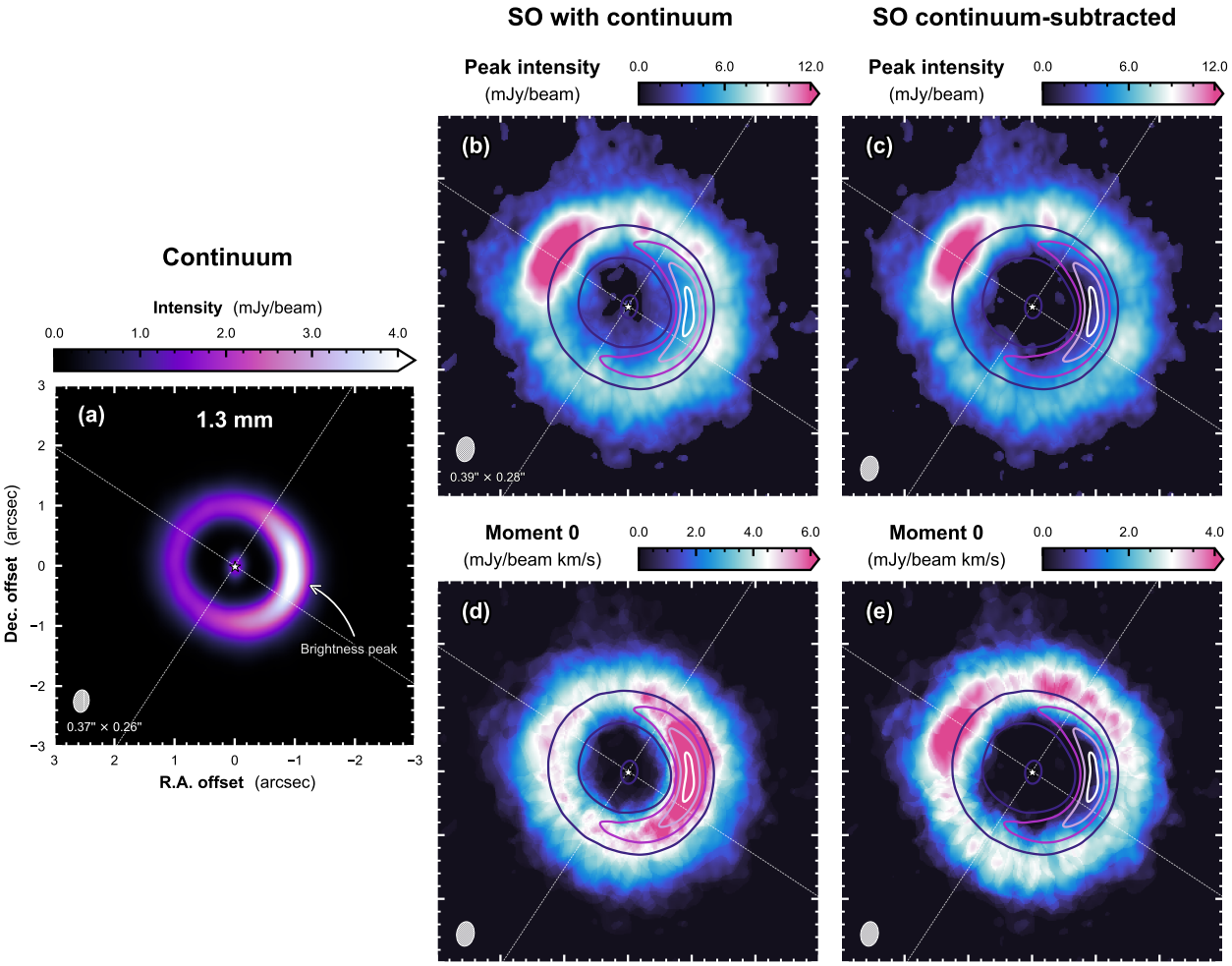

Figure 5.A.1: **The influence of the continuum ring substructure on the observed SO ring substructure in peak intensity vs. integrated intensity maps. (a)** ALMA continuum image at 233.0 GHz from the program presented in this work. The continuum is overlaid in contours at 1.0, 2.0, 3.0 and 4.0 mJy/beam in all other panels. **(b)** ALMA SO $J_N = 5_6 - 4_5$ peak intensity map before continuum subtraction, and **(c)** after continuum subtraction (shown in the main text). These two maps are shown on the same colorbar scale. **(d)** ALMA SO $J_N = 5_6 - 4_5$ integrated intensity map before and **(e)** after continuum subtraction.

of the dust continuum asymmetry. As shown in the top row of Figure 5.A.1, the two *peak* intensity maps are very similar: the inclusion of the continuum extends the ring's apparent width inward, but the exterior substructure is brighter than the continuum and remains unchanged. In contrast, the substructure seen in an *integrated* intensity map of SO is greatly influenced by the presence or subtraction of the continuum, as shown in the bottom row of Figure 5.A.1.

Table 5.B.1: Keplerian Mask Parameters

Transition	$M_\star$ [a] ($M_\odot$)	d [b] (pc)	i [c] (°)	P.A. [a] (°)	$v_{\rm sys}$ [a] (m/s)	$r_{\rm out}$ ($''$)	ΔV_0 (m/s)	ΔV_q	z/r	$\theta_{\rm conv}$ ($''$)
^{12}CO $J=2-1$	2.23	155.9	23.2	236.7	5850	20.0	700.0	0.0	0.0	None

[a] Speedie et al. (2024). [b] Gaia Collaboration et al. (2023). [c] Tang et al. (2012, 2017).

5.B Keplerian and Anti-Keplerian Masks

Our process to disentangle the bulk rotating component of ^{12}CO $J=2-1$ emission from all other emission was inspired by Huang et al. (2021) and broadly follows their approach to isolate the extended ^{12}CO structures in GM Aur (see their Figure 17 and Appendix C).

First, we generate a Keplerian mask using the `keplerian_mask` script of Teague (2020). The result is a cube of the same dimensions as the data but filled with Boolean values reflecting the position-position-velocity (PPV) volume of the ^{12}CO emitting region (e.g., see §5.1 of Czekala et al., 2021). This volume is calculated given a specified stellar mass $M_\star$, distance d, disk inclination i, position angle, systemic velocity $v_{\rm sys}$, outer radius $r_{\rm out}$, constant emission surface slope z/r, and intrinsic line width parameters ΔV_0 and ΔV_q. The intrinsic line width profile is described by:

$$\Delta V(r) = \Delta V_0 \left(\frac{r}{1''}\right)^{\Delta V_q}. \tag{5.B.1}$$

Table 5.B.1 lists the parameters we adopted. Our choices for $r_{\rm out}$, z/r, ΔV_0 and ΔV_q were found by experimentation, with the goal of capturing the disk emission at large radii (made tricky by super-Keplerian rotation) while evading non-Keplerian emission at small radii (made tricky by S1). The `keplerian_mask` routine additionally offers the option to convolve the mask with a 2D Gaussian beam (of FWHM $\theta_{\rm conv}$) to account for emission broadening, which we opted not to do for simplicity.

Next, we generate an anti-Keplerian mask as an exact copy of the Keplerian mask but with its Boolean values switched (`1`s to `0`s and vice versa). The result is a second cube of the same dimensions as the data, now with a 'hole' reflecting the PPV volume of the ^{12}CO emitting region.

The top half of Figure 5.B.2 provides a view of the Keplerian and anti-Keplerian masks at this stage in the process. For what follows, note that the spectrum in each spatial pixel of the Keplerian mask is a top hat function (and in the anti-Keplerian mask it is an upside-down top hat function).

From here, we perform post-processing on the masks to mitigate artifacts created in the moment maps from the hard (discontinuous) edges of the PPV volumes (c.f. Figure 17 of Huang

et al., 2021). We spectrally smooth the masks by convolving the spectrum in each spatial pixel with a Gaussian 5 channels wide. This transforms Boolean masks into 3D weighting functions and has the desired effect of softening the edges of the PPV volumes. Insofar as the weights in the edges are modulated (from `1` to slightly less than `1`, or from `0` to slightly more than `0`), the spectral smoothing introduces 'overlap' between the PPV volumes in each cube. The bottom half of Figure 5.B.2 provides a view of the Keplerian and anti-Keplerian masks at the end of the process.

As a final note of nuance, we considered defining an anti-Keplerian mask as a Keplerian mask of opposite *inclination*; however, the resulting two masks would be identical at the disk minor axis, and ineffective at separating the ^{12}CO emission components identified here.

5.C Connection to larger environment

Figure 5.C.3 provides a multi-wavelength view of AB Aur's environment from 10^5 au to 10^2 au scales. The top panel shows where AB Aur is situated within the L1517 cloud in the Taurus-Auriga complex (Luhman, 2023; Garufi et al., 2024; Ribas et al., 2017), in photometric observations of dust emission from the Herschel SPIRE instrument (Pilbratt et al., 2010; Griffin et al., 2010) at 250 μm. The second row of panels zooms into a $10' \times 10'$ square, and shows the location of AB Aur in Herschel PACS (Poglitsch et al., 2010) and SPIRE maps at increasing wavelengths (70 μm, 160 μm, 250 μm and 350 μm). These four maps are Level 2.5 data products retrieved from the Herschel Science Archive, from the Herschel Key Project Gould Belt Survey (André et al., 2010; HGBS Team, 2020) with OBSIDs 1342204843 and 1342204844 (OD 492). SU Aurigae is within $3'$ of AB Aur on the sky. The bottom row zooms into a $38'' \times 38''$ square centered on AB Aur, showing the field of view of our ALMA observations outlined in yellow. In this panel we present a moment 0 map of ^{12}CO emission imaged with a Briggs weighting of `robust=1.5`, showing the faint 'tail-like' emission structure extending from the disk to the south. We stress that this image has not been primary beam corrected (see below). In the bottom left panel, we overlay the ALMA field of view as a yellow circle onto the R-band (647 nm) image toward AB Aur obtained by the University of Hawaii 2.2 m Telescope (Grady et al., 1999; Nakajima & Golimowski, 1995) showing the arc-shaped reflection nebula surrounding AB Aur from the east to the south (Dullemond et al., 2019; Kuffmeier et al., 2020; Gupta et al., 2023).

While a detailed kinematic analysis is outside the scope of this work, we describe that the ^{12}CO tail is comprised of subcomponents: the first is observed blueshifted of $v_{\rm sys}$ (between 5.010 – 5.850 km/s in LSRK) due south of the star, and the second is observed redshifted of $v_{\rm sys}$ (between 5.976 – 6.942 km/s in LSRK) ever so slightly counter-clockwise of south. The latter ex-

hibits a substructure like three 'whiskers' over several channels. Animated ^{12}CO channel maps are available (Figure 5.C.3) in the online article.

As discussed in §5.5.1, our detection of the ^{12}CO tail suffers from the reduced response of the ALMA 12m antenna at the edge of our imaged FOV, where the sensitivity is 5× lower than at the pointing center, and, as stressed above, the image in Figure 5.C.3 has not been corrected for this effect. We show the non-primary beam corrected image without the quantification of a colorbar to reflect that it should be considered for morphology only. Aliases of the tail also appear multiple times around the edge of the FOV. Such aliasing artifacts are known to be introduced by bright sources outside the primary beam (ALMA Technical Handbook, §11.5). Observations with a larger FOV and sensitivity to larger spatial scales are needed to achieve improved sensitivity to extended emission, in order to investigate the ^{12}CO tail and hypothesized association between the cloudlet.

5.D Radial and Azimuthal PV Slices

Figure 5.D.4 explores the trajectories of S1, S2 and S3 in in radial and azimuthal PV diagrams. The left column of Figure 5.D.4 shows radial PV cross sections at varying azimuths around the eastern (blueshifted) major axis. The right column shows azimuthal PV cross sections at varying radii between $r = 1'' - 2''$. As in the main text, the background colormap shows slices taken through the (unmasked) ^{12}CO image cube, and the filled contours are from slices taken through the SO image cube. Orange contours are overplotted using slices through the Keplerian weighted ^{12}CO cube to delineate emission associated with the disk. Cyan contours encircle S1, S2 and S3 from slices through the anti-Keplerian weighted ^{12}CO cube. We inspected a fine and complete grid of PV slice orientations to build an understanding of their $v_{\rm LOS}$ behaviour as a function of azimuth and radius, available as animations in the online article. A representative selection of slices is shown in Figure 5.D.4, demonstrating where ^{12}CO emission from S1 and S2 becomes indistinguishable from the emission from the disk.

5.E Streamline Parameters and 3D Rendering

Table 5.E.2 provides the parameters describing the streamline solutions presented in §5.4.2. The angular frequency of the sphere's rigid-body rotation is represented by Ω, and r_0 is its radius. The initial radial velocity of the 'particle' is $v_{r,0}$, while ϕ_0 and θ_0 are its initial azimuthal and polar angles, respectively. θ_0 is measured from the positive z axis (such that $\theta_0 = 90°$ defines

Table 5.E.2: Parameters describing the PIMS streamline solutions, and resulting properties.

Streamline	Ω (Hz)	r_0 (au)	$v_{r,0}$ (km/s)	ϕ_0 (°)	θ_0 (°)	$i_{\rm pims}$ (°)	$\rm PA_{pims}$ (°)	$r_{\rm cent}$ (au)	$v_{r,\rm term}$ (km/s)	$v_{\phi,\rm term}$ (km/s)	$v_{z,\rm term}$ (km/s)
S1	1.50×10^{-11}	650	1.5	374	80	-56.8	43.3	350	1.4	4.1	0.7
S2	8.00×10^{-12}	1000	1.0	30	55	-56.8	53.3	557	1.7	3.0	2.0
S3	1.40×10^{-11}	325	0.25	290	135	-66.8	33.3	19	5.4	1.3	3.3

the sphere's equatorial plane), and ϕ_0 is measured from the positive x axis toward the positive y axis. The angles $i_{\rm pims}$ and $\rm PA_{pims}$ are used in the two rotational transformations to project the streamline's 'native' coordinates onto the sky. The inclination $i_{\rm pims}$ defines rotation about the native x axis, and negative inclination corresponds to viewing the sphere's midplane "from below", i.e., up from along the negative z axis. $\rm PA_{pims}$ is defined as rotation about the native y axis, where $\rm PA_{pims} = 0°$ aligns minor axis of the midplane with north.

Following the discussion in §5.5.3, we provide the intrinsic velocity components at the terminal ends of the three model streamlines in the frame of the rigid rotating sphere: the inward radial velocity $v_{r,\rm term}$, the azimuthal velocity $v_{\phi,\rm term}$, and the downward vertical velocity $v_{z,\rm term}$ (Table 5.E.2). The terminal velocities of the S1 and S2 streamlines range $0.7-4.1$ km/s. Table 5.E.2 also lists the streamlines' centrifugal radii, $r_{\rm cent}$. Sakai et al. (2014) connected an observed enhancement of SO to the centrifugal radius in ALMA observations of L1527, which has since been seen in more sources (e.g., Oya et al., 2016; Sakai et al., 2017). Our model streamline solution for S1 has a centrifugal radius of ~ 350 au, conspicuously close to the observed radius of the SO ring ($150-300$ au). For S2 the value is larger (~ 550 au). We caution direct comparisons here though: since the model is ballistic, angular momentum loss by friction is not considered.

In Figure 5.E.5, we show a rendering of the disk+streamline system in 3D spatial coordinates, $\langle \rm RA, Dec, LOS\rangle$, using the software `pyvista` (Sullivan & Kaszynski, 2019). The SO peak intensity map is rendered, semi-transparent, onto a planar disk with the orientation of AB Aur's midplane for comparison with the terminal ends of S1 and S2. It is significant that despite letting all parameters vary (save for the central mass M; §5.4.1), we find a family of streamline solutions for each of S1 and S2 that are physically coherent in 3D spatial coordinates.

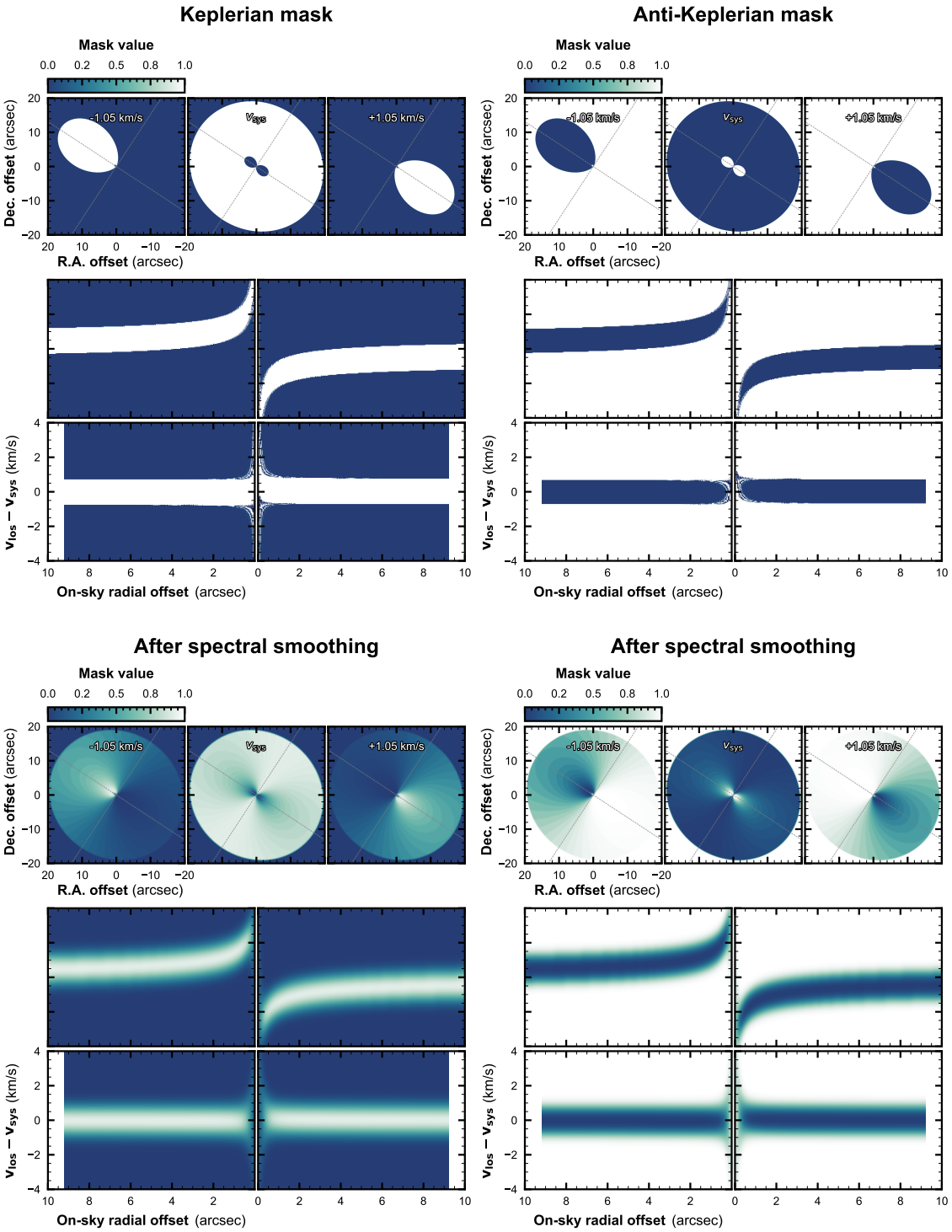

Figure 5.B.2: **A presentation of the Keplerian and anti-Keplerian masks. Top:** Boolean versions prior to spectral smoothing. The topmost panels show three channel maps from the masks at three demonstrative velocities. The panels immediately below show PV slices taken through the masks along the disk major and minor axes, as in Figure 5.3.2. **Bottom:** Smoothed versions after convolving the spectra in each spatial pixel of the masks with a Gaussian kernel. These are used as 3D weighting functions to separate the observed ^{12}CO emission into its constituent disk and exo-disk components.

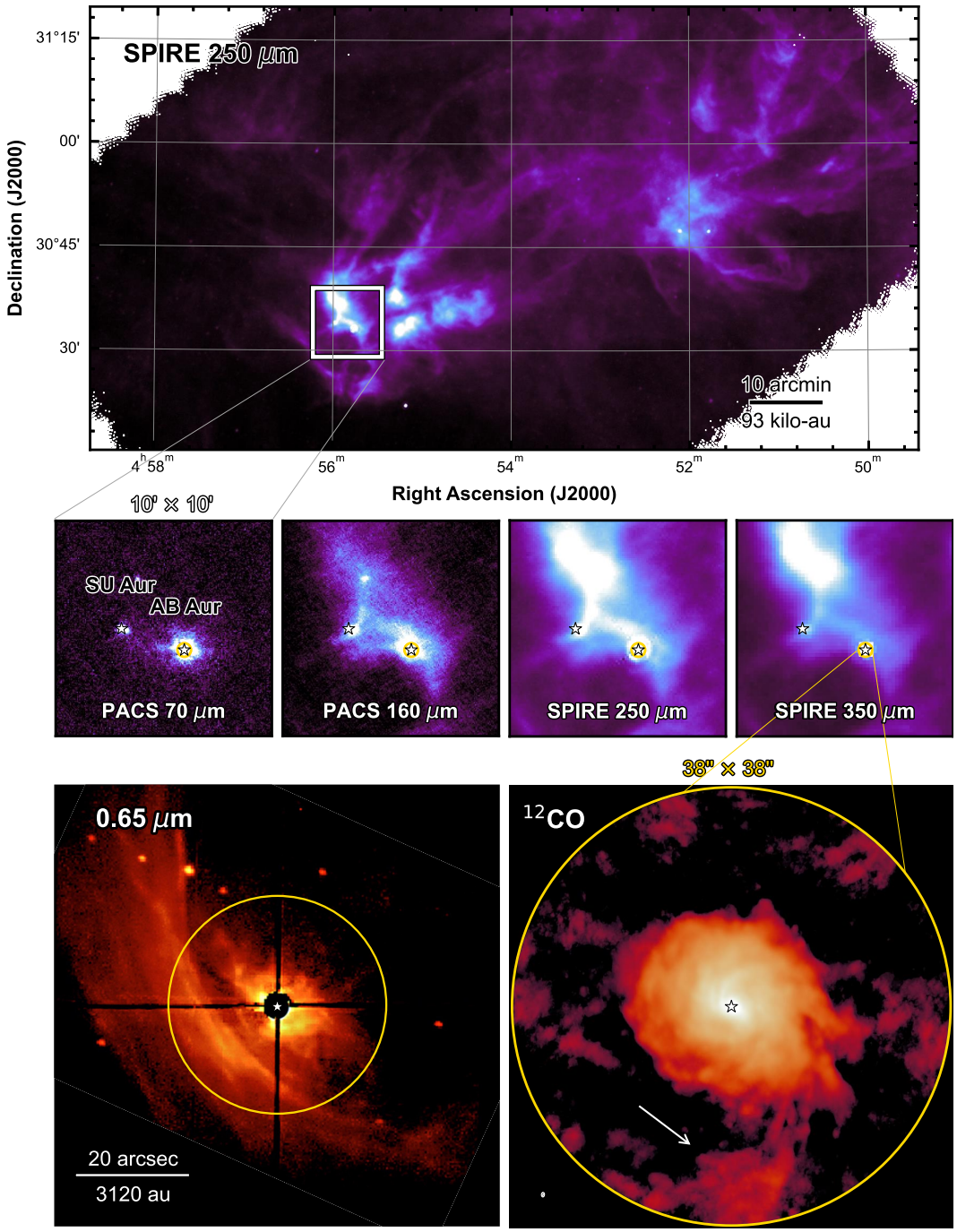

Figure 5.C.3: **Multi-wavelength view of AB Aur's kilo-au environment and a tentative tail in ^{12}CO. Top:** Herschel SPIRE 250 μm map of the L1517 cloud. A scale bar in the bottom right corner shows 10′ or 93 kilo-au. **Middle:** $10' \times 10'$ zoom-in toward AB Aur in Herschel PACS and SPIRE maps at 70 μm, 160 μm, 250 μm and 350 μm. The location of SU Aurigae is also marked. **Bottom right:** ALMA ^{12}CO $J = 2-1$ moment 0 map, imaged with Briggs `robust=1.5` and without primary beam correction. The white arrow points to the tail. **Bottom left:** Optical image toward AB Aur at 647 nm from the University of Hawaii 2.2 m Telescope (PI: P. Kalas; Grady et al., 1999). This image is used with permission of P. Kalas. In all panels, the yellow circle marks the edge of our imaged ALMA field of view (§5.2).

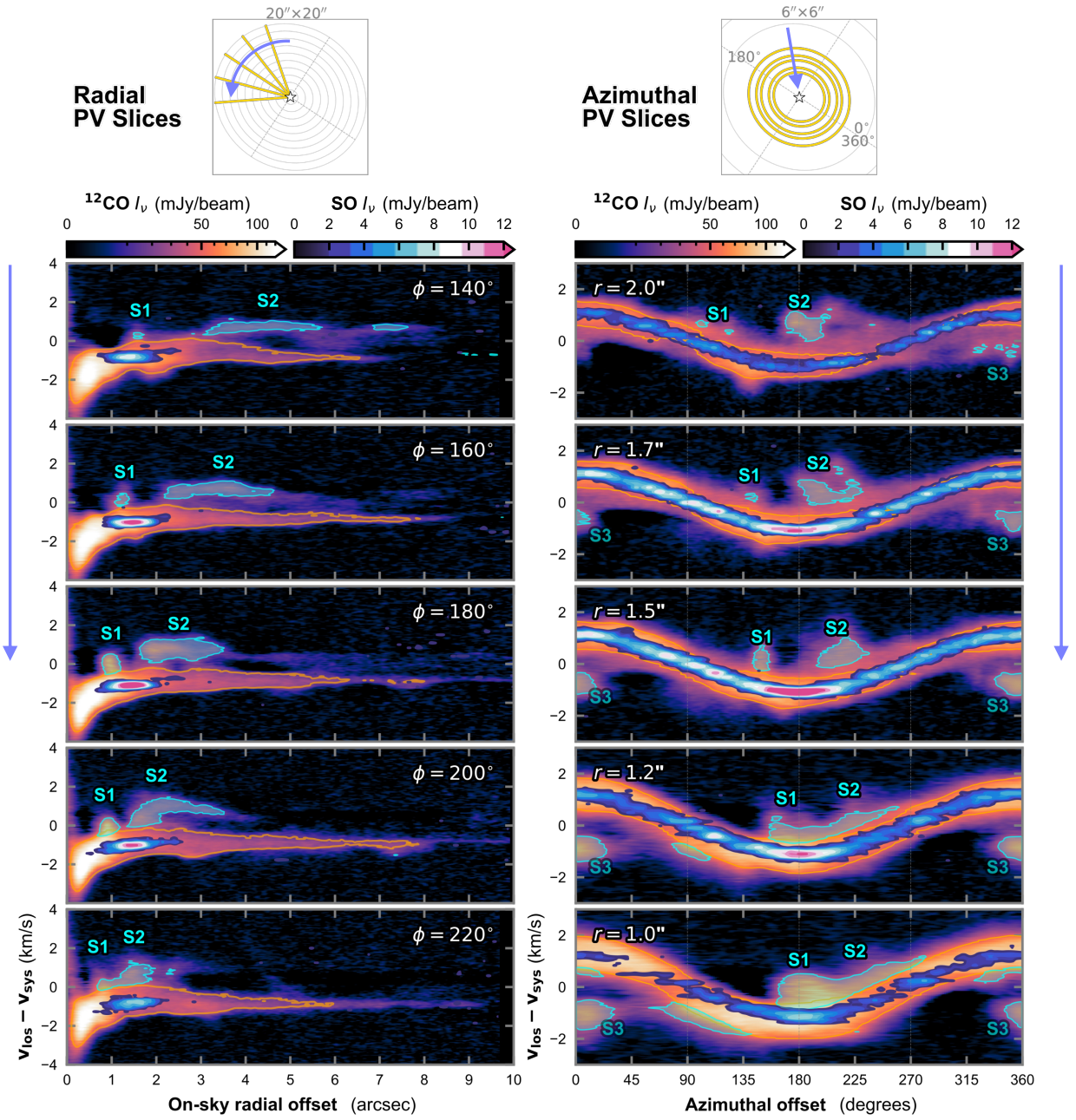

Figure 5.D.4: **Radial and azimuthal PV cross sections in ^{12}CO and SO.** The yellow lines and circles in the diagram above each column shows the slice paths of the PV diagrams in the panels below. In the left column, panels are ordered top to bottom by their azimuthal angle in the direction the disk rotates (counter-clockwise). In the right column, panels are ordered by decreasing radius. PV slices are shown for the three ^{12}CO cubes: the full unweighted ^{12}CO cube (colormap), the Keplerian weighted ^{12}CO cube (orange contours), and the anti-Keplerian weighted ^{12}CO cube (cyan contours). PV slices in the SO $J_N = 5_6 - 4_5$ image cube are overplotted as filled contours in increments of 2σ starting at 3σ.

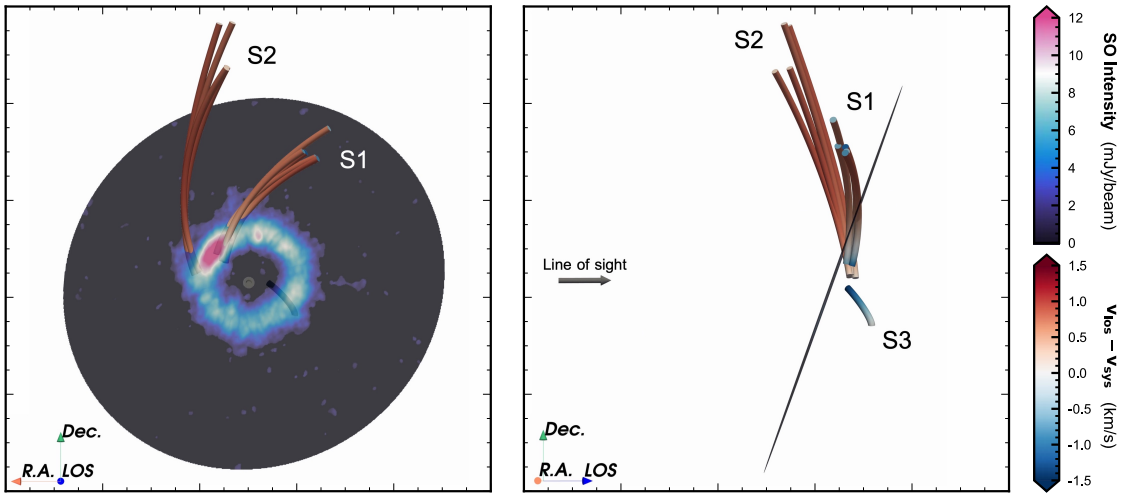

Figure 5.E.5: **3D rendering of the AB Aur disk plane and streamline solutions.** The left panel shows the system oriented as viewed from Earth (the RA-Dec plane), and the right panel shows a view from within the plane of the sky (the Dec-LOS plane). The streamlines are rendered as 'tubes' and coloured by their line-of-sight velocity, $v_{\rm LOS}$. The SO peak intensity map is rendered onto a disk with same orientation as the AB Aur midplane. The layer is given 80% transparency to show objects behind the disk. This rendering was enabled by `pyvista` (Sullivan & Kaszynski, 2019).

Chapter 6

Summary and Future Prospects

To understand the origins of our Solar System, and those of the numerous planetary systems in our galaxy, astronomers must study the disk-shaped reservoirs of pre-planetary material surrounding stars just a few million years old. The young planets suspected to be actively forming within these reservoirs are obscured, and few have been detected to date. Similarly indeterminate are the physical processes responsible for assembling them.

This chapter conceptualizes the key contributions of this dissertations as stepping stones, and highlights how they have —or may in the future— serve as springboards for future investigations within the planet formation community (§6.1). I then conclude by offering preliminary demonstrations of ideas toward tackling some open questions of this dissertation's time, building on the techniques developed herein (§6.2).

6.1 Stepping stones and springboards

Planet-hunting. In Chapter 2 of this dissertation, I developed a pipeline to generate synthetic ALMA continuum observations from 2D gas+dust hydrodynamic and radiative transfer simulations. Using this pipeline to explore a wide parameter space of disk properties and observing conditions, I demonstrated the capability of ALMA to detect the faint spiral wakes created by young planets embedded in circumstellar disks. The complete suite of 432 synthetic continuum images from this study was made publicly available[37] to the community.

This work catalyzed further investigation into using spiral wakes as a planet-hunting technique. With Chapter 2's suite of data, Stevenson et al. (2024) developed a way to search for planetary wakes working with the visibilities directly in the Fourier plane. By computing the 2D Fourier transform of the spiral wake as a template in a matched filtering process, Stevenson et al. (2024) were able to recover the planet's location in my synthetic ALMA data, where —in the image plane— the signal was buried in noise (see Figure 6.1.1). Importantly, this approach made it possible to *quantify the significance* of the recovered planetary detections, for the first time.

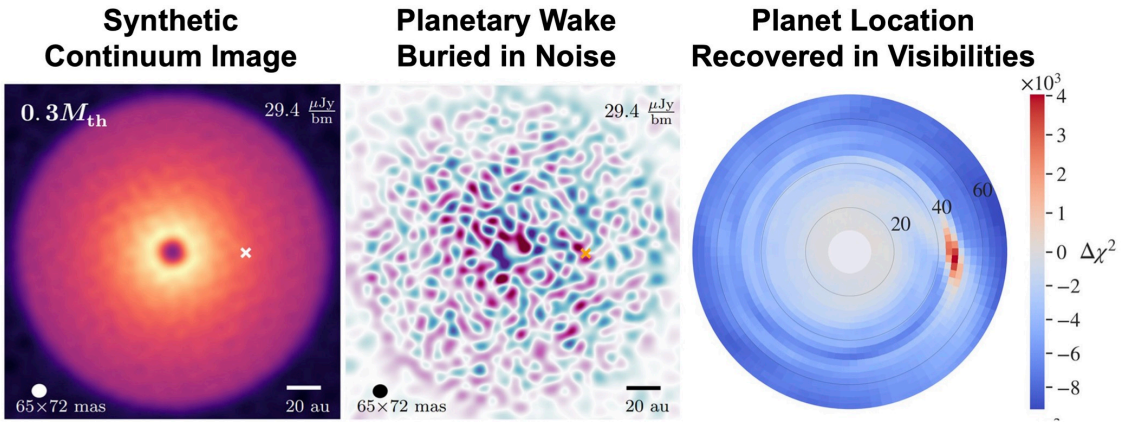

Figure 6.1.1: Matched-filtering a Fourier-plane template of the planetary wake to the observed visibilities successfully recovers the planet location in synthetic ALMA continuum data (right), even when the wake cannot be seen in the image plane (middle and left). A quantification of the detection significance is enabled by comparing the χ^2 improvement over an axisymmetric Fourier template (the null hypothesis). Adapted from Stevenson et al. (2024) and Speedie et al. (2022) (Chapter 2).

Gravitational instability. Chapter 4 embarked on a journey to find long sought-after evidence for a well-known but unproven pathway to form giant planets and companions. Our kinematic

[37] https://doi.org/10.6084/m9.figshare.19148912

detection of gravitational instability (GI) in the AB Aur disk has transformed this instability from a process studied in simulations to a process we can also study in *observations*. We now have an object that we can point to in the sky for an example of this process in action. Overall, this work helped to advance a longstanding debate in the community and bring GI to the forefront as a formation pathway that warrants consideration alongside —and possibly acting in concert with— the canonical core accretion pathways.

Looking forward, the AB Aur system can be an ideal testbed for understanding how planet formation is facilitated by GI-induced spiral arms. There are two immediate next questions that I can see: (i) What are the masses of the candidate planets in formation amongst the spiral arms of this disk? and (ii) Is it the gas component of a spiral arm that fragments into bound objects, or the dust layer — or both?

This study was published with coordinated press releases[38] around the world; it was also the first *Nature* paper to be lead-authored by a physics or astronomy graduate student at the University of Victoria, and was recognized by the university through a personal letter and university-wide news story.

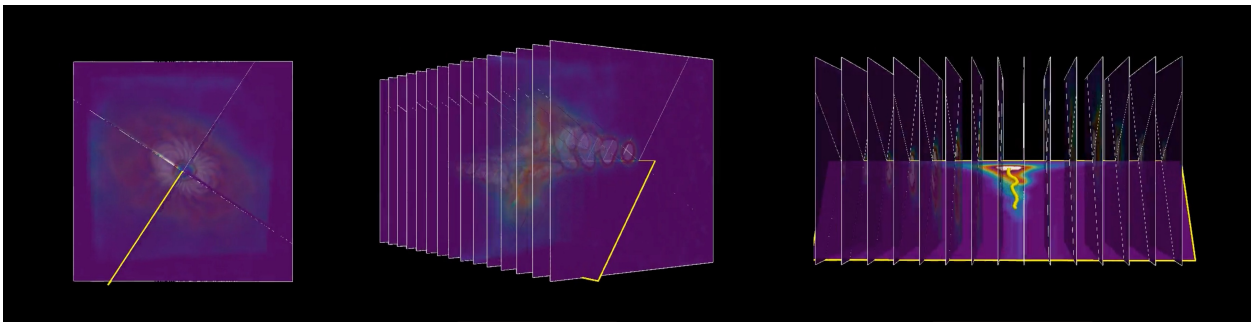

Figure 6.1.2: Three frames from a press release animation visualizing how the GI wiggle is revealed in a position-velocity slice through the ALMA cube. Credits: ALMA (ESO/NAOJ/NSF NRAO), J. Speedie.

Analysis techniques and community resources. In addition to science results, this dissertation developed techniques that are broadly applicable to ALMA spectral cube data, as well as to 2D image data of any kind.

Chapter 4 developed `expanding_kernel`: a variation on the conventional high-pass filtering (a.k.a. unsharp masking) technique, which is a widely used technique to increase the visual contrast of variations in an image. The conventional method is to convolve the image with a spatially constant Gaussian kernel and subtract the blurred image from the original. I introduced a way to perform the convolution with a radially expanding kernel, as visualized in Figure

[38] https://public.nrao.edu/news/alma-detects-wiggle/

6.1.3. A radially expanding kernel highlights variations more evenly throughout the image when the spatial scales and the dynamical range of the variations change with radius. I used this technique to reveal global spiral structure in the AB Aur disk in Chapter 4 and 5, and provided[39] the code to the community.

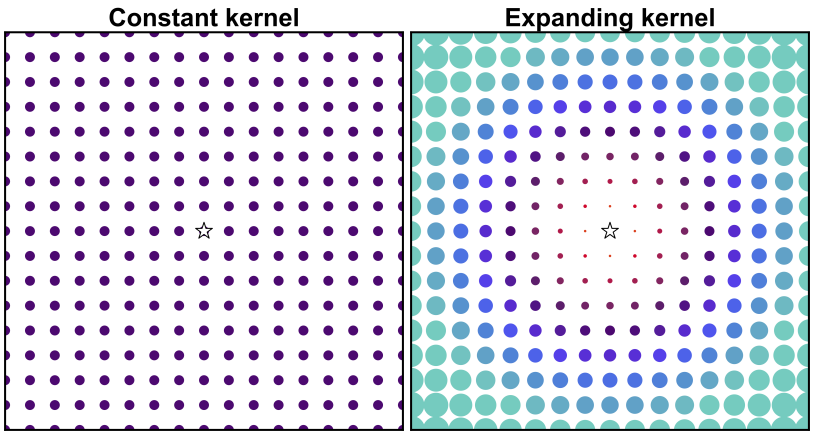

Figure 6.1.3: A visual comparison between the conventional high-pass filtering technique (left), and the new technique I developed and applied in Chapter 4 and 5(right).

In Chapter 5, I established "anti-Keplerian masking" as a method to disentangle disk emission from highly disordered surrounding gas by leveraging the characteristic spatio-kinematic volumetric shape of Keplerian rotation. This method effectively inverts the "Keplerian masking" technique broadly in use over the last half decade (Teague, 2020). As the community increasingly turns its attention to study "streamers" and infall from the cloud onto the disk across various stages of disk evolution, forthcoming ALMA spectral line observations are expected to exhibit comparable levels of complexity. My approach offers an intuitive means of isolating the disk signal from such complex emission, allowing the two components to be studied independently. This is a key step towards a clear analysis.

Across this dissertation, I ensured to make the data and tools behind each study available to the community. Datasets (synthetic or real) from all the chapters are publicly available for download. As a community resource, I released an extensive online guide[40] detailing the step-by-step process I took in Chapters 4 and 5 to align, combine and image the raw ALMA data into the published science products.

[39] https://github.com/jjspeedie/expanding_kernel
[40] https://jspeedie.com/guide.2021.1.00690.S/intro.html

6.2 Future Directions

One could argue that the field of planet formation today is at a similar stage to the field of exoplanet research thirty years ago. Just as the field of exoplanet research saw the first detections of fully mature planets in the mid-1990s, today's field of protoplanet research is achieving the first images and signatures of protoplanets still forming deep within their birth environments.

Radio interferometry offers a unique avenue to drive advances, enabling us to penetrate deep into the planet-forming environment and probe the midplane of circumstellar disks. With early glimpses of embedded planets recently found in the (sub)mm continuum (PDS 70 c; Benisty et al., 2021) and in molecular line emission (AS 209 b; Bae et al., 2022a), we are at the dawn of protoplanet discovery in the (sub)millimeter.

At present, detections of embedded protoplanets are still scarce and our understanding is still rudimentary. We currently have no model-independent way to constrain protoplanet mass, and the circumplanetary disk that mediates a protoplanet's growth (a region of order $10^3\times$ larger than the protoplanet itself) is largely uncharacterized. The scarcity of detections poses a significant challenge: *How can we study planet formation without knowing where the protoplanets are?* New protoplanet detection techniques —and innovations in existing ones— are needed to overcome our current observational barriers and drive the future of protoplanet discovery.

Identifying velocity kinks of planetary origin. Unambiguous identification of kinematic features driven by planets vs. non-planetary mechanisms is currently missing in the field. The findings of Chapter 3 suggest that not all localized velocity kinks in intensity channels are unequivocally associated with planets. It is imperative that we distinguish the myriad of non-planetary velocity disturbances from those of planets reliably, in order to fully wield the power of kinematics as a planet-hunting technique.

This dissertation propounds that opportunities for progress on this front lie in position-velocity (PV) space. Chapters 4 and 5 showed how PV slicing is a powerful tool to robustly identify the morphology of velocity disturbances and quantify them in natural units. Specifically, PV slicing along paths of constant disk azimuth in Chapter 4 enabled us to morphologically identify GI-wiggles, quantify their magnitude in units of velocity, and make apples-to-apples comparisons with models. In Chapter 5, PV slicing along paths of constant azimuth and radius enabled us to precisely pinpoint the 2D (r,ϕ) zone where streamers merge within the disk. However, there is a *third* geometric path that is inherently natural to a rotating disk: paths of constant velocity. *What could we achieve with PV slicing along Keplerian isovelocity contours?*

Figure 6.2.4 provides a preliminary demonstration of the diagnostic power of PV slicing

along Keplerian isovelocity contours. This technique is applied to a synthetic ALMA ^{12}CO image cube of HD 163296 (Calcino et al., 2022), the first system linked to observed planetary velocity kinks (Pinte et al., 2018b). When the correct (frontside) emission surface is adopted, the resulting PV diagram displays the (frontside) emission spectra along a perfectly flat line, and the planet-induced velocity kink can be recognized as a *wake-shaped* deviation.

Keplerian isovelocity slicing thus may hold the key to morphologically identify planet-driven velocity wakes, quantify their magnitude in units of velocity, and even constrain planet mass by fitting the measured pattern to analytic models (e.g., Bollati et al., 2021). Furthermore, this approach may allow for the fitting of flexible emission surfaces as a function of slice velocity, since the optimal contour corresponds to the one that yields flattened spectra. A module to perform this optimization could be readily implemented into the infrastructure of `eddy` (Teague, 2019a).

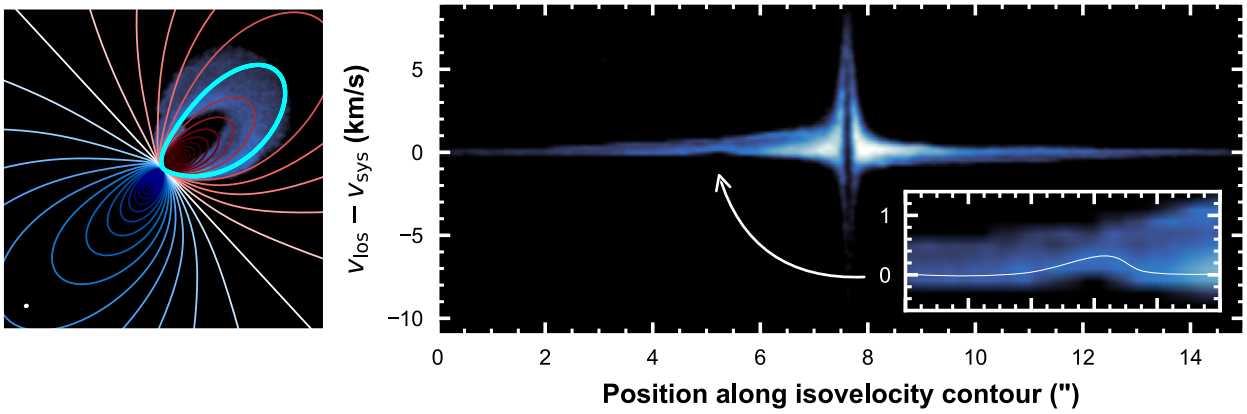

Figure 6.2.4: Position-velocity experiment, slicing along a Keplerian isovelocity contour (cyan contour on left). The resulting PV diagram is shown on the right. With the right emission surface, the spectra lie globally flat, and subtle perturbations can be recognized. The inset panel zooms into the planetary velocity kink, with an annotated white curve to guide the eye. The disk backside is also visible. The underlying model cube used for this experiment is from Calcino et al. (2022) with channel spacing 0.2 km s^{-1}.

Harnessing ALMA's full potential for planet-hunting in the continuum. The near ubiquity of gap/ring substructure observed in circumstellar disks (e.g., Andrews, 2020) must be communicating something fundamental about where, and how, planets are assembled. However, the community is still unclear as to whether these substructures are sites of planetesimals *in the making now* (i.e., rings are sites of planetesimal formation) or signs of unseen giant planets *already formed earlier* (i.e., gaps are sites of orbiting planets). A pressing science question thus arises: Are dust gaps really empty of planets, or have we not looked deep enough?

As ALMA finishes Cycle 11, the ALMA Science Archive now holds a decadal wealth of data,

and *time* represents an emerging dimension to exploit for increased sensitivity. In parallel, the NRAO's newly-launched Science Ready Data Products initiative and automated self calibration pipeline are minimizing the manual time to procure (self-)calibrated datasets. Furthermore, with the ALMA Wideband Sensitivity (WSU) deployment expected to negatively impact available observing time as soon as Cycle 13, archival science will be key in the coming years.

We thus may look to harness ALMA's full potential as a planet-hunting machine by combining continuum data accumulated over its entire operational lifetime. As illustrated in Figure 6.2.5, the ALMA Archive contains enormous untapped potential for achieving unprecedented sensitivity —and correspondingly deep detection limits— in some of the most intensively studied systems, if only these data were combined. No such effort has yet been undertaken. A project of this scope would transform how we see ALMA: not just as a "one science goal, one program" facility, but as a decade-long, ground-based *mission*.

In combining data over such timescales, the usual assumption that our source is not variable in time starts to break down. Figure 6.2.6 shows the expected Keplerian orbital motion over the relevant years in the same three well-studied targets. The angular extent is particularly

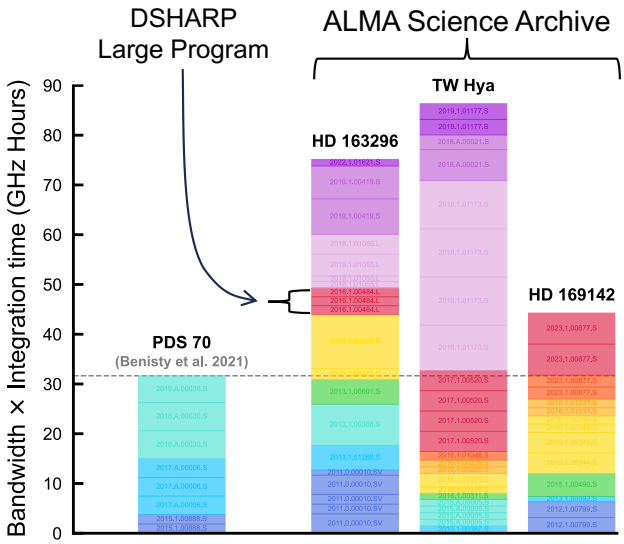

Figure 6.2.5: **Rightmost 3 bar graphs:** Amount of continuum data available in the ALMA Science Archive for three disks with compelling evidence of embedded planets, but no direct detections in the (sub)millimeter. The y-axis is in units of GHz Hours (proportional to sensitivity squared). Only Band 6 data is shown, except for HD 169142 which also includes Band 7. Different colours denote different ALMA Programs. Note that the observation dates span 2012-2023, 2015-2021 and 2015-2024. Horizontal lines within a Program delineate spectral windows. A spectral window is considered here only if it contributes at least 1 GHz Hour (bandwidth × integration time). There are otherwise no constraints on spectral or angular resolution. **Left bar graph:** For comparison, the Band 7 continuum data combined by Benisty et al. (2021) that yielded a successful detection of PDS 70 c.

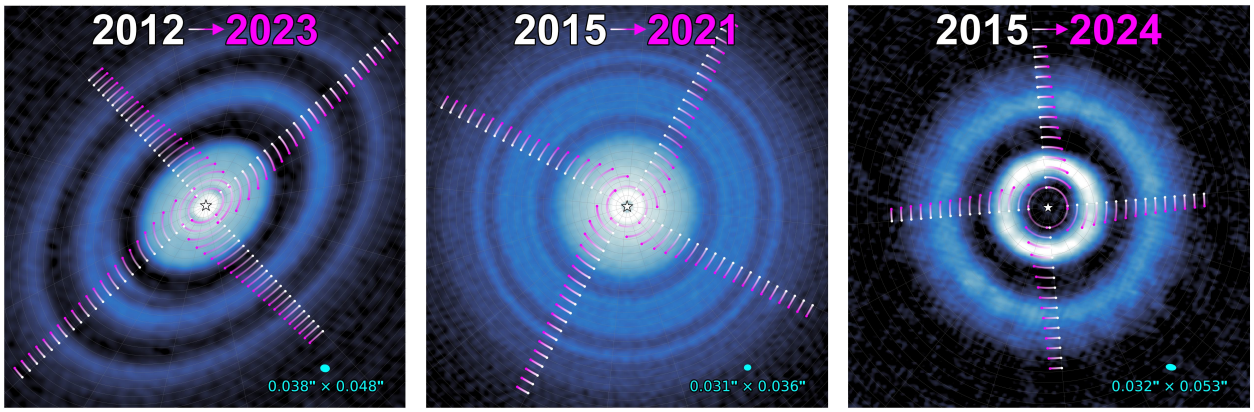

Figure 6.2.6: Angular extent of Keplerian orbital motion in HD 163296, TW Hya, and HD 169142 over the observation dates of the ALMA Programs included in Figure 6.2.5. Underlying continuum images are from Andrews et al. (2018), Macías et al. (2021) and Law et al. (2023). All panels are $1'' \times 1''$.

appreciable at small radii. To fully harness ALMA's 10-year observational baseline and enhance flux from putative planets, it will likely be necessary to 'de-shear' the visibility measurements to correct for Keplerian orbital motion and align data from different epochs, prior to combining datasets.

The development of a de-shearing algorithm for application on the full ALMA archive would deliver the tightest constraints achievable on the presence of planets in dust continuum gaps. Whether young planets are detected within these gaps or they are found to be empty, the results would have consequential implications for our understanding of planet formation.

Leveraging spectral resolution with ALMA WSU. Chapter 1 (§1.2) introduced the breakthrough detection of a rotating circumstellar disk around HL Tau during the *Protostars and Planets III* era. Observations of ^{13}CO molecular line emission with the Owens Valley Radio Observatory revealed a characteristic double-peaked line profile — an unmistakable signature of Keplerian rotation (Sargent & Beckwith, 1987).

Fast-forwarding 35 years to the era of *Protostars and Planets VII*, the frontier has shifted to considerably smaller spatial scales. We now have the first candidate detection of molecular line emission from a circum*planetary* disk, observed in ^{13}CO with ALMA around AS 209 b (Bae et al., 2022a). However, the spectral resolution of the data remains insufficient to determine whether the emission arises from a rotationally supported circumplanetary disk, or a more spherical circumplanetary envelope.

Despite this frontier shift to smaller spatial scale, there is a core physical principle that remains the same: Doppler shifts in molecular line emission reveal the gravitational influence

of a central mass (see Figure 6.2.7). Just as this principle provided the first dynamical insights into circumstellar disks, the line profile of circumplanetary gas has the potential to unlock the dynamics of the immediate circumplanetary environment.

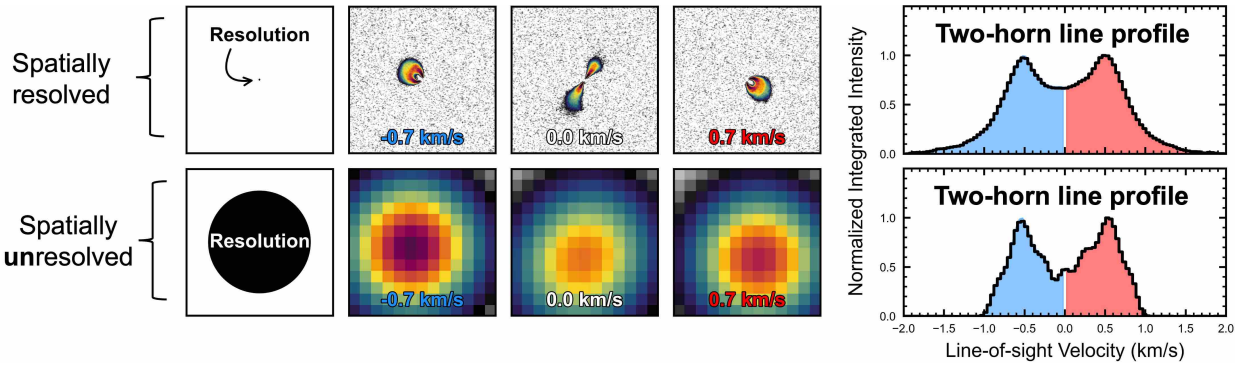

Figure 6.2.7: A two-horn line profile —a signature of rotation— can be spectrally resolved even when the observed disk is not spatially resolved. This is a preliminary experiment using 3D hydrodynamic and radiative transfer simulations of a circum*stellar* disk in rotation around a star, generated with the pipeline developed in Chapter 4.

Fulfilling this potential likely requires a leap in spectral resolution — one that the ALMA Wideband Sensitivity Upgrade (WSU), due to come online in 2028, is poised to deliver. This upgrade will offer ultra-high spectral resolutions of $13.5/N$ kHz, where the Zoom Factor $N \in [1,2,4,8]$ (Carpenter et al., 2022). For ^{13}CO $J = 2-1$ ($\nu_{\rm rest} \approx 200$ GHz) and a Zoom Factor of $N = 8$, this translates to a remarkable velocity resolution of 2.3 m s^{-1}. Such precision will facilitate the disentanglement of circumplanetary emission from surrounding circumstellar contamination, and resolve the morphology of circumplanetary line profiles in detail. At a minimum, this spectral fidelity will make it possible to differentiate between a rotationally-supported circumplanetary disk and a more isotropic envelope.

Even more profoundly, it may open the door to the most weighty goal of all: measuring the mass of a forming planet directly from dynamics, just as we do for stars today. Estimating protoplanet mass has remained one of the field's most persistent challenges, with existing methods relying on indirect indicators and yielding model-dependent answers. If we can isolate the rotational contribution to the line profile's morphology, we may directly obtain a dynamical constraint, akin to the $M_{\rm p}\sin(i)$ values so foundational to exoplanet science. Such a breakthrough would place the study of forming planets on the same empirical footing as that of mature exoplanets — bridging the observational divide between nascent and evolved planetary systems, and unifying the two fields that study them.

References

Adams, F. C., Lada, C. J., & Shu, F. H. 1987, ApJ, 312, 788, doi: 10.1086/164924

Alarcón, F., Bergin, E. A., & Cugno, G. 2024, ApJ, 966, 225, doi: 10.3847/1538-4357/ad3938

Alexander, R., Pascucci, I., Andrews, S., Armitage, P., & Cieza, L. 2014, in Protostars and Planets VI, ed. H. Beuther, R. S. Klessen, C. P. Dullemond, & T. Henning, 475–496, doi: 10.2458/azu_uapress_9780816531240-ch021

ALMA Partnership, Fomalont, E. B., Vlahakis, C., et al. 2015a, ApJ, 808, L1, doi: 10.1088/2041-8205/808/1/L1

ALMA Partnership, Brogan, C. L., Pérez, L. M., et al. 2015b, ApJ, 808, L3, doi: 10.1088/2041-8205/808/1/L3

Andre, P., Ward-Thompson, D., & Barsony, M. 1993, ApJ, 406, 122, doi: 10.1086/172425

André, P., Men'shchikov, A., Bontemps, S., et al. 2010, A&A, 518, L102, doi: 10.1051/0004-6361/201014666

Andrews, S. M. 2020, ARA&A, 58, 483, doi: 10.1146/annurev-astro-031220-010302

Andrews, S. M., Hughes, A. M., Wilner, D. J., & Qi, C. 2008, ApJ, 678, L133, doi: 10.1086/588730

Andrews, S. M., Teague, R., Wirth, C. P., Huang, J., & Zhu, Z. 2024, ApJ, 970, 153, doi: 10.3847/1538-4357/ad5285

Andrews, S. M., Huang, J., Pérez, L. M., et al. 2018, ApJ, 869, L41, doi: 10.3847/2041-8213/aaf741

Andrews, S. M., Elder, W., Zhang, S., et al. 2021a, ApJ, 916, 51, doi: 10.3847/1538-4357/ac00b9

—. 2021b, ApJ, 916, 51, doi: 10.3847/1538-4357/ac00b9

Aota, T., Inoue, T., & Aikawa, Y. 2015, ApJ, 799, 141, doi: 10.1088/0004-637X/799/2/141

Armitage, P. J. 2019, Saas-Fee Advanced Course, 45, 1, doi: 10.1007/978-3-662-58687-7_1

Arzamasskiy, L., & Rafikov, R. R. 2018, ApJ, 854, 84, doi: 10.3847/1538-4357/aaa8e8

Asaki, Y., Alcalde Pampliega, B., Edwards, P. G., Iguchi, S., & Murphy, E. J. 2023, Nature Reviews Methods Primers volume 3, 3, 89, doi: 10.1038/s43586-023-00273-4

Astropy Collaboration, Robitaille, T. P., Tollerud, E. J., et al. 2013, A&A, 558, A33, doi: 10.1051/0004-6361/201322068

Astropy Collaboration, Price-Whelan, A. M., Sipőcz, B. M., et al. 2018, AJ, 156, 123, doi: 10.3847/1538-3881/aabc4f

Avenhaus, H., Quanz, S. P., Garufi, A., et al. 2018, ApJ, 863, 44, doi: 10.3847/1538-4357/aab846

Bae, J., Hartmann, L., & Zhu, Z. 2015, ApJ, 805, 15, doi: 10.1088/0004-637X/805/1/15

Bae, J., Teague, R., & Zhu, Z. 2021, ApJ, 912, 56, doi: 10.3847/1538-4357/abe45e

Bae, J., & Zhu, Z. 2018a, ApJ, 859, 118, doi: 10.3847/1538-4357/aabf8c

—. 2018b, ApJ, 859, 119, doi: 10.3847/1538-4357/aabf93

Bae, J., Zhu, Z., & Hartmann, L. 2017, ApJ, 850, 201, doi: 10.3847/1538-4357/aa9705

Bae, J., Teague, R., Andrews, S. M., et al. 2022a, ApJ, 934, L20, doi: 10.3847/2041-8213/ac7fa3

—. 2022b, arXiv e-prints, arXiv:2207.05923. https://arxiv.org/abs/2207.05923

Balbus, S. A., & Hawley, J. F. 1991, ApJ, 376, 214, doi: 10.1086/170270

Barrière-Fouchet, L., Gonzalez, J. F., Murray, J. R., Humble, R. J., & Maddison, S. T. 2005, A&A, 443, 185, doi: 10.1051/0004-6361:20042249

Bate, M. R., Bonnell, I. A., & Price, N. M. 1995, MNRAS, 277, 362, doi: 10.1093/mnras/277.2.362

Beck, T. L., & Bary, J. S. 2019, ApJ, 884, 159, doi: 10.3847/1538-4357/ab4259

Beckwith, S. V. W., & Sargent, A. I. 1993, in Protostars and Planets III, ed. E. H. Levy & J. I. Lunine, 521

Beckwith, S. V. W., Sargent, A. I., Chini, R. S., & Guesten, R. 1990, AJ, 99, 924, doi: 10.1086/115385

Benisty, M., Juhász, A., Facchini, S., et al. 2018, A&A, 619, A171, doi: 10.1051/0004-6361/201833913

Benisty, M., Bae, J., Facchini, S., et al. 2021, ApJ, 916, L2, doi: 10.3847/2041-8213/ac0f83

Benítez-Llambay, P., & Masset, F. S. 2016, ApJS, 223, 11, doi: 10.3847/0067-0049/223/1/11

Benz, W., Ida, S., Alibert, Y., Lin, D., & Mordasini, C. 2014, in Protostars and Planets VI, ed. H. Beuther, R. S. Klessen, C. P. Dullemond, & T. Henning, 691–713, doi: 10.2458/azu_uapress_9780816531240-ch030

Berghea, C. T., Bayyari, A., Sitko, M. L., et al. 2024, ApJ, 967, L3, doi: 10.3847/2041-8213/ad43e3

Bertin, G., & Lodato, G. 1999, A&A, 350, 694, doi: 10.48550/arXiv.astro-ph/9908095

Biddle, L. I., Bowler, B. P., Zhou, Y., Franson, K., & Zhang, Z. 2024, AJ, 167, 172, doi: 10.3847/1538-3881/ad2a52

Birnstiel, T., Fang, M., & Johansen, A. 2016, Space Sci. Rev., 205, 41, doi: 10.1007/s11214-016-0256-1

Birnstiel, T., Dullemond, C. P., Zhu, Z., et al. 2018a, ApJ, 869, L45, doi: 10.3847/2041-8213/aaf743

—. 2018b, ApJ, 869, L45, doi: 10.3847/2041-8213/aaf743

Black, D. C., & Matthews, M. S., eds. 1985, Protostars and planets II

Blandford, R. D., & Payne, D. G. 1982, MNRAS, 199, 883, doi: 10.1093/mnras/199.4.883

Boccaletti, A., Di Folco, E., Pantin, E., et al. 2020, A&A, 637, L5, doi: 10.1051/0004-6361/202038008

Boccaletti, A., Pantin, E., Ménard, F., et al. 2021, A&A, 652, L8, doi: 10.1051/0004-6361/202141177

Bohn, A. J., Benisty, M., Perraut, K., et al. 2022, A&A, 658, A183, doi: 10.1051/0004-6361/202142070

Bollati, F., Lodato, G., Price, D. J., & Pinte, C. 2021, MNRAS, 504, 5444, doi: 10.1093/mnras/stab1145

Bondi, H. 1952, MNRAS, 112, 195, doi: 10.1093/mnras/112.2.195

Booth, R. A., & Clarke, C. J. 2016, MNRAS, 458, 2676, doi: 10.1093/mnras/stw488

Booth, R. A., Sijacki, D., & Clarke, C. J. 2015, MNRAS, 452, 3932, doi: 10.1093/mnras/stv1486

Boss, A. P. 1997, Science, 276, 1836, doi: 10.1126/science.276.5320.1836

Bouwman, J., de Koter, A., van den Ancker, M. E., & Waters, L. B. F. M. 2000, A&A, 360, 213

Bowler, B. P. 2016, PASP, 128, 102001, doi: 10.1088/1538-3873/128/968/102001

Brauer, F., Dullemond, C. P., & Henning, T. 2008, A&A, 480, 859, doi: 10.1051/0004-6361:20077759

Braun, R., & Walterbos, R. A. M. 1985, A&A, 143, 307

Briggs, D. S. 1995, PhD thesis, New Mexico Institute of Mining and Technology

Briggs, D. S., Schwab, F. R., & Sramek, R. A. 1999, in Astronomical Society of the Pacific Conference Series, Vol. 180, Synthesis Imaging in Radio Astronomy II, ed. G. B. Taylor, C. L. Carilli, & R. A. Perley, 127

Brown-Sevilla, S. B., Keppler, M., Barraza-Alfaro, M., et al. 2021, arXiv e-prints, arXiv:2107.13560. https://arxiv.org/abs/2107.13560

Bruderer, S., van der Marel, N., van Dishoeck, E. F., & van Kempen, T. A. 2014, A&A, 562, A26, doi: 10.1051/0004-6361/201322857

Burke, J. R., & Hollenbach, D. J. 1983, ApJ, 265, 223, doi: 10.1086/160667

Cacciapuoti, L., Macias, E., Gupta, A., et al. 2024, A&A, 682, A61, doi: 10.1051/0004-6361/202347486

Cadman, J., Rice, K., & Hall, C. 2021, MNRAS, 504, 2877, doi: 10.1093/mnras/stab905

Calcino, J., Hilder, T., Price, D. J., et al. 2022, ApJ, 929, L25, doi: 10.3847/2041-8213/ac64a7

Calcino, J., Price, D. J., Hilder, T., et al. 2024, arXiv e-prints, arXiv:2410.18521, doi: 10.48550/arXiv.2410.18521

Carpenter, J., Brogan, C., Iono, D., & Mroczkowski, T. 2022, The ALMA2030 Wideband Sensitivity Upgrade, ALMA Memo 621

Casassus, S., Cárcamo, M., Hales, A., Weber, P., & Dent, B. 2022, ApJ, 933, L4, doi: 10.3847/2041-8213/ac75e8

Casassus, S., & Pérez, S. 2019, ApJ, 883, L41, doi: 10.3847/2041-8213/ab4425

Casassus, S., Christiaens, V., Cárcamo, M., et al. 2021, MNRAS, 507, 3789, doi: 10.1093/mnras/stab2359

Cassen, P., & Moosman, A. 1981, Icarus, 48, 353, doi: 10.1016/0019-1035(81)90051-8

Chevance, M., Krumholz, M. R., McLeod, A. F., et al. 2023, in Astronomical Society of the Pacific Conference Series, Vol. 534, Protostars and Planets VII, ed. S. Inutsuka, Y. Aikawa, T. Muto, K. Tomida, & M. Tamura, 1, doi: 10.48550/arXiv.2203.09570

Chiang, E., & Youdin, A. N. 2010, Annual Review of Earth and Planetary Sciences, 38, 493, doi: 10.1146/annurev-earth-040809-152513

Chiang, E. I., & Goldreich, P. 1997, ApJ, 490, 368, doi: 10.1086/304869

Choksi, N., & Chiang, E. 2025, MNRAS, 537, 2945, doi: 10.1093/mnras/stae2530

Cleeves, L. I., Bergin, E. A., & Harries, T. J. 2015, ApJ, 807, 2, doi: 10.1088/0004-637X/807/1/2

Cornwell, T. J. 2008, IEEE Journal of Selected Topics in Signal Processing, 2, 793, doi: 10.1109/JSTSP.2008.2006388

Cossins, P., Lodato, G., & Clarke, C. J. 2009, MNRAS, 393, 1157, doi: 10.1111/j.1365-2966.2008.14275.x

Crida, A., Morbidelli, A., & Masset, F. 2006, Icarus, 181, 587, doi: 10.1016/j.icarus.2005.10.007

Cullen, L., & Dehnen, W. 2010, MNRAS, 408, 669, doi: 10.1111/j.1365-2966.2010.17158.x

Currie, T. 2024, Research Notes of the American Astronomical Society, 8, 146, doi: 10.3847/2515-5172/ad50ce

Currie, T., Lawson, K., Schneider, G., et al. 2022, Nature Astronomy, 6, 751, doi: 10.1038/s41550-022-01634-x

Czekala, I., Loomis, R. A., Teague, R., et al. 2021, ApJS, 257, 2, doi: 10.3847/1538-4365/ac1430

D'Alessio, P., Cantö, J., Calvet, N., & Lizano, S. 1998, ApJ, 500, 411, doi: 10.1086/305702

de Gregorio-Monsalvo, I., Ménard, F., Dent, W., et al. 2013, A&A, 557, A133, doi: 10.1051/0004-6361/201321603

de Laplace, P. S. 1796, Exposition du système du monde, doi: 10.3931/e-rara-497

de Val-Borro, M., Edgar, R. G., Artymowicz, P., et al. 2006, MNRAS, 370, 529, doi: 10.1111/j.1365-2966.2006.10488.x

Deng, H., Mayer, L., & Helled, R. 2021, Nature Astronomy, 5, 440, doi: 10.1038/s41550-020-01297-6

DeWarf, L. E., Sepinsky, J. F., Guinan, E. F., Ribas, I., & Nadalin, I. 2003, ApJ, 590, 357, doi: 10.1086/374979

Dipierro, G., Lodato, G., Testi, L., & de Gregorio Monsalvo, I. 2014, MNRAS, 444, 1919, doi: 10.1093/mnras/stu1584

Disk Dynamics Collaboration, Armitage, P. J., Bae, J., et al. 2020, arXiv e-prints, arXiv:2009.04345. https://arxiv.org/abs/2009.04345

Doi, K., & Kataoka, A. 2021, ApJ, 912, 164, doi: 10.3847/1538-4357/abe5a6

Dong, R., & Fung, J. 2017a, ApJ, 835, 146, doi: 10.3847/1538-4357/835/2/146

—. 2017b, ApJ, 835, 38, doi: 10.3847/1538-4357/835/1/38

Dong, R., Fung, J., & Chiang, E. 2016a, ApJ, 826, 75, doi: 10.3847/0004-637X/826/1/75

Dong, R., Hall, C., Rice, K., & Chiang, E. 2015, ApJ, 812, L32, doi: 10.1088/2041-8205/812/2/L32

Dong, R., Li, S., Chiang, E., & Li, H. 2017, ApJ, 843, 127, doi: 10.3847/1538-4357/aa72f2

—. 2018a, ApJ, 866, 110, doi: 10.3847/1538-4357/aadadd

Dong, R., Najita, J. R., & Brittain, S. 2018b, ApJ, 862, 103, doi: 10.3847/1538-4357/aaccfc

Dong, R., Rafikov, R. R., & Stone, J. M. 2011a, ApJ, 741, 57, doi: 10.1088/0004-637X/741/1/57

Dong, R., Rafikov, R. R., Stone, J. M., & Petrovich, C. 2011b, ApJ, 741, 56, doi: 10.1088/0004-637X/741/1/56

Dong, R., Vorobyov, E., Pavlyuchenkov, Y., Chiang, E., & Liu, H. B. 2016b, ApJ, 823, 141, doi: 10.3847/0004-637X/823/2/141

Dong, R., Liu, S.-y., Eisner, J., et al. 2018c, ApJ, 860, 124, doi: 10.3847/1538-4357/aac6cb

Draine, B. T. 2003, ApJ, 598, 1017, doi: 10.1086/379118

—. 2016, ApJ, 831, 109, doi: 10.3847/0004-637X/831/1/109

Drążkowska, J., Bitsch, B., Lambrechts, M., et al. 2023, in Astronomical Society of the Pacific Conference Series, Vol. 534, Protostars and Planets VII, ed. S. Inutsuka, Y. Aikawa, T. Muto, K. Tomida, & M. Tamura, 717, doi: 10.48550/arXiv.2203.09759

Duffell, P. C., & Chiang, E. 2015, ApJ, 812, 94, doi: 10.1088/0004-637X/812/2/94

Dullemond, C. P., & Dominik, C. 2005, A&A, 434, 971, doi: 10.1051/0004-6361:20042080

Dullemond, C. P., Dominik, C., & Natta, A. 2001, ApJ, 560, 957, doi: 10.1086/323057

Dullemond, C. P., Isella, A., Andrews, S. M., Skobleva, I., & Dzyurkevich, N. 2020, A&A, 633, A137, doi: 10.1051/0004-6361/201936438

Dullemond, C. P., Kimmig, C. N., & Zanazzi, J. J. 2022, MNRAS, 511, 2925, doi: 10.1093/mnras/stab2791

Dullemond, C. P., Küffmeier, M., Goicovic, F., et al. 2019, A&A, 628, A20, doi: 10.1051/0004-6361/201832632

Dullemond, C. P., Birnstiel, T., Huang, J., et al. 2018, ApJ, 869, L46, doi: 10.3847/2041-8213/aaf742

Dunham, M. M., Stutz, A. M., Allen, L. E., et al. 2014, in Protostars and Planets VI, ed. H. Beuther, R. S. Klessen, C. P. Dullemond, & T. Henning, 195–218, doi: 10.2458/azu_uapress_9780816531240-ch009

Durisen, R. H., Boss, A. P., Mayer, L., et al. 2007, in Protostars and Planets V, ed. B. Reipurth, D. Jewitt, & K. Keil, 607, doi: 10.48550/arXiv.astro-ph/0603179

Dutrey, A., Guilloteau, S., & Simon, M. 1994, A&A, 286, 149

Dutrey, A., Chapillon, E., Guilloteau, S., et al. 2024, arXiv e-prints, arXiv:2408.14276, doi: 10.48550/arXiv.2408.14276

Edgar, R. 2004, NewAR, 48, 843, doi: 10.1016/j.newar.2004.06.001

Ediss, G. A., Carter, M., Cheng, J., et al. 2004, in Fifteenth International Symposium on Space Terahertz Technology, ed. G. Narayanan, 181–188

Evans, II, N. J., Dunham, M. M., Jørgensen, J. K., et al. 2009, ApJS, 181, 321, doi: 10.1088/0067-0049/181/2/321

Fairbairn, C. W., & Rafikov, R. R. 2022, arXiv e-prints, arXiv:2207.14637. https://arxiv.org/abs/2207.14637

Faridani, S., Bigiel, F., Flöer, L., Kerp, J., & Stanimirović, S. 2018, Astronomische Nachrichten, 339, 87, doi: 10.1002/asna.201713381

Flores, C., Ohashi, N., Tobin, J. J., et al. 2023, ApJ, 958, 98, doi: 10.3847/1538-4357/acf7c1

Frank, A., Ray, T. P., Cabrit, S., et al. 2014, in Protostars and Planets VI, ed. H. Beuther, R. S. Klessen, C. P. Dullemond, & T. Henning, 451–474, doi: 10.2458/azu_uapress_9780816531240-ch020

Fuente, A., Cernicharo, J., Agúndez, M., et al. 2010, A&A, 524, A19, doi: 10.1051/0004-6361/201014905

Fukagawa, M., Hayashi, M., Tamura, M., et al. 2004, ApJ, 605, L53, doi: 10.1086/420699

Fung, J., & Chiang, E. 2016, ApJ, 832, 105, doi: 10.3847/0004-637X/832/2/105

Fung, J., & Dong, R. 2015, ApJ, 815, L21, doi: 10.1088/2041-8205/815/2/L21

Fung, J., Shi, J.-M., & Chiang, E. 2014, ApJ, 782, 88, doi: 10.1088/0004-637X/782/2/88

Gaia Collaboration, Prusti, T., de Bruijne, J. H. J., et al. 2016a, A&A, 595, A1, doi: 10.1051/0004-6361/201629272

—. 2016b, A&A, 595, A1, doi: 10.1051/0004-6361/201629272

Gaia Collaboration, Vallenari, A., Brown, A. G. A., et al. 2022, arXiv e-prints, arXiv:2208.00211. https://arxiv.org/abs/2208.00211

—. 2023, A&A, 674, A1, doi: 10.1051/0004-6361/202243940

Galloway-Sprietsma, M., Bae, J., Izquierdo, A. F., et al. 2025, ApJ, 984, L10, doi: 10.3847/2041-8213/adc437

Gammie, C. F. 2001, ApJ, 553, 174, doi: 10.1086/320631

Garaud, P., Barrière-Fouchet, L., & Lin, D. N. C. 2004, ApJ, 603, 292, doi: 10.1086/381385

Garufi, A., Avenhaus, H., Pérez, S., et al. 2020, A&A, 633, A82, doi: 10.1051/0004-6361/201936946

Garufi, A., Dominik, C., Ginski, C., et al. 2022a, A&A, 658, A137, doi: 10.1051/0004-6361/202141692

Garufi, A., Podio, L., Codella, C., et al. 2022b, A&A, 658, A104, doi: 10.1051/0004-6361/202141264

Garufi, A., Ginski, C., van Holstein, R. G., et al. 2024, arXiv e-prints, arXiv:2403.02158, doi: 10.48550/arXiv.2403.02158

Ginski, C., Stolker, T., Pinilla, P., et al. 2016, A&A, 595, A112, doi: 10.1051/0004-6361/201629265

Ginski, C., Facchini, S., Huang, J., et al. 2021, ApJ, 908, L25, doi: 10.3847/2041-8213/abdf57

Godon, P., & Livio, M. 1999, ApJ, 523, 350, doi: 10.1086/307720

Goldreich, P., & Tremaine, S. 1978, The Astrophysical Journal, 222, 850, doi: 10.1086/156203

—. 1979a, ApJ, 233, 857, doi: 10.1086/157448

—. 1979b, ApJ, 233, 857, doi: 10.1086/157448

—. 1980, ApJ, 241, 425, doi: 10.1086/158356

Goodman, J., & Rafikov, R. R. 2001, ApJ, 552, 793, doi: 10.1086/320572

Grady, C. A., Woodgate, B., Bruhweiler, F. C., et al. 1999, ApJ, 523, L151, doi: 10.1086/312270

Greene, T. P., Wilking, B. A., Andre, P., Young, E. T., & Lada, C. J. 1994, ApJ, 434, 614, doi: 10.1086/174763

Griffin, M. J., Abergel, A., Abreu, A., et al. 2010, A&A, 518, L3, doi: 10.1051/0004-6361/201014519

Gupta, A., Miotello, A., Williams, J. P., et al. 2024, A&A, 683, A133, doi: 10.1051/0004-6361/202348007

Gupta, A., Miotello, A., Manara, C. F., et al. 2023, A&A, 670, L8, doi: 10.1051/0004-6361/202245254

Guzmán-Díaz, J., Mendigutía, I., Montesinos, B., et al. 2021, A&A, 650, A182, doi: 10.1051/0004-6361/202039519

Gyeol Yun, H., Kim, W.-T., Bae, J., & Han, C. 2019, ApJ, 884, 142, doi: 10.3847/1538-4357/ab3fab

Haffert, S. Y., Bohn, A. J., de Boer, J., et al. 2019, Nature Astronomy, 3, 749, doi: 10.1038/s41550-019-0780-5

Hall, C., Dong, R., Rice, K., et al. 2019, ApJ, 871, 228, doi: 10.3847/1538-4357/aafac2

Hall, C., Forgan, D., Rice, K., et al. 2016, MNRAS, 458, 306, doi: 10.1093/mnras/stw296

Hall, C., Dong, R., Teague, R., et al. 2020, ApJ, 904, 148, doi: 10.3847/1538-4357/abac17

Hammond, I., Christiaens, V., Price, D. J., et al. 2023, MNRAS, 522, L51, doi: 10.1093/mnrasl/slad027

Hanawa, T., Garufi, A., Podio, L., Codella, C., & Segura-Cox, D. 2024, MNRAS, 528, 6581, doi: 10.1093/mnras/stae338

Harada, N., Tokuda, K., Yamasaki, H., et al. 2023, ApJ, 945, 63, doi: 10.3847/1538-4357/acb930

Harris, C. R., Millman, K. J., van der Walt, S. J., et al. 2020, Nature, 585, 357, doi: 10.1038/s41586-020-2649-2

Harsono, D., Alexander, R. D., & Levin, Y. 2011, MNRAS, 413, 423, doi: 10.1111/j.1365-2966.2010.18146.x

Hartmann, L., Calvet, N., Gullbring, E., & D'Alessio, P. 1998, ApJ, 495, 385, doi: 10.1086/305277

Hashimoto, J., Tamura, M., Muto, T., et al. 2011, ApJ, 729, L17, doi: 10.1088/2041-8205/729/2/L17

Hennebelle, P., Lesur, G., & Fromang, S. 2017, A&A, 599, A86, doi: 10.1051/0004-6361/201629779

Henning, T., Burkert, A., Launhardt, R., Leinert, C., & Stecklum, B. 1998, A&A, 336, 565

Herbst, E., & van Dishoeck, E. F. 2009, ARA&A, 47, 427, doi: 10.1146/annurev-astro-082708-101654

HGBS Team. 2020, Herschel Gould Belt Survey, IPAC, doi: 10.26131/IRSA72

Hilder, T., Fasano, D., Bollati, F., & Vandenberg, J. 2023, The Journal of Open Source Software, 8, 4863, doi: 10.21105/joss.04863

Hillenbrand, L. A., Strom, S. E., Vrba, F. J., & Keene, J. 1992, ApJ, 397, 613, doi: 10.1086/171819

Högbom, J. A. 1974, A&AS, 15, 417

Holdaway, M. A. 1999, in Astronomical Society of the Pacific Conference Series, Vol. 180, Synthesis Imaging in Radio Astronomy II, ed. G. B. Taylor, C. L. Carilli, & R. A. Perley, 401

Huang, J., Bergin, E. A., Le Gal, R., et al. 2024, arXiv e-prints, arXiv:2407.01679, doi: 10.48550/arXiv.2407.01679

Huang, J., Andrews, S. M., Dullemond, C. P., et al. 2018a, ApJ, 869, L42, doi: 10.3847/2041-8213/aaf740

Huang, J., Andrews, S. M., Pérez, L. M., et al. 2018b, ApJ, 869, L43, doi: 10.3847/2041-8213/aaf7a0

Huang, J., Andrews, S. M., Cleeves, L. I., et al. 2018c, ApJ, 852, 122, doi: 10.3847/1538-4357/aaa1e7

Huang, J., Bergin, E. A., Öberg, K. I., et al. 2021, ApJS, 257, 19, doi: 10.3847/1538-4365/ac143e

Hunter, J. D. 2007, Computing in Science and Engineering, 9, 90, doi: 10.1109/MCSE.2007.55

Iguchi, S., Morita, K.-I., Sugimoto, M., et al. 2009, PASJ, 61, 1, doi: 10.1093/pasj/61.1.1

Ilee, J. D., Walsh, C., Jennings, J., et al. 2022, MNRAS, 515, L23, doi: 10.1093/mnrasl/slac048

Isella, A., Benisty, M., Teague, R., et al. 2019, ApJ, 879, L25, doi: 10.3847/2041-8213/ab2a12

Izquierdo, A. F., Facchini, S., Rosotti, G. P., van Dishoeck, E. F., & Testi, L. 2022, ApJ, 928, 2, doi: 10.3847/1538-4357/ac474d

Izquierdo, A. F., Testi, L., Facchini, S., Rosotti, G. P., & van Dishoeck, E. F. 2021, A&A, 650, A179, doi: 10.1051/0004-6361/202140779

Jeans, J. H. 1902, Philosophical Transactions of the Royal Society of London Series A, 199, 1, doi: 10.1098/rsta.1902.0012

Jenkins, F. A., & White, H. E. 2001, Fundamentals of Optics, 4th edn. (New York: McGraw-Hill). https://archive.org/details/in.ernet.dli.2015.109790

Jennings, J., Booth, R. A., Tazzari, M., Clarke, C. J., & Rosotti, G. P. 2021, arXiv e-prints, arXiv:2103.02392. https://arxiv.org/abs/2103.02392

—. 2022a, MNRAS, 509, 2780, doi: 10.1093/mnras/stab3185

Jennings, J., Booth, R. A., Tazzari, M., Rosotti, G. P., & Clarke, C. J. 2020, MNRAS, 495, 3209, doi: 10.1093/mnras/staa1365

Jennings, J., Tazzari, M., Clarke, C. J., Booth, R. A., & Rosotti, G. P. 2022b, MNRAS, 514, 6053, doi: 10.1093/mnras/stac1770

Johansen, A., Blum, J., Tanaka, H., et al. 2014, in Protostars and Planets VI, ed. H. Beuther, R. S. Klessen, C. P. Dullemond, & T. Henning, 547–570, doi: 10.2458/azu_uapress_9780816531240-ch024

Johansen, A., & Lambrechts, M. 2017, Annual Review of Earth and Planetary Sciences, 45, 359, doi: 10.1146/annurev-earth-063016-020226

Johansen, A., & Youdin, A. 2007, ApJ, 662, 627, doi: 10.1086/516730

Johansen, A., Youdin, A., & Mac Low, M.-M. 2009, ApJ, 704, L75, doi: 10.1088/0004-637X/704/2/L75

Johnson, B. M., & Gammie, C. F. 2005, ApJ, 635, 149, doi: 10.1086/497358

Jorsater, S., & van Moorsel, G. A. 1995, AJ, 110, 2037, doi: 10.1086/117668

Juhász, A., & Rosotti, G. P. 2018, MNRAS, 474, L32, doi: 10.1093/mnrasl/slx182

Kamp, I., & Dullemond, C. P. 2004, ApJ, 615, 991, doi: 10.1086/424703

Kanagawa, K. D., Muto, T., & Tanaka, H. 2021, arXiv e-prints, arXiv:2109.09579. https://arxiv.org/abs/2109.09579

Kanagawa, K. D., Muto, T., Tanaka, H., et al. 2016, PASJ, 68, 43, doi: 10.1093/pasj/psw037

Kanagawa, K. D., Tanaka, H., Muto, T., Tanigawa, T., & Takeuchi, T. 2015, MNRAS, 448, 994, doi: 10.1093/mnras/stv025

Kataoka, A., Muto, T., Momose, M., et al. 2015a, ApJ, 809, 78, doi: 10.1088/0004-637X/809/1/78

—. 2015b, ApJ, 809, 78, doi: 10.1088/0004-637X/809/1/78

Kawamura, A., Mizuno, Y., Minamidani, T., et al. 2009, ApJS, 184, 1, doi: 10.1088/0067-0049/184/1/1

Kenyon, S. J., & Hartmann, L. 1987, ApJ, 323, 714, doi: 10.1086/165866

Kepley, A. A., Tsutsumi, T., Brogan, C. L., et al. 2020, PASP, 132, 024505, doi: 10.1088/1538-3873/ab5e14

Keppler, M., Benisty, M., Müller, A., et al. 2018, A&A, 617, A44, doi: 10.1051/0004-6361/201832957

Kley, W., D'Angelo, G., & Henning, T. 2001, ApJ, 547, 457, doi: 10.1086/318345

Koerner, D. W., Sargent, A. I., & Beckwith, S. V. W. 1993, Icarus, 106, 2, doi: 10.1006/icar.1993.1154

Kokubo, E., & Ida, S. 2000, Icarus, 143, 15, doi: 10.1006/icar.1999.6237

Krapp, L., Kratter, K. M., & Youdin, A. N. 2021, arXiv e-prints, arXiv:2110.02428. https://arxiv.org/abs/2110.02428

Kratter, K., & Lodato, G. 2016a, ARA&A, 54, 271, doi: 10.1146/annurev-astro-081915-023307

—. 2016b, ARA&A, 54, 271, doi: 10.1146/annurev-astro-081915-023307

Kraus, S., Kreplin, A., Fukugawa, M., et al. 2017, ApJ, 848, L11, doi: 10.3847/2041-8213/aa8edc

Kruegel, E. 2003, The physics of interstellar dust, IoP Series in astronomy and astrophysics (Bristol, UK: The Institute of Physics)

Kuffmeier, M., Dullemond, C. P., Reissl, S., & Goicovic, F. G. 2021, A&A, 656, A161, doi: 10.1051/0004-6361/202039614

Kuffmeier, M., Frimann, S., Jensen, S. S., & Haugbølle, T. 2018, MNRAS, 475, 2642, doi: 10.1093/mnras/sty024

Kuffmeier, M., Goicovic, F. G., & Dullemond, C. P. 2020, A&A, 633, A3, doi: 10.1051/0004-6361/201936820

Kuffmeier, M., Jensen, S. S., & Haugbølle, T. 2023, European Physical Journal Plus, 138, 272, doi: 10.1140/epjp/s13360-023-03880-y

Kuffmeier, M., Pineda, J. E., Segura-Cox, D., & Haugbølle, T. 2024, arXiv e-prints, arXiv:2405.12670, doi: 10.48550/arXiv.2405.12670

Kurtovic, N. T., & Pinilla, P. 2024, A&A, 687, A188, doi: 10.1051/0004-6361/202449667

Kurtovic, N. T., Pérez, L. M., Benisty, M., et al. 2018, ApJ, 869, L44, doi: 10.3847/2041-8213/aaf746

Kuznetsova, A., Bae, J., Hartmann, L., & Mac Low, M.-M. 2022, ApJ, 928, 92, doi: 10.3847/1538-4357/ac54a8

Lada, C. J. 1987, in IAU Symposium, Vol. 115, Star Forming Regions, ed. M. Peimbert & J. Jugaku, 1

Lambrechts, M., & Johansen, A. 2012, A&A, 544, A32, doi: 10.1051/0004-6361/201219127

Larson, R. B. 1969, MNRAS, 145, 271, doi: 10.1093/mnras/145.3.271

Law, C. J., Booth, A. S., & Öberg, K. I. 2023, ApJ, 952, L19, doi: 10.3847/2041-8213/acdfd0

Law, C. J., Teague, R., Loomis, R. A., et al. 2021, ApJS, 257, 4, doi: 10.3847/1538-4365/ac1439

Leroy, A. K., Hughes, A., Liu, D., et al. 2021, ApJS, 255, 19, doi: 10.3847/1538-4365/abec80

Lesur, G., Hennebelle, P., & Fromang, S. 2015, A&A, 582, L9, doi: 10.1051/0004-6361/201526734

Lesur, G., Flock, M., Ercolano, B., et al. 2023, in Astronomical Society of the Pacific Conference Series, Vol. 534, Protostars and Planets VII, ed. S. Inutsuka, Y. Aikawa, T. Muto, K. Tomida, & M. Tamura, 465, doi: 10.48550/arXiv.2203.09821

Lesur, G. R. J. 2021, A&A, 650, A35, doi: 10.1051/0004-6361/202040109

Li, D., Pantin, E., Telesco, C. M., et al. 2016, ApJ, 832, 18, doi: 10.3847/0004-637X/832/1/18

Lin, S.-Y., Ohashi, N., Lim, J., et al. 2006, ApJ, 645, 1297, doi: 10.1086/504368

Lissauer, J. J. 1993, ARA&A, 31, 129, doi: 10.1146/annurev.aa.31.090193.001021

Lissauer, J. J., Batalha, N. M., & Borucki, W. J. 2023, in Astronomical Society of the Pacific Conference Series, Vol. 534, Protostars and Planets VII, ed. S. Inutsuka, Y. Aikawa, T. Muto, K. Tomida, & M. Tamura, 839, doi: 10.48550/arXiv.2311.04981

Liu, B., & Ji, J. 2020, Research in Astronomy and Astrophysics, 20, 164, doi: 10.1088/1674-4527/20/10/164

Liu, H. B. 2019, ApJ, 877, L22, doi: 10.3847/2041-8213/ab1f8e

Lodato, G. 2008, New Astronomy Reviews, 52, 21, doi: 10.1016/j.newar.2008.04.002

Lodato, G., & Rice, W. K. M. 2004, MNRAS, 351, 630, doi: 10.1111/j.1365-2966.2004.07811.x

—. 2005, MNRAS, 358, 1489, doi: 10.1111/j.1365-2966.2005.08875.x

Lodato, G., Dipierro, G., Ragusa, E., et al. 2019, MNRAS, 486, 453, doi: 10.1093/mnras/stz913

Lodato, G., Rampinelli, L., Viscardi, E., et al. 2023, MNRAS, 518, 4481, doi: 10.1093/mnras/stac3223

Longarini, C., Armitage, P. J., Lodato, G., Price, D. J., & Ceppi, S. 2023a, MNRAS, 522, 6217, doi: 10.1093/mnras/stad1400

Longarini, C., Lodato, G., Bertin, G., & Armitage, P. J. 2023b, MNRAS, 519, 2017, doi: 10.1093/mnras/stac3653

Longarini, C., Lodato, G., Toci, C., et al. 2021a, ApJ, 920, L41, doi: 10.3847/2041-8213/ac2df6

—. 2021b, arXiv e-prints, arXiv:2108.11387. https://arxiv.org/abs/2108.11387

Loomis, R. A., Öberg, K. I., Andrews, S. M., et al. 2018, AJ, 155, 182, doi: 10.3847/1538-3881/aab604

Lovelace, R. V. E., Li, H., Colgate, S. A., & Nelson, A. F. 1999, ApJ, 513, 805, doi: 10.1086/306900

Lubow, S. H., & Zhu, Z. 2014, ApJ, 785, 32, doi: 10.1088/0004-637X/785/1/32

Luhman, K. L. 2023, AJ, 165, 37, doi: 10.3847/1538-3881/ac9da3

Lynden-Bell, D., & Pringle, J. E. 1974, MNRAS, 168, 603, doi: 10.1093/mnras/168.3.603

Macías, E., Guerra-Alvarado, O., Carrasco-González, C., et al. 2021, A&A, 648, A33, doi: 10.1051/0004-6361/202039812

Mamajek, E. E. 2009, in American Institute of Physics Conference Series, Vol. 1158, Exoplanets and Disks: Their Formation and Diversity, ed. T. Usuda, M. Tamura, & M. Ishii (AIP), 3–10, doi: 10.1063/1.3215910

Manara, C. F., Ansdell, M., Rosotti, G. P., et al. 2023, in Astronomical Society of the Pacific Conference Series, Vol. 534, Protostars and Planets VII, ed. S. Inutsuka, Y. Aikawa, T. Muto, K. Tomida, & M. Tamura, 539, doi: 10.48550/arXiv.2203.09930

Martire, P., Longarini, C., Lodato, G., et al. 2024, A&A, 686, A9, doi: 10.1051/0004-6361/202348546

Mathis, J. S., Rumpl, W., & Nordsieck, K. H. 1977, ApJ, 217, 425, doi: 10.1086/155591

Maury, A. J., André, P., Men'shchikov, A., Könyves, V., & Bontemps, S. 2011, A&A, 535, A77, doi: 10.1051/0004-6361/201117132

Mawet, D., Absil, O., Montagnier, G., et al. 2012, A&A, 544, A131, doi: 10.1051/0004-6361/201219662

Mayor, M., & Queloz, D. 1995, Nature, 378, 355, doi: 10.1038/378355a0

McKinney, W. 2011, Python for High Performance and Scientific Computing, 14, 1

McMullin, J. P., Waters, B., Schiebel, D., Young, W., & Golap, K. 2007a, in Astronomical Society of the Pacific Conference Series, Vol. 376, Astronomical Data Analysis Software and Systems XVI, ed. R. A. Shaw, F. Hill, & D. J. Bell, 127

—. 2007b, in Astronomical Society of the Pacific Conference Series, Vol. 376, Astronomical Data Analysis Software and Systems XVI, ed. R. A. Shaw, F. Hill, & D. J. Bell, 127

McNally, C. P., Nelson, R. P., Paardekooper, S.-J., & Benítez-Llambay, P. 2019, MNRAS, 484, 728, doi: 10.1093/mnras/stz023

Mendoza, S., Tejeda, E., & Nagel, E. 2009, MNRAS, 393, 579, doi: 10.1111/j.1365-2966.2008.14210.x

Meru, F., Juhász, A., Ilee, J. D., et al. 2017, ApJ, 839, L24, doi: 10.3847/2041-8213/aa6837

Meru, F., Rosotti, G. P., Booth, R. A., Nazari, P., & Clarke, C. J. 2019, MNRAS, 482, 3678, doi: 10.1093/mnras/sty2847

Miotello, A., Kamp, I., Birnstiel, T., Cleeves, L. C., & Kataoka, A. 2023, in Astronomical Society of the Pacific Conference Series, Vol. 534, Protostars and Planets VII, ed. S. Inutsuka, Y. Aikawa, T. Muto, K. Tomida, & M. Tamura, 501, doi: 10.48550/arXiv.2203.09818

Miranda, R., & Rafikov, R. R. 2019a, ApJ, 875, 37, doi: 10.3847/1538-4357/ab0f9e

—. 2019b, ApJ, 878, L9, doi: 10.3847/2041-8213/ab22a7

—. 2020a, ApJ, 904, 121, doi: 10.3847/1538-4357/abbee7

—. 2020b, ApJ, 892, 65, doi: 10.3847/1538-4357/ab791a

Miura, H., Yamamoto, T., Nomura, H., et al. 2017, ApJ, 839, 47, doi: 10.3847/1538-4357/aa67df

Mizuno, H. 1980, Progress of Theoretical Physics, 64, 544, doi: 10.1143/PTP.64.544

Monnier, J. D., Harries, T. J., Aarnio, A., et al. 2017, ApJ, 838, 20, doi: 10.3847/1538-4357/aa6248

Monsch, K., Lovell, J. B., Berghea, C. T., et al. 2024, ApJ, 967, L2, doi: 10.3847/2041-8213/ad3bb0

Morbidelli, A., Szulágyi, J., Crida, A., et al. 2014, Icarus, 232, 266, doi: 10.1016/j.icarus.2014.01.010

Mori, S., Aikawa, Y., Oya, Y., Yamamoto, S., & Sakai, N. 2024, ApJ, 961, 31, doi: 10.3847/1538-4357/ad0634

Moscadelli, L., Sanna, A., Beuther, H., Oliva, A., & Kuiper, R. 2022, Nature Astronomy, 6, 1068, doi: 10.1038/s41550-022-01754-4

Muley, D., Dong, R., & Fung, J. 2021, arXiv e-prints, arXiv:2107.06323. https://arxiv.org/abs/2107.06323

Mundt, R. 1985, in Protostars and Planets II, ed. D. C. Black & M. S. Matthews, 414–433

Muro-Arena, G. A., Dominik, C., Waters, L. B. F. M., et al. 2018, A&A, 614, A24, doi: 10.1051/0004-6361/201732299

Muto, T., Grady, C. A., Hashimoto, J., et al. 2012, ApJ, 748, L22, doi: 10.1088/2041-8205/748/2/L22

Nakajima, T., & Golimowski, D. A. 1995, AJ, 109, 1181, doi: 10.1086/117351

Natta, A., Prusti, T., Neri, R., et al. 2001, A&A, 371, 186, doi: 10.1051/0004-6361:20010334

Nayakshin, S., Tsukagoshi, T., Hall, C., et al. 2020, MNRAS, 495, 285, doi: 10.1093/mnras/staa1132

Nazari, P., Booth, R. A., Clarke, C. J., et al. 2019, MNRAS, 485, 5914, doi: 10.1093/mnras/stz836

Nelson, R. P., Gressel, O., & Umurhan, O. M. 2013, MNRAS, 435, 2610, doi: 10.1093/mnras/stt1475

Newton, I. 1687, Philosophiae Naturalis Principia Mathematica., doi: 10.3931/e-rara-440

Norfolk, B. J., Pinte, C., Calcino, J., et al. 2022a, arXiv e-prints, arXiv:2208.02542. https://arxiv.org/abs/2208.02542

—. 2022b, ApJ, 936, L4, doi: 10.3847/2041-8213/ac85ed

Öberg, K. I., & Bergin, E. A. 2021, Phys. Rep., 893, 1, doi: 10.1016/j.physrep.2020.09.004

Ogilvie, G. I., & Lubow, S. H. 2002, MNRAS, 330, 950, doi: 10.1046/j.1365-8711.2002.05148.x

Oppenheimer, B. R., Brenner, D., Hinkley, S., et al. 2008, ApJ, 679, 1574, doi: 10.1086/587778

Ormel, C. W. 2017, in Astrophysics and Space Science Library, Vol. 445, Formation, Evolution, and Dynamics of Young Solar Systems, ed. M. Pessah & O. Gressel, 197, doi: 10.1007/978-3-319-60609-5_7

Ormel, C. W., & Klahr, H. H. 2010, A&A, 520, A43, doi: 10.1051/0004-6361/201014903

Oya, Y., Sakai, N., López-Sepulcre, A., et al. 2016, ApJ, 824, 88, doi: 10.3847/0004-637X/824/2/88

Pacheco-Vázquez, S., Fuente, A., Baruteau, C., et al. 2016, A&A, 589, A60, doi: 10.1051/0004-6361/201527089

Paczynski, B. 1978, Acta Astronomica, 28, 91

Paneque-Carreño, T., Miotello, A., van Dishoeck, E. F., Rosotti, G., & Tabone, B. 2025, arXiv e-prints, arXiv:2501.08294, doi: 10.48550/arXiv.2501.08294

Paneque-Carreño, T., Miotello, A., van Dishoeck, E. F., et al. 2022, arXiv e-prints, arXiv:2210.01130. https://arxiv.org/abs/2210.01130

Paneque-Carreño, T., Pérez, L. M., Benisty, M., et al. 2021a, ApJ, 914, 88, doi: 10.3847/1538-4357/abf243

—. 2021b, ApJ, 914, 88, doi: 10.3847/1538-4357/abf243

Pascucci, I., Cabrit, S., Edwards, S., et al. 2023, in Astronomical Society of the Pacific Conference Series, Vol. 534, Protostars and Planets VII, ed. S. Inutsuka, Y. Aikawa, T. Muto, K. Tomida, & M. Tamura, 567, doi: 10.48550/arXiv.2203.10068

Pavlyuchenkov, Y., Akimkin, V., Wiebe, D., & Vorobyov, E. 2019, MNRAS, 486, 3907, doi: 10.1093/mnras/stz1046

Pelkonen, V.-M., Padoan, P., Juvela, M., Haugbølle, T., & Nordlund, Å. 2024, arXiv e-prints, arXiv:2405.06520, doi: 10.48550/arXiv.2405.06520

Pérez, L. M., Carpenter, J. M., Andrews, S. M., et al. 2016, Science, 353, 1519, doi: 10.1126/science.aaf8296

Pérez, L. M., Benisty, M., Andrews, S. M., et al. 2018a, ApJ, 869, L50, doi: 10.3847/2041-8213/aaf745

Pérez, S., Casassus, S., Baruteau, C., et al. 2019, AJ, 158, 15, doi: 10.3847/1538-3881/ab1f88

Pérez, S., Casassus, S., & Benítez-Llambay, P. 2018b, MNRAS, 480, L12, doi: 10.1093/mnrasl/sly109

Perez, S., Dunhill, A., Casassus, S., et al. 2015, ApJ, 811, L5, doi: 10.1088/2041-8205/811/1/L5

Pérez, S., Casassus, S., Hales, A., et al. 2020, ApJ, 889, L24, doi: 10.3847/2041-8213/ab6b2b

Perri, F., & Cameron, A. G. W. 1974, Icarus, 22, 416, doi: 10.1016/0019-1035(74)90074-8

Perrin, M. D., Schneider, G., Duchene, G., et al. 2009, ApJ, 707, L132, doi: 10.1088/0004-637X/707/2/L132

Piétu, V., Guilloteau, S., & Dutrey, A. 2005, A&A, 443, 945, doi: 10.1051/0004-6361:20042050

Pilbratt, G. L., Riedinger, J. R., Passvogel, T., et al. 2010, A&A, 518, L1, doi: 10.1051/0004-6361/201014759

Pineda, J. E., Segura-Cox, D., Caselli, P., et al. 2020, Nature Astronomy, 4, 1158, doi: 10.1038/s41550-020-1150-z

Pineda, J. E., Arzoumanian, D., Andre, P., et al. 2023, in Astronomical Society of the Pacific Conference Series, Vol. 534, Protostars and Planets VII, ed. S. Inutsuka, Y. Aikawa, T. Muto, K. Tomida, & M. Tamura, 233, doi: 10.48550/arXiv.2205.03935

Pinilla, P., Birnstiel, T., Ricci, L., et al. 2012, A&A, 538, A114, doi: 10.1051/0004-6361/201118204

Pinte, C., Harries, T. J., Min, M., et al. 2009, A&A, 498, 967, doi: 10.1051/0004-6361/200811555

Pinte, C., Ménard, F., Duchêne, G., & Bastien, P. 2006, A&A, 459, 797, doi: 10.1051/0004-6361:20053275

Pinte, C., Teague, R., Flaherty, K., et al. 2022, arXiv e-prints, arXiv:2203.09528. https://arxiv.org/abs/2203.09528

Pinte, C., Ménard, F., Duchêne, G., et al. 2018a, A&A, 609, A47, doi: 10.1051/0004-6361/201731377

Pinte, C., Price, D. J., Ménard, F., et al. 2018b, ApJ, 860, L13, doi: 10.3847/2041-8213/aac6dc

Pinte, C., van der Plas, G., Ménard, F., et al. 2019, Nature Astronomy, 3, 1109, doi: 10.1038/s41550-019-0852-6

Pinte, C., Price, D. J., Ménard, F., et al. 2020, ApJ, 890, L9, doi: 10.3847/2041-8213/ab6dda

Pinte, C., Ilee, J. D., Huang, J., et al. 2025, ApJ, 984, L15, doi: 10.3847/2041-8213/adc433

Poglitsch, A., Waelkens, C., Geis, N., et al. 2010, A&A, 518, L2, doi: 10.1051/0004-6361/201014535

Pollack, J. B., Hubickyj, O., Bodenheimer, P., et al. 1996, Icarus, 124, 62, doi: 10.1006/icar.1996.0190

Price, D. J., Wurster, J., Tricco, T. S., et al. 2018, Publications of the Astronomical Society of Australia, 35, e031, doi: 10.1017/pasa.2018.25

Quillen, A. C., Varniere, P., Minchev, I., & Frank, A. 2003, arXiv e-prints, astro. https://arxiv.org/abs/astro-ph/0312647

Rabago, I., & Zhu, Z. 2021, MNRAS, 502, 5325, doi: 10.1093/mnras/stab447

Rafikov, R. R. 2002a, ApJ, 569, 997, doi: 10.1086/339399

—. 2002b, ApJ, 569, 997, doi: 10.1086/339399

Remijan, A., Biggs, A., Cortes, P. A., et al. 2019, ALMA Technical Handbook,ALMA Doc. 7.3, ver. 1.1, 2019, ALMA Technical Handbook,ALMA Doc. 7.3, ver. 1.1ISBN 978-3-923524-66-2, doi: 10.5281/zenodo.4511522

Ren, B., Dong, R., van Holstein, R. G., et al. 2020, ApJ, 898, L38, doi: 10.3847/2041-8213/aba43e

Ribas, Á., Espaillat, C. C., Macías, E., et al. 2017, ApJ, 849, 63, doi: 10.3847/1538-4357/aa8e99

Rice, W. K. M., & Armitage, P. J. 2009, MNRAS, 396, 2228, doi: 10.1111/j.1365-2966.2009.14879.x

Rice, W. K. M., Armitage, P. J., Bonnell, I. A., et al. 2003, MNRAS, 346, L36, doi: 10.1111/j.1365-2966.2003.07317.x

Rice, W. K. M., Lodato, G., & Armitage, P. J. 2005, MNRAS, 364, L56, doi: 10.1111/j.1745-3933.2005.00105.x

Rice, W. K. M., Lodato, G., Pringle, J. E., Armitage, P. J., & Bonnell, I. A. 2004, MNRAS, 355, 543, doi: 10.1111/j.1365-2966.2004.08339.x

Rivière-Marichalar, P., Fuente, A., Le Gal, R., et al. 2020, A&A, 642, A32, doi: 10.1051/0004-6361/202038549

Rivière-Marichalar, P., Macías, E., Baruteau, C., et al. 2024, A&A, 683, A141, doi: 10.1051/0004-6361/202347464

Robitaille, T., Beaumont, C., Qian, P., Borkin, M., & Goodman, A. 2018, glueviz v0.13.1: multidimensional data exploration, 0.13.1, Zenodo, doi: 10.5281/zenodo.1237692

Rodríguez, L. F., Zapata, L. A., Dzib, S. A., et al. 2014, ApJ, 793, L21, doi: 10.1088/2041-8205/793/1/L21

Rosenfeld, K. A., Andrews, S. M., Hughes, A. M., Wilner, D. J., & Qi, C. 2013, ApJ, 774, 16, doi: 10.1088/0004-637X/774/1/16

Rosotti, G. P., Juhasz, A., Booth, R. A., & Clarke, C. J. 2016, MNRAS, 459, 2790, doi: 10.1093/mnras/stw691

Rosotti, G. P., Teague, R., Dullemond, C., Booth, R. A., & Clarke, C. J. 2020a, MNRAS, 495, 173, doi: 10.1093/mnras/staa1170

Rosotti, G. P., Benisty, M., Juhász, A., et al. 2020b, MNRAS, 491, 1335, doi: 10.1093/mnras/stz3090

Rowther, S., Meru, F., Kennedy, G. M., Nealon, R., & Pinte, C. 2020, ApJ, 904, L18, doi: 10.3847/2041-8213/abc704

Rowther, S., Nealon, R., & Meru, F. 2022, MNRAS, doi: 10.1093/mnras/stac3106

Rowther, S., Nealon, R., Meru, F., et al. 2024a, MNRAS, 528, 2490, doi: 10.1093/mnras/stae167

Rowther, S., Price, D. J., Pinte, C., et al. 2024b, MNRAS, doi: 10.1093/mnras/stae2167

Rucinski, S. M. 1985, AJ, 90, 2321, doi: 10.1086/113937

Ryle, M., & Hewish, A. 1960, MNRAS, 120, 220, doi: 10.1093/mnras/120.3.220

Safronov, V. S. 1972, Evolution of the protoplanetary cloud and formation of the earth and planets.

Sai, J., Ohashi, N., Saigo, K., et al. 2020, ApJ, 893, 51, doi: 10.3847/1538-4357/ab8065

Sakai, N., Sakai, T., Hirota, T., et al. 2014, Nature, 507, 78, doi: 10.1038/nature13000

Sakai, N., Oya, Y., Higuchi, A. E., et al. 2017, MNRAS, 467, L76, doi: 10.1093/mnrasl/slx002

Salyk, C., Herczeg, G. J., Brown, J. M., et al. 2013, ApJ, 769, 21, doi: 10.1088/0004-637X/769/1/21

Sargent, A. I., & Beckwith, S. 1987, ApJ, 323, 294, doi: 10.1086/165827

Sargent, A. I., & Beckwith, S. V. W. 1991, ApJ, 382, L31, doi: 10.1086/186207

Segura-Cox, D. M., Schmiedeke, A., Pineda, J. E., et al. 2020, Nature, 586, 228, doi: 10.1038/s41586-020-2779-6

Shakura, N. I., & Sunyaev, R. A. 1973, A&A, 500, 33

Shu, F. H. 1977, ApJ, 214, 488, doi: 10.1086/155274

Shu, F. H., Adams, F. C., & Lizano, S. 1987, ARA&A, 25, 23, doi: 10.1146/annurev.aa.25.090187.000323

Sicilia-Aguilar, A., Henning, T., & Hartmann, L. W. 2010, ApJ, 710, 597, doi: 10.1088/0004-637X/710/1/597

Sierra, A., & Lizano, S. 2020, ApJ, 892, 136, doi: 10.3847/1538-4357/ab7d32

Snell, R. L., Loren, R. B., & Plambeck, R. L. 1980, ApJ, 239, L17, doi: 10.1086/183283

Speedie, J., Booth, R. A., & Dong, R. 2022, ApJ, 930, 40, doi: 10.3847/1538-4357/ac5cc0

Speedie, J., Dong, R., Hall, C., et al. 2024, arXiv e-prints, arXiv:2409.02196, doi: 10.48550/arXiv.2409.02196

Stadler, J., Benisty, M., Winter, A. J., et al. 2025, ApJ, 984, L11, doi: 10.3847/2041-8213/adb152

Stapper, L. M., Hogerheijde, M. R., van Dishoeck, E. F., et al. 2023, arXiv e-prints, arXiv:2312.03835. https://arxiv.org/abs/2312.03835

Stevenson, E. T., Ribas, Á., Speedie, J., Booth, R. A., & Clarke, C. J. 2024, MNRAS, 530, 4802, doi: 10.1093/mnras/stae1094

Sturm, J. A., Rosotti, G. P., & Dominik, C. 2020a, A&A, 643, A92, doi: 10.1051/0004-6361/202038919

—. 2020b, A&A, 643, A92, doi: 10.1051/0004-6361/202038919

Sullivan, C. B., & Kaszynski, A. 2019, Journal of Open Source Software, 4, 1450, doi: 10.21105/joss.01450

Szulágyi, J., Morbidelli, A., Crida, A., & Masset, F. 2014, ApJ, 782, 65, doi: 10.1088/0004-637X/782/2/65

Szulágyi, J., Plas, G. v. d., Meyer, M. R., et al. 2018, MNRAS, 473, 3573, doi: 10.1093/mnras/stx2602

Takeuchi, T., & Lin, D. N. C. 2002, ApJ, 581, 1344, doi: 10.1086/344437

Tang, Y. W., Guilloteau, S., Piétu, V., et al. 2012, A&A, 547, A84, doi: 10.1051/0004-6361/201219414

Tang, Y.-W., Guilloteau, S., Dutrey, A., et al. 2017, ApJ, 840, 32, doi: 10.3847/1538-4357/aa6af7

Tanigawa, T., Ohtsuki, K., & Machida, M. N. 2012, ApJ, 747, 47, doi: 10.1088/0004-637X/747/1/47

Teague, R. 2017, PhD thesis, Ruprecht-Karls University of Heidelberg, Germany

—. 2019a, The Journal of Open Source Software, 4, 1220, doi: 10.21105/joss.01220

—. 2019b, The Journal of Open Source Software, 4, 1632, doi: 10.21105/joss.01632

—. 2019c, Research Notes of the American Astronomical Society, 3, 74, doi: 10.3847/2515-5172/ab2125

Teague, R. 2020, richteague/keplerian_mask: Initial Release, 1.0, Zenodo, doi: 10.5281/zenodo.4321137

Teague, R., Bae, J., Bergin, E. A., Birnstiel, T., & Foreman-Mackey, D. 2018a, ApJ, 860, L12, doi: 10.3847/2041-8213/aac6d7

Teague, R., Bae, J., Birnstiel, T., & Bergin, E. A. 2018b, ApJ, 868, 113, doi: 10.3847/1538-4357/aae836

Teague, R., & Foreman-Mackey, D. 2018a, Research Notes of the American Astronomical Society, 2, 173, doi: 10.3847/2515-5172/aae265

—. 2018b, bettermoments: A robust method to measure line centroids, v1.0, Zenodo, Zenodo, doi: 10.5281/zenodo.1419754

Teague, R., Law, C., Huang, J., & Meng, F. 2021a, The Journal of Open Source Software, 6, 3827, doi: 10.21105/joss.03827

Teague, R., Bae, J., Aikawa, Y., et al. 2021b, ApJS, 257, 18, doi: 10.3847/1538-4365/ac1438

Teague, R., Bae, J., Andrews, S. M., et al. 2022, arXiv e-prints, arXiv:2208.04837. https://arxiv.org/abs/2208.04837

Teague, R., Benisty, M., Facchini, S., et al. 2025, ApJ, 984, L6, doi: 10.3847/2041-8213/adc43b

Terebey, S., Shu, F. H., & Cassen, P. 1984, ApJ, 286, 529, doi: 10.1086/162628

Terry, J. P., Hall, C., Longarini, C., et al. 2022, MNRAS, 510, 1671, doi: 10.1093/mnras/stab3513

Testi, L., Birnstiel, T., Ricci, L., et al. 2014, in Protostars and Planets VI, ed. H. Beuther, R. S. Klessen, C. P. Dullemond, & T. Henning, 339–361, doi: 10.2458/azu_uapress_9780816531240-ch015

The pandas development team. 2020, doi: 10.5281/zenodo.3509134

Thieme, T. J., Lai, S.-P., Lin, S.-J., et al. 2022, ApJ, 925, 32, doi: 10.3847/1538-4357/ac382b

Thompson, A. R., Moran, J. M., & Swenson, Jr., G. W. 2017, Interferometry and Synthesis in Radio Astronomy, 3rd Edition, doi: 10.1007/978-3-319-44431-4

Tomida, K., Machida, M. N., Hosokawa, T., Sakurai, Y., & Lin, C. H. 2017, ApJ, 835, L11, doi: 10.3847/2041-8213/835/1/L11

Turner, N. J., Fromang, S., Gammie, C., et al. 2014, in Protostars and Planets VI, ed. H. Beuther, R. S. Klessen, C. P. Dullemond, & T. Henning, 411–432, doi: 10.2458/azu_uapress_9780816531240-ch018

Ulrich, R. K. 1976, ApJ, 210, 377, doi: 10.1086/154840

Valdivia-Mena, M. T., Pineda, J. E., Segura-Cox, D. M., et al. 2022, A&A, 667, A12, doi: 10.1051/0004-6361/202243310

—. 2023, A&A, 677, A92, doi: 10.1051/0004-6361/202346357

van Cittert, P. H. 1934, Physica, 1, 201, doi: 10.1016/S0031-8914(34)90026-4

van den Ancker, M. E., The, P. S., Tjin A Djie, H. R. E., et al. 1997, A&A, 324, L33

van der Marel, N., Dong, R., di Francesco, J., Williams, J. P., & Tobin, J. 2019, ApJ, 872, 112, doi: 10.3847/1538-4357/aafd31

van der Marel, N., Birnstiel, T., Garufi, A., et al. 2021, AJ, 161, 33, doi: 10.3847/1538-3881/abc3ba

van der Velden, E. 2020, The Journal of Open Source Software, 5, 2004, doi: 10.21105/joss.02004

van Dishoeck, E. F., & Black, J. H. 1988, ApJ, 334, 771, doi: 10.1086/166877

van Gelder, M. L., Tabone, B., van Dishoeck, E. F., & Godard, B. 2021, A&A, 653, A159, doi: 10.1051/0004-6361/202141591

Veronesi, B., Lodato, G., Dipierro, G., et al. 2019, MNRAS, 489, 3758, doi: 10.1093/mnras/stz2384

Veronesi, B., Paneque-Carreño, T., Lodato, G., et al. 2021, ApJ, 914, L27, doi: 10.3847/2041-8213/abfe6a

Vigan, A., Bonavita, M., Biller, B., et al. 2017, A&A, 603, A3, doi: 10.1051/0004-6361/201630133

Villenave, M., Ménard, F., Dent, W. R. F., et al. 2020, A&A, 642, A164, doi: 10.1051/0004-6361/202038087

Virtanen, P., Gommers, R., Oliphant, T. E., et al. 2020, Nature Methods, 17, 261, doi: 10.1038/s41592-019-0686-2

Weber, P., Pérez, S., Benítez-Llambay, P., et al. 2019, ApJ, 884, 178, doi: 10.3847/1538-4357/ab412f

Weidenschilling, S. J. 1977, MNRAS, 180, 57, doi: 10.1093/mnras/180.2.57

Weintraub, D. A., Masson, C. R., & Zuckerman, B. 1989, ApJ, 344, 915, doi: 10.1086/167859

Whipple, F. L. 1972, in From Plasma to Planet, ed. A. Elvius, 211

Williams, J. P., & Cieza, L. A. 2011, ARA&A, 49, 67, doi: 10.1146/annurev-astro-081710-102548

Wilson, T. L., Rohlfs, K., & Hüttemeister, S. 2013, Tools of Radio Astronomy, doi: 10.1007/978-3-642-39950-3

Winn, J. N., & Fabrycky, D. C. 2015, ARA&A, 53, 409, doi: 10.1146/annurev-astro-082214-122246

Winter, A. J., Benisty, M., & Andrews, S. M. 2024, ApJ, 972, L9, doi: 10.3847/2041-8213/ad6d5d

Youdin, A. N. 2011, ApJ, 731, 99, doi: 10.1088/0004-637X/731/2/99

Youdin, A. N., & Goodman, J. 2005, ApJ, 620, 459, doi: 10.1086/426895

Zernike, F. 1938, Physica, 5, 785, doi: 10.1016/S0031-8914(38)80203-2

Zhang, S., & Zhu, Z. 2020, MNRAS, 493, 2287, doi: 10.1093/mnras/staa404

Zhang, S., Zhu, Z., Huang, J., et al. 2018, ApJ, 869, L47, doi: 10.3847/2041-8213/aaf744

Zhang, Y., Ginski, C., Huang, J., et al. 2023, A&A, 672, A145, doi: 10.1051/0004-6361/202245577

Zhou, Y., Bowler, B. P., Yang, H., et al. 2023, arXiv e-prints, arXiv:2308.16223, doi: 10.48550/arXiv.2308.16223

Zhu, Z., Andrews, S. M., & Isella, A. 2018, MNRAS, 479, 1850, doi: 10.1093/mnras/sty1503

Zhu, Z., Dong, R., Stone, J. M., & Rafikov, R. R. 2015, ApJ, 813, 88, doi: 10.1088/0004-637X/813/2/88

Zhu, Z., Hartmann, L., Nelson, R. P., & Gammie, C. F. 2012a, ApJ, 746, 110, doi: 10.1088/0004-637X/746/1/110

Zhu, Z., Stone, J. M., & Rafikov, R. R. 2012b, ApJ, 758, L42, doi: 10.1088/2041-8205/758/2/L42

Zhu, Z., & Zhang, R. M. 2022, MNRAS, 510, 3986, doi: 10.1093/mnras/stab3641

Zhu, Z., Zhang, S., Jiang, Y.-F., et al. 2019, ApJ, 877, L18, doi: 10.3847/2041-8213/ab1f8c

Ziampras, A., Ataiee, S., Kley, W., Dullemond, C. P., & Baruteau, C. 2020, A&A, 633, A29, doi: 10.1051/0004-6361/201936495

Zinnecker, H., & Yorke, H. W. 2007, ARA&A, 45, 481, doi: 10.1146/annurev.astro.44.051905.092549